

SPIN-ORBIT-COUPLED ULTRACOLD BOSONS IN CONTINUUM AND OPTICAL LATTICES

A Thesis Submitted

in Partial Fulfilment of the Requirements

for the Degree of

DOCTOR OF PHILOSOPHY

by

Pardeep Kaur

(2018PHZ0004)



DEPARTMENT OF PHYSICS

INDIAN INSTITUTE OF TECHNOLOGY ROPAR

September, 2023

Pardeep Kaur: *Spin-orbit-coupled Ultracold Bosons in Continuum and Optical Lattices*

Copyright ©2023, Indian Institute of Technology Ropar

All Rights Reserved

This thesis is dedicated to

My Parents

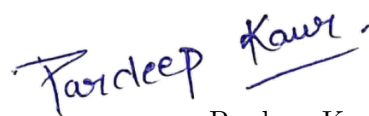
and

Waheguru

Declaration of Originality

I hereby declare that the work being presented in the thesis entitled “**Spin-orbit-coupled Ultracold Bosons in Continuum and Optical Lattices**” has been solely authored by me. It presents the result of my own independent investigation/research conducted during the time period from July 2018 to September 2023 under the supervision of Dr. Sandeep Gautam, Assistant Professor, IIT Ropar. To the best of my knowledge, it is an original work, both in terms of research content and narrative, and has not been submitted or accepted elsewhere, in part or in full, for the award of any degree, diploma, fellowship, associateship, or similar title of any university or institution. Further, due credit has been attributed to the relevant state-of-the-art and collaborations with appropriate citations and acknowledgements, in line with established ethical norms and practices. I also declare that any idea/data/fact/source stated in my thesis has not been fabricated/falsified/misrepresented. All the principles of academic honesty and integrity have been followed. I fully understand that if the thesis is found to be unoriginal, fabricated, or plagiarized, the Institute reserves the right to withdraw the thesis from its archive and revoke the associated Degree conferred. Additionally, the Institute also reserves the right to appraise all concerned sections of society of the matter for their information and necessary action (if any). If accepted, I hereby consent for my thesis to be available online in the Institute’s Open Access repository, inter-library loan, and the title & abstract to be made available to outside organizations.

September 2023



Pardeep Kaur

2018PHZ0004

PhD Research Scholar

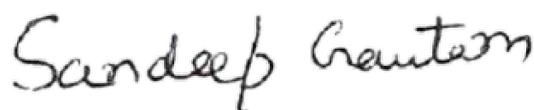
Department of Physics

Indian Institute of Technology Ropar

Certificate

This is to certify that the thesis entitled “**Spin-orbit-coupled Ultracold Bosons in Continuum and Optical Lattices**”, submitted by **Pardeep Kaur (2018PHZ0004)** for the award of the degree of **Doctor of Philosophy** of Indian Institute of Technology Ropar, is a record of bonafide research work carried out under my guidance and supervision. To the best of my knowledge and belief, the work presented in this thesis is original and has not been submitted, either in part or full, for the award of any other degree, diploma, fellowship, associateship or similar title of any university or institution.

In my opinion, the thesis has reached the standard of fulfilling the requirements of the regulations relating to the Degree.



Dr. Sandeep Gautam

Assistant Professor

Department of Physics

Indian Institute of Technology Ropar

Rupnagar, Punjab 140001

September 2023

Acknowledgements

The chapter of my PhD journey is coming to an end, and all I feel is gratitude towards countless people who have made this journey possible. I take this opportunity to express my sincere acknowledgement to them.

First and foremost, I am grateful to my supervisor Dr. Sandeep Gautam for giving me an opportunity to work with him and for his unwavering support at each and every step of my PhD. His valuable teachings have shaped my understanding of the subject matter and enhanced my research skills. I admire him as a scientist and also his teaching prowess. Without his guidance and support, this journey would not be possible.

I want to express my sincere thanks to Professor S.K. Adhikari for giving me the opportunity to work on collaborative projects with him. His wealth of research experience has been invaluable, and I've learned so much from him. I want to express my heartfelt thanks to Prof. Angom Dilip Kumar Singh whose broad research experience has helped me develop a scientific temperament. Next, I would like to thank Dr. Arko Roy, for sharing precious knowledge about academic writing and codes during the initial years of PhD. I extend my gratitude to Dr. Kuldeep Suthar who provided valuable input in our collaborative projects and enhanced my knowledge with fruitful discussions.

I would also like to thank my Doctoral Committee members at IIT Ropar, Dr. Sourav Bhattacharya, Dr. Rakesh Kumar, Dr. Partha Sharathi Dutta, Dr. Shankhadeep Chakraborty and chairperson Dr. Shubhrangshu Dasgupta for their careful evaluation of my progress during my PhD. I want to express my special thanks towards Dr. Subhendu Sarkar, Dr. Deepika Choudhary, Dr. Debangsu Roy and Dr. Vishwa Pal, for the wonderful interactions during my time of teaching assistantship with them. I am thankful to the IIT Ropar for financial support. I also thank the Department of Physics for the infrastructure. I would also like to acknowledge the help that I received from Anshu Sir, IT, Academic and Research section during my PhD.

I have been surrounded by very good friends who have made my PhD tenure fantastic and memorable. First of all, I would like to thank my group members cum friends, Paramjeet, Rajat and Ritu, for providing me with all the help that I ever needed. I especially thank Param for the memorable time we have spent together developing codes and chit-chatting on random topics. I would also like to express my sincere gratitude towards Sahil Dani, who has always been there for me. I have never come across such a selfless person. I always wish the best for you and will cherish our friendship forever. Raghav, Nitin and Mukesh, you guys have been great friends. Thank you for all the memories, help and discussions. I would like to thank Rakhi, Daman, Manju and Sanjay for all the conversations, party nights and memories. I feel extremely blessed to have come across and know Ajit. My words would not be enough to express my gratitude towards you. I consider myself fortunate to have friends from senior batches, particularly Anita Di, I thank her for abundant love, care, and blessings. I'd also like to extend my gratitude to

Megha Di, Shinki Di, and Nisika Di for the cherished memories we've created together. I count myself as fortunate to have friends from junior batches as well. Firstly, I'd like to express my gratitude to Prarena for her care, and discussions about our future goals. I thank Renu for being a cheerful friend and mess buddy. I'm truly thankful for Katyani, who happens to be my cute, angelic, and wonderful little sister. I would especially like to thank Poonam, for all the hospitality and care during my stay with her. Poonam, you are really very sweet. My special thanks go to Arpit Maurya, for being so kind and offering every help possible. I also extend my thanks to Rahul for all the scientific as well as non-scientific discussions. I thank all of my other juniors cum friends Nancy, Parkhi, Jaspreet, Soni, Pawan, Sanjit, Preet Kamal, Diksha, and Nitesh. I cannot express enough gratitude to my other friends outside of IIT Ropar, especially Deepak, Meghna, Rashmi, Saman, and Ajay; random chatting with you guys has always boosted my mood. I would like to thank Hrushi and Deepak from the bottom of my heart, for teaching me the basics of strongly correlated physics during my visit to PRL. I especially thank Deepak and Meghna for all the hospitality at PRL. You both have been adorable and wonderful friends. I also want to thank Soumik and Rukmani di for giving all the guidance and also the random treats.

At last, I cannot thank enough my Dad and Mom for blindly trusting me in every decision of my life, and for giving me the wings that any child desires. I am also thankful to my sibling, Kamal, for his selfless love and immense support. I am proud and lucky to have you all in my life. I shall always strive to make you guys proud and happy!!

Pardeep Kaur
Indian Institute of Technology Ropar,
India-140001
September 2023

Abstract

The spin-orbit coupling (SOC) is a central theme explored in several research endeavors due to its fascinating effects, including quantum spin-Hall states and topological insulators. It also has immense potential for use in various quantum devices and information processing. Among the spin-orbit-coupled (SO-coupled) physical systems, ultracold quantum gases with synthetic SOC are of special interest due to their pristine and tunable nature.

In this thesis, we have studied the Rashba SO-coupled spinor condensates in the continuum as well as optical lattices. Our study explores the emergence of self-trapped supersolid-like crystalline structures in a quasi-two-dimensional (q2D) SO-coupled spin-2 condensate. Different strengths of SOC and interatomic interactions result in a variety of nontrivial density patterns. For small SOC strengths, $\gamma \approx |c_0| \approx 0.5$ where γ and c_0 are (dimensionless) SOC and spin-independent interaction strengths, the ground state is an axisymmetric multiring soliton for polar, cyclic and weakly ferromagnetic interactions, whereas for stronger ferromagnetic interactions, a circularly asymmetric soliton emerges as the ground state. Depending on the values of interaction parameters, a stripe phase may emerge as the ground state with an increase in SOC strength. A triangular-lattice soliton can emerge in all magnetic phases, for $\gamma \approx 2|c_0| \approx 1$ in addition to the aforementioned solitons. Further increases in SOC strength result in a square-lattice and a superstripe soliton as quasidegenerate states. We have also demonstrated the spontaneous generation of spatially periodic supersolid-like superlattice and stripe solitons in q2D Rashba SO-coupled spin-1 and spin-2 *nonmagnetic* BECs, which are generally thought to be associated with spinor interactions. The emergence of all these solitons can be inferred from a study of solutions of the single-particle Hamiltonian.

In addition to this, we have studied quantum phase transitions of a two-dimensional two-component Bose-Hubbard model in the presence of a Rashba SOC, both with and without thermal fluctuations. Our analysis reveals that the interplay of single-particle hopping, the strength of the SOC, and the interspin interaction leads to superfluid phases with distinct properties. We have found that when the interspin interaction is weaker than the intraspin interaction, the SOC induces two finite-momentum superfluid phases. One of these is a phase-twisted superfluid that exists at low hopping strengths and reduces the domain of insulating phases. At higher hopping strengths, there is a transition from the phase-twisted to a finite-momentum stripe superfluid. On the other hand, when the interspin interaction is stronger than the intraspin interaction, the system exhibits a phase-twisted to a ferromagnetic phase transition. However, at finite temperatures, the thermal fluctuations destroy the phase-twisted superfluidity and lead to a wide region of normal-fluid states.

On the dynamics front, we have studied the quench dynamics in a two-component bosonic mixture within an optical lattice, finding qualitative differences from one-component Bose gas. We have examined quench dynamics across both first- and second-order Mott insulator (MI) to

superfluid (SF) phase transitions, observing critical slowing down of dynamics near the transition point in semblance with the Kibble-Zurek mechanism. In the case of second-order MI-SF transitions with homogeneous lattice-site distributions in the MI phase, our numerical simulations yield dynamical critical exponents close to mean-field predictions.

Contents

List of Figures	xviii
List of Tables	xx
List of Abbreviations	xxi
1 Introduction	1
1.1 Background	1
1.2 Scalar BEC	2
1.2.1 Mean-field theory	3
1.3 Spinor BEC	5
1.3.1 Mean-field model for a spin-1 BEC	6
1.3.2 Mean-field model for a spin-2 BEC	8
1.3.3 Spin-orbit-coupled spinor condensates	10
1.4 Solitons	15
1.5 Supersolid-like structures	17
1.6 Optical lattice	19
1.6.1 Bose-Hubbard model	20
1.6.2 Quantum quench dynamics	22
1.7 Outline of the thesis	23
2 Supersolid-like solitons in spin-orbit-coupled condensates	25
2.1 Mean-field model for spin-orbit-coupled spin-2 BEC	26
2.1.1 Phase requirement	28

2.1.2	Single-particle Hamiltonian	31
2.2	Numerical results	34
2.2.1	Small SOC strength	37
2.2.2	Intermediate SOC strength	40
2.2.3	Large SOC strength	41
2.2.4	Dynamical stability	44
2.2.5	Bifurcations	46
2.2.6	Experimentally feasible bright solitons	47
2.2.7	Spin texture	48
2.2.8	Moving $(-2, -1, 0, +1, +2)$ -type soliton	48
2.3	Non-magnetic spinor condensates	51
2.4	Mean-field model for nonmagnetic case	52
2.5	Numerical results for nonmagnetic condensates	54
2.5.1	Nonmagnetic q2D solitons in an SO-coupled spin-1 BEC	54
2.5.2	Nonmagnetic q2D solitons in an SO-coupled spin-2 BEC	59
2.6	Summary	62
3	Spin-orbit-coupling-driven superfluid phases in optical lattices	65
3.1	The Model and the method	66
3.1.1	Weakly interacting limit	69
3.2	Quantum phases and order parameters	69
3.3	Results and discussion	72
3.3.1	$U_{\uparrow\downarrow} = 0.5$	73
3.3.2	$U_{\uparrow\downarrow} = 1.5$	79
3.4	Finite temperature	81
3.4.1	Finite-temperature results for $U_{\uparrow\downarrow} = 0.5$	82
3.4.2	Finite-temperature results for $U_{\uparrow\downarrow} = 1.5$	85
3.5	Conclusions	86
4	Out-of-equilibrium dynamics of Bose-Bose mixtures in optical lattices	87
4.1	Two-component Bose-Hubbard Hamiltonian	89
4.1.1	Equilibrium phase diagrams	89

4.2	Quench dynamics	92
4.2.1	Time-dependent Gutzwiller approach	92
4.2.2	Kibble-Zurek mechanism	94
4.3	Results and discussion	96
4.3.1	$U_{\uparrow\downarrow} = 0.5$	96
4.3.2	$U_{\uparrow\downarrow} = 0.9$	102
4.3.3	$U_{\uparrow\downarrow} = 1.5$	103
4.4	Conclusions	105
5	Summary and future outlook	107
5.1	Thesis summary	107
5.2	Future directions	109
A	Coupled Gross-Pitaevskii equations for an SO-coupled spin-1 BEC	111
A.1	Important conserved quantities of a spin-1 BEC	112
A.2	Chemical potential	113
A.3	Dimensionless formulation of three-dimensional CGPEs	113
A.4	Dimensionless CGPEs for a q2D spin-1 BEC	114
A.5	Dimensionless CGPEs for a q1D spin-1 BEC	115
B	Fourier pseudospectral method to solve CGPEs	117
B.1	Solution of q1D CGPEs	117
B.2	Solution of q2D CGPEs	120
B.3	Solution of 3D CGPEs	122
B.4	Discretization scheme	123
B.5	Imaginary-time propagation	124
C	FORTTRAN programs for solving the CGPEs for spin-1 BECs	125
C.1	Modules	125
C.2	Functions and subroutines	127
C.3	2D and 3D programs	128
C.4	Running the programs	128

C.5	Description of output files	128
C.6	Output samples from the codes	129
C.7	OpenMP parallelization	130
D	Sample numerical results	133
D.1	Results for q1D spin-1 BECs	133
D.1.1	Without SOC, $\gamma_x = 0$	133
D.1.2	With SOC, $\gamma_x \neq 0$	134
D.2	Real-time check	136
D.3	Results for q2D and 3D spin-1 BECs	138
	List of Publications	142

List of Figures

1.1	(Color online) Three lower energy states are coupled to the higher energy state using two Raman lasers of nearly the same frequency. Raman lasers effectively generate spatially-varying coupling between $ - 1 \rangle$ and $ 0 \rangle$, and between $ 0 \rangle$ and $ + 1 \rangle$ states through second-order process [1, 2].	12
2.1	(Color online) The c_2 vs c_1 phase plot (not to scale) illustrating ferromagnetic, antiferromagnetic, and cyclic phases in the absence of SOC.	28
2.2	(Color online) Contour plot of eigenenergy $E(k_x, k_y)$ in Eq. (2.18) for $\gamma = 1$. The minimum corresponding to $k_x^2 + k_y^2 = 4$ is a circle of radius 2. A typical \mathbf{k} with magnitude 2 and oriented at a polar angle φ is also shown.	33
2.3	(Color online) 2D contour plots of densities of the components $j = \pm 2, \pm 1$, and 0 and total density corresponding to Φ_{ST} (stripe) are shown in panels (a)-(d) for SOC strength $\gamma = 1$. The same for Φ_{TL} (triangular lattice), Φ_{SL} (square lattice), and Φ_{MR} (multiring) are shown in (e)-(h), (i)-(l), and (m)-(p), respectively. . . .	34

- 2.4 (Color online) The c_2 vs γ phase plots for the ground states are shown (a) for the ferromagnetic phase with $c_0 = -0.5$ and $c_1 = -0.025$ and (b) for the cyclic and polar phases with $c_0 = -0.5$ and $c_1 = 0.025$. In subfigure (a) for small SOC strengths the axisymmetric $(-2, -1, 0, +1, +2)$ state is the ground state similar to the state shown in Figs. 2.5(a)-2.5(d), whereas for larger SOC strengths the asymmetric soliton state is the ground state similar to the state shown in Figs. 2.6(f)-2.6(j). In subfigure (b) for small SOC strengths the axisymmetric $(-2, -1, 0, +1, +2)$ state is the ground state similar to the state shown in Figs. 2.5(a)-2.5(d), whereas for larger SOC strengths the ST (stripe) soliton state is the ground state similar to the state shown in Figs. 2.9(a)-2.9(d). Difference in energy of other quasidegenerate solitons from these ground states is $\gtrsim 10^{-4}$. As an illustration, one of the quasidegenerate states is the TL (triangular lattice) state similar to the state shown in Figs. 2.7(a)-2.7(d), which occupies a narrow region near $\gamma = 1$ and is shown by a red shaded strip. The energy differences between the TL state and the $(-2, -1, 0, +1, +2)$ -type multiring ground state in plots (a) and (b) are 10^{-4} - 10^{-3} . The energies have been obtained by using Eq. (2.6) in Sec. 2.1. 36
- 2.5 (Color online) Contour plot of density of the components (a) $j = \pm 2$, (b) $j = \pm 1$, (c) $j = 0$, and (d) total density of an axisymmetric $(-2, -1, 0, +1, +2)$ -type multiring soliton with $c_0 = -0.5$, $c_1 = -0.025$, $c_2 = 0.25$ (ferromagnetic phase), and $\gamma = 0.5$ with energy $E = -0.4992$. The energy has been obtained by using Eq. (2.6) in Sec. 2.1. 37
- 2.6 (Color online) Contour plot of density of components (a) $j = +2$, (b) $j = +1$, (c) $j = 0$, (d) $j = -1$, and (e) $j = -2$ of an axisymmetric $(-1, 0, +1, +2, +3)$ -type multiring soliton with $c_0 = -0.5$, $c_1 = -0.025$, $c_2 = 0.25$ (ferromagnetic phase), $\gamma = 0.5$, and energy $E = -0.4991$, and the same of a circularly asymmetric soliton with $c_0 = -0.5$, $c_1 = -0.1$, $c_2 = 0.25$ (strongly ferromagnetic phase), $\gamma = 0.5$, and energy $E = -0.4996$ in panels (f)-(j). The energies have been obtained by using Eq. (2.6) in Sec. 2.1. 39

2.7	(Color online) Contour plot of density of components (a) $j = \pm 2$, (b) $j = \pm 1$, (c) $j = 0$, and (d) total density of a triangular-lattice soliton with $c_0 = -0.5$, $c_1 = 0.025$, $c_2 = 0.25$ (cyclic phase), $\gamma = 1$, and energy $E = -1.9989$, and the same of a $(-2, -1, 0, +1, +2)$ -type multiring soliton for the same parameters and $E = -1.9990$ in panels (e)-(h). The energies have been obtained by using Eq. (2.6) in Sec. 2.1.	40
2.8	(Color online) Contour plot of density of a square-lattice soliton of components (a) $j = \pm 2$, (b) $j = \pm 1$, (c) $j = 0$, and (d) total density for $c_0 = -0.5$, $c_1 = -0.025$, $c_2 = 0.25$ (ferromagnetic phase), $\gamma = 4$, and $E = -31.9988$; for the same parameters, we show the component and total densities of a $(-2, -1, -0, +1, +2)$ -type multiring soliton in panels (e)-(h) with $E = -31.9999$. The energies have been obtained by using Eq. (2.6) in Sec. 2.1.	41
2.9	(Color online) Contour plot of the density of a stripe soliton of components (a) $j = \pm 2$, (b) $j = \pm 1$, (c) $j = 0$, and (d) total density with $c_0 = -0.5$, $c_1 = 0.025$, $c_2 = 0.25$ (cyclic phase), $\gamma = 4$, and $E = -32.0006$; the same of a square-lattice soliton for the same parameters in panels (e)-(h) with $E = -31.9990$. The energies have been obtained by using Eq. (2.6) in Sec. 2.1.	43
2.10	(Color online) Contour plot of the density of a square-lattice soliton of components (a) $j = \pm 2$, (b) $j = \pm 1$, (c) $j = 0$, and (d) total density with $c_0 = -0.5$, $c_1 = 0.025$, $c_2 = -0.25$ (polar phase), $\gamma = 4$, and $E = -31.9987$, and the same of a superstripe soliton for the same parameters in panels (e)-(h) with $E = -32.0023$. The energies have been obtained by using Eq. (2.6) in Sec. 2.1.	44
2.11	(Color online) Contour plot of component densities of the triangular-lattice soliton of Figs. 2.7(a)-(d) for components (a) $j = \pm 2$, (b) $j = \pm 1$, (c) $j = 0$, and (d) total density after 100 units of time, and the same of the square-lattice soliton of Figs. 2.8(a)-(d) for components (e) $j = \pm 2$, (f) $j = \pm 1$, (g) $j = 0$, and (h) total density, after real-time simulation over 100 units of time. The initial state used in real-time propagation is obtained by adding a random noise (2.21) to the stationary-state imaginary-time solutions shown in Figs. 2.7(a)-(d) for panels (a)-(d) and Figs. 2.8(a)-(d) for panels (e)-(h). The energies have been obtained by using Eq. (2.6) in Sec. 2.1.	45

- 2.12 (Color online) (a) The bifurcation diagram in the ΔE - γ plane for the ferromagnetic phase corresponding to a cut in the phase diagram in Fig. 2.4(a) at $c_2 = 0.15$. The same for the cyclic phase is shown in panel (b) by taking a cut at $c_2 = 0.15$ in the phase diagram in Fig. 2.4(b). In the polar domain of the phase diagram in Fig. 2.4(b), a cut is taken at $c_2 = -0.15$, and the bifurcation picture is shown in panel (c). $\Delta E = E + 2\gamma^2$, where E is the energy of the state obtained from Eq. (2.6) in Sec. 2.1 and $-2\gamma^2$ is the single-particle solution's energy, corresponding to various quasidegenerate states, is plotted by using different symbols as well as different colors. SST corresponds to the superstripe similar to the state shown in Figs. 2.10(e)-(h), SL corresponds to the square lattice similar to the state shown in Figs. 2.8(a)-(d), TL corresponds to the triangular lattice similar to the state shown in Figs. 2.7(a)-(d), MR corresponds to the $(-2, -1, 0, +1, +2)$ -type multiring solution similar to the state shown in Figs. 2.5(a)-(d), EMR corresponds to the $(-1, 0, +1, +2, +3)$ -type excited-state multiring solution similar to the state shown in Figs. 2.6(a)-(e), ST corresponds to the stripe solution similar to the state shown in Figs. 2.9(a)-(d), and ASYMM corresponds to the circularly asymmetric solution similar to the state shown in Figs. 2.6(f)-(j). 46
- 2.13 (Color online) Contour plot of density ρ_j of a $(-1, 0, +1)$ -type multiring SO-coupled BEC soliton for components (a) $\rho_{\pm 1}$, (b) ρ_0 , and (c) total density ρ for $c_0 = -0.84$, $c_1 = 7.80$, and $\gamma = 1$ 47
- 2.14 (Color online) Spin-texture for (a) $(-2, -1, 0, +1, +2)$ multiring soliton, (b) circularly asymmetric soliton, and (c) stripe soliton. In (a) $F_z(x, y)$ is zero throughout and in (c) \mathbf{F} has a reflection symmetry about $x = 0$ line. The spin textures in (a), (b), and (c) correspond to the densities shown in Fig. 2.5, Figs. 2.6(f)-(j), and Figs. 2.9(a)-(d), respectively. 48
- 2.15 (Color online) Contour plot of density of components (a) $j = +2$, (b) $j = +1$, (c) $j = 0$, (d) $j = -1$, and (e) $j = -2$ with $c_0 = -2.5$, $c_1 = -0.025$, $c_2 = 0.25$, and $\gamma = 0.5$ moving with $v = 0.03$ along $+y$, and the same densities for velocity $v = 0.1$ in panels (f)-(j). 50

2.16	(Color online) Contour plot of time evolution of total density $\rho(0, y, t)$ as a function of y and t during the head-on collision between the two solitons with $c_0 = -2.5$, $c_1 = -0.025$, $c_2 = 0.25$, and $\gamma = 0.5$ moving with velocity (a) $ v = \pm 0.03$ and (b) $ v = \pm 0.1$ along the y axis in the opposite direction.	50
2.17	The c_0 - γ phase plot illustrating the collapse and soliton formation.	55
2.18	The $\delta E \equiv E + \gamma^2/2$ vs γ phase plot for Rashba SO-coupled $(-1, 0, +1)$ -, $(0, +1, +2)$ -type multiring, asymmetric, stripe, and square-lattice solitons. E is the energy of various states calculated using Eq. (2.28) in Sec. 2.4	56
2.19	Top row: (a) component density of $j = \pm 1$, (b) $j = 0$, and (c) total density ρ of a $(-1, 0, +1)$ -type multiring soliton of the SO-coupled spin-1 BEC with $c_0 = -0.6$ and $\gamma = 4$. Similarly, middle row: (d) component density of $j = +1$, (e) $j = 0$, and (f) $j = -1$ of a $(0, +1, +2)$ -type multiring soliton of the BEC with the same interaction and coupling strengths. Bottom row: phase distributions of wave-function components (g) ϕ_{+1} , (h) ϕ_{-1} of the $(-1, 0, +1)$ -type multiring BEC soliton and those of wave-function components (i) ϕ_0 , (j) ϕ_{-1} of the $(0, +1, +2)$ -type multiring BEC soliton. E is calculated using Eq. (2.28) in Sec. 2.4	57
2.20	Top row: (a) component density of $j = +1$, (b) $j = 0$, and (c) $j = -1$ of an asymmetric soliton of the SO-coupled spin-1 BEC with $c_0 = -0.6$ and $\gamma = 4$. Middle row: (d) component density of $j = \pm 1$, (e) $j = 0$, and (f) total density ρ of a stripe soliton and bottom row: (g) component density of $j = \pm 1$, (h) $j = 0$, and (i) total density ρ of a square-lattice soliton for the same interaction and coupling strengths. E is calculated using Eq. (2.28) in Sec. 2.4	58
2.21	The $\delta E \equiv E + 2\gamma^2$ vs γ phase plot for Rashba SO-coupled $(-2, -1, 0, +1, +2)$ - and $(-1, 0, +1, +2, +3)$ -type multiring, asymmetric, triangular-lattice, stripe, and square-lattice solitons. E is calculated using Eq. (2.6) in Sec. 2.1.	59
2.22	Upper row: (a) component density $\rho_{\pm 2}$, (b) $\rho_{\pm 1}$, (c) ρ_0 , and (d) total density ρ of a $(-2, -1, 0, +1, +2)$ -type multiring soliton of the SO-coupled spin-2 BEC with $c_0 = -0.2$ and $\gamma = 4$. Lower row: phase distributions of wave-function components (e) ϕ_{+2} , (f) ϕ_{+1} , (g) ϕ_{-1} , and (h) ϕ_{-2} in the same soliton. E is calculated using Eq. (2.6) in Sec. 2.1	60

2.23	Upper row: (a) component density ρ_{+2} , (b) ρ_{+1} , (c) ρ_0 , (d) ρ_{-1} , and (e) ρ_{-2} of a $(-1, 0, +1, +2, +3)$ -type multiring soliton of the SO-coupled spin-1 BEC with $c_0 = -0.2$ and $\gamma = 4$. Bottom row: (f) component density ρ_{+2} , (g) ρ_{+1} , (h) ρ_0 , (i) ρ_{-1} , and (j) ρ_{-2} of an asymmetric soliton for the same interaction and coupling strengths. E is calculated using Eq. (2.6) in Sec. 2.1.	61
2.24	(a) Component density $\rho_{\pm 2}$, (b) $\rho_{\pm 1}$, (c) ρ_0 , and (d) total density ρ of a triangular-lattice soliton of the SO-coupled spin-2 BEC with $c_0 = -0.2$ and $\gamma = 1$. E is calculated using Eq. (2.6) in Sec. 2.1	61
2.25	Upper row: (a) component density $\rho_{\pm 2}$, (b) $\rho_{\pm 1}$, (c) ρ_0 , and (d) total density ρ of a stripe soliton with $c_0 = -0.2$ and $\gamma = 4$. Lower row: (a) component density $\rho_{\pm 2}$, (b) $\rho_{\pm 1}$, (c) ρ_0 , and (d) total density ρ of a square-lattice soliton with the same c_0 and γ . E is calculated using Eq. (2.6) in Sec. 2.1	62
3.1	Noninteracting band structure of the 2D square optical lattice for two regimes. (a) The case $\gamma/J = 0$ represents the single minimum at $\mathbf{k} = 0$ in the absence of SOC. The other case in (b) is shown for finite SOC of $\gamma/J = 8$, where the competition between γ and J determines the band structure. Here the SOC breaks the rotational symmetry and the minima occur at four finite wave vectors in the lower branch. This is evident from the projection of the lower-energy branch onto the k_x - k_y plane. As γ/J decreases, the minimum of the lower branch tends to approach $\mathbf{k} = 0$	70

3.2	Zero-temperature ground-state phase diagram in the presence of Rashba SOC for various SOC strengths: (a) $\gamma = 0U$, (b) $\gamma = 0.02U$, (c) $\gamma = 0.03U$, and (d) $\gamma = 0.04U$. The Mott insulator regime is represented by MI(n), where $n = n^\uparrow + n^\downarrow$ is the total filling or occupancy of the lobe. The interspin interaction $U_{\uparrow\downarrow} = 0.5U$. At $\gamma = 0$, the system exhibits an MI-SF transition, where the SF phase Bose condenses at zero momentum and hence is referred to as the ZM-SF state. The finite γ results in finite-momentum superfluid phases. Here as J is varied, the system undergoes the PT-ST superfluid phase transition, shown by blue dashed lines. The phase diagrams are obtained using random complex initial states with 50 random configurations. The system size $L = 8 \times 8$ and periodic boundary conditions are considered.	73
3.3	The lattice-site distributions of the phase variation and spin-dependent momentum distributions of various superfluid states. The upper panel represents the phase distributions for (a) PT, (b) ST, and (c) ZM superfluid whereas the lower panel (d)-(f) the corresponding momentum distributions. The finite-momentum superfluids are obtained using the Gutzwiller mean-field approach for $\gamma = 0.02U$ and $\mu = 1.5U$. The hopping amplitude in terms of U corresponding to PT and ST are 0.015 and 0.04, respectively. The (c) ZM superfluid is plotted for $\gamma = 0$, $\mu = 1.5$, and $J = 0.04U$. The spatial variation of phase and momentum distributions are shown for one of the components, as the other component also has the similar distributions. The peak in the spin-dependent momentum distributions appears at $\mathbf{k} \neq 0$ for (d) PT and (e) ST states, whereas for (f) ZM superfluid it appears at $\mathbf{k} = 0$. Here, a is the lattice constant.	76
3.4	Evolution of the order parameter Φ , characterizing the finite-momentum PT and ST superfluid states, as a function of the hopping strength J/U . The chemical potential $\mu/U = 1.8$ and interspin interaction $U_{\uparrow\downarrow} = 0.5U$. The Φ is defined in Sec. 3.2. The variation in Φ from zero to a finite value shows the PT(MI)-ST phase transition.	78

- 3.5 Lattice-site distributions in the ST_{den} phase obtained using the cluster Gutzwiller approach. The (a) occupancy, (b) amplitude of the order parameter, and (c) phase of a ST_{den} state are shown. The parameters are $\gamma = 0.02U$, $\mu = 1.8U$, and $J = 0.05U$. These distributions are shown for interspin interaction $U_{\uparrow\downarrow} = 0.5U$. . 79
- 3.6 Zero-temperature ground-state phase diagram in the presence of Rashba SOC for various SOC strengths: (a) $\gamma = 0U$, (b) $\gamma = 0.02U$, (c) $\gamma = 0.03U$, and (d) $\gamma = 0.04U$. The filling or occupancy of the Mott lobe is represented by n in $\text{MI}(n)$. The interspin interaction $U_{\uparrow\downarrow} = 1.5U$. The superfluidity near the MI lobes is twisted in character, while at higher J the system is in the zFM state. . 80
- 3.7 Width of the first Mott lobe $\text{MI}(1)$ at $J = 0.01U$ as a function of temperature for various SOC strengths. The values of γ in units of U are shown in the legend. Here the interspin interaction $U_{\uparrow\downarrow} = 0.5U$. At lower temperatures, the melting of the MI lobe depends on the value of γ , and at higher $k_B T$ the width remains similar to the $\gamma = 0$ case. For all cases, with and without SOC, the $\text{MI}(1)$ phase completely melts and replaced by NF phase at $k_B T/U \approx 0.046$ 83
- 3.8 Finite-temperature phase diagram of the TBHM for different values of γ at $k_B T/U = 0.03$: (a) $\gamma = 0U$, (b) $\gamma = 0.02U$, (c) $\gamma = 0.03U$, and (d) $\gamma = 0.04U$. The interspin interaction $U_{\uparrow\downarrow} = 0.5U$. The shaded green bands are the insulating MI regions which are distinguished from the NF phase present at finite T . The reemergence of insulating regimes and destruction of PT superfluidity at finite temperatures are observed. The constant width of $\text{MI}(1)$ for both zero and finite SOC confirms the behavior reported in Fig. 3.7. The blue dashed line represents the PT-ST superfluid phase transition obtained using the finite-temperature Gutzwiller mean-field approach. 84

- 3.9 Finite-temperature phase diagram of the TBHM for different values of SOC strengths at $U_{\uparrow\downarrow} = 1.5U$: (a) $\gamma = 0U$, (b) $\gamma = 0.02U$, (c) $\gamma = 0.03U$, and (d) $\gamma = 0.04U$. The shaded green bands represent the residual insulating domains in the presence of thermal fluctuations. Outside the bands tiny white regions show the NF phase. The thermal energy corresponding to temperature is $k_B T/U = 0.03$. The finite temperature stabilizes the MI phases against the SOC and suppress the finite-momentum superfluidity. This is evident from (c) and (d), as compared to the corresponding zero temperature cases shown in Figs. 3.6(c)-3.6(d). 85
- 4.1 Phase diagrams of the TBHM in J - μ plane for (a) $U_{\uparrow\downarrow} = 0.5$ and (b) $U_{\uparrow\downarrow} = 0.9$. The number in parentheses is the total average atomic occupancy. The phase transitions across all boundaries are of second order except for the green curve in (b) across which the MI(2) to SF transition is of the first order in nature. For $U_{\uparrow\downarrow} = 0.9$, the $|\Phi|$ as a function of J are shown for (c) the MI(1)-SF transition at $\mu = 0.39$ and (d) the MI(2)-SF transition at $\mu = 1.32$. In the panels (e)-(h), sample atomic occupancy distributions ($n_{p,q}^\alpha$) of both components on an 8×8 square lattice are shown. (e) and (g) correspond to $n_{p,q}^\uparrow$ and $n_{p,q}^\downarrow$, respectively, in the MI(1) phase. The same for the MI(2) phase are shown in (f) and (h). 90
- 4.2 (a) The phase diagram of the TBHM in $J - \mu$ plane in the immiscible regime. (b) The variation of $|\Phi|$ as a function of J with $\mu = 0.415$, corresponding to the MI(1)-SF phase transition and (c) with $\mu = 1.45$ corresponding to the MI(2)-SF transition; these are plotted for $U_{\uparrow\downarrow} = 1.5$. The sample $n_{p,q}^\uparrow$ distributions in (d) MI(1), (e) MI(2), and (f) SF phases for $U_{\uparrow\downarrow} = 1.5$. Similarly, corresponding $n_{p,q}^\downarrow$ distributions are in (g), (h), and (i). 92
- 4.3 The time evolution of $|\Phi|$ for the MI(2)-SF transition with $U_{\uparrow\downarrow} = 0.5$, $\mu = 1$, and $\tau_Q = 100$. Blue points indicate temporal markers referred to in the main text. In the inset, we show the enlarged view of the dynamical evolution at shorter times from $t = 20$ to $t = 200$. $|\Phi|$ is nearly zero for $t < \hat{t} = 31$ 97

4.4	$ \phi_{p,q}^\uparrow $ at (a) $t = -100$, (b) $t = 31$, (c) $t = 160$, and (d) $t = 2000$ for the MI(2)-SF phase transitions corresponding to the time evolution in Fig. 4.3. Similarly, $ \phi_{p,q}^\downarrow $ at the same instants are in panels (e)-(h). Phases corresponding to $ \phi_{p,q}^\uparrow $ in panels (a)-(d) are shown in panels (i)-(l), and the same for $ \phi_{p,q}^\downarrow $ in panels (e)-(h) are in panels (m)-(p).	98
4.5	For the MI(2)-SF transition with $U_{\uparrow\downarrow} = 0.5$: (a) \hat{t} as a function of τ_Q on a log-log scale with the critical exponent of 0.49 ± 0.01 and (b) E_{res} as a function of τ_Q on the log-log scale with -0.46 ± 0.02 as the critical exponent. (c) and (d) are, similarly, the \hat{t} and E_{res} as functions of τ_Q on the log-log scale for MI(1)-SF transition with $U_{\uparrow\downarrow} = 0.5$	99
4.6	$ \Phi $ as a function of time t for the MI(1)-SF transitions at $U_{\uparrow\downarrow} = 0.5$, $\mu = 0.25$, and $\tau_Q = 100$. Blue points are the temporal markers referred to in the main text. $ \Phi $ remains nearly zero for $t < \hat{t} = 116$. The hopping quench is performed until $t = 130$. The exponential increase in $ \Phi $ followed by oscillations are shown in the inset with t varying from $t = 0$ to $t = 200$	100
4.7	$ \phi_{p,q}^\uparrow $ at (a) $t = -100$, (b) $t = 116$, (c) $t = 155$, and (d) $t = 2000$ for the MI(1)-SF phase transitions corresponding to the time evolution in Fig. 4.6. Similarly, $ \phi_{p,q}^\downarrow $ at the same instants are in panels (e)-(h). Phases corresponding to $ \phi_{p,q}^\uparrow $ in panels (a)-(d) are shown in panels (i)-(l), and the same for $ \phi_{p,q}^\downarrow $ in panels (e)-(h) are in panels (m)-(p).	101
4.8	For the first-order MI(2)-SF phase transition at $U_{\uparrow\downarrow} = 0.9$ and $\mu = 1.33$: (a) \hat{t} as a function of τ_Q with the critical exponent of 0.36 ± 0.02 and (b) E_{res} as a function of τ_Q on log-log scale with -0.35 ± 0.02 as the critical exponent.	102
4.9	The evolution of $ \Phi $ with t for the MI(2)-SF transitions at $U_{\uparrow\downarrow} = 1.5$, $\mu = 1.45$, and $\tau_Q = 100$. Blue points indicate the temporal markers referred to in the main text. $ \Phi $ is close to zero until $\hat{t} = 67$. The exponential increase in $ \Phi $ followed by oscillations are shown in the inset with t varying from $t = 0$ to $t = 150$	103

4.10	$ \phi_{p,q}^\uparrow $ at (a) $t = -100$, (b) $t = 67$, (c) $t = 130$, and (d) $t = 2000$ for MI(2)-SF phase transitions corresponding to the time evolution in Fig. 4.9. Similarly, $ \phi_{p,q}^\downarrow $ at the same instants are in panels (e)-(h). Phases corresponding to $ \phi_{p,q}^\uparrow $ in panels (a)-(d) are shown in panels (i)-(l), and the same for $ \phi_{p,q}^\downarrow $ in panels (e)-(h) are in panels (m)-(p).	104
4.11	For MI(2)-SF phase transition at $U_{\uparrow\downarrow} = 1.5$: (a) \hat{t} as a function of τ_Q with the critical exponent of 0.76 ± 0.01 and (b) E_{res} as a function of τ_Q on log-log scale with -0.29 ± 0.01 as the critical exponents. The critical exponents are similar to those displayed in Figs. 4.5(c)-(d).	105
C.1	(Color online) (a) Execution times for 1000 iterations (in seconds) as a function of the number of threads for 1D code compiled with GNU Fortran 5.4.0 and Intel Fortran 19.1.0.166 compilers for imaginary- and real-time propagation. (b) and (c) are the same for 2D and 3D codes.	131
C.2	(Color online) Speedup and efficiency as a function of number of threads n are shown for imaginary- (left column) and real-time propagation (right column). The top, middle, and bottom row figures show the results for 1D, 2D, and 3D codes, respectively.	132
D.1	(Color online) Absolute values of component wave functions $ \phi_j(x) $ in the ground state of ^{87}Rb for (a) $M = 0$ and (b) $M = 0.5$. (c) and (d) are the same for ^{23}Na with $M = 0$ and $M = 0.5$, respectively. These are in agreement with [3, 4].	136
D.2	(Color online) Ground-state density of SO-coupled ^{87}Rb for (a) $\gamma_x = 0.5$, (b) $\gamma_x = 1$. (c) and (d) are the same for ^{23}Na with $\gamma_x = 0.5$ and $\gamma_x = 1.0$, respectively. $M = 0$ in all the cases.	137
D.3	(Color online) (a) Ground-state density of an SO-coupled spin-1 BEC with $c_0 = -1.5, c_1 = -0.3$ in the absence of trap and $\gamma_x = 1$. (b) The same for $c_0 = -1.2, c_1 = 0.3$. These results are in agreement with Ref. [5] and correspond to $M = 0$	139
D.4	(Color online) (a) Root-mean-square sizes of the three components of ^{87}Rb with $c_0 = -1.5, c_1 = -0.3$ and $\gamma_x = 0.5$ in the absence of trap as a function of time. (b) The energy of the vector soliton as a function of time.	139

D.5	The 2D contour plot of densities of (a) $m_f = +1$, (b) $m_f = 0$, and (c) $m_f = -1$ components of an asymmetric vortex-bright soliton with $c_0 = -4$, $c_1 = -0.6$, and $\gamma_x = \gamma_y = 0.5$. The corresponding phases are shown in (d) for $m_f = +1$, (e) for $m_f = 0$, and (f) for $m_f = -1$ components.	140
D.6	The 2D contour plots of densities of components in $z = 0$ plane for (a) $m_f = +1$, (b) $m_f = 0$, and (c) $m_f = -1$ of an asymmetric vortex-bright soliton with $c_0 = -10$, $c_1 = -1$, and $\gamma_x = \gamma_y = \gamma_z = 1$. The corresponding phases are shown in (d) for $m_f = +1$, (e) for $m_f = 0$, and (f) for $m_f = -1$ components.	141

List of Tables

4.1	The $J(\hat{t})$ for different τ_Q s during quench dynamics from MI(2) to SF phase with $\mu = 1$ and $U_{\uparrow\downarrow} = 0.5$. The critical value of hopping strength J_c is 0.042.	99
4.2	The $J(\hat{t})$ for different τ_Q 's during the quench dynamics from MI(1) to SF phase with $\mu = 0.25$ and $U_{\uparrow\downarrow} = 0.5$. The critical hopping strength is $J_c = 0.0268$	100
D.1	Ground-state energies for ^{87}Rb and ^{23}Na q1D BECs obtained using FORTRESS [6] with $\Delta x \leq 0.015625$ and $\Delta t \approx 0.1\Delta x^2$ along with the same from Ref. [3] for the various values of magnetization M	134
D.2	Comparison of the ground-state energy of q1D ^{87}Rb condensate reported in Ref. [4] with the value obtained using FORTRESS [6] with $\Delta x \leq 0.015625$ and $\Delta t \approx 0.1\Delta x^2$	134
D.3	Comparison of the chemical potential values for ^{87}Rb and ^{23}Na condensate reported in Ref. [3] with the values obtained using FORTRESS [6] with $\Delta x = 0.0025$, $\Delta t = 0.0000095$. For ^{23}Na , $\mu = (\mu_{+1} + \mu_{-1})/2$, whereas for ^{87}Rb $\mu = \mu_0 = \mu_{\pm 1}$	135
D.4	Ground-state energies of ^{87}Rb and ^{23}Na condensates in the presence of harmonic trap and SOC with $\Delta x = 0.015625$, $\Delta t \approx 0.1(\Delta x)^2$. The (c_0, c_1) values are $(0.08716N, -0.001748N)$ and $(0.0241N, 0.00075N)$ with $N = 10000$ for ^{87}Rb and ^{23}Na , respectively.	135
D.5	Ground-state energies for self-trapped ferromagnetic and antiferromagnetic condensates in the presence of SOC obtained with $\Delta x = 0.015625$, $\Delta t \approx 0.1(\Delta x)^2$. . .	138

D.6	Ground-state energies for ^{87}Rb and ^{23}Na q2D BECs obtained with $\Delta x = 0.05$, $\Delta y = 0.05$ and $\Delta t = 0.1\Delta x\Delta y/2$ for the various values of magnetization M . 10^4 atoms of each species were considered in trap with $\alpha_x = \alpha_y = 1$, $\alpha_z = 20$, $\omega_x/(2\pi) = 20$ Hz. Together with scattering lengths (a_0, a_2) , these parameters define c_0 and c_1 as per Eq. (A.15).	140
-----	---	-----

List of Abbreviations

1D - one dimensional

2D - two dimensional

3D - three dimensional

ASYMM - asymmetric

BEC - Bose-Einstein condensate

BECs - Bose-Einstein condensates

BHM - Bose-Hubbard model

CGA - cluster Gutzwiller approach

CGPEs - coupled Gross-Pitaevskii equations

EMR - excited state multi-ring

GP - Gross-Pitaevskii

KE - kinetic energy

MI - Mott insulator

MR - multi-ring

NF - normal fluid

NN - nearest neighbour

ODLRO - off-diagonal long-range order

PT - phase-twisted

q1D - quasi-one-dimensional

q2D - quasi-two-dimensional

QPT - quantum phase transition

QPTs - quantum phase transitions

SF - superfluid

SO-coupled - spin-orbit-coupled

SOC - spin-orbit coupling

SL - square lattice

ST - stripe

TBHM - two-component Bose-Hubbard model

TL - triangular lattice

zFM - z-polarized ferromagnetic

Chapter 1

Introduction

1.1 Background

Nearly seven decades after its theoretical prediction in 1925 [7,8], the long-awaited experimental realization of Bose-Einstein Condensate (BEC) finally occurred in 1995 [9–11]. This groundbreaking achievement not only validated the theoretical framework but also ignited a new era of research, leading to remarkable advancements and ongoing explorations in the field of quantum physics to this day [12–14].

The substantial time gap between the theoretical prediction and experimental realization of BEC is generally attributed to the refinement of quantum mechanics and the technical challenges associated with achieving the necessary conditions for condensation, such as ultra-low temperatures and precise control over atomic interactions, requisite advancements in experimental techniques, and cooling technologies [15]. The phase transition to the Bose condensed phase is an intriguing phenomenon because it occurs even in an ideal gas without interaction, making Bose-Einstein condensation a pure quantum-statistical effect.

To achieve a BEC, the thermal de Broglie wavelength must be comparable to the mean interatomic distances in the quantum gas. The de Broglie wavelength can be calculated using the equation $\lambda = \sqrt{2\pi\hbar^2/mk_B T_c}$, where m is the mass of the bosonic atom and T_c is the critical temperature for Bose-Einstein condensation. The mean interatomic distance can be expressed as $\langle r \rangle = 1/n^{1/3}$, where n denotes the number of bosons per unit volume. This overlap of the de Broglie wavelengths means that atoms can no longer be considered as distinct particles but

rather be described as a collective quantum object known as a BEC. This requirement sets the stage for two primary factors influencing the realization of a BEC: density and temperature. Accordingly, one approach to realize a BEC could be to increase the density of the quantum gas, but this can lead to the formation of molecules or a transition to a liquid or solid state, making high-density gases impractical for achieving the desired condensed state. To overcome this challenge, researchers have opted for the second approach, which focuses on reducing the temperature to extremely low levels (of the order of some hundred nano-Kelvin). By decreasing the temperature, the particles' thermal energies decrease, reducing their momenta and, thus, increasing the thermal de Broglie wavelengths. Consequently, the mean interatomic distances can become comparable to the de Broglie wavelength. However, the particle density is set to be around $10^{14} - 10^{15} \text{ cm}^{-3}$ [12]. This value is significantly lower (around four to five orders of magnitude) than the air density under standard conditions.

Alkali atoms, such as rubidium [11] and sodium [9], are commonly employed in creating Bose-Einstein condensates (BECs) due to their favorable properties. Alkali atoms possess a single valence electron, making them amenable to laser cooling techniques [15]. Furthermore, they have a simple energy level structure that facilitates precise manipulation and control of the atomic system. There are three essential steps to creating a BEC in a laboratory. Firstly, laser cooling is used to gradually decrease the thermal energy of atoms. After that, trapping mechanisms, predominantly magnetic traps, confine the cooled atoms within spatially localized regions by employing magnetic fields. Finally, evaporative cooling is employed to selectively remove high-energy atoms, enabling the attainment of ultracold temperatures required to create a BEC [12].

1.2 Scalar BEC

BECs are fascinating systems that present a complex many-body problem. The Quantum Field Theory framework is suitable for studying BECs as quantum fields. This theory can accommodate systems with an infinite number of particles and allows one to analyze the BEC as a coherent entity, taking into account the interactions among the particles in a unified manner.

The Hamiltonian of a Bose gas with two-body inter-boson interactions is given by [16]

$$\hat{H} = \hat{H}_0 + \hat{H}_{\text{int}}, \quad (1.1)$$

where \hat{H}_0 includes the kinetic energy and trapping potential terms and \hat{H}_{int} is the part for mutual interaction between particles. These two constituents of the Hamiltonian (1.1) are defined as

$$\hat{H}_0 = \int d\mathbf{r} \hat{\Psi}^\dagger(\mathbf{r}, t) \left(-\frac{\hbar^2}{2m} \nabla^2 + V(\mathbf{r}, t) \right) \hat{\Psi}(\mathbf{r}, t), \quad (1.2)$$

$$\hat{H}_{\text{int}} = \frac{1}{2} \int d\mathbf{r} d\mathbf{r}' \hat{\Psi}^\dagger(\mathbf{r}, t) \hat{\Psi}^\dagger(\mathbf{r}', t) U(\mathbf{r} - \mathbf{r}') \hat{\Psi}(\mathbf{r}', t) \hat{\Psi}(\mathbf{r}, t), \quad (1.3)$$

where \hbar is the reduced Planck's constant, m is the mass of an atom, and $U(\mathbf{r} - \mathbf{r}')$ is the interatomic interaction potential. The field operator $\hat{\Psi}$ [$\hat{\Psi}^\dagger$] annihilates [creates] a particle at position \mathbf{r} and obeys the usual bosonic commutation relations:

$$\begin{aligned} [\hat{\Psi}(\mathbf{r}), \hat{\Psi}^\dagger(\mathbf{r}')] &= \delta(\mathbf{r} - \mathbf{r}'), \\ [\hat{\Psi}(\mathbf{r}), \hat{\Psi}(\mathbf{r}')] &= [\hat{\Psi}^\dagger(\mathbf{r}), \hat{\Psi}^\dagger(\mathbf{r}')] = 0, \end{aligned} \quad (1.4)$$

where $\delta(\mathbf{r} - \mathbf{r}')$ is the Dirac delta function. The evolution of the field operator $\hat{\Psi}(\mathbf{r}, t)$ is described by the Heisenberg equation of motion given as

$$i\hbar \frac{\partial \hat{\Psi}(\mathbf{r}, t)}{\partial t} = [\hat{\Psi}(\mathbf{r}, t), \hat{H}]. \quad (1.5)$$

In the dilute and ultracold BEC, the low-energy interactions between particles are mostly two-body interactions. To represent these interactions, one can use a delta function potential $U(\mathbf{r} - \mathbf{r}') = g\delta(\mathbf{r} - \mathbf{r}')$, where $g = 4\pi\hbar^2 a/m$ represents the strength of the interaction [17]. The sign of g , determined by the s -wave scattering length a , determines whether the interaction is attractive ($g < 0$) or repulsive ($g > 0$).

1.2.1 Mean-field theory

In 1947, Bogoliubov [18] proposed a mean-field approximation to describe the BEC, treating the field operator $\hat{\Psi}(\mathbf{r}, t)$ as the sum of a mean field $\psi(\mathbf{r}, t)$, representing the central core of the BEC,

and fluctuation operator $\delta\hat{\Psi}(\mathbf{r}, t)$ which accounts for the thermal and quantum fluctuations, i.e.

$$\hat{\Psi}(\mathbf{r}, t) \approx \psi(\mathbf{r}, t) + \delta\hat{\Psi}(\mathbf{r}, t). \quad (1.6)$$

Assuming the temperature of the gas is well below the critical temperature T_c , a significant fraction of the particles will occupy the same ground state, forming the condensed BEC. So, the fluctuation operator can be neglected. By incorporating the delta function interaction potential and the mean-field approximation (1.6) in \hat{H} and evaluating the commutator in the right-hand side of Eq. (1.5), we obtain the zeroth-order model for a three-dimensional (3D) BEC known as the Gross-Pitaevskii (GP) equation [19, 20]:

$$i\hbar \frac{\partial \psi(\mathbf{r}, t)}{\partial t} = -\frac{\hbar^2}{2m} \nabla^2 \psi(\mathbf{r}, t) + V(\mathbf{r})\psi(\mathbf{r}, t) + g|\psi(\mathbf{r}, t)|^2\psi(\mathbf{r}, t), \quad (1.7)$$

where $\psi(\mathbf{r}, t)$ represents the order parameter of the BEC and $|\psi(\mathbf{r}, t)|^2$ represents the density of particles at position \mathbf{r} and time t .

The GP equation, analogous to the nonlinear Schrödinger equation, governs the evolution of the BEC, providing insights into quantities like momentum and energy distributions, as well as the stability of nonlinear-wave structures. This equation has earlier been extensively explored in the context of nonlinear phenomena in optics [21, 22], plasma physics [23], and fluid dynamics [24]. However, when applied to BECs, the equation presents unique characteristics and flexibilities that distinguish it from previous studies. These include but are not limited to the presence of external potentials and the ability to manipulate these potentials, the effective nonlinearity, and the dimensionality of the model. Understanding the GP equation is crucial for gaining valuable insights into predicting and characterizing essential non-linear effects. Notably, this includes the study of solitons [25, 26] and vortices [27], which are highly relevant and experimentally observable phenomena. By delving into the GP equation, researchers gain a deeper understanding of the intricate dynamics and properties exhibited by these nonlinear entities in various physical systems [12–14].

1.3 Spinor BEC

Magnetic traps confine the cooled atoms within spatially localized regions by employing magnetic fields resulting in the selective trapping of atoms in the weak-field-seeking states. The strong Zeeman shifts caused by the magnetic field freeze out any spin-exchange collisions, resulting in the atoms almost behaving like scalar particles in the condensate, which can now be described by a scalar field [12]. This is in contrast to an optical trap, where all the states can be trapped by spin-independent potential and spin-degrees of freedom are not frozen [28]. In the case of an optical trap, the condensate can be described by a spinor with $2f + 1$ components having hyperfine spin f , rendering such systems rich in novel physics [29]. Notably, commonly observed BEC species, such as ^{87}Rb and ^{23}Na , correspond to hyperfine manifolds with $f = 1$ and $f = 2$ [30]. In contrast, ^{52}Cr [31] and ^{85}Rb BECs possess $f = 3$ phases [29]. Optical traps mainly employ laser fields, and the trapping is based on the interaction between the induced dipole moment of the atom and spatially varying electric field [28]. Spinor condensates exhibit many quantum phenomena with no analogue in single-component or multicomponent scalar BECs, *e.g.* spin dynamics [32], spin waves [33], spin mixing [34] etc.

The hyperfine spin states of the atoms can change during the two-body scattering events in spinor Bose gases. To properly account for this in the interaction part of the Hamiltonian, the total hyperfine spin of the two particles must be considered. If two identical spin- f bosonic particles collide, they may have a total spin of $\mathcal{F} = 0, 2, \dots, 2f$ since symmetry considerations prohibit odd \mathcal{F} in the s -wave limit. The scattering length, which depends on the total spin \mathcal{F} , can have up to $f + 1$ different values, denoted as a_0, \dots, a_{2f} [29].

The interatomic interaction Hamiltonian \hat{H}_{int} for a spinor condensates can be written as [29]

$$\hat{H}_{\text{int}} = \frac{1}{2} \int d\mathbf{r} \sum_{m_1 m_2 m'_1 m'_2} C_{m'_1 m'_2}^{m_1 m_2} \hat{\psi}_{m_1}^\dagger(\mathbf{r}) \hat{\psi}_{m_2}^\dagger(\mathbf{r}) \hat{\psi}_{m'_2}(\mathbf{r}) \hat{\psi}_{m'_1}(\mathbf{r}), \quad (1.8)$$

where m_1 and m_2 are magnetic quantum number and can take a value from $f, f - 1, \dots, -f$ and

$$C_{m'_1 m'_2}^{m_1 m_2} \equiv \frac{4\pi\hbar^2}{M} \sum_{\mathcal{F}=0,2,\dots,2f} a_{\mathcal{F}} \left\langle f, m_1; f, m_2 \left| \hat{\mathcal{P}}_{\mathcal{F}} \right| f, m'_1; f, m'_2 \right\rangle, \quad (1.9)$$

with $\hat{\mathcal{P}}_{\mathcal{F}} = \sum_{\mathcal{M}=-\mathcal{F}}^{\mathcal{F}} |\mathcal{F}, \mathcal{M}\rangle \langle \mathcal{F}, \mathcal{M}|$ being the projection operator onto a two-body state with

the total spin angular momentum \mathcal{F} . The interaction potential can be divided according to the spin channel \mathcal{F} as

$$\hat{H}_{\text{int}} = \sum_{\mathcal{F}=0,2,\dots,2f} \hat{H}_{\text{int}}^{\mathcal{F}}, \quad (1.10)$$

where $\hat{H}_{\text{int}}^{\mathcal{F}}$ is the interaction Hamiltonian corresponding to the two bosons getting scattered with a total spin \mathcal{F} [29]. For the contact interaction potential, $\hat{H}_{\text{int}}^{\mathcal{F}}$ can be written as

$$\hat{H}_{\text{int}}^{\mathcal{F}} = \frac{g_{\mathcal{F}}}{2} \int d\mathbf{r} \sum_{\mathcal{M}=-\mathcal{F}}^{\mathcal{F}} \hat{A}_{\mathcal{F}\mathcal{M}}^{\dagger}(\mathbf{r}) \hat{A}_{\mathcal{F}\mathcal{M}}(\mathbf{r}), \quad (1.11)$$

where $g_{\mathcal{F}} = 4\pi\hbar^2 a_{\mathcal{F}}/m$, and $\hat{A}_{\mathcal{F}\mathcal{M}}(\mathbf{r})$ is the irreducible operator that annihilates a pair of bosons at \mathbf{r} . The irreducible operator is related to a pair of field operators via the Clebsch-Gordan coefficients $\langle \mathcal{F}, \mathcal{M} | f, m; f, m' \rangle$ as follows:

$$\hat{A}_{\mathcal{F}\mathcal{M}}(\mathbf{r}) = \sum_{m,m'=-f}^f \langle \mathcal{F}, \mathcal{M} | f, m; f, m' \rangle \hat{\psi}_m(\mathbf{r}) \hat{\psi}_{m'}(\mathbf{r}). \quad (1.12)$$

The operator $\sum_{\mathcal{M}=-\mathcal{F}}^{\mathcal{F}} \hat{A}_{\mathcal{F}\mathcal{M}}^{\dagger}(\mathbf{r}) \hat{A}_{\mathcal{F}\mathcal{M}}(\mathbf{r})$ for spin f can be expressed in terms of $f+1$ operators [29].

1.3.1 Mean-field model for a spin-1 BEC

The second-quantized Hamiltonian for $f=1$ is given by [29]

$$\begin{aligned} \hat{H} = \int d\mathbf{r} \left[\sum_j \hat{\psi}_j^{\dagger} \left(-\frac{\hbar^2}{2m} \nabla^2 + V \right) \hat{\psi}_j + \frac{g_0}{2} \hat{A}_{00}^{\dagger}(\mathbf{r}) \hat{A}_{00}(\mathbf{r}) \right. \\ \left. + \frac{g_2}{2} \sum_{\mathcal{M}=-2}^2 \hat{A}_{2\mathcal{M}}^{\dagger}(\mathbf{r}) \hat{A}_{2\mathcal{M}}(\mathbf{r}) \right], \end{aligned} \quad (1.13)$$

where the irreducible operators can be expressed in terms of total density operator $\hat{\rho}(\mathbf{r})$ and spin-density operator $\hat{F}_{\nu}(\mathbf{r})$. Thus, in the mean-field approximation, the energy functional for a

spin-1 BEC becomes

$$E = \int d\mathbf{r} \left[\sum_j \psi_j^* \left(-\frac{\hbar^2}{2m} \nabla^2 + V \right) \psi_j + \frac{c_0}{2} \rho^2 + \frac{c_1}{2} |\mathbf{F}|^2 \right], \quad (1.14)$$

where

$$c_0 = \frac{4\pi\hbar^2(a_0 + 2a_2)}{3m}, \quad c_1 = \frac{4\pi\hbar^2(a_2 - a_0)}{3m}, \quad (1.15)$$

and $\rho(\mathbf{r}) = \sum_j |\psi_j(r)|^2$ is the total density of particles with $j = +1, 0$, or -1 as the magnetic quantum numbers of magnetic sublevels. In Eq. (1.14), $\mathbf{F} = (F_x, F_y, F_z)$ is the spin-density vector defined as

$$F_\nu(\mathbf{r}) = \sum_{j',j} \psi_{j'}^*(\mathbf{r}) (f_\nu)_{j',j} \psi_j, \quad (1.16)$$

where ν is (x, y, z) and f_x , f_y , and f_z are the irreducible representations of the x , y , and z components of the angular momentum operators for a spin- f particle, respectively. The (j, j') th element of these $(2f+1) \times (2f+1)$ matrices are

$$(f_x)_{j,j'} = \frac{1}{2} \left[\sqrt{(f-j+1)(f+j)} \delta_{j-1,j'} + \sqrt{(f+j+1)(f-j)} \delta_{j+1,j'} \right], \quad (1.17a)$$

$$(f_y)_{j,j'} = \frac{1}{2i} \left[\sqrt{(f-j+1)(f+j)} \delta_{j-1,j'} - \sqrt{(f+j+1)(f-j)} \delta_{j+1,j'} \right], \quad (1.17b)$$

$$(f_z)_{j,j'} = j \delta_{j,j'}, \quad (1.17c)$$

where j and j' can have values from $f, f-1, \dots, -f$. The mean-field dynamics of a spinor BEC is governed by (1.14)

$$i\hbar \frac{\partial \psi_j}{\partial t} = \frac{\delta E}{\delta \psi_j^*}, \quad (1.18)$$

which for spin-1 BEC yields three coupled GP equations

$$i\hbar \frac{\partial \psi_{\pm 1}}{\partial t} = \left(-\frac{\hbar^2 \nabla^2}{2m} + V + c_0 \rho \pm c_1 F_z \right) \psi_{\pm 1} + \frac{c_1}{\sqrt{2}} F_{\mp} \psi_0, \quad (1.19a)$$

$$i\hbar \frac{\partial \psi_0}{\partial t} = \left(-\frac{\hbar^2 \nabla^2}{2m} + V + c_0 \rho \right) \psi_0 + \frac{c_1}{\sqrt{2}} F_- \psi_{-1}, \quad (1.19b)$$

where

$$F_{\pm} = F_x \pm iF_y, \quad F_x = \frac{1}{\sqrt{2}}[\psi_1^* \psi_0 + \psi_0^* (\psi_1 + \psi_{-1}) + \psi_{-1}^* \psi_0], \quad (1.20a)$$

$$F_z = |\psi_1|^2 - |\psi_{-1}|^2, \quad F_y = \frac{i}{\sqrt{2}}[-\psi_1^* \psi_0 + \psi_0^* (\psi_1 - \psi_{-1}) + \psi_{-1}^* \psi_0]. \quad (1.20b)$$

If c_1 is positive, the energy functional in Eq. (1.14) is minimized with a non-magnetized spinor, and the antiferromagnetic or polar phase is the ground-state phase. In the opposite case of negative c_1 , the ground-state phase is ferromagnetic. The interactions in a spin-1 condensate share similarities with those observed in condensed matter physics. The ferromagnetic state can be considered polarized or magnetic, exhibiting a net magnetization. Conversely, the antiferromagnetic and polar phases lack magnetization due to an equal distribution of populations in spin states with magnetic quantum numbers $j = \pm 1$ or all the atoms in the spin state with $j = 0$. [29].

1.3.2 Mean-field model for a spin-2 BEC

The second-quantized Hamiltonian for $f = 2$ is given by [29]

$$\begin{aligned} \hat{H} = \int d\mathbf{r} \left[\sum_j \hat{\psi}_j^\dagger \left(-\frac{\hbar^2}{2m} \nabla^2 + V \right) \hat{\psi}_j + \frac{g_0}{2} \hat{A}_{00}^\dagger(\mathbf{r}) \hat{A}_{00}(\mathbf{r}) \right. \\ \left. + \frac{g_2}{2} \sum_{\mathcal{M}=-2}^2 \hat{A}_{2\mathcal{M}}^\dagger(\mathbf{r}) \hat{A}_{2\mathcal{M}}(\mathbf{r}) + \frac{g_4}{2} \sum_{\mathcal{M}=-4}^2 \hat{A}_{4\mathcal{M}}^\dagger(\mathbf{r}) \hat{A}_{4\mathcal{M}}(\mathbf{r}) \right], \end{aligned} \quad (1.21)$$

where j can take values $+2, +1, 0, -1, -2$ and the irreducible operators can be expressed in terms of total density operator $\hat{\rho}(\mathbf{r})$, spin density operator $\hat{F}_\nu(\mathbf{r})$, and singlet-pair operator $\hat{A}_{00}(\mathbf{r})$. In the mean-field approximation, the energy functional for a spin-2 BEC can then be written as

$$E = \int d\mathbf{r} \left[\sum_j \psi_j^* \left(-\frac{\hbar^2}{2m} \nabla^2 + V \right) \psi_j + \frac{c_0}{2} \rho^2 + \frac{c_1}{2} |\mathbf{F}|^2 + \frac{c_2}{2} |\Theta|^2 \right], \quad (1.22)$$

where

$$c_0 = \frac{4\pi\hbar^2(4a_2 + 3a_4)}{7m}, \quad c_1 = \frac{4\pi\hbar^2(a_4 - a_2)}{7m}, \quad c_2 = \frac{4\pi\hbar^2(7a_0 - 10a_2 + 3a_4)}{7m}, \quad (1.23)$$

$\rho(\mathbf{r}) = \sum_j |\psi_j(r)|^2$ is the total density, and Θ is the spin-singlet pair amplitude given by

$$\Theta = \frac{1}{\sqrt{5}}(2\psi_{+2}\psi_{-2} - 2\psi_{+1}\psi_{-1} + \psi_0^2). \quad (1.24)$$

For the spin-2 BEC, we get the following five coupled GP equations by minimizing the energy functional Eq. (1.22) and using Eq. (1.18)

$$i\hbar \frac{\partial \psi_{\pm 2}}{\partial t} = \mathcal{H}\psi_{\pm 2} + c_1(F_{\mp}\psi_{\pm 1} \pm 2F_z\psi_{\pm 2}) + \frac{c_2}{\sqrt{5}}\Theta\psi_{\mp 2}^*, \quad (1.25a)$$

$$i\hbar \frac{\partial \psi_{\pm 1}}{\partial t} = \mathcal{H}\psi_{\pm 1} + c_1\left[\sqrt{\frac{3}{2}}F_{\mp}\psi_0 + F_{\pm}\psi_{\pm 2} \pm F_z\psi_{\pm 1}\right] - \frac{c_2}{\sqrt{5}}\Theta\psi_{\mp 1}^*, \quad (1.25b)$$

$$i\hbar \frac{\partial \psi_0}{\partial t} = \mathcal{H}\psi_0 + c_1\sqrt{\frac{3}{2}}(F_{-}\psi_{-1} + F_{+}\psi_{+1}) + \frac{c_2}{\sqrt{5}}\Theta\psi_0^*, \quad (1.25c)$$

where

$$\mathcal{H} = \left(-\frac{\hbar^2 \nabla^2}{2m} + V + c_0\rho\right), \quad F_z = \sum_j j|\psi_j|^2, \quad (1.26a)$$

$$F_{-} = F_{+}^* = 2\psi_{-2}^*\psi_{-1} + \sqrt{6}\psi_{-1}^*\psi_0 + \sqrt{6}\psi_0^*\psi_{+1} + 2\psi_{+2}\psi_{+1}^*. \quad (1.26b)$$

Depending on the values of c_1 and c_2 , we can have three magnetic phases [29,35] – ferromagnetic, anti-ferromagnetic, and cyclic. The scattering lengths, which determine the strength of interactions, can (in principle) be manipulated using optical or magnetic Feshbach resonances [36].

To generalize, in the mean-field approximation, a spin- f BEC is described by a set of $2f+1$ coupled time-dependent nonlinear partial differential equations with first-order derivative in time and second-order derivatives in space known as coupled Gross-Pitaevskii equations (CGPEs) [29,37–39]. For $f=1$ and $f=2$, we have derived these CGPEs in Eqs. (1.19a)-(1.19b) and Eqs. (1.25a)-(1.25c), respectively. There is no general analytic approach to solve a set of CGPEs, one needs to solve the equations numerically, and this has spurred many studies on the numerical solutions of spinor BECs [3,4,40]. However, to solve these equations numerically, it is preferable to have these CGPEs in dimensionless units. Appendix A discusses the dimensionless formulations of these equations for quasi-one-dimensional (q1D), quasi-two-dimensional (q2D), and 3D cases, specifically for a spin-1 BEC. A wide range of numerical techniques have been employed in literature to study single-component scalar [41–46], multicomponent scalar [47] as

well as spinor BECs [3, 4, 40, 48]. One of the most widely used methods to determine the ground state of scalar BECs is the imaginary-time method followed by an appropriate discretization scheme to evolve the resultant gradient flow equations [42, 43]. The extension of this method to compute the ground states of spinor systems, for example for a spin-1 BEC, is not straightforward, as there are only two constraints, i.e. the conservation of the total number of atoms and longitudinal magnetization, while one would need three projection parameters for normalization of three components of the wave function [3, 4, 40]. However, the imaginary-time method has been used in the literature with simultaneous conservation of norm and magnetization achieved through the introduction of the third normalization condition [3, 4, 40]. There have been different discretization schemes used which include, among others, centered finite difference schemes and spectral methods for spatial discretization and forward Euler, backward Euler, and Crank-Nicolson schemes for time discretization. The non-linear terms can be handled easily by first using the time-splitting technique, which in the case of scalar GP equation amounts to approximating the solution by successively solving two equations- one of which is just a free particle Schrödinger equation, and the other containing the non-linear term can be solved exactly [44]. The free particle Schrödinger equation can be handled by Crank-Nicolson [45] or spectral discretization [46, 49]. In this thesis, we use the Fourier pseudospectral discretization for solving the free particle Schrödinger equation. A couple of advantages of choosing this method: firstly, it can be extended easily to the higher dimensional systems because of the ease of dealing with the differential operators in the Fourier space, and secondly, its spectral accuracy. Details of this method for the spin-1 system are discussed in Appendix B. We have implemented this method to develop codes in FORTRAN 90/95 programming language for imaginary- and real-time propagation. The details of these codes are provided in Appendix C. To ensure the reliability of our codes, we have compared the results for various parameters with published literature, and we have included these sample results in Appendix D.

1.3.3 Spin-orbit-coupled spinor condensates

Spin-orbit coupling (SOC) is a fundamental phenomenon in various physical systems. The coupling of spin with momentum brings quantum mechanics to the forefront. It has important implications in various systems, including materials. SOC can give rise to intriguing effects like quantum spin Hall states [50] and topological insulators [51]. These exotic states of matter

exhibit unique electronic properties and hold great potential for applications in quantum devices and information processing [51].

In conventional atomic physics systems, the presence of SOC gives rise to atomic fine-structure splitting. In materials, SOC arises due to symmetry breaking. A lack of mirror symmetry in two-dimensional (2D) systems results in Rashba SOC [52], whereas a lack of inversion symmetry in bulk crystals leads to linear Dresselhaus SOC [53].

Charged particles in the presence of external magnetic fields experience a Lorentz force. In atomic gases, this possibility is ruled out because of their neutrality. In the experimental realizations of synthetic electric [54] and magnetic fields [55], researchers engineer Hamiltonians with spatially or time-dependent vector potentials. These engineered vector potentials produce artificial magnetic fields $\mathbf{B} = \nabla \times \mathbf{A}$ or electric fields $\mathbf{E} = -\partial\mathbf{A}/\partial t$ for neutral atoms. By manipulating these synthetic gauge fields, Spielman's group at the Joint Quantum Institute achieved a breakthrough through successfully creating synthetic SOC [54–56] within ultracold Bose gases, opening new frontiers for investigating quantum systems in this exciting domain.

1.3.3.1 Raman-coupled Hamiltonian

Consider the schematic in Fig. 1.1, where lasers couple three lower-energy states to a high-energy state [1, 2]. The frequencies of these lasers are ω_1 and ω_2 , which are chosen near to the resonance, resulting in the coupling of three lower-energy states via a second-order two-photon process. The coupling between the internal states by laser fields occur through dipolar coupling, $H_{\text{dip}} = -\mathbf{d} \cdot \mathbf{E}$, where \mathbf{d} is the dipole operator, and \mathbf{E} is the electric field, which for the two Raman lasers is

$$\mathbf{E} = \mathbf{E}_1 \cos(\mathbf{k}_1 \cdot \mathbf{r} - \omega_1 t) + \mathbf{E}_2 \cos(\mathbf{k}_2 \cdot \mathbf{r} - \omega_2 t). \quad (1.27)$$

Electric-dipole interaction Hamiltonian is given as

$$H(t) = \begin{pmatrix} -E_g & 0 & 0 & \mathbf{d}_{14} \cdot \mathbf{E}(\mathbf{r}, t) \\ 0 & 0 & 0 & \mathbf{d}_{24} \cdot \mathbf{E}(\mathbf{r}, t) \\ 0 & 0 & E_g & \mathbf{d}_{34} \cdot \mathbf{E}(\mathbf{r}, t) \\ [\mathbf{d}_{14} \cdot \mathbf{E}(\mathbf{r}, t)]^* & [\mathbf{d}_{24} \cdot \mathbf{E}(\mathbf{r}, t)]^* & [\mathbf{d}_{34} \cdot \mathbf{E}(\mathbf{r}, t)]^* & E_e \end{pmatrix}, \quad (1.28)$$

where the basis states are $|+1\rangle, |0\rangle, |-1\rangle, |e\rangle$ with energies $(-E_g, 0, E_g, E_e)$, respectively. $\mathbf{d}_{ij} = \langle i|\mathbf{d}|j\rangle$ and

$$\mathbf{d}_{i4} \cdot \mathbf{E}(\mathbf{r}, t) = \Omega_1 \cos(\mathbf{k}_1 \cdot \mathbf{r} - \omega_1 t) + \Omega_2 \cos(\mathbf{k}_2 \cdot \mathbf{r} - \omega_2 t), \quad (1.29)$$

here $\Omega_1 = \mathbf{d}_{i4} \cdot \mathbf{E}_1$ and $\Omega_2 = \mathbf{d}_{i4} \cdot \mathbf{E}_2$. To get rid of the time dependence, we apply a time-

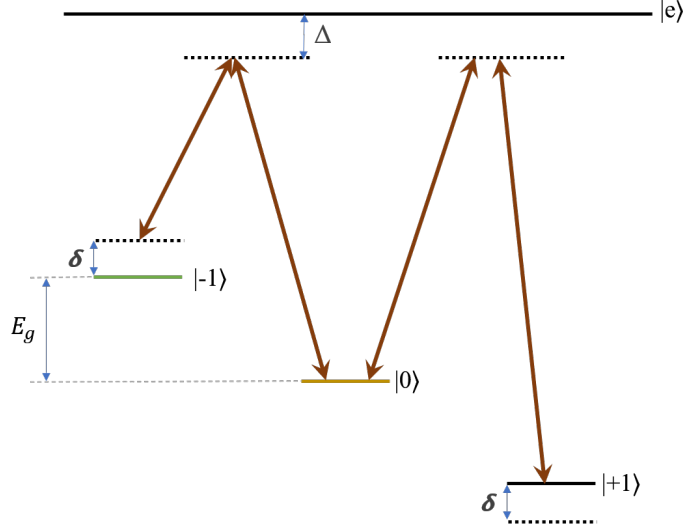


Figure 1.1: (Color online) Three lower energy states are coupled to the higher energy state using two Raman lasers of nearly the same frequency. Raman lasers effectively generate spatially-varying coupling between $|-1\rangle$ and $|0\rangle$, and between $|0\rangle$ and $|+1\rangle$ states through second-order process [1, 2].

dependent unitary transformation to our system, yielding transformed wavefunction $\psi' = U\psi$ and transformed Hamiltonian $H' = UH U^\dagger - iU\partial_t U^\dagger$. The apt unitary operator for the transformation is

$$U = \begin{pmatrix} e^{i(\omega_2 - \omega_1)t} & 0 & 0 & 0 \\ 0 & 1 & 0 & 0 \\ 0 & 0 & e^{-i(\omega_2 - \omega_1)t} & 0 \\ 0 & 0 & 0 & e^{-i\omega_1 t} \end{pmatrix}, \quad (1.30)$$

resulting in [2]

$$H' = \begin{pmatrix} \delta & 0 & 0 & \mathbf{d}_{14} \cdot \mathbf{E} e^{i\omega_2 t} \\ 0 & 0 & 0 & \mathbf{d}_{24} \cdot \mathbf{E} e^{i\omega_1 t} \\ 0 & 0 & -\delta & \mathbf{d}_{34} \cdot \mathbf{E} e^{2i\omega_1 t - i\omega_2 t} \\ [\mathbf{d}_{14} \cdot \mathbf{E} e^{i\omega_2 t}]^* & [\mathbf{d}_{24} \cdot \mathbf{E} e^{i\omega_1 t}]^* & [\mathbf{d}_{34} \cdot \mathbf{E} e^{2i\omega_1 t - i\omega_2 t}]^* & \Delta \end{pmatrix}, \quad (1.31)$$

where $\delta = (\omega_1 - \omega_2) - E_g$ and $\Delta = E_e - \omega_1$. Since Δ is the largest energy scale in the problem, one can adiabatically eliminate state $|e\rangle$ to study the low-energy physics of the system. The Schrödinger equation of the problem can be written as $i\partial_t \mathbf{c} = H' \mathbf{c}$, where $\mathbf{c} = (c_1, c_2, c_3, c_4)^T$ then $i\partial_t c_4 \ll \Delta c_4$ and $c_4 \approx -(H'_{14}c_1 + H'_{24}c_2 + H'_{34}c_3)/\Delta$, which we substitute into the equations of motion for c_1, c_2 , and c_3 resulting in an effective 3×3 Hamiltonian. We neglect the fast-oscillating terms using the rotating-wave approximation, which gives the following Hamiltonian [2]

$$H' = \begin{pmatrix} \delta - \frac{|\Omega_1|^2 + |\Omega_2|^2}{4\Delta} & -\frac{\Omega_1 \Omega_2^*}{4\Delta} e^{-i(\mathbf{k}_1 - \mathbf{k}_2) \cdot \mathbf{r}} & 0 \\ -\frac{\Omega_2 \Omega_1^*}{4\Delta} e^{i(\mathbf{k}_1 - \mathbf{k}_2) \cdot \mathbf{r}} & -\frac{|\Omega_1|^2 + |\Omega_2|^2}{4\Delta} & -\frac{\Omega_1 \Omega_2^*}{4\Delta} e^{-i(\mathbf{k}_1 - \mathbf{k}_2) \cdot \mathbf{r}} \\ 0 & -\frac{\Omega_2 \Omega_1^*}{4\Delta} e^{i(\mathbf{k}_1 - \mathbf{k}_2) \cdot \mathbf{r}} & -\delta - \frac{|\Omega_1|^2 + |\Omega_2|^2}{4\Delta} \end{pmatrix}. \quad (1.32)$$

The SOC effect originates from the spin-flipping process described by the off-diagonal terms in Eq. (1.32) with a momentum transfer of $(\mathbf{k}_1 - \mathbf{k}_2)$; the diagonal contribution $|\Omega_1|^2 + |\Omega_2|^2 / 4\Delta$ in Eq. (1.32) is the AC Stark shift. Redefining the Hamiltonian by changing the zero-energy reference, we get [2, 56]

$$H' = \frac{\hbar^2 \mathbf{k}^2}{2m} + \begin{pmatrix} 3\delta/2 & \frac{\Omega_R}{2} e^{-i\mathbf{k}_L \cdot \mathbf{r}} & 0 \\ \frac{\Omega_R^*}{2} e^{i\mathbf{k}_L \cdot \mathbf{r}} & \delta/2 & \frac{\Omega_R}{2} e^{-i\mathbf{k}_L \cdot \mathbf{r}} \\ 0 & \frac{\Omega_R^*}{2} e^{i\mathbf{k}_L \cdot \mathbf{r}} & -\delta/2 \end{pmatrix}, \quad (1.33)$$

where $\Omega_R = -\Omega_1 \Omega_2^* / 2\Delta$, $\mathbf{k}_L = \mathbf{k}_1 - \mathbf{k}_2$, and $\mathbf{k} = -i\nabla$.

Spielman's group at the Joint Quantum Institute achieved a breakthrough through the successful creation of synthetic SOC [56] within ultracold Bose gases, using a method based on Raman coupling. In this experiment, for the $F = 1$ manifold, the energy difference between $|1, +1\rangle$ and $|1, 0\rangle$ is quite large due to the quadratic Zeeman shift as compared to the $|1, 0\rangle$ and $|1, -1\rangle$. This makes the system effectively a two-level system by adiabatic elimination of $|1, +1\rangle$ state. The two states of this effective two-level system are labelled as $|1, 0\rangle = |\uparrow\rangle$, $|1, -1\rangle = |\downarrow\rangle$. Now, considering counterpropagating Raman laser beams along x -direction, the corresponding Hamiltonian is [2]

$$\hat{H}_0 = \frac{\hbar^2 \mathbf{k}^2}{2m} + \frac{\Omega_R}{2} [\cos(2k_L x) \sigma_x - \sin(2k_L x) \sigma_y] + \frac{\delta}{2} \sigma_z. \quad (1.34)$$

We now apply a unitary transformation to Eq. (1.34) defined by a unitary operator $U =$

$\exp(-ik_L x \sigma_z)$ to illustrate the presence of SOC more distinctly. The resultant Hamiltonian is [2, 56]

$$\hat{H}_0 = \frac{\hbar^2 \mathbf{k}^2}{2m} + \frac{\hbar^2 k_L k_x}{m} \sigma_z + \frac{\Omega_R}{2} \sigma_x + \frac{\delta}{2} \sigma_z, \quad (1.35)$$

which contains an SOC term that couples k_x and σ_z .

This generates the desired SOC, leading to the degeneracies in the energy-momentum dispersion. As a result, the spinor BECs with SOC exhibit a wide variety of phases and a more intricate phase diagram than systems without SOC. The specific phases and the transitions among them in the ground-state phase diagram depend on various factors, such as the strength and nature of the SOC and the interactions between the atoms [57, 58].

In condensed matter systems, SOC is an intrinsic property and cannot be tuned [59]. In contrast, it is possible to vary the strength of synthetic SOC in ultracold atoms by tuning the Raman coupling between pseudospin states, and thereby different phase transitions can be explored [56, 60, 61]. For example, a spin-orbit-coupled (SO-coupled) pseudospin-1/2 Bose gas undergoes two successive magnetic phase transitions as the strength of Raman coupling is increased. The first transition is from a stripe to a magnetized plane-wave phase, and the second is from the magnetized plane-wave to a non-magnetic zero-momentum superfluid state for the Raman coupling of the order of the recoil energy [62].

Before the advent of synthetic SOC in ultracold atoms, studies on SO-coupled systems were primarily constrained to the fermionic systems [51]. As many atomic species are bosonic, the first physical realization of an SO-coupled bosonic system [56] raised many new questions, for instance, how SOC affects the behaviour of bosonic superfluid? In contrast to spin-1/2 electrons, many atoms possess spin much larger than 1/2. How does SOC affect these gases, especially those with high spins like Rb, Na, Cr, Er, and Dy? Making use of the tunability of the SOC, one can also study the physics of a topological insulator and superconductor in a more flexible and disorder-free setting. SO-coupled ultracold systems can also be used for quantum simulations [58], opening new research directions which can lead to novel quantum states and quantum phenomena.

Various configurations of SOC can be created by coupling different internal atomic states using additional laser beams [63]. This flexibility allows for the generation of tunable combinations of Rashba and Dresselhaus SOC [63]. There are several theoretical proposals for generating

various SOC models that don't even have analogues in any naturally occurring systems [64], which opens the door for exploring exotic quantum phenomena and potentially harnessing them for future technological advancements. However, there are technological challenges, such as addressing the heating caused by Raman laser beams, etc., that need to be overcome to engineer various SOC models.

The implementation of SOC has led to many studies on spinor BECs. For instance, in an optical lattice potential, a 2D SOC exhibits inversion and C_4 symmetries, opening up new avenues for studying topological band structures and quantum effects. A recent experiment explored the interaction-driven quantum phase transition (QPT) and topological region of such a 2D system [65]. These experimental advances have led to several theoretical studies on magnetic ordering, including spin-spiral ordering [66], vortex and Skyrmion crystal [67], and ferromagnetic and antiferromagnetic phases [68]. Additionally, several investigations have examined the effects of SOC strength and symmetry on the ground state [69], crystal momentum distributions [70], and SOC-driven Mott insulator (MI) to superfluid (SF) phase transition [71]. Moreover, in the continuum, combining mean-field nonlinearities with SOC has attracted significant attention, giving rise to remarkable phenomena, including vortices [72–76], monopoles [77], skyrmions [78, 79], multidomain patterns [80], structures induced by nonlocal interactions [81], tricritical points [82], solitons [83–85], and many more. The interest in multidimensional self-trapped structures has been renewed, particularly after the prediction of stable 2D and 3D bright solitons in an SO-coupled pseudo-spinor system without any confining potential in free space [86, 87]. Recently, quantum *droplets*, a self-trapped phase unlike a bright soliton, have been experimentally realized in dipolar BECs [88–90] and two-component BECs [91, 92], where beyond mean-field interactions inhibit the mean-field collapse. In the following section, we will introduce one of the self-trapped solutions, namely bright solitons, in the context of this thesis.

1.4 Solitons

Solitons [93, 94], remarkable phenomena observed in various nonlinear systems such as shallow water, plasmas, and optical fibers, have been the subject of extensive theoretical and experimental investigations. While true solitons are mathematically the solutions of exactly integrable models [93, 95], physical systems that closely approximate integrable models are often referred

to as solitons, especially in experimental contexts. Solitons are characterized by their non-dispersive nature, retaining their initial shape for all time and exhibiting localization properties. They can also pass through other solitons while preserving their size and shape [96]. These can be attributed to the interplay between nonlinearity and dispersion. Nonlinearity compensates for the dispersive effects, enabling solitons to maintain their shape over time. In the realm of BECs, the mean-field equation (1.7) has a term corresponding to external potential. In the theoretical scenario of one dimension and without trapping, Eq. (1.7) simplifies to the one-dimensional (1D) nonlinear Schrödinger equation that features exact analytical solutions in the nonlinear regime, known as solitary waves or solitons. Solitons exhibiting density depressions are referred to as “dark” solitons. This category further distinguishes between “black” solitons, with a minimum density of zero, and “grey” solitons, with a minimum density greater than zero. Conversely, solitons with a density maximum are termed “bright” solitons [12]. For the existence of bright solitons, attractive interactions are needed in the system, whereas for the occurrence of dark solitons, repulsive interactions are needed. In the context of nonlinear optics, these can be described as focusing and defocusing Kerr-type nonlinearities, respectively. These so-called “solitons” in physical systems can survive collisions and propagate over long distances, although they do display dispersion and attenuation over sufficiently large distances, e.g. in fiber-optic systems. In the context of ultracold atomic gas experiments, the controlled creation of bright solitary matter waves is made possible through the use of magnetically tunable Feshbach resonances [36]. These resonances enable precise control over interatomic interactions by varying the magnetic field, allowing for manipulation of the s -wave scattering length over a wide range of positive and negative values.

In higher-dimensional systems, the nonlinear Schrödinger equation loses its integrability [93, 95]. Generating 2D and 3D bright solitons is a significantly more difficult task compared to 1D. The primary challenge arises from the presence of a cubic local self-attractive nonlinearity, which leads to critical and supercritical collapse (blowup) in 2D and 3D geometry, respectively. This collapse arises due to the interplay between attractive forces and kinetic energy, leading to a breakdown of the condensate’s stability [97].

Multicomponent BECs have further enriched the study of solitons in the matter waves. These introduce additional tunable parameters, such as interspecies interaction, and give rise to novel nonlinear structures that are not observed in scalar BECs. As an example, a two-

component BEC introduces new nonlinear structures, including dark-bright solitons (combining dark and bright components) [98–100], dark-dark solitons [101], bright-bright solitons [102, 103], and domain walls [104, 105]. The studies on solitons in multicomponent BECs have expanded our understanding of nonlinear phenomena in matter waves. However, even in multicomponent BEC, stable bright solitons in two or three dimensions have not been reported in free space, solely relying on contact interactions.

Various theoretical approaches have been developed for stabilizing 2D and 3D solitons. These approaches involve utilizing trapping potentials, advanced nonlinear interactions, or nonlocal nonlinearity. [97, 106]. After the successful generation of synthetic SOC, a fascinating possibility is to stabilize bright solitons (including vortex solitons) with an interplay of SOC and mean-field nonlinearity [86, 87]. Stabilization by SOC introduces new features in these solitons differing from a conventional BEC. For example, the shape of a soliton does not change with velocity due to the Galilean invariance of the conventional system, whereas there is a lack of Galilean invariance due to SOC [84, 107]. One of the most remarkable outcomes of the investigations on SO-coupled BECs in 2D and 3D geometries is the stabilization of vortex-bright solitons [86, 87, 107, 108]. These solitons not only possess localized states but also incorporate vorticity, allowing for the embedding of vortex structures. The vorticity within these solitons is characterized by an integer phase winding number, also known as the topological charge denoted by w . This charge corresponds to a total phase change ($\Delta = 2\pi w$) that accumulates as one traverses a closed trajectory surrounding the pivot or phase singularity. A distinctive feature of the vortex soliton is the presence of a hole in the density of the component with a phase singularity. In addition to the stabilization of vortex solitons, another interesting theoretical proposal has been made to realize self-trapped supersolid-like structures in SO-coupled BECs [109]. In the next section, we will introduce the concept of a supersolid, its experimental realization, and the self-trapped supersolid-like structures.

1.5 Supersolid-like structures

A supersolid [110–112] is a captivating quantum state that defies our conventional understanding of matter. It combines the characteristics of a crystalline solid with its ordered structure and stable arrangement of particles and a superfluid with its remarkable ability to flow without

friction or resistance. This unique state breaks two fundamental symmetries in physics: continuous translational invariance, which is responsible for the solid-like properties, and continuous gauge invariance, which governs the superfluid behaviour [113, 114]. Both diagonal long-range and off-diagonal long-range orders (ODLRO) exist simultaneously and appear spontaneously in a supersolid [114].

Supersolidity, an idea initially proposed as a theoretical concept [110–112], have been the subject of significant scientific research. Despite decades of exploration, a supersolid state in helium remains elusive [115]. However, scientists have recently revisited the concept in relation to ultracold atoms. Theoretical suggestions have explored the possibility of creating supersolids using finite-range and dipolar interactions [116], followed by exciting experimental developments and culminating in the realization of a supersolid phase in dipolar BECs [117–120]. By fine-tuning the ratio between dipolar and contact interactions, these systems undergo a phase transition, first entering a supersolid phase. Subsequently, with a further decrease in the strength of contact interactions [117–120], a crossover to an insulating phase occurs. The observation of the excitation spectrum provides further confirmation of the supersolid phase, as it reveals a simultaneous and spontaneous breaking of both continuous translational and global gauge symmetries. Another candidate to realize supersolidity is an SO-coupled spinor BEC, where a supersolid stripe phase, characterized by both diagonal and off-diagonal orders, has been experimentally observed in a pseudospin-1/2 spinor condensate [121]. Recently, this system has been claimed to be a paradigmatic supersolid which is demonstrated by the nonrigidity of the density stripes [122]. This discovery has further confirmed that SO-coupled spinor BECs are an enticing playground to uncover many exciting physics.

The three necessary hallmarks of a supersolid are periodic density modulation, global phase coherence and phase rigidity [123]. Different experiments have claimed the existence of supersolidity in these ultracold systems by identifying spatial modulations of the density profile and simultaneous global phase coherence [118–121]. The experimental realization of a state that simultaneously shows all these three properties was first shown by Pfau’s group [123] for dipolar dysprosium atoms.

Combining the themes of self-trapping and supersolidity, an interesting theoretical proposal has been made to realize self-trapped supersolid-like structures in SO-coupled spin-1 BECs [109], where periodic spatial patterns in total density are expected to possess supersolid-like proper-

ties. ‘Supersolid-like’ terminology is a reference to the fact that these structures manifestly share one of the three properties of a supersolid. Moreover, these supersolid-like structures are found to be self-trapped, hence termed as supersolid-like solitons. We have explored these self-trapped structures, having square-lattice- and triangular-lattice-like spatial structures in the total density, in this thesis. A supersolid-like soliton represents a remarkable phenomenon of spontaneous 2D crystallization within a quantum degenerate gas. Further studies on these can provide valuable insights into the fundamental mechanisms underlying crystal formation in solids under controlled conditions. One of the aims of this thesis is to explore the properties and behaviour of 2D bright solitons and other self-trapped structures that emerge in SO-coupled spinor condensates.

1.6 Optical lattice

Optical lattices have an important role in studying many-body physics. These lattices are composed of light that creates an artificial crystal through the interference patterns generated by two or more coherent laser beams travelling in opposite directions [124]. If the laser beams are incoherent, the light intensity with no interference pattern is dictated by the beam profiles that create an optical trapping potential used for the generation of spinor condensates. The spatial periodicity of the lattice is defined by the wavelengths λ_i of the laser beams. When two lasers with equal wavelengths propagate along the x -axis but in opposite directions, they produce a standing wave with an intensity pattern that exhibits spatial periodicity. The periodicity of the intensity pattern is equal to half of the wavelength of the lasers. Optical lattices use the AC Stark effect of detuned laser light to create periodic potentials that trap neutral atoms. By far-detuning the lasers from atomic resonances, the electric field of the laser induces dipole moments in the atoms, leading to a force caused by the gradient of the inhomogeneous light field. Laser light is used for creating deep potential wells that trap the atoms strongly at the lattice sites [124].

The optical lattices are effective in limiting atomic motion, resulting in a greater emphasis on interaction energy in comparison to kinetic energy. These lattices can be tailored to create diverse single-particle dispersions, and the balance between interaction and kinetic energies can be fine-tuned by adjusting the lattice depth. By simulating solid-state systems with cold gases,

optical lattices offer access to properties and processes that are typically difficult to observe in real materials. Researchers are able to establish a direct correlation between systems found in solid-state materials by modelling electrons with atoms in quantum simulators. The tight-binding model is often used to establish a direct correspondence between optical lattices and ionic lattices in solid-state systems. Optical lattices offer several advantages over traditional condensed matter systems, such as parameter control, defect-free systems, and the ability to achieve different lattice geometries and dimensions. Furthermore, the simplified interactions, primarily through isotropic scattering [125], make it easier to study. These experimental controls have led to the use of cold atoms in optical lattices as quantum simulators [126], allowing for the replication of the physical behaviour of specific models from condensed matter. These innovative concepts draw inspiration from Feynman’s original ideas [127].

1.6.1 Bose-Hubbard model

In the regime of full coherence, where a single macroscopically occupied matter wave accurately describes the system, the GP treatment is well suited [128]. However, as the field of BECs advanced, the need to “go beyond GP” became apparent. This was driven by both theoretical interest and experimental opportunities to explore the strongly correlated regime. Strong interactions, ultrafast rotations, and unique trapping potentials like optical lattice potentials can challenge the validity of the GP equation.

To capture the essential characteristics of a Bose gas in an optical lattice, the Bose-Hubbard model (BHM) is commonly used [129, 130]. This model captures the competition between kinetic energy, which promotes particle delocalization and uniform spatial distribution, and potential energy, which localizes particles on lattice sites by minimizing repulsion. BHM provides a simple yet powerful framework for understanding the behaviour of Bose gases in optical lattices.

The grand canonical many-body Hamiltonian for a system of interacting bosonic neutral atoms confined in optical lattice potential is

$$\begin{aligned} \hat{H} = & \int d\mathbf{r} \hat{\Psi}^\dagger(\mathbf{r}) \left(-\frac{\hbar^2}{2m} \nabla^2 + V(\mathbf{r}) \right) \hat{\Psi}(\mathbf{r}) - \mu \int d\mathbf{r} \hat{\Psi}^\dagger(\mathbf{r}) \hat{\Psi}(\mathbf{r}) \\ & + \frac{1}{2} \int d\mathbf{r} d\mathbf{r}' \hat{\Psi}^\dagger(\mathbf{r}) \hat{\Psi}^\dagger(\mathbf{r}') U(\mathbf{r} - \mathbf{r}') \hat{\Psi}(\mathbf{r}') \hat{\Psi}(\mathbf{r}), \end{aligned} \quad (1.36)$$

where $\hat{\Psi}(\mathbf{r})$ is the time-independent bosonic field operator, which creates an atom at position

\mathbf{r} . The confining potential V is an optical lattice potential, and the interatomic interaction $U(\mathbf{r} - \mathbf{r}')$ can be approximated by the contact pseudopotential. We work in the grand canonical ensemble wherein chemical potential μ fixes the total number of particles.

In a periodic potential, the energy spectrum of a single particle exhibits bands of allowed energies and energy gaps [131]. The corresponding wave functions can be described using Bloch functions $u_{\alpha,\mathbf{p}}(\mathbf{r})$, which are characterized by a band index α and quasi-momentum \mathbf{p} . For deep periodic potentials, a tight-binding limit is applicable. In this limit, the width of energy bands becomes smaller than the gap energy, and the Wannier functions localized at the lattice wells become the convenient basis to expand the wave functions of the system. The Wannier functions are defined as Fourier transform of Bloch functions as

$$w_{i,\alpha}(\mathbf{r}) = \sum_{\mathbf{p} \in BZ} e^{-i\mathbf{p}(\mathbf{r} - \mathbf{R}_i)} u_{\alpha,\mathbf{p}}(\mathbf{r}), \quad (1.37)$$

where \mathbf{R}_i is a lattice vector pointing at site i . In low-temperature systems with weak inter-particle interactions, transitions between different bands can be neglected. Consequently, the system's dynamics are restricted to the lowest Bloch band, also referred to as the single-band approximation. This can only occur when the energy gap between the first and second bands exceeds the thermal and interaction energies per atom. In this scenario, we can expand the field operators in relation to the Wannier functions linked to the lowest band as

$$\hat{\Psi}(\mathbf{r}) = \sum_i w_{i,0}(\mathbf{r}) \hat{b}_i, \quad (1.38)$$

where the subscript 0 of $w_{i,0}$ denotes the lowest band, and \hat{b}_i corresponds to the annihilation operator for the atoms at the i^{th} lattice site. Substituting Eq. (1.38) in Eq. (1.36), and then keeping terms corresponding to nearest neighbor (NN) tunnelling and onsite interaction, we can obtain

$$\hat{H}_{\text{BHM}} = - \sum_{\langle i,j \rangle} J_{ij} \hat{b}_i^\dagger \hat{b}_j + \frac{U}{2} \sum_i \hat{n}_i (\hat{n}_i - 1) - \sum_i \mu_i \hat{n}_i, \quad (1.39)$$

where $\langle i, j \rangle$ denotes the sum over the nearest neighbors. The operator $\hat{n}_i = \hat{b}_i^\dagger \hat{b}_i$ represents the

number of particles at site i . The hopping strength is

$$J_{ij} = - \int d\mathbf{r} w_{i,0}^*(\mathbf{r}) \left[-\frac{\hbar^2 \nabla^2}{2m} + V(\mathbf{r}) \right] w_{j,0}(\mathbf{r}), \quad (1.40)$$

and the strength of the onsite interaction is

$$U = \frac{4\pi\hbar^2 a}{m} \int d\mathbf{r} |w_{i,0}(\mathbf{r})|^4. \quad (1.41)$$

It is justifiable to limit the hopping term to NN sites and the interaction term to onsite in the BHM when the offsite Wannier functions have negligible overlap. This is especially true for deep optical lattices. Eq. (1.39) is the lowest band Hamiltonian of the BHM, which is expressed using bosonic creation and annihilation operators, \hat{b}_i^\dagger and \hat{b}_i , which satisfy usual canonical commutation relations.

At zero temperature, there are two ground-state phases in BHM (1.39): MI and SF phases. These phases arise from the competition between kinetic energy (considering $J_{ij} = J$) and on-site inter-atomic interaction energy (U). The SF phase is characterized by the dominance of kinetic energy over the on-site interaction energy ($J \gg U$), allowing atoms to move between nearest neighbour sites. This leads to delocalization and ODLRO in the system. Conversely, the MI phase is characterized by the dominance of on-site interaction energy over the kinetic energy ($J \ll U$), resulting in localized atoms that cannot move between lattice sites. As a result, there are fixed number of atoms across the lattice sites but no phase coherence, leading to the absence of ODLRO. Among the two quantum phases, the MI phase corresponds to the strongly interacting regime and the SF phase corresponds to the weakly interacting regime. A QPT from MI to SF was experimentally first realized in a pioneering work by Greiner et al. in 2002 [132].

1.6.2 Quantum quench dynamics

The study of the dynamical evolution of the quantum state is of great importance and has been extensively studied in the field [133–135]. The equilibrium conditions are often an idealization, it is crucial to study the out-of-equilibrium dynamics of quantum systems. An important insight can be gained by understanding the route to equilibrium of a non-equilibrium initial quantum state. Understanding the dynamics of these quantum systems is crucial for developing quantum

technologies like quantum computing [136]. There are various ways to take a system out of equilibrium, such as connecting it to a bath and pumping energies and particles into the system, as in transport studies. Due to the presence of the bath, the system is not a closed one, and hence, its dynamics is not unitary. One other possibility is by changing one of the parameters of the underlying Hamiltonian of the system, which causes the initial quantum state to go out of equilibrium and try to approach the eigenstate of the final Hamiltonian corresponding to the changed parameter value under unitary evolution. This process is called a quantum quench and can be of two types: sudden quench or slow quench [134]. There are several research pursuits in this broad field, including thermalization and relaxation of quantum systems after a quench [133], spontaneous symmetry breaking and associated universal scaling laws [134, 135, 137, 138], phase-ordering kinetics and domain growth laws [139, 140].

Ultracold atoms in optical lattices have been utilized in experimental advancements to study quantum states. These atoms are particularly suitable for research on closed quantum systems due to their minimal environmental interaction. Initial investigations were focused on studying dynamics around the BEC transition to study the associated defect production [141–144], phase-ordering kinetics and domain growth [145]. A recent experiment [146] has revealed an exciting study on the dynamics of QPT from the MI to the SF phase and studied the critical exponent of the correlation length. Motivated by this, in this thesis, we have studied the out-of-equilibrium dynamics of various MI to SF phase transitions in two-component Bose Hubbard model (TBHM).

1.7 Outline of the thesis

The thesis is structured into five chapters. In this chapter, we have discussed a brief review of the literature relevant to the thesis to provide the state-of-the-art in the field of SO-coupled spinor BECs and related research directions. In the subsequent chapters, we elaborate on how we contribute to the field by addressing some of the open questions. The overview of the chapters in the rest of the thesis is as follows.

In the first part of **Chapter 2**, we introduce and discuss the eigenfunctions of the single-particle Rashba SO-coupled Hamiltonian for a spin-2 BEC. For an attractively interacting SO-coupled spin-2 BEC, we solve homogeneous CGPEs numerically to obtain the ground-state phase diagram. The characteristic self-trapped solutions for small, medium, and large SOC strengths

in cyclic, ferromagnetic, and polar domains are identified. Later, we introduce the Galilean-transformed mean-field model to study the moving bright soliton solutions. In the second part of the chapter, we extend the study to nonmagnetic SO-coupled spin-1 and spin-2 BECs

In **Chapter 3**, we introduce the TBHM for an SO-coupled pseudospinor BEC in a square optical lattice. We discuss the single-site Gutzwiller mean-field (SGMF) theory to solve the TBHM and investigate the zero- and finite-temperature phase diagrams in the presence and absence of synthetic SOC.

Chapter 4 discusses the quantum quench dynamics across MI-SF QPTs of the TBHM. We first discuss the equilibrium phase diagrams for three different values of the interspecies interactions that correspond to the miscible-immiscible phase transition. We then study the quantum quench dynamics across MI-SF QPTs using the dynamical Gutzwiller equations for both the first- and second-order phase transitions and obtain the Kibble Zurek scaling laws.

The concluding chapter (**Chapter 5**) summarizes the results discussed in the aforementioned chapters of the thesis. We also consider some future directions that might aid in gaining a deeper understanding of SO-coupled spinor BECs and their properties.

The thesis contains four appendices. In **Appendix A**, we discuss the dimensionless formulation of CGPEs for q1D, q2D, and 3D spin-1 BECs, as well as important conserved quantities. **Appendix B** details the numerical methods we used to solve the CGPEs in our thesis. In **Appendix C**, we describe our numerical codes in-depth, including modules, functions, subroutines, and other parameters declared in the code. In **Appendix D**, we compare our codes' results with existing literature to verify their reliability and compare energy, chemical potential, and density profiles against existing results.

Chapter 2

Supersolid-like solitons in spin-orbit-coupled condensates

A vector-bright soliton is a self-bound multicomponent solitary wave that maintains its shape while moving with a constant velocity. As discussed in Sec. 1.4, it has been theoretically demonstrated that the SOC leads to a stabilization of self-trapped solutions like bright solitons in q2D [86, 107] and 3D [87, 108] spinor BECs. Vector-bright solitons have been studied extensively in SO-coupled q1D [84, 85], q2D [86, 147, 148], and 3D pseudospin-1/2 BECs [87]. These self-trapped solitary waves have also been predicted to emerge in SO-coupled q1D [5], q2D [107, 109], and 3D spin-1 BECs [108]. In an SO-coupled q2D spin-1 BEC, the existence of square-lattice solitons with a square-lattice modulation in the total density has also been demonstrated [109]. However, these self-trapped solitons are still unexplored in the case of q2D SO-coupled spin-2 condensates, and we undertake a comprehensive study of the same in this chapter. The SO-coupled spin-2 BEC exhibits more complex symmetry properties compared to the spin-1 case and the interplay of spin-independent and two spin-dependent interactions with SOC leads to a richer variety of emergent patterns in a spin-2 BEC [75, 149]. In this chapter, our aim is to look for supersolid-like solitons in SO-coupled spinor condensates. We have termed these structures as supersolid-like because there are spatial modulations in the total density, which is one of the properties of a supersolid. It is to be mentioned here that we have not calculated the superfluid fraction or confirmed the phase rigidity of these structures.

This chapter is organized as follows. In Sec. 2.1, we present the mean-field CGPEs of an SO-

coupled spin-2 BEC and establish the allowed phase winding numbers for the system in Sec. 2.1.1. In Sec. 2.1.2, we demonstrate the solutions of the noninteracting system. In Sec. 2.2, we discuss numerical results for small, medium, and large SOC strength γ and their dynamical stability in Sec. 2.2.4. The Galilean-transformed mean-field model for the condensate is introduced in Sec. 2.2.8, which we use to study the moving solitons and collisions between them. Sec. 2.3 provides the description of nonmagnetic spinor condensates. In Sec. 2.4, we discuss the mean-field model for nonmagnetic spin-1 and spin-2 condensates. In Sec. 2.5, we discuss the numerical results for nonmagnetic spin-1 and spin-2 condensates. We summarize the chapter in Sec. 2.6.

2.1 Mean-field model for spin-orbit-coupled spin-2 BEC

We consider an SO-coupled spin-2 spinor BEC free in the x - y plane and confined by a harmonic trap $V(\mathbf{r}) = m\omega_z^2 z^2/2$ along the z direction to its Gaussian ground state. The trapping frequency ω_z is strong enough to freeze the dynamics along the z direction. The single-particle Hamiltonian of this system in the presence of Rashba SOC is given by [58, 150]

$$H_0 = \frac{p_x^2 + p_y^2}{2m} + \gamma(p_y f_x - p_x f_y), \quad (2.1)$$

where $p_x = -i\hbar\partial_x \equiv -i\hbar\partial/\partial x$ and $p_y = -i\hbar\partial_y \equiv -i\hbar\partial/\partial y$ are the momentum operators along x and y axes, respectively; γ is the strength of SOC; f_x and f_y are the irreducible representations of the x and y components of angular momentum operators for the spin-2 particle, respectively and are given by Eqs. (1.17a)-(1.17b) for general f . Spinor BEC for $f = 2$ can be described by the five CGPEs (1.25a)-(1.25c) in the absence of Rashba SOC. Eqs. (1.25a)-(1.25c) after including SOC are then converted into a dimensionless form for a q2D setting by following the procedure described in Appendix A for spin-1 BEC, which can be extended to a spin-2 BEC. The q2D SO-coupled spin-2 BEC is, thus, described by the following set of CGPEs in the dimensionless

form [29, 35]:

$$i\partial_t\phi_{\pm 2} = (\mathcal{H} + c_0\rho)\phi_{\pm 2} + c_1(F_{\mp}\phi_{\pm 1} \pm 2F_z\phi_{\pm 2}) + \frac{c_2}{\sqrt{5}}\Theta\phi_{\mp 2}^* + \Gamma_{\pm 2}, \quad (2.2a)$$

$$i\partial_t\phi_{\pm 1} = (\mathcal{H} + c_0\rho)\phi_{\pm 1} + c_1\left[\sqrt{\frac{3}{2}}F_{\mp}\phi_0 + F_{\pm}\phi_{\pm 2} \pm F_z\phi_{\pm 1}\right] - \frac{c_2}{\sqrt{5}}\Theta\phi_{\mp 1}^* + \Gamma_{\pm 1}, \quad (2.2b)$$

$$i\partial_t\phi_0 = (\mathcal{H} + c_0\rho)\phi_0 + c_1\sqrt{\frac{3}{2}}(F_{-}\phi_{-1} + F_{+}\phi_{+1}) + \frac{c_2}{\sqrt{5}}\Theta\phi_0^* + \Gamma_0, \quad (2.2c)$$

where

$$\mathcal{H} = -\frac{1}{2}(\partial_x^2 + \partial_y^2), \quad \Theta = \frac{1}{\sqrt{5}}(2\phi_{+2}\phi_{-2} - 2\phi_{+1}\phi_{-1} + \phi_0^2), \quad (2.3a)$$

$$F_{-} = F_{+}^* = 2\phi_{-2}^*\phi_{-1} + \sqrt{6}\phi_{-1}^*\phi_0 + \sqrt{6}\phi_0^*\phi_{+1} + 2\phi_{+2}\phi_{+1}^*, \quad F_z = \sum_j j|\phi_j|^2. \quad (2.3b)$$

$\partial_t \equiv \partial/\partial t$; $\rho_j(x, y) = |\phi_j(x, y)|^2$ are component densities; $\rho(x, y) \equiv \sum_j \rho_j(x, y)$ is the total density; $F_{\pm} = F_x \pm iF_y$; $|\mathbf{F}|^2 = F_x^2 + F_y^2 + F_z^2 \equiv F_{+}F_{-} + F_z^2$, where F_x , F_y , and F_z are the three components of the spin-density vector \mathbf{F} ; and Θ is the spin-singlet pair amplitude. In Eqs. (2.2a)-(2.2c), the interaction parameters and SOC terms are defined as

$$c_0 = \frac{2\sqrt{2\pi}N(4a_2 + 3a_4)}{7a_{\text{osc}}}, c_1 = \frac{2\sqrt{2\pi}N(a_4 - a_2)}{7a_{\text{osc}}}, c_2 = \frac{2\sqrt{2\pi}N(7a_0 - 10a_2 + 3a_4)}{7a_{\text{osc}}}, \quad (2.4)$$

$$\Gamma_{\pm 2} = -i\gamma(\partial_y \pm i\partial_x)\phi_{\pm 1}, \quad \Gamma_{\pm 1} = -i\sqrt{\frac{3}{2}}\gamma(\partial_y \pm i\partial_x)\phi_0 - i\gamma(\partial_y \mp i\partial_x)\phi_{\pm 2}, \quad (2.5a)$$

$$\Gamma_0 = -i\sqrt{\frac{3}{2}}\gamma[(\partial_y - i\partial_x)\phi_{+1} + (\partial_y + i\partial_x)\phi_{-1}], \quad (2.5b)$$

where a_0 , a_2 , and a_4 are s -wave scattering lengths in the total spin channels 0, 2 and 4, respectively, for a spin-2 BEC, and N is the total number of bosons. In this chapter, we will consider a self-attractive ($c_0 < 0$) system. Depending on the values of c_1 and c_2 , we can have three magnetic phases [29, 35] – ferromagnetic, antiferromagnetic, and cyclic – as illustrated in Fig. 2.1. The units of length, density, time, and energy considered in Eqs. (2.2a)-(2.2c) are oscillator length $a_{\text{osc}} = \sqrt{\hbar/m\omega_z}$, a_{osc}^{-2} , ω_z^{-1} , and $\hbar\omega_z$, respectively. The dimensionless formulation of the mean-field model for the condensate has the normalization condition $\int \rho(x, y)dx dy = 1$.

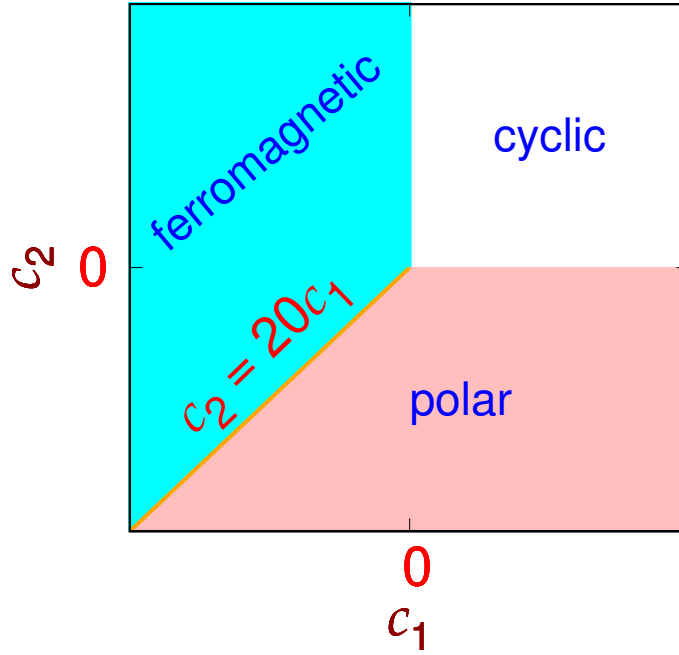


Figure 2.1: (Color online) The c_2 vs c_1 phase plot (not to scale) illustrating ferromagnetic, antiferromagnetic, and cyclic phases in the absence of SOC.

The number of particles along with the energy

$$E = \int dxdy \left[\sum_{j=-2}^{+2} \phi_j^* \mathcal{H} \phi_j + \frac{c_0}{2} \rho^2 + \frac{c_1}{2} |\mathbf{F}|^2 + \frac{c_2}{2} |\Theta|^2 + \sum_{j=-2}^{+2} \phi_j^* \Gamma_j \right], \quad (2.6)$$

are two conserved quantities of an SO-coupled BEC. In the presence of SOC ($\gamma \neq 0$), magnetization ($\equiv \int F_z dxdy = \int dxdy [2\rho_{+2}(x, y) - 2\rho_{-2}(x, y) + \rho_{+1}(x, y) - \rho_{-1}(x, y)]$) is not a conserved quantity, although it is conserved for $\gamma = 0$.

2.1.1 Phase requirement

Exotic ground states have been predicted to emerge in SO-coupled spinor condensates including vortex-bright solitons. Vortex-bright solitons have been studied extensively in SO-coupled pseudospin-1/2 [86, 87, 147, 148] and spin-1 BECs [107–109]. In this context, the permitted vortex configurations in a spinor BEC depend on the intercomponent phase relationships. Considering a circular symmetry, the spinor order parameter for a vortex configuration in circular polar

coordinates (r, θ) can be written in terms of amplitude and phase parts as

$$\phi_j(r, \theta) = R_j(r) e^{i(w_j \theta + \alpha_j)}, \quad (2.7)$$

where $R_j = |\phi_j(r, \theta)| \geq 0$ and $j = 0, \pm 1, \pm 2$. The phases of the component wave functions have contributions from the winding number w_j of the phase singularity which is an integer and any other constant phase α_j . For a spin-2 BEC, the spin-dependent interaction energy is given as [29, 35]

$$E_{\text{int}} = \int \left(\frac{c_1}{2} |\mathbf{F}|^2 + \frac{c_2}{2} |\Theta|^2 \right) r dr d\theta. \quad (2.8)$$

Using *ansatz* in Eq. (2.7), the contribution of phase-dependent terms in the spin-dependent interaction energy in Eq. (2.8) can be written as

$$\begin{aligned} E_{\text{int}}^{\text{phase}} = & \left(6c_1 - \frac{2c_2}{5} \right) \int R_0^2 R_{+1} R_{-1} r dr \int \cos[(w_{+1} + w_{-1} - 2w_0)\theta + k] d\theta \\ & + 2\sqrt{6}c_1 \int R_0 R_{+1} R_{+2} R_{-1} r dr \int \cos[(w_{+2} + w_{-1} - w_0 - w_{+1})\theta + l] d\theta \\ & + 2\sqrt{6}c_1 \int R_0 R_{+1} R_{-1} R_{-2} r dr \int \cos[(w_{+1} + w_{-2} - w_0 - w_{-1})\theta + m] d\theta \\ & + t \int R_{+1} R_{+2} R_{-1} R_{-2} r dr \int \cos[(w_{+2} + w_{-2} - w_{+1} - w_{-1})\theta + n] d\theta \\ & + 2\sqrt{6}c_1 \int R_0 R_{+1}^2 R_{+2} r dr \int \cos[(w_0 - 2w_{+1} + w_{+2})\theta + o] d\theta \\ & + 2\sqrt{6}c_1 \int R_0 R_{-1}^2 R_{-2} r dr \int \cos[(w_0 + w_{-2} - 2w_{-1})\theta + p] d\theta \\ & + \frac{2c_2}{5} \int R_{+2} R_{-2} R_0^2 r dr \int \cos[(2w_0 - w_{+2} - w_{-2})\theta + q] d\theta, \end{aligned} \quad (2.9)$$

where

$$k = \alpha_{+1} + \alpha_{-1} - 2\alpha_0, \quad l = \alpha_{+2} + \alpha_{-1} - \alpha_0 - \alpha_{+1}, \quad m = \alpha_{+1} + \alpha_{-2} - \alpha_0 - \alpha_{-1}, \quad (2.10a)$$

$$n = \alpha_{+2} + \alpha_{-2} - \alpha_1 - \alpha_{-1}, \quad o = \alpha_0 - 2\alpha_{+1} + \alpha_{+2}, \quad p = (\alpha_0 + \alpha_{-2} - 2\alpha_{-1}), \quad (2.10b)$$

$$q = (2\alpha_0 - \alpha_{+2} - \alpha_{-2}), \quad t = \left[4c_1 - \frac{4c_2}{5} \right]. \quad (2.10c)$$

A typical θ -dependent term in Eq. (2.9) can be written as [151]

$$\int_0^{2\pi} \cos(w_s \theta + \alpha_s) d\theta = \frac{\sin(2\pi w_s + \alpha_s)}{w_s} - \frac{\sin \alpha_s}{w_s}, \quad (2.11)$$

where w_s and α_s , represent any of the linear combinations of w_j s and α_j s appearing as arguments of cosine, respectively. As w_s can only be an integer including zero, the absolute value of integral in Eq. (2.11) is 2π if $w_s = 0$ and α_s is an integer multiple of π . The exact values of α_s have to be determined by minimizing energy (2.9) with $w_s = 0$. The permitted independent winding number relations thus are

$$w_{+1} + w_{-1} - 2w_0 = 0, \quad w_{+2} + w_{-2} - w_{+1} - w_{-1} = 0, \quad w_0 + w_{-2} - 2w_{-1} = 0. \quad (2.12)$$

The energy contribution from SOC terms, obtained by using ansatz (2.7), is

$$\begin{aligned} E_{\text{soc}} &= \int dx dy \sum_j \phi_j^* \Gamma_j \\ &= \gamma \int d\mathbf{r} \left\{ R_{+2} e^{i[(w_{+1}-w_{+2}-1)\theta+(\alpha_{+1}-\alpha_{+2})]} \left[\frac{\partial R_{+1}}{\partial r} + w_{+1} \frac{R_{+1}}{r} \right] \right. \\ &\quad + R_{-1} e^{i[(w_{-2}-w_{+1}-1)\theta+(\alpha_{-2}-\alpha_{-1})]} \left[\frac{\partial R_{-2}}{\partial r} + \frac{w_{-2} R_{-2}}{r} \right] \\ &\quad + R_{+1} e^{i[(w_{+2}-w_{+1}+1)\theta+(\alpha_{+2}-\alpha_{+1})]} \left[\frac{-\partial R_{+2}}{\partial r} + \frac{w_{+2} R_{+2}}{r} \right] \\ &\quad + R_{-2} e^{i[(w_{-1}-w_{-2}+1)\theta+(\alpha_{-1}-\alpha_{-2})]} \left[\frac{-\partial R_{-1}}{\partial r} + w_{-1} \frac{R_{-1}}{r} \right] \Big\} \\ &\quad + \sqrt{\frac{3}{2}} \gamma \int d\mathbf{r} \left\{ R_{+1} e^{i[(w_0-w_{+1}-1)\theta+(\alpha_0-\alpha_{+1})]} \left[\frac{\partial R_0}{\partial r} + \frac{w_0 R_0}{r} \right] \right. \\ &\quad + R_{-1} e^{i[(w_0-w_{-1}+1)\theta+(\alpha_0-\alpha_{-1})]} \left[\frac{-\partial R_0}{\partial r} + \frac{w_0 R_0}{r} \right] \\ &\quad + R_0 e^{i[(w_{-1}-w_0-1)\theta+(\alpha_{-1}-\alpha_0)]} \left[\frac{\partial R_{-1}}{\partial r} + \frac{w_{-1} R_{-1}}{r} \right] \\ &\quad + R_0 e^{i[(w_{+1}-w_0+1)\theta+(\alpha_{+1}-\alpha_0)]} \left[\frac{-\partial R_{+1}}{\partial r} + \frac{w_{+1} R_{+1}}{r} \right] \Big\}. \end{aligned} \quad (2.13)$$

where $\mathbf{r} \equiv \{x, y\} \equiv \{r, \theta\}$. Again, a minimization of E_{soc} requires that

$$w_{+2} - w_{+1} + 1 = 0, \quad w_{+1} - w_0 + 1 = 0, \quad (2.14a)$$

$$w_{-2} - w_{-1} - 1 = 0, \quad w_{-1} - w_0 - 1 = 0, \quad (2.14b)$$

and linear combinations of α_j s appearing in Eq. (2.13) are integer multiple of π . The winding number relations in Eq. (2.12) are not independent as all can be obtained from winding num-

ber relations in Eqs. (2.14a)-(2.14b). The following are independent relationships among the permitted winding numbers:

$$w_{+2} - w_{+1} + 1 = 0, \quad w_{+1} - w_0 + 1 = 0, \quad (2.15a)$$

$$w_{-2} - w_{-1} - 1 = 0, \quad w_{-1} - w_0 - 1 = 0. \quad (2.15b)$$

The allowed winding number combinations are $(-2, -1, 0, +1, +2)$, $(-1, 0, +1, +2, +3)$, $(0, +1, +2, +3, +4)$, and higher. It is to be also noted that an axisymmetric configuration without any phase singularity in any of the components, i.e., with a winding number combination of $(0, 0, 0, 0, 0)$, is not allowed as per Eqs. (2.15a)-(2.15b). Using Eq. (2.7), the phase-dependent part of the kinetic energy (KE) of the condensate is

$$\text{KE} = \sum_{j=-2}^{+2} w_j^2 \int \frac{\pi \phi_j^2}{r} dr, \quad (2.16)$$

which indicates that the system might end up favoring small winding numbers.

2.1.2 Single-particle Hamiltonian

The emergence of the axisymmetric solutions to Eqs. (2.2a)-(2.2c) in the form of a $(-2, -1, 0, +1, +2)$ -type multiring state can be inferred from the eigenfunction of the single-particle (or noninteracting) Hamiltonian in Eq. (2.1). One eigenfunction of the single-particle Hamiltonian with (minimum) energy $-2\gamma^2$ is

$$\Phi = \frac{1}{4} \begin{pmatrix} e^{-2i\varphi} \\ -2e^{-i\varphi} \\ \sqrt{6} \\ -2e^{i\varphi} \\ e^{2i\varphi} \end{pmatrix} e^{ixk_x + iyk_y} \equiv \zeta(\varphi) e^{ixk_x + iyk_y}, \quad (2.17)$$

where $\varphi = \tan^{-1}(k_y/k_x)$ and $k^2 = k_x^2 + k_y^2 = (2\gamma)^2$, which corresponds to the minimum of eigenenergy

$$E(k_x, k_y) = \frac{1}{2} \left(k_x^2 + k_y^2 - 4\gamma \sqrt{k_x^2 + k_y^2} \right). \quad (2.18)$$

The 2D contour plot of eigenenergy $E(k_x, k_y)$ for $\gamma = 1$ is shown in Fig. 2.2. The eigenenergy is minimum along a circle of radius 2, i.e., for $k_x^2 + k_y^2 = 4$. Hence a typical $\mathbf{k} \equiv (k_x, k_y)$ which minimizes the eigenenergy is as shown in Fig. 2.2, where φ can vary from 0 to 2π . The eigenfunctions with different orientations of the vector $\mathbf{k} \equiv \{k_x, k_y\}$ in the $k_x - k_y$ plane, as shown in Fig. 2.2, are all degenerate. Another solution to the single-particle Hamiltonian can be obtained by considering an equal-weight superposition of eigenfunctions in Eq. (2.17) with \mathbf{k} allowed to point along all the directions in 2D plane. The solution so obtained is

$$\Phi_{\text{MR}} = \frac{1}{8\pi} \int_0^{2\pi} \begin{pmatrix} e^{-2i\varphi} \\ -2e^{-i\varphi} \\ \sqrt{6} \\ -2e^{i\varphi} \\ e^{i2\varphi} \end{pmatrix} e^{i2\gamma r \cos(\varphi-\theta)} d\varphi = \frac{1}{4} \begin{pmatrix} -e^{-2i\theta} J_2(2\gamma r) \\ -2ie^{-i\theta} J_1(2\gamma r) \\ \sqrt{6} J_0(2\gamma r) \\ -2ie^{i\theta} J_1(2\gamma r) \\ -e^{2i\theta} J_2(2\gamma r) \end{pmatrix}, \quad (2.19)$$

where $\theta = \tan^{-1} y/x$, and $J_n(2\gamma r)$ with $n = 0, 1, 2$ is the Bessel function of first kind of order n and where Φ_{MR} has the phase singularities of a multiring soliton. Solution (2.19) agrees with the permissible winding number combination of $(-2, -1, 0, +1, +2)$ obtained earlier based on energetic considerations, viz., Eqs. (2.15a)-(2.15b), and corresponds to a $(-2, -1, 0, +1, +2)$ -type multiring soliton. As the component densities, $\rho_j \sim |J_{|j|}|^2$, the densities would have a long undulating tail and in the asymptotic region with $r \rightarrow \infty$, $\rho_j \sim \sqrt{2/(2\pi\gamma r)} \cos(2\gamma r - \pi|j|/2 - \pi/4)$.

Besides superposition of an infinite number of plane waves, viz., Eq. (2.19), one can also have a superposition of (a) two counterpropagating plane waves, (b) three plane waves the propagation vectors of which make an angle $2\pi/3$ with each other, or (c) four plane waves the propagation vectors of which make an angle $\pi/2$ with each other. Choosing the x direction as the direction for one of these wave vectors, these superpositions, representing a stripe (ST), triangular lattice (TL), and square lattice (SL), respectively, are

$$\Phi_{\text{ST}} = \frac{1}{\sqrt{2}} [\zeta(0)e^{i2\gamma x} + \zeta(\pi)e^{-i2\gamma x}], \quad (2.20a)$$

$$\Phi_{\text{TL}} = \frac{1}{\sqrt{3}} \left[\zeta(0)e^{i2\gamma x} + \zeta(2\pi/3)e^{i(-\gamma x + \gamma\sqrt{3}y)} + \zeta(4\pi/3)e^{i(-\gamma x - \gamma\sqrt{3}y)} \right], \quad (2.20b)$$

$$\Phi_{\text{SL}} = \frac{1}{2} [\zeta(0)e^{i2\gamma x} + \zeta(\pi/2)e^{i2\gamma y} + \zeta(\pi)e^{-i2\gamma x} + \zeta(3\pi/2)e^{-i2\gamma y}]. \quad (2.20c)$$

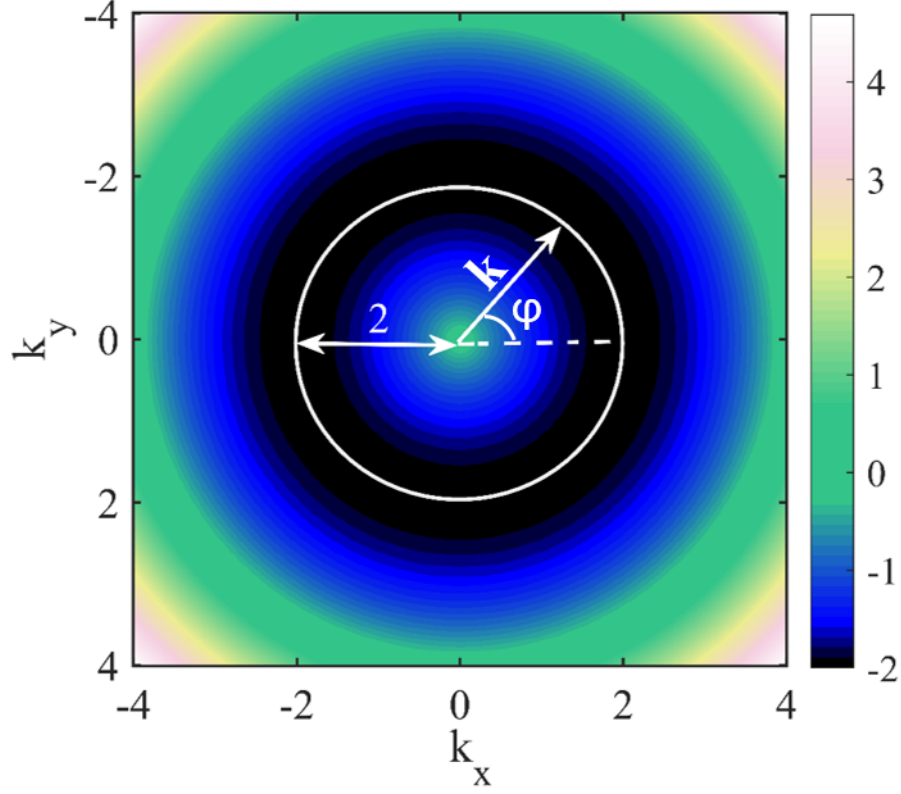


Figure 2.2: (Color online) Contour plot of eigenenergy $E(k_x, k_y)$ in Eq. (2.18) for $\gamma = 1$. The minimum corresponding to $k_x^2 + k_y^2 = 4$ is a circle of radius 2. A typical \mathbf{k} with magnitude 2 and oriented at a polar angle φ is also shown.

The component densities and corresponding total density for these degenerate solutions corresponding to $|\Phi_{ST}|^2$, $|\Phi_{TL}|^2$, $|\Phi_{SL}|^2$, and $|\Phi_{MR}|^2$ are shown in Figs. 2.3(a)-(d), 2.3(e)-(h), 2.3(i)-(l), and 2.3(m)-(p), respectively. If one examines the total density corresponding to these superpositions in Eqs. (2.19)-(2.20c) as plotted in Figs. 2.3(d), 2.3(h), 2.3(l), and 2.3(p), then in the total density corresponding to $|\Phi_{MR}|^2$ and $|\Phi_{ST}|^2$ there is no spatially periodic modulation, whereas the total density $|\Phi_{TL}|^2$ and $|\Phi_{SL}|^2$ will have a hexagonal and a square-lattice crystallization, respectively. The localized solitons for Eqs. (2.2a)-(2.2c) can be qualitatively approximated by the single-particle solutions in Eqs. (2.19)-(2.20c) multiplied by a localized Gaussian function. In the numerical solution by an imaginary-time propagation such approximations can be used as the initial functions for different solitons with appropriate symmetry.

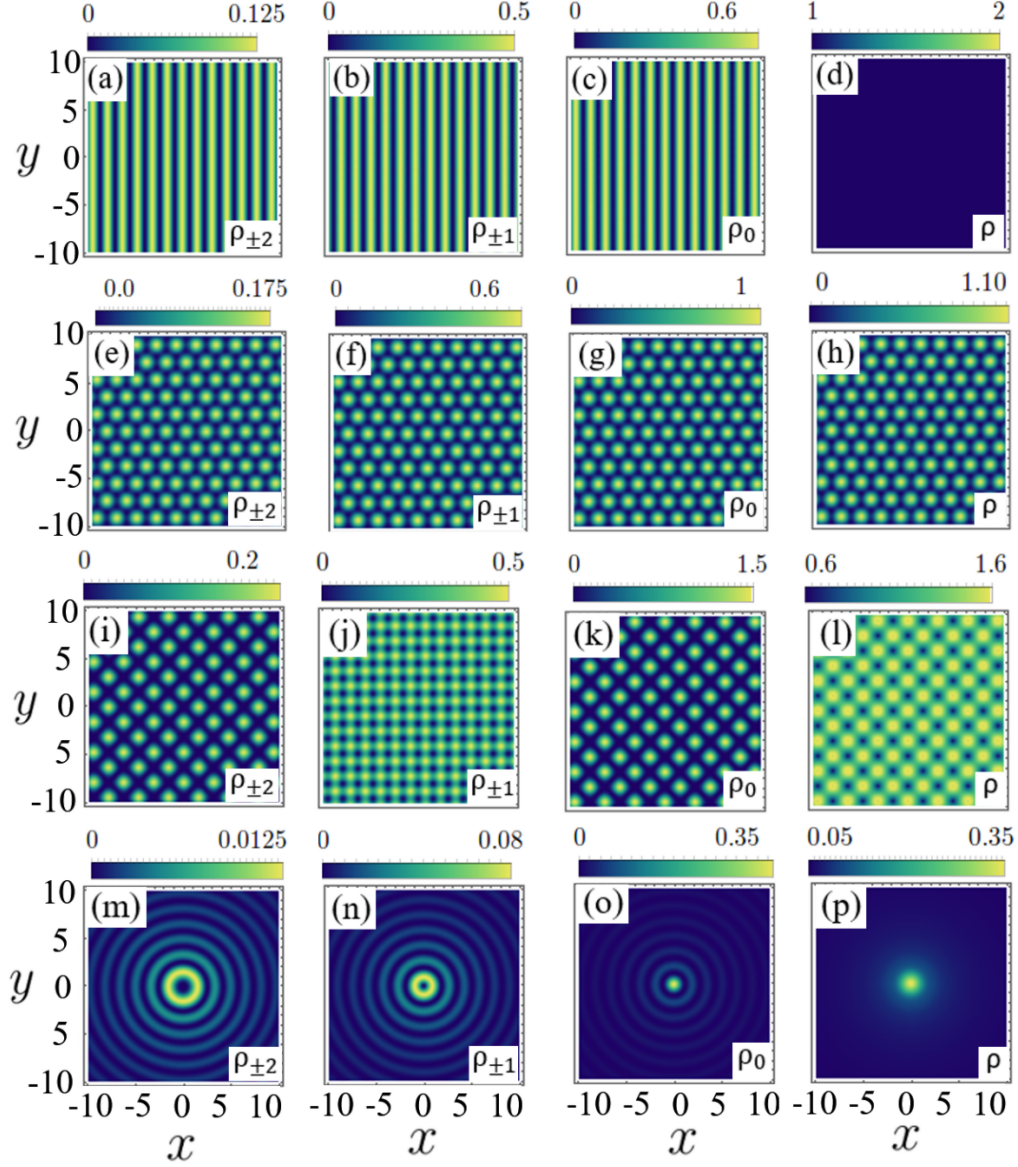


Figure 2.3: (Color online) 2D contour plots of densities of the components $j = \pm 2, \pm 1$, and 0 and total density corresponding to Φ_{ST} (stripe) are shown in panels (a)-(d) for SOC strength $\gamma = 1$. The same for Φ_{TL} (triangular lattice), Φ_{SL} (square lattice), and Φ_{MR} (multiring) are shown in (e)-(h), (i)-(l), and (m)-(p), respectively.

2.2 Numerical results

We numerically solve the CGPEs (2.2a)-(2.2c) using split time-step Fourier pseudospectral method. Details of this method are discussed in Appendix B. For SOC strengths up to $\gamma = 1$, we consider the spatial step sizes $\Delta x = \Delta y = 0.1$. Here the 2D box size for solving the

CGPEs is 60×60 . For $\gamma > 1$, the step sizes and box size considered are $\Delta x = \Delta y = 0.05$, $\Delta t = 0.00025$ and 40×40 , respectively. The time steps for imaginary- and real-time propagation are $\Delta t = 0.1 \times \Delta x^2$ and $0.05 \times \Delta x^2$, respectively. The imaginary-time propagation method is used for finding the lowest-energy state of a specific symmetry, whereas real-time propagation is used to study the dynamics. The initial guesses for an order parameter to obtain the stripe, triangular-lattice, and square-lattice solitons are considered as solutions to the noninteracting condensate, viz., Eqs. (2.20a)-(2.20c), multiplied by a localized Gaussian state, and the same for the multiring soliton is a 2D Gaussian function with appropriate vortices phase imprinted on different components. As magnetization is not conserved, during time propagation magnetization is allowed to evolve freely and attain a final converged value independent of the magnetization of the initial state. The dynamic stability of the solutions is demonstrated by real-time evolution with a small random noise added to the order parameter at $t = 0$, wherein they retain their structure for long periods of up to 400 units of time. For any solution obtained through imaginary-time propagation, evolving it sufficiently long in real-time propagation is advisable to check its stability.

Our numerical studies reveal that an SO-coupled spin-2 BEC with attractive interactions can have a variety of self-trapped stationary solutions including the cases where the total density of the condensate exhibits regular hexagonal or square patterns. The ground-state phase diagrams of a ferromagnetic BEC with $c_0 = -0.5$ and $c_1 = -0.025$ and polar and cyclic BECs with $c_0 = -0.5$ and $c_1 = 0.025$ in c_2 - γ planes are shown in Figs. 2.4(a) and 2.4(b), respectively. For the ferromagnetic BEC, as the strength of the SOC is increased, the ground state changes from an axisymmetric multiring soliton to an asymmetric soliton. For the polar and cyclic BECs, the ground-state phase changes from a multiring soliton to a stripe soliton above a critical SOC for the chosen set of interaction parameters. In a narrow strip near $\gamma = 1$, a triangular-lattice soliton appears as one of the quasidegenerate ground states in all three magnetic phases as shown by shaded regions in Figs. 2.4(a)-(b). It is also pertinent to point out that the energy difference between the quasidegenerate states decreases (increases) with a decrease (increase) in $|c_0|$.

2 Supersolid-like solitons in spin-orbit-coupled condensates

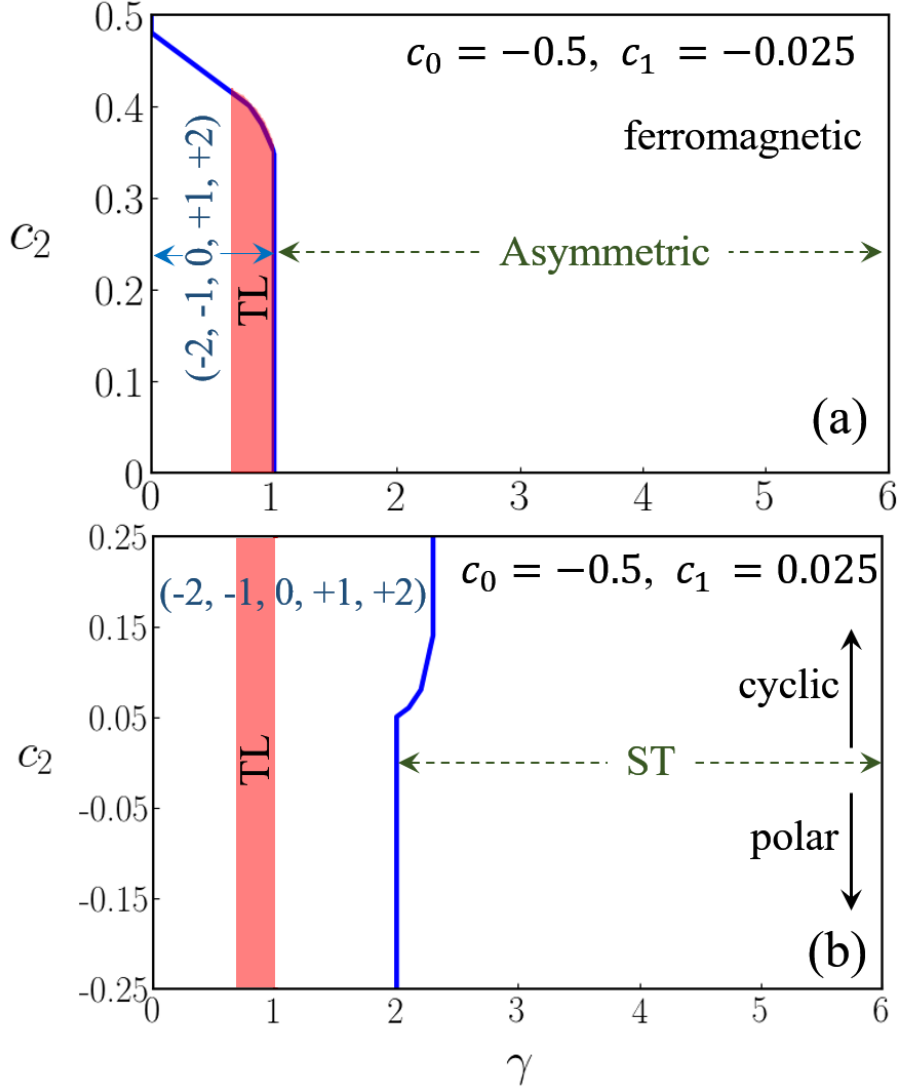


Figure 2.4: (Color online) The c_2 vs γ phase plots for the ground states are shown (a) for the ferromagnetic phase with $c_0 = -0.5$ and $c_1 = -0.025$ and (b) for the cyclic and polar phases with $c_0 = -0.5$ and $c_1 = 0.025$. In subfigure (a) for small SOC strengths the axisymmetric $(-2, -1, 0, +1, +2)$ state is the ground state similar to the state shown in Figs. 2.5(a)-2.5(d), whereas for larger SOC strengths the asymmetric soliton state is the ground state similar to the state shown in Figs. 2.6(f)-2.6(j). In subfigure (b) for small SOC strengths the axisymmetric $(-2, -1, 0, +1, +2)$ state is the ground state similar to the state shown in Figs. 2.5(a)-2.5(d), whereas for larger SOC strengths the ST (stripe) soliton state is the ground state similar to the state shown in Figs. 2.9(a)-2.9(d). Difference in energy of other quasidegenerate solitons from these ground states is $\gtrsim 10^{-4}$. As an illustration, one of the quasidegenerate states is the TL (triangular lattice) state similar to the state shown in Figs. 2.7(a)-2.7(d), which occupies a narrow region near $\gamma = 1$ and is shown by a red shaded strip. The energy differences between the TL state and the $(-2, -1, 0, +1, +2)$ -type multiring ground state in plots (a) and (b) are 10^{-4} - 10^{-3} . The energies have been obtained by using Eq. (2.6) in Sec. 2.1.

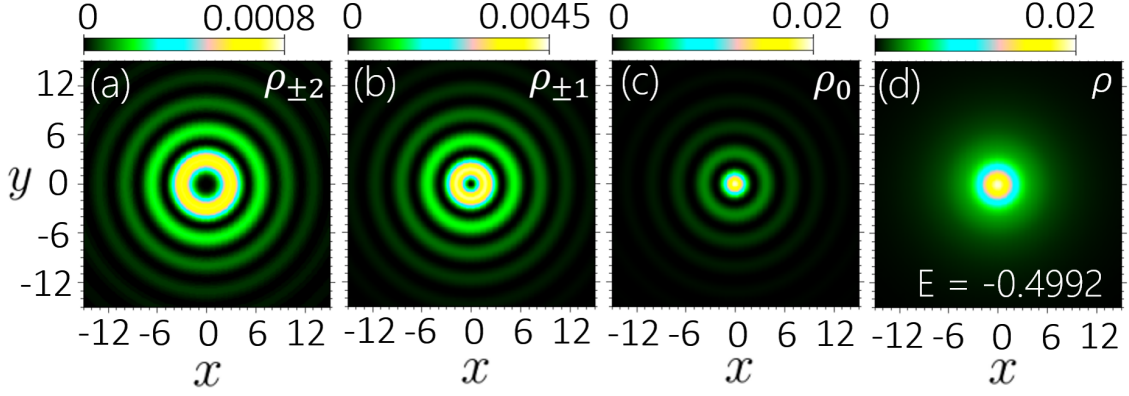


Figure 2.5: (Color online) Contour plot of density of the components (a) $j = \pm 2$, (b) $j = \pm 1$, (c) $j = 0$, and (d) total density of an axisymmetric $(-2, -1, 0, +1, +2)$ -type multiring soliton with $c_0 = -0.5$, $c_1 = -0.025$, $c_2 = 0.25$ (ferromagnetic phase), and $\gamma = 0.5$ with energy $E = -0.4992$. The energy has been obtained by using Eq. (2.6) in Sec. 2.1.

2.2.1 Small SOC strength

2.2.1.1 Ferromagnetic phase

In an SO-coupled spin-2 BEC with specific interaction parameters, namely $c_0 < 0$, $c_1^{(1)} \leq c_1 < 0$, and $c_2 > 0$, the system can exhibit weak ferromagnetism as depicted in Figure 2.1; here $c_1^{(1)}$ is a constant. The system's ground state is characterized by an axisymmetric density pattern corresponding to a $(-2, -1, 0, +1, +2)$ -type multiring soliton. On the other hand, higher energy states can display either axisymmetric or circularly asymmetric density patterns. For smaller c_1 , i.e., $c_1 < c_1^{(1)}$, the interactions become (relatively) strongly ferromagnetic, and the ground state corresponds to a circularly asymmetric soliton. The $(-2, -1, 0, +1, +2)$ -type axisymmetric multiring soliton continues to exist in this case but is no longer the ground state. With a further decrease of c_1 below another constant $c_1^{(2)}$ an increase of attractive interaction leads to a collapse of the condensate and no solution exists. The explicit values of the constants $c_1^{(1)}$ and $c_1^{(2)}$ are dependent on the parameters c_0 , c_2 , and γ .

a. Axisymmetric multiring soliton. As an example in the ferromagnetic phase, we consider $c_0 = -0.5$, $c_1 = -0.025 > c_1^{(1)} = -0.05$, $c_2 = 0.25$, and $\gamma = 0.5$. The ground-state solution for this set of parameters is an axisymmetric $(-2, -1, 0, +1, +2)$ -type multiring soliton with energy $E = -0.4992$ as exhibited in Fig. 2.5 through a contour plot of the component densities (a) $\rho_{\pm 2}$, (b) $\rho_{\pm 1}$, and (c) ρ_0 , and (d) the total density ρ . The densities of components $\pm j$ with $j = 1, 2$

are equal. This state has the same rotational symmetry as the ground state of the noninteracting SO-coupled condensate governed by Eq. (2.19) and has a long undulating tail of decreasing amplitude consistent with the asymptotic behavior of Bessel functions. If the wave function in Eq. (2.19) is multiplied by a localized Gaussian function, the resultant function qualitatively produces the density of the state displayed in Fig. 2.5. Hence the density and symmetry properties of the actual physical state can be inferred from a study of the eigenfunctions of the single-particle Hamiltonian. The total density has no core at the center as the vortex cores of $j = \pm 2$ and ± 1 components are filled by a nonzero density at the center of the $j = 0$ component. The first zeros of $J_0(r)$, $J_1(r)$, and $J_2(r)$ are 2.40483, 3.83171, and 5.13562, respectively, and these agree very well with the results presented in Fig. 2.5. Numerically, this solution is obtained by evolving Eqs. (2.2a)-(2.2c) in imaginary time and using, as an initial guess, a 2D Gaussian function multiplied by an appropriate phase factor of $\exp(-ij\varphi)$ for the j^{th} component. For the same set of parameters, we also have a $(-1, 0, +1, +2, +3)$ -type multiring soliton with an energy -0.4991 as shown in Figs. 2.6(a)-(e) through a contour plot of component densities (a) ρ_{+2} , (b) ρ_{+1} , (c) ρ_0 , (d) ρ_{-1} , and (e) ρ_{-2} . The quasidegeneracy between the two solutions shown in Figs. 2.5(a)-(d) and 2.6(a)-(e) is lifted with an increase in $|c_0|$. The winding number combinations for these axisymmetric solutions are in accordance with relations given in Eqs. (2.15a)-(2.15b).

b. Circularly asymmetric soliton: For the relatively stronger ferromagnetic interaction, the ground state is a circularly asymmetric soliton, *e.g.* for $c_0 = -0.5$, $c_1 = -0.1$, $c_2 = 0.25$, and $\gamma = 0.5$, contour plots of circularly-asymmetric component densities are shown in Figs. 2.6(f)-(j). For the same set of parameters, the excited state is a $(-2, -1, 0, +1, +2)$ -type multiring soliton. Asymmetry of the ground state solution arises, in this case, as different from the $(-2, -1, 0, +1, +2)$ -type soliton displayed in Figs. 2.5(a)-(d), the phase singularities in $\pm j$ components of the circularly asymmetric soliton exhibited in Figs. 2.6(f)-(j) do not overlap. When we keep on decreasing c_1 further, then these singularities in $\pm j$ components move further apart along the y axis. For $c_0 = -0.5$, $c_1 = -1.3$, $c_2 = 0.25$, and $\gamma = 0.5$, phase singularities lie in the region where the condensate density is quite small (not shown here) and hence no perceptible density hole is visible in the component densities ρ_j . If we decrease c_1 below $c_1^{(2)} = -1.3$, while keeping c_0 , c_2 , and γ fixed, then the condensate collapses.

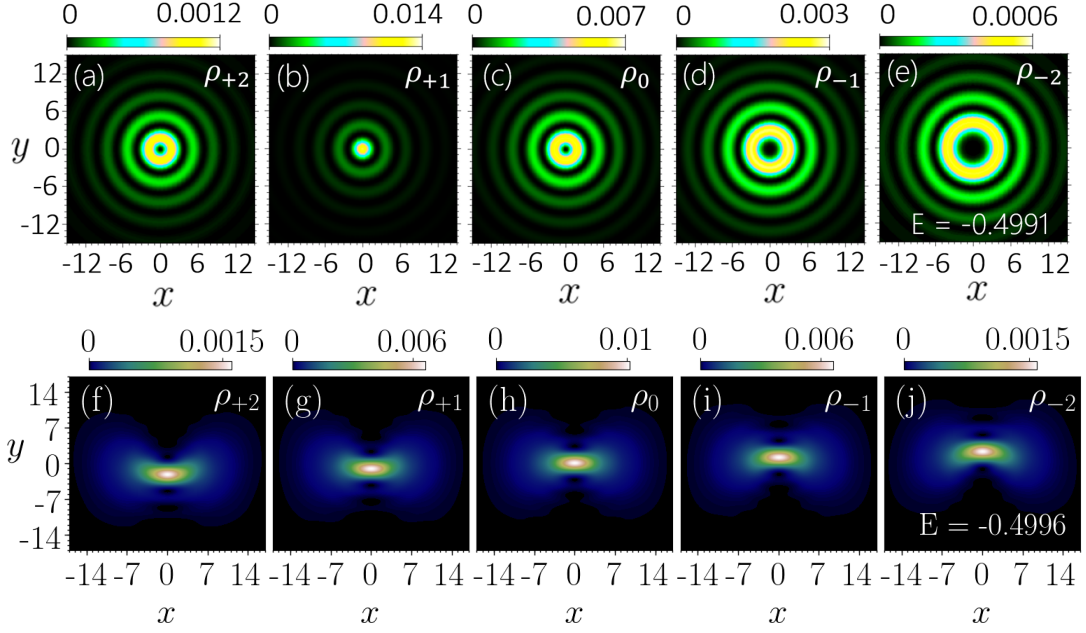


Figure 2.6: (Color online) Contour plot of density of components (a) $j = +2$, (b) $j = +1$, (c) $j = 0$, (d) $j = -1$, and (e) $j = -2$ of an axisymmetric $(-1, 0, +1, +2, +3)$ -type multiring soliton with $c_0 = -0.5$, $c_1 = -0.025$, $c_2 = 0.25$ (ferromagnetic phase), $\gamma = 0.5$, and energy $E = -0.4991$, and the same of a circularly asymmetric soliton with $c_0 = -0.5$, $c_1 = -0.1$, $c_2 = 0.25$ (strongly ferromagnetic phase), $\gamma = 0.5$, and energy $E = -0.4996$ in panels (f)-(j). The energies have been obtained by using Eq. (2.6) in Sec. 2.1.

2.2.1.2 Cyclic and polar phases

For small SOC strengths, in both cyclic and polar phases, similar to the ferromagnetic phase, the axisymmetric $(-2, -1, 0, +1, +2)$ -type multiring soliton emerges as the ground state, whereas the axisymmetric $(-1, 0, +1, +2, +3)$ -type soliton appears as a metastable state (result not shown here). For example, with $c_0 = -0.5$, $c_1 = 0.025$, $c_2 = 0.25$, and $\gamma = 0.5$ corresponding to the cyclic phase, viz., Fig. 2.1, the axisymmetric $(-2, -1, 0, +1, +2)$ -type and $(-1, 0, +1, +2, +3)$ -type multiring solitons have energies -0.4992 and -0.3864 , respectively. Similarly, with $c_0 = -0.5$, $c_1 = 0.025$, $c_2 = -0.25$, and $\gamma = 0.5$, corresponding to the polar phase, the respective energies of axisymmetric $(-2, -1, 0, +1, +2)$ -type and $(-1, 0, +1, +2, +3)$ -type multiring solitons are -0.4994 and -0.3855 . In both cases, the $(-2, -1, 0, +1, +2)$ -type multiring soliton is the ground state.

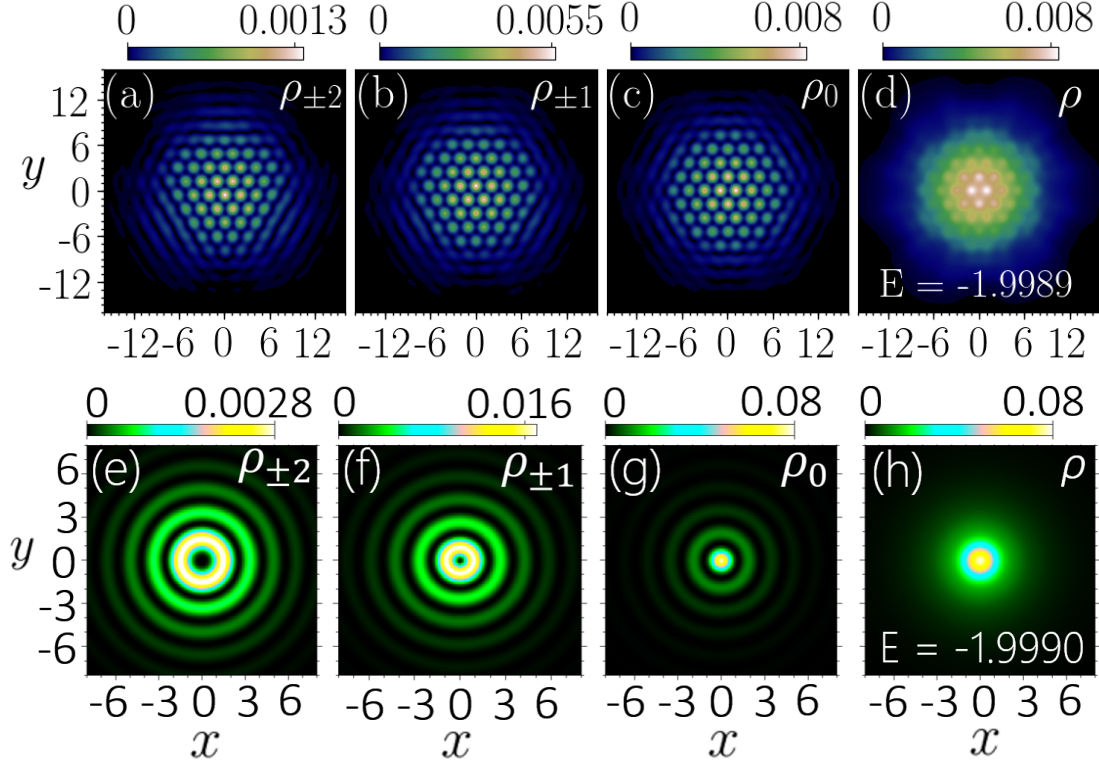


Figure 2.7: (Color online) Contour plot of density of components (a) $j = \pm 2$, (b) $j = \pm 1$, (c) $j = 0$, and (d) total density of a triangular-lattice soliton with $c_0 = -0.5$, $c_1 = 0.025$, $c_2 = 0.25$ (cyclic phase), $\gamma = 1$, and energy $E = -1.9989$, and the same of a $(-2, -1, 0, +1, +2)$ -type multiring soliton for the same parameters and $E = -1.9990$ in panels (e)-(h). The energies have been obtained by using Eq. (2.6) in Sec. 2.1.

2.2.2 Intermediate SOC strength

For intermediate SOC strengths, we get a triangular-lattice soliton, with a hexagonal-lattice crystallization in components and total densities, in all three magnetic phases – ferromagnetic, polar, and cyclic. Although a square-lattice soliton has been earlier identified in Ref. [109], a triangular-lattice soliton was not found in the spin-1 case. For example, in the cyclic phase with $c_0 = -0.5$, $c_1 = 0.025$, $c_2 = 0.25$, and $\gamma = 1$, the triangular-lattice soliton is shown in Fig. 2.7 through a contour density plot of component densities (a) $\rho_{\pm 2}$, (b) $\rho_{\pm 1}$, (c) ρ_0 , and (d) total density. The triangular-lattice structure is a result of the superposition of three plane waves and corresponds to a solution of the noninteracting system given by Eq. (2.20b). However, to get a localized hexagonal structure as in Figs. 2.7(a)-2.7(d), the function (2.20b) has to be multiplied by a localized Gaussian function. For the same parameters, an axisymmetric $(-2, -1, 0, +1, +2)$ -

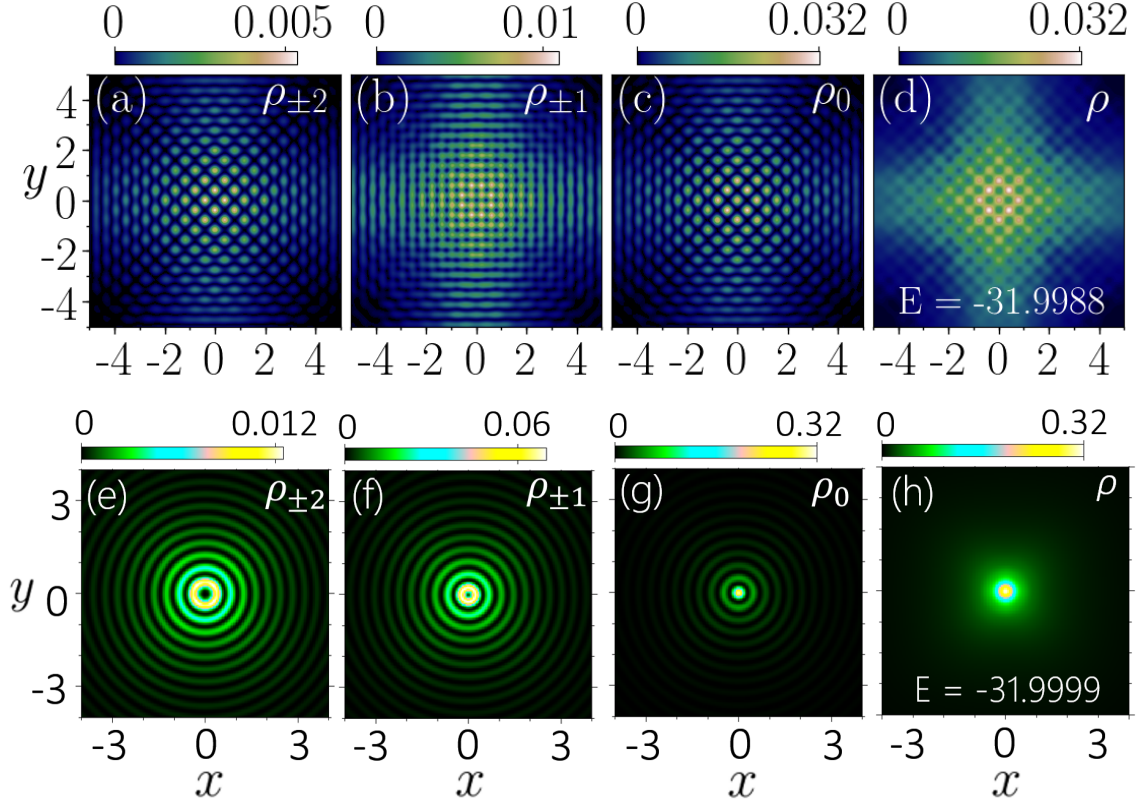


Figure 2.8: (Color online) Contour plot of density of a square-lattice soliton of components (a) $j = \pm 2$, (b) $j = \pm 1$, (c) $j = 0$, and (d) total density for $c_0 = -0.5$, $c_1 = -0.025$, $c_2 = 0.25$ (ferromagnetic phase), $\gamma = 4$, and $E = -31.9988$; for the same parameters, we show the component and total densities of a $(-2, -1, -0, +1, +2)$ -type multiring soliton in panels (e)-(h) with $E = -31.9999$. The energies have been obtained by using Eq. (2.6) in Sec. 2.1.

type multiring soliton corresponding to the single-particle solution (2.19) is also a solution as illustrated in Figs. 2.7(e)-2.7(h). Both these states, the multiring and the triangular-lattice solitons, have approximately the same numerical energy ($E = -1.9990$ and -1.9989) and are quasidegenerate. This degeneracy between the two solutions is removed with an increase in $|c_0|$ resulting in the $(-2, -1, 0, +1, +2)$ -type multiring soliton as the ground state.

2.2.3 Large SOC strength

When γ is increased further, different types of degenerate states appear with approximately the same energy in the three different magnetic phases. As an example, in the ferromagnetic phase with $c_0 = -0.5$, $c_1 = -0.025$, $c_2 = 0.25$, and $\gamma \gtrsim 4$, we get the following five types of quasidegenerate solitons: (1) a square-lattice soliton, where as shown in Figs. 2.8(a)-2.8(d)

the component as well as the total densities show square-lattice crystallization consistent with the single-particle order parameter (2.20c); (2) a multiring soliton, corresponding to the single-particle order parameter (2.19), as shown in Figs. 2.8(e)-2.8(h); (3) a circularly asymmetric soliton; (4) a stripe soliton with stripe modulation in component densities corresponding to the single-particle order parameter (2.20a); and (5) a superstripe soliton which has stripe patterns in component densities $\rho_{\pm 1}$ and square-lattice crystallization in component densities $\rho_{\pm 2}$, ρ_0 , and total density. The three latter solitons are not shown here. In the case of the square-lattice soliton, viz., Figs. 2.8(a)-2.8(d), the square-lattice crystallizations in components $j = \pm 2$ and 0 are quite similar, whereas the square-lattice pattern in the components $j = \pm 1$ is different. The lattice in components $j = \pm 2$ and 0 makes an angle of 45° with the lattice in component $j = \pm 1$, and this is consistent with a density pattern corresponding to Φ_{SL} as shown in Figs. 2.3(i)-2.3(l). The prominent square lattice in total density has the same alignment as in components $j = \pm 2$ and 0. A similar square-lattice soliton was predicted in an SO-coupled spin-1 spinor BEC [109]. The densities of components $j = \pm 2$ and 0 ($j = \pm 1$) of the square-lattice soliton of Figs. 2.8(a)-2.8(d) are quite similar to the densities of components $j = \pm 1$ ($j = 0$) of the same in an SO-coupled spin-1 spinor BEC [109]; the total densities in the two cases are also quite similar. The energies of these five different types of solitons are, respectively, -31.9988 , -31.9999 , -32.0071 , -31.9998 , and -32.0020 , and hence these solitons are quasidegenerate.

In the cyclic phase, with $c_0 = -0.5$, $c_1 = 0.025$, $c_2 = 0.25$, and $\gamma \gtrsim 4$, we again obtain four of the aforementioned quasidegenerate solitons except the circularly asymmetric soliton. The component and total densities corresponding to stripe soliton and square-lattice soliton are shown in Figs. 2.9(a)-2.9(d) and 2.9(e)-2.9(h), respectively. The stripe soliton of Figs. 2.9(a)-2.9(d) is quite similar to the one in an SO-coupled spin-1 spinor BEC [109] for $\gamma = 4$ in both ferromagnetic and polar phases. In both cases, the stripe pattern appears only in the component densities with the total density showing no modulation. The respective energies of the stripe and the square-lattice solitons are -32.0006 and -31.9990 . The superstripe soliton with energy -32.0002 and multiring soliton with energy -31.9999 are not shown here.

In the polar phase, with $c_0 = -0.5$, $c_1 = 0.025$, $c_2 = -0.25$, and $\gamma \gtrsim 4$, we get the same four quasidegenerate solitons as in the cyclic phase discussed above. Two of these, the square-lattice soliton with energy -31.9987 and superstripe soliton with energy -32.0023 , are

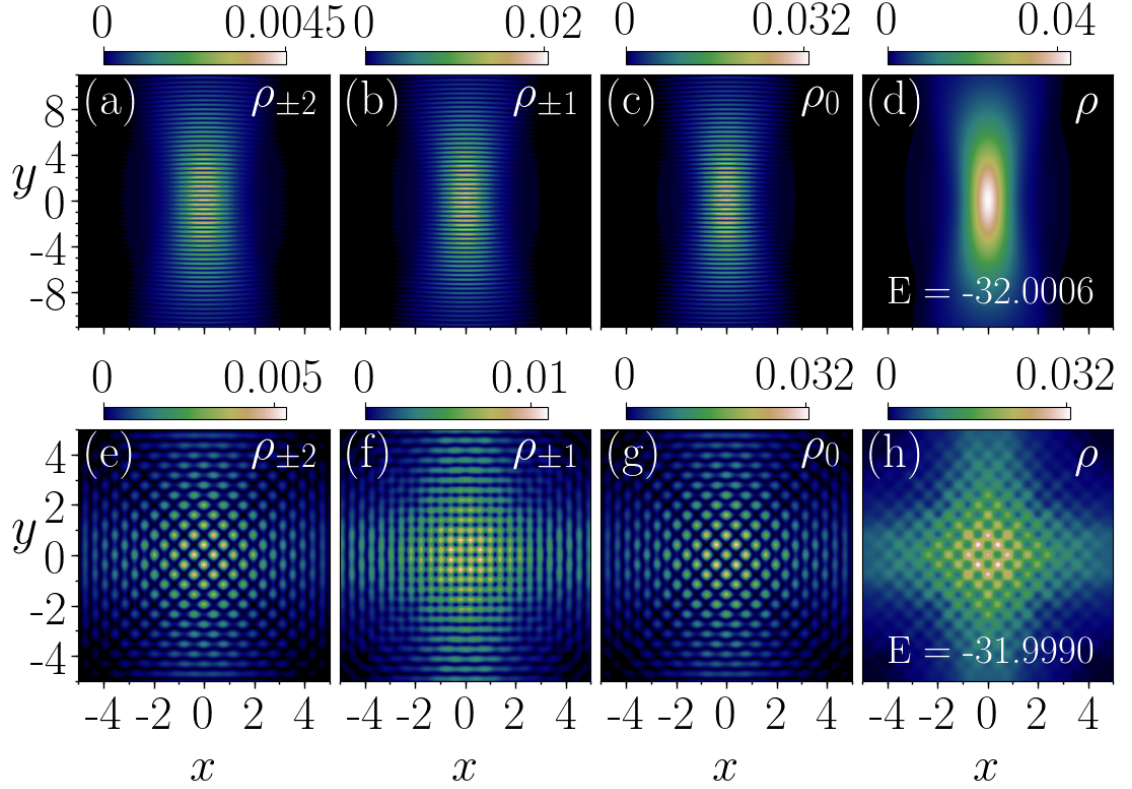


Figure 2.9: (Color online) Contour plot of the density of a stripe soliton of components (a) $j = \pm 2$, (b) $j = \pm 1$, (c) $j = 0$, and (d) total density with $c_0 = -0.5$, $c_1 = 0.025$, $c_2 = 0.25$ (cyclic phase), $\gamma = 4$, and $E = -32.0006$; the same of a square-lattice soliton for the same parameters in panels (e)-(h) with $E = -31.9990$. The energies have been obtained by using Eq. (2.6) in Sec. 2.1.

shown in Figs. 2.10(a)-2.10(d) and 2.10(e)-2.10(h), respectively. The superstripe soliton has a square-lattice-type spatial modulation superposed on stripes in components $j = \pm 2$ and 0 and a stripe modulation in component $j = \pm 1$, whereas total density has a square-lattice-type pattern. The square-lattice soliton is quite similar to the same of Figs. 2.8(a)-2.8(d) and 2.9(e)-2.9(h). However, the superstripe soliton of Figs. 2.10(e)-2.10(h) has now acquired a square-lattice pattern in total density quite similar to a superstripe soliton of an SO-coupled spin-1 spinor BEC for $\gamma = 8$ [109] in both ferromagnetic and polar phases. The stripe soliton with energy -32.0044 and multiring soliton with energy -32.0009 are not shown here.

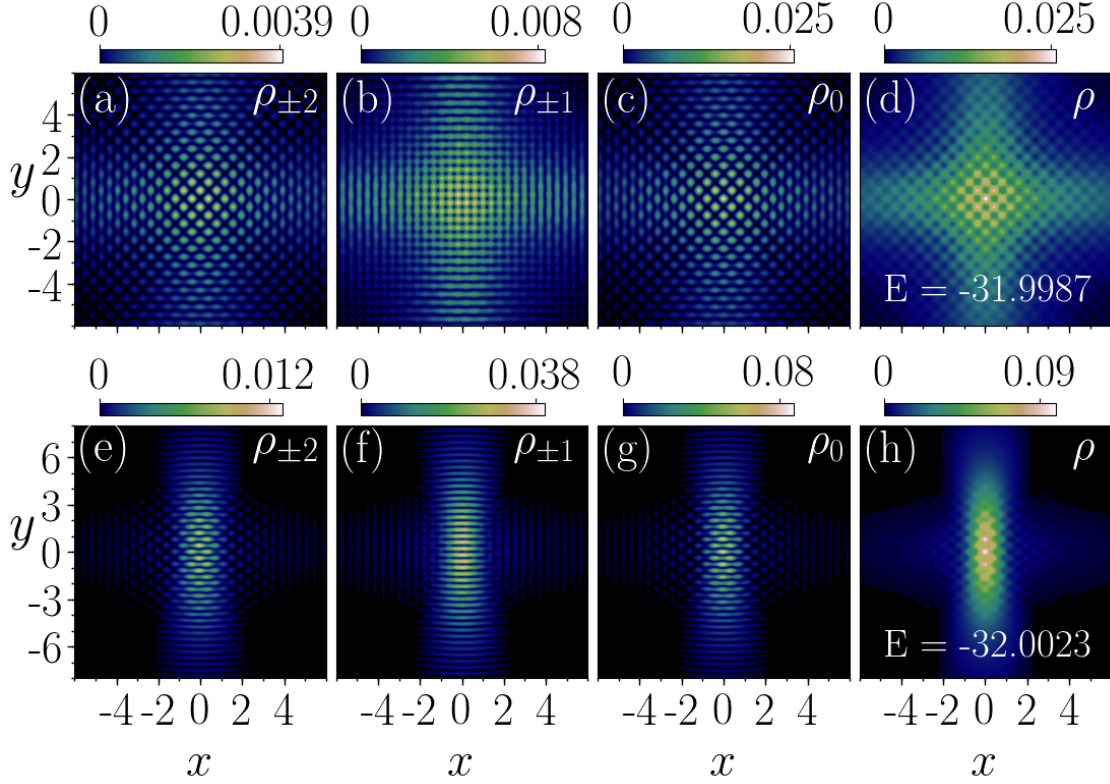


Figure 2.10: (Color online) Contour plot of the density of a square-lattice soliton of components (a) $j = \pm 2$, (b) $j = \pm 1$, (c) $j = 0$, and (d) total density with $c_0 = -0.5$, $c_1 = 0.025$, $c_2 = -0.25$ (polar phase), $\gamma = 4$, and $E = -31.9987$, and the same of a superstripe soliton for the same parameters in panels (e)-(h) with $E = -32.0023$. The energies have been obtained by using Eq. (2.6) in Sec. 2.1.

2.2.4 Dynamical stability

We confirm the dynamical stability of the stationary states of the SO-coupled spin-2 BEC discussed in Sec.(2.2.1)-(2.2.3) via a real-time propagation over an extended period of time up to $t = 500$. In addition to this, we have also tested the stability of these solutions by adding an initial random noise $\delta\phi_j^{\text{noise}}$ to the respective order parameters at $t = 0$ and then studying their real-time dynamics. We consider the random noise as

$$\delta\phi_j^{\text{noise}}(x, y) = 10^{-3} \sqrt{\mathcal{N}_j} R_g(x, y) e^{iR_u(x, y)}, \quad (2.21)$$

where $\mathcal{N}_j = \int \rho_j(x, y) d\mathbf{r}$. The amplitude of this noise is randomized by random numbers $R_g(x, y)$ which follow the Gaussian distribution, whereas phase of the noise is randomized by $R_u(x, y)$

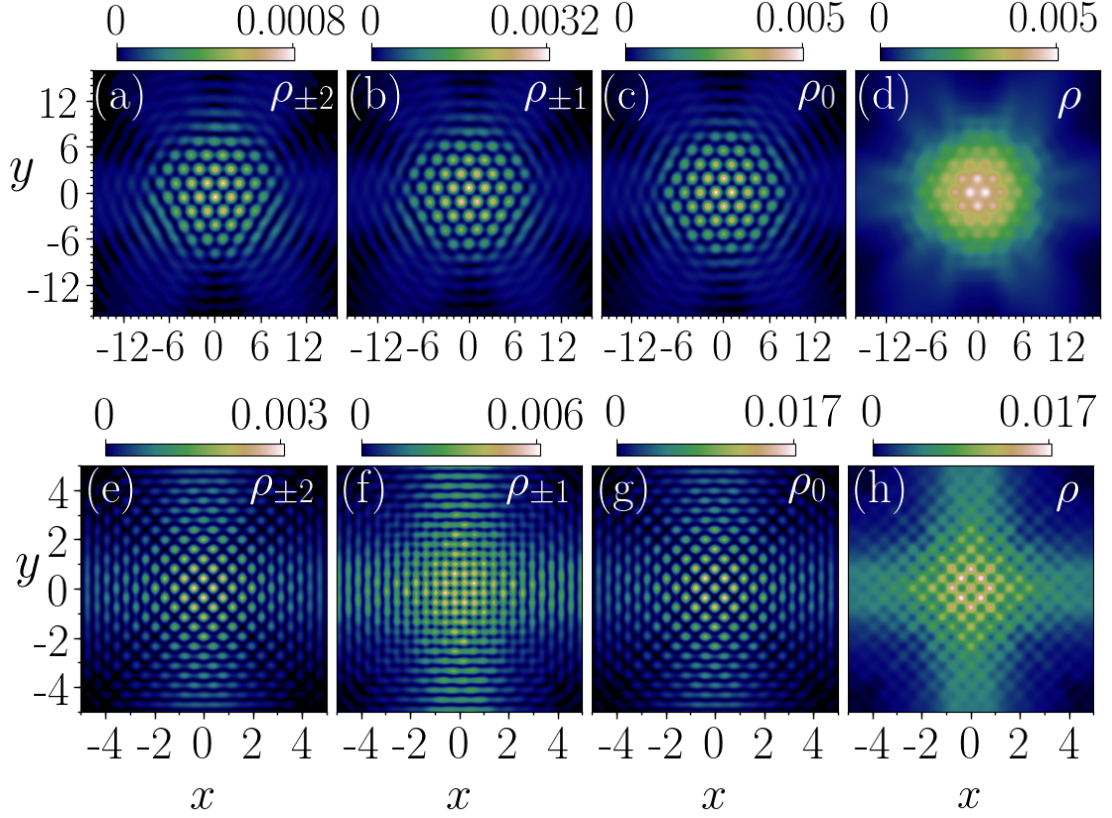


Figure 2.11: (Color online) Contour plot of component densities of the triangular-lattice soliton of Figs. 2.7(a)-(d) for components (a) $j = \pm 2$, (b) $j = \pm 1$, (c) $j = 0$, and (d) total density after 100 units of time, and the same of the square-lattice soliton of Figs. 2.8(a)-(d) for components (e) $j = \pm 2$, (f) $j = \pm 1$, (g) $j = 0$, and (h) total density, after real-time simulation over 100 units of time. The initial state used in real-time propagation is obtained by adding a random noise (2.21) to the stationary-state imaginary-time solutions shown in Figs. 2.7(a)-(d) for panels (a)-(d) and Figs. 2.8(a)-(d) for panels (e)-(h). The energies have been obtained by using Eq. (2.6) in Sec. 2.1.

which follows a uniform probability distribution over the interval $[0, 2\pi]$. As an illustration, we consider the triangular-lattice soliton of Figs. 2.7(a)-2.7(d) and the square-lattice soliton of Figs. 2.8(a)-2.8(d). At $t = 0$, $\delta\phi_j^{\text{noise}}$ is added to the respective order parameters and the resultant order parameters are considered initial solutions to Eqs. (2.2a)-(2.2c), which are now solved (evolved) in real time up to $t = 100$. The resultant component and total densities at $t = 100$ are displayed in Figs. 2.11(a)-2.11(d) and 2.11(e)-2.11(h), respectively. The periodic density patterns survive with slightly different peak densities compared to the $t = 0$ solutions, demonstrating the dynamical stability of the solitons.

2.2.5 Bifurcations

In the noninteracting system, various solutions are completely degenerate, whereas on the introduction of interactions, solutions of Eqs. (2.2a)-(2.2c) exhibit a bifurcating behavior. As the energies of these solutions are very close, to make the nature of these bifurcations clear, we calculate the difference ΔE between total energy of the solution and the single-particle solution's energy, i.e., $-2\gamma^2$ as discussed in Sec. 2.1.2. A cut is now considered in the phase diagram in Fig. 2.4(a) at an appropriate c_2 , say $c_2 = 0.15$, for the ferromagnetic phase, and ΔE as a function of SOC strength γ is evaluated for the various solutions. Similarly, a cut at $c_2 = 0.15$ for the cyclic phase in Fig. 2.4(b) and at $c_2 = -0.15$ for the polar phase in Fig. 2.4(b) are considered. The resultant bifurcation plots showing ΔE as a function of the SOC strength γ are shown in Figs. 2.12(a)-2.12(c) for the three magnetic phases. Bifurcation points agree with the critical points in the phase diagrams shown in Figs. 2.4(a)-(b).

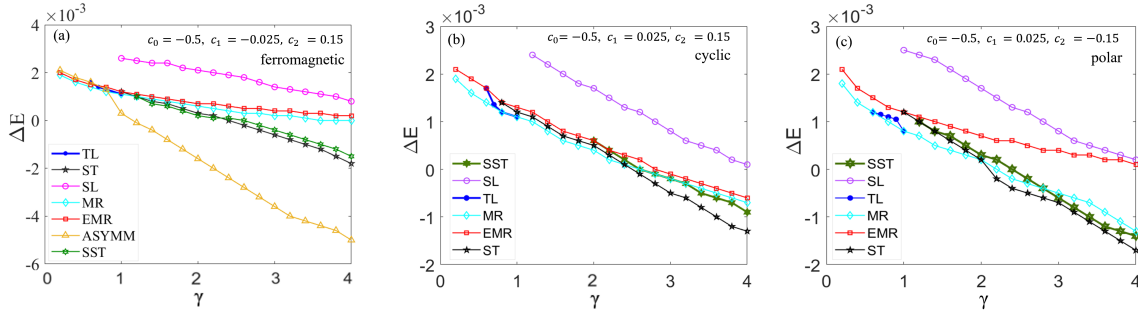


Figure 2.12: (Color online) (a) The bifurcation diagram in the ΔE - γ plane for the ferromagnetic phase corresponding to a cut in the phase diagram in Fig. 2.4(a) at $c_2 = 0.15$. The same for the cyclic phase is shown in panel (b) by taking a cut at $c_2 = 0.15$ in the phase diagram in Fig. 2.4(b). In the polar domain of the phase diagram in Fig. 2.4(b), a cut is taken at $c_2 = -0.15$, and the bifurcation picture is shown in panel (c). $\Delta E = E + 2\gamma^2$, where E is the energy of the state obtained from Eq. (2.6) in Sec. 2.1 and $-2\gamma^2$ is the single-particle solution's energy, corresponding to various quasidegenerate states, is plotted by using different symbols as well as different colors. SST corresponds to the superstripe similar to the state shown in Figs. 2.10(e)-(h), SL corresponds to the square lattice similar to the state shown in Figs. 2.8(a)-(d), TL corresponds to the triangular lattice similar to the state shown in Figs. 2.7(a)-(d), MR corresponds to the $(-2, -1, 0, +1, +2)$ -type multiring solution similar to the state shown in Figs. 2.5(a)-(d), EMR corresponds to the $(-1, 0, +1, +2, +3)$ -type excited-state multiring solution similar to the state shown in Figs. 2.6(a)-(e), ST corresponds to the stripe solution similar to the state shown in Figs. 2.9(a)-(d), and ASYMM corresponds to the circularly asymmetric solution similar to the state shown in Figs. 2.6(f)-(j).

2.2.6 Experimentally feasible bright solitons

One must tune two of the three scattering lengths to get the supersolid-like bright solitons for the spin-2 BEC. Although tuning one scattering length is possible through Feshbach resonance, tuning multiple scattering lengths is an experimental challenge that has still not been achieved. Notwithstanding, by tuning one of the scattering lengths, supersolid-like bright solitons have been predicted [109] and could be realized experimentally in lower spin systems like pseudospinor-1/2 and spin-1 BECs. To illustrate this, we consider 1000 atoms of ^{23}Na spin-1 BEC free in the x - y plane and confined by a harmonic trap along the z direction with trapping frequency $\omega_z = 2\pi \times 100$ Hz. It results in $a_{\text{osc}} = 2.1 \mu\text{m}$, where $a_{\text{osc}} = \sqrt{\hbar/m\omega_z}$. Interaction strengths c_0 and c_1 for the q2D spin-1 BEC in the dimensionless units are

$$c_0 = \sqrt{8\pi} \frac{N(a_0 + 2a_2)}{3a_{\text{osc}}}, \quad c_1 = \sqrt{8\pi} \frac{N(a_2 - a_0)}{3a_{\text{osc}}}, \quad (2.22)$$

where $a_0 = 50a_B$ and $a_2 = 55.01a_B$ for experimentally realizable ^{23}Na spin-1 BEC [152]. We keep a_2 fixed and tuned a_0 to $-130a_B$. This results in $c_0 = -0.84$ and $c_1 = 7.80$. The ground-state $(-1, 0, +1)$ -type multiring soliton obtained by solving the CGPEs (A.13a)-(A.13b) is shown in Fig. 2.13. These parameters $c_0 = -0.84$, $c_1 = 7.80$, and $\gamma = 1$ corresponds to the phase diagram

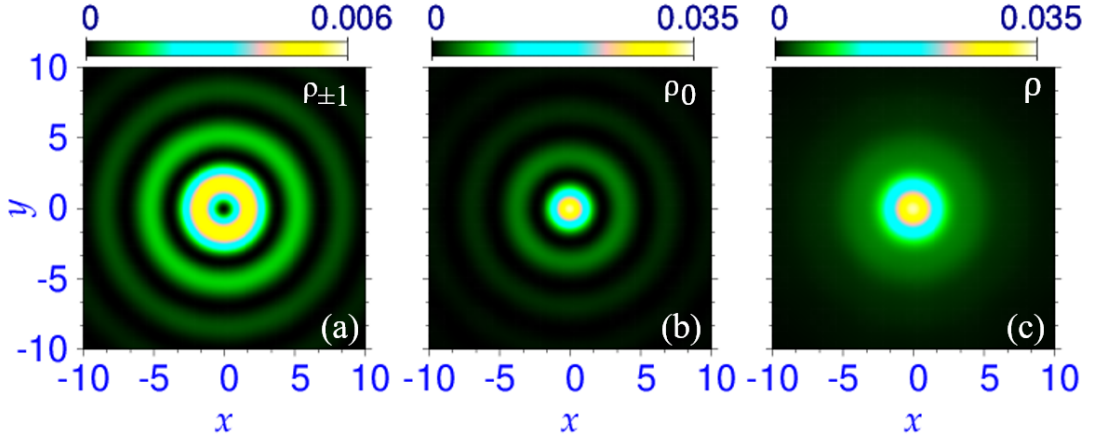


Figure 2.13: (Color online) Contour plot of density ρ_j of a $(-1, 0, +1)$ -type multiring SO-coupled BEC soliton for components (a) $\rho_{\pm 1}$, (b) ρ_0 , and (c) total density ρ for $c_0 = -0.84$, $c_1 = 7.80$, and $\gamma = 1$.

in Ref. [109] which also predicts $(-1, 0, +1)$ multiring soliton. Similarly, all other supersolid-like

solitons depicted in the Ref. [109] for SO-coupled spin-1 BEC can be related to the realistic set of parameters.

2.2.7 Spin texture

We examine the spin texture of the ground state phases by calculating the spin-density vector $\mathbf{F}(x, y)$ in Eq. 1.16. The spin-density vector is normalized to 2. We have shown the spin-texture for $(-2, -1, 0, +1, +2)$ multiring soliton in Fig. 2.14(a), for the circularly asymmetric soliton in Fig. 2.14(b) and stripe soliton in Fig. 2.14(c). The arrows in the spin texture represent the transverse spin vector (F_x, F_y) and the colour of each arrow indicates the magnitude of F_z . Other quasi-degenerate supersolid-like bright solitons exhibit exotic spin-textures (not shown here).

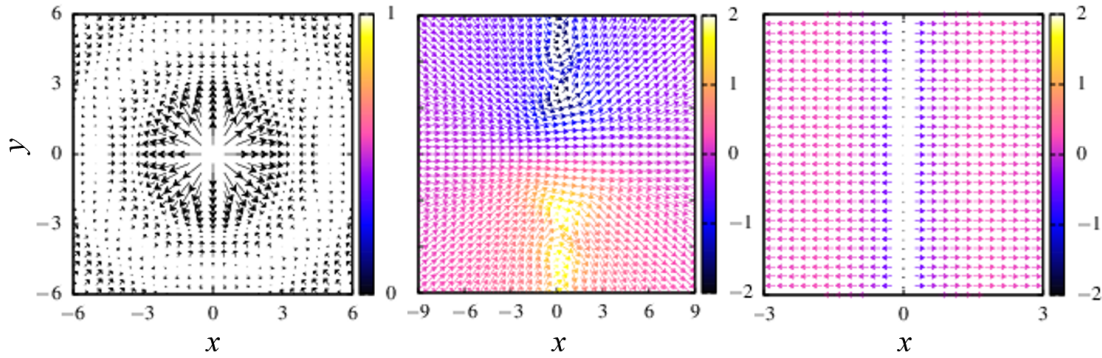


Figure 2.14: (Color online) Spin-texture for (a) $(-2, -1, 0, +1, +2)$ multiring soliton, (b) circularly asymmetric soliton, and (c) stripe soliton. In (a) $F_z(x, y)$ is zero throughout and in (c) \mathbf{F} has a reflection symmetry about $x = 0$ line. The spin textures in (a), (b), and (c) correspond to the densities shown in Fig. 2.5, Figs. 2.6(f)-(j), and Figs. 2.9(a)-(d), respectively.

2.2.8 Moving $(-2, -1, 0, +1, +2)$ -type soliton

The SOC breaks the Galilean invariance of the mean-field model of the spinor BECs [84, 107, 153]. Explicitly, considering the Galilean transformation $x' = x, y' = y - vt, t' = t$, where v is the relative velocity along the y axis of a primed coordinate system with respect to an unprimed coordinate system, along with the following transformation of the wave function

$$\phi_j(x, y, t) = \psi_j'(x', y', t') e^{i v y' + i v^2 t' / 2}, \quad (2.23)$$

we get from Eqs. (2.2a)-(2.2c)

$$i\partial_{t'}\psi'_{\pm 2} = \mathcal{H}\psi'_{\pm 2} + c_0\rho\psi'_{\pm 2} + c_1(F'_{\mp}\psi'_{\pm 1} \pm 2F'_z\psi'_{\pm 2}) + \frac{c_2}{\sqrt{5}}\Theta\psi'_{\mp 2} - i\gamma\partial_{\mp}\psi'_{\pm 1} + \gamma\psi'_{\pm 1}v, \quad (2.24a)$$

$$i\partial_{t'}\psi'_{\pm 1} = \mathcal{H}\psi'_{\pm 1} + c_0\rho\psi'_{\pm 1} + c_1\left(\sqrt{\frac{3}{2}}F'_{\mp}\psi'_0 + F'_{\pm}\psi'_{\pm 2} \pm F'_z\psi'_{\pm 1}\right) - \frac{c_2}{\sqrt{5}}\Theta\psi'_{\mp 1} - i\gamma\sqrt{\frac{3}{2}}\partial_{\mp}\psi'_0 - i\gamma\partial_{\pm}\psi'_{\pm 2} + \gamma\left(\sqrt{\frac{3}{2}}\psi'_0 + \psi'_{\pm 2}\right)v, \quad (2.24b)$$

$$i\partial_{t'}\psi'_0 = \mathcal{H}\psi'_0 + c_0\rho\psi'_0 + c_1\sqrt{\frac{3}{2}}(F'_-\psi'_{-1} + F'_+\psi'_{+1}) + \frac{c_2}{\sqrt{5}}\Theta\psi'_0 - i\sqrt{\frac{3}{2}}\gamma\partial_+(\psi'_{+1} + \psi'_{-1}) + \gamma\sqrt{\frac{3}{2}}(\psi'_{+1} + \psi'_{-1})v, \quad (2.24c)$$

where $\partial_{\pm} = (\partial_{x'} \pm i\partial_{y'})$. These equations are distinct from Eqs. (2.2a)-(2.2c) indicating a breakdown of the Galilean invariance. For an SO-coupled spin-2 BEC, the moving solitons are the stationary solutions of Eqs. (2.24a)-(2.24c) multiplied by a factor of e^{ivy} . The structure of the moving soliton depends on the magnitude as well as the direction of velocity. Here we study the fate of a moving $(-2, -1, 0, +1, +2)$ -type multiring soliton by solving Eqs. (2.24a)-(2.24c) numerically, for small SOC strength, as the velocity is increased. For example, considering $c_0 = -2.5, c_1 = -0.025, c_2 = 0.25$, and $\gamma = 0.5$ with (a) $v = 0.03$ and (b) $v = 0.1$, the component densities of the moving solitons are shown in Figs. 2.15(a)-2.15(e) and 2.15(f)-2.15(j), respectively. The structures of the moving soliton at two different velocities are quite distinct as can be seen in Fig. 2.15. With the increase of velocity along the y axis, the component phase singularities move along the x axis to the region of low density away from the center, resulting in component densities without any vortex core at velocity $v = 0.1$. For $c_0 = -2.5, c_1 = -0.025, c_2 = 0.25$, and $\gamma = 0.5$, a self-trapped moving soliton with $v > 0.3$ does not exist.

We have also studied the head-on collision of these solitons. At low velocities, the collision is inelastic while the solitons come close to each other, interact, and form a bound entity and never come out. On the other hand, at large initial velocities, the collision is quasi-elastic. In this case, the solitons tend to pass through each other without any change of velocity; nonetheless, solitons undergo minor changes in shape and a perceptible change in the peak densities after the collision. In contrast in an elastic collision, the colliding solitons pass through each other without any change either in their shape or velocities. For example, the head-on collision between the solitons moving with $|v| = 0.03$ and $c_0 = -2.5, c_1 = -0.025, c_2 = 0.25$, and $\gamma = 0.5$ is shown

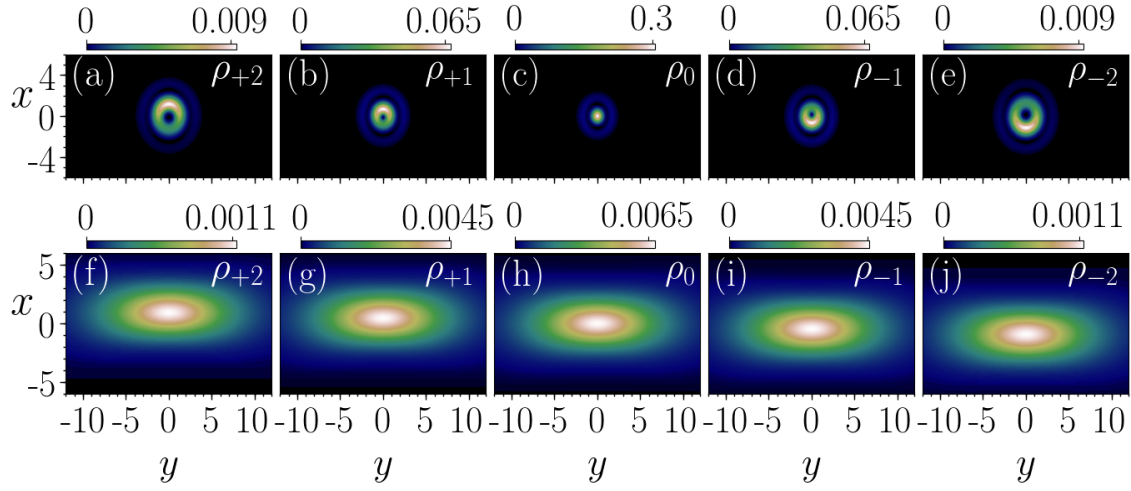


Figure 2.15: (Color online) Contour plot of density of components (a) $j = +2$, (b) $j = +1$, (c) $j = 0$, (d) $j = -1$, and (e) $j = -2$ with $c_0 = -2.5$, $c_1 = -0.025$, $c_2 = 0.25$, and $\gamma = 0.5$ moving with $v = 0.03$ along $+y$, and the same densities for velocity $v = 0.1$ in panels (f)-(j).

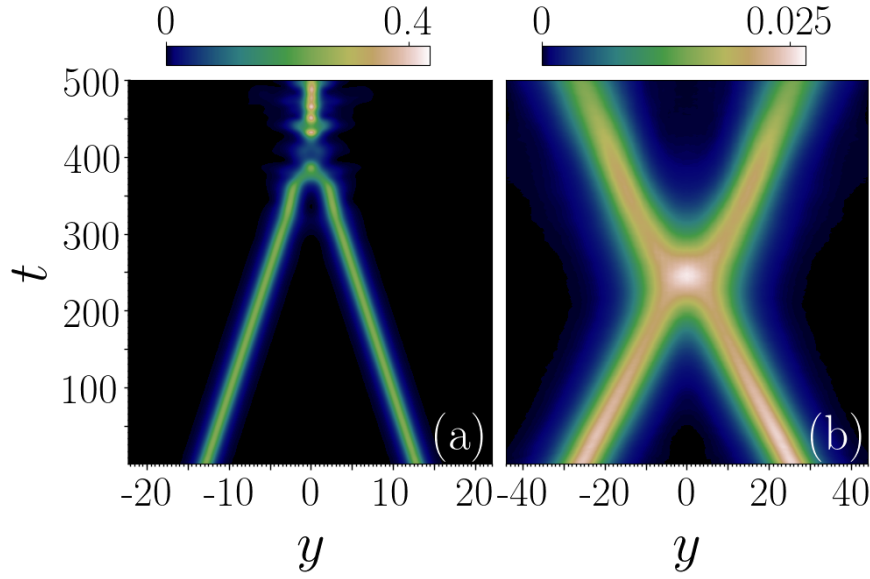


Figure 2.16: (Color online) Contour plot of time evolution of total density $\rho(0, y, t)$ as a function of y and t during the head-on collision between the two solitons with $c_0 = -2.5$, $c_1 = -0.025$, $c_2 = 0.25$, and $\gamma = 0.5$ moving with velocity (a) $|v| = \pm 0.03$ and (b) $|v| = \pm 0.1$ along the y axis in the opposite direction.

in Fig. 2.16(a) through a contour plot of time evolution of total density $\rho(0, y, t)$ in the $t - y$ plane. Similarly, a quasi-elastic collision between two solitons moving with velocity $|v| = 0.1$ is shown in Fig. 2.16(b). The collision dynamics is consistent with similar observations for two SO-coupled spin-1 BECs [107].

2.3 Non-magnetic spinor condensates

Distinct periodic structures are obtained in different magnetic phases of SO-coupled spin-1 or spin-2 BECs as discussed in the previous sections [109, 154, 155]. Trapped spin-1 spinor BEC under rotation or azimuthal gauge potential also have similar states with vorticity as the ground states [156, 157]. Hence, the spatially periodic structures are generally thought to be associated with these magnetic phases. Hence, one may conclude that the complicated spinor interactions in spin-1 and spin-2 BECs are necessary for generating these states with intrinsic vorticity. In view of this, it is interesting to see if these periodic structures survive in the SO-coupled nonmagnetic spin-1 and spin-2 BECs. The scattering lengths, corresponding to different permissible total spin channels, are close to one another in many spinor BECs [158, 159]. A nonmagnetic phase of a spinor BEC corresponds to the case where these scattering lengths are equal. This can be achieved by tuning the scattering lengths by manipulating an external electromagnetic field in the neighborhood of a Feshbach resonance(s) [36, 160]. We consider $a_0 = a_2 = a_4$, while, in the absence of SOC, a spin-1 or spin-2 BEC becomes nonmagnetic with no magnetic behavior. The resultant systems are SO-coupled three- (spin-1) and five-component (spin-2) BECs without any spinor interactions. The appearance of these spatially periodic states in a much simpler model will allow the study of these supersolid-like states easily, without the complications of spinor interactions and provide a better understanding of the origin of these states.

2.4 Mean-field model for nonmagnetic case

The CGPEs of the q2D SO-coupled nonmagnetic spin-1 BEC considering ($a_0 = a_2$) are [29, 109]

$$i\partial_t\phi_0 = \mathcal{H}\phi_0 - i\frac{\gamma}{\sqrt{2}}[\partial_-\phi_{+1} + \partial_+\phi_{-1}], \quad (2.25a)$$

$$i\partial_t\phi_{\pm 1} = \mathcal{H}\phi_{\pm 1} - i\frac{\gamma}{\sqrt{2}}\partial_{\pm}\phi_0, \quad (2.25b)$$

and those of the SO-coupled spin-2 BEC, obtained by substituting $c_1 = c_2 = 0$ in Eqs. (2.2a)-(2.2c), are

$$i\partial_t\phi_0 = \mathcal{H}\phi_0 - i\sqrt{\frac{3}{2}}\gamma[\partial_-\phi_{+1} + \partial_+\phi_{-1}], \quad (2.26a)$$

$$i\partial_t\phi_{\pm 1} = \mathcal{H}\phi_{\pm 1} - i\gamma\left[\sqrt{\frac{3}{2}}\partial_{\pm}\phi_0 + \partial_{\mp}\phi_{\pm 2}\right], \quad (2.26b)$$

$$i\partial_t\phi_{\pm 2} = \mathcal{H}\phi_{\pm 2} - i\gamma\partial_{\pm}\phi_{\pm 1}. \quad (2.26c)$$

In Eqs. (2.25a)-(2.25b) and Eqs. (2.26a)-(2.26c), $\mathcal{H} = -\frac{1}{2}(\partial_x^2 + \partial_y^2) + c_0\rho$; $c_0 = 2N\sqrt{2\pi}a_0$; $\partial_t = \partial/\partial t$; $\partial_{\pm} = \partial_y \pm i\partial_x$; whereas the rest of the symbols and units are defined in Sec. (2.1). The order parameter satisfies the normalization condition

$$\int \rho(x, y) dx dy = 1. \quad (2.27)$$

Although, spin-exchange spinor interaction is absent in nonmagnetic spin-1 and spin-2 condensates, the SOC interaction will allow the mixing of different components, and the number of atoms in each component will not be conserved in this case. The energy functional corresponding to the mean-field CGPEs (2.25a)-(2.25b) for a spin-1 case is

$$E = \int dx dy \left[\sum_{j=-1}^{+1} \phi_j^* \mathcal{H} \phi_j + \frac{1}{2} c_0 \rho^2 - \frac{i\gamma}{\sqrt{2}} \{ \phi_{+1}^* \partial_+ \phi_0 + \phi_0^* \partial_- \phi_{+1} + \phi_0^* \partial_+ \phi_{-1} + \phi_{-1}^* \partial_- \phi_0 \} \right], \quad (2.28)$$

whereas for spin-2 BEC it is given in Eq. (2.6) with $c_0 = c_2 = 0$.

In the absence of interactions, Eqs. (2.25a)-(2.25b) for $f = 1$ or Eqs. (2.26a)-(2.26c) for $f = 2$ reduce to an eigenvalue problem for the single-particle Hamiltonian H_0 in Eq. (2.1) which

is exactly solvable. The minimum energy eigenfunction and eigenenergy of H_0 for $f = 1$ are

$$\Phi_{f=1} = \frac{1}{2} \begin{pmatrix} -e^{-i\varphi} \\ -\sqrt{2}i \\ e^{i\varphi} \end{pmatrix} e^{ixk_x + iyk_y} \equiv \zeta(\varphi) e^{ixk_x + iyk_y}, \quad (2.29)$$

$$E(k_x, k_y) = \frac{1}{2} \left(k_x^2 + k_y^2 - 2\gamma \sqrt{k_x^2 + k_y^2} \right), \quad (2.30)$$

respectively, where $\varphi = \tan^{-1}(k_y/k_x)$ denotes the orientation of propagation vector $\mathbf{k} = (k_x, k_y)$. The magnitude of the propagation vector is fixed by minimizing the dispersion in Eq. (2.30) which gives $k_x^2 + k_y^2 = \gamma^2$. All the plane-wave eigenfunctions in Eq. (2.29) with different φ are degenerate. The equal weight superposition of these degenerate plane-wave states yields

$$\Phi_{\text{MR}}^{f=1} = \frac{1}{4\pi} \int_0^{2\pi} \begin{pmatrix} -e^{-i\varphi} \\ -\sqrt{2}i \\ e^{i\varphi} \end{pmatrix} e^{i\gamma r \cos(\varphi-\theta)} d\varphi = \frac{1}{2} \begin{pmatrix} -ie^{-i\theta} J_1(\gamma r) \\ -\sqrt{2}i J_0(\gamma r) \\ ie^{i\theta} J_1(\gamma r) \end{pmatrix}, \quad (2.31)$$

where polar coordinate $\theta = \tan^{-1} y/x$; $J_0(\gamma r)$ and $J_1(\gamma r)$ are the Bessel functions of the first kind of order 0 and 1, respectively. The function $\Phi_{\text{MR}}^{f=1}$ carries the phase singularities with the same winding numbers as a $(-1, 0, +1)$ -type multiring soliton. Rather than considering the superposition of infinite plane waves as in Eq. (2.31), the superpositions of a finite number of plane waves like a pair of counter-propagating plane waves, or of three plane waves propagating at mutual angles of $2\pi/3$, or of two pairs of counter-propagating plane waves with propagation vectors of one pair perpendicular to the other are

$$\Phi_{\text{ST}}^{f=1} = \frac{1}{\sqrt{2}} [\zeta(0)e^{i\gamma x} + \zeta(\pi)e^{-i\gamma x}], \quad (2.32a)$$

$$\Phi_{\text{TL}}^{f=1} = \frac{1}{\sqrt{3}} \left[\zeta(0)e^{i\gamma x} + \zeta(2\pi/3)e^{i\gamma(-x+\sqrt{3}y)/2} + \zeta(4\pi/3)e^{i\gamma(-x-\sqrt{3}y)/2} \right], \quad (2.32b)$$

$$\Phi_{\text{SL}}^{f=1} = \frac{1}{2} [\zeta(0)e^{i\gamma x} + \zeta(\pi/2)e^{i\gamma y} + \zeta(\pi)e^{-i\gamma x} + \zeta(3\pi/2)e^{-i\gamma y}], \quad (2.32c)$$

respectively. The total density corresponding $\Phi_{\text{ST}}^{f=1}$, $\Phi_{\text{TL}}^{f=1}$, and $\Phi_{\text{SL}}^{f=1}$ have stripe, triangular-lattice, and square-lattice patterns, respectively. For a spin-2 BEC, solutions are discussed in Sec (2.1.2). We see in our numerical study that these three types of states – stripe, triangular lattice and square lattice – indeed appear in the spin-2 case. However, in the spin-1 case, we

could only identify stripe and square-lattice states.

2.5 Numerical results for nonmagnetic condensates

As discussed earlier in Sec (2.2) for numerical solution of Eqs. (2.2a)-(2.2c) for magnetic case, here also we numerically solve Eqs. (2.25a)-(2.25b) for $f = 1$ and Eqs. (2.26a)-(2.26c) for $f = 2$ for nonmagnetic case, over a finite spatial domain, given an initial solution and boundary conditions, using Crank-Nicolson [45, 161–163] or Fourier pseudospectral methods [37–39] complemented with time-splitting to treat the nonlinear terms more efficiently. To calculate stationary state solutions, Eqs. (2.25a)-(2.25b) and Eqs. (2.26a)-(2.26c) are first transformed by changing $t \rightarrow -i\bar{t}$ and then solved by imaginary-time propagation [37–39, 164] using appropriate initial guesses. In order to confirm the dynamical stability of a solution, we study its real-time propagation [37–39, 164] as governed by the CGPEs. The space step used in the calculation was typically $\Delta \sim 0.05$ and the time step was $\sim 0.1\Delta^2$ in the imaginary-time propagation and $\sim 0.05\Delta^2$ in the real-time propagation. The SOC will allow mixing between different spin components and, hence, the number of atoms in different components will not be conserved during imaginary-time propagation in numerical calculations. Nevertheless, the total number of atoms will be preserved, and we impose condition (2.27) during the time propagation. As the number of atoms in each component is not conserved, the final conserved result is independent of the initial choice of number of atoms in each component.

2.5.1 Nonmagnetic q2D solitons in an SO-coupled spin-1 BEC

To obtain q2D solitons with a self-attractive ($c_0 < 0$) nonmagnetic SO-coupled spin-1 BEC for different SOC strengths γ , we consider a BEC with $c_0 = -0.6$ and vary γ . We consider $c_0 = -0.6$, because this value gives an adequate size of the soliton. A decrease in c_0 results in more attraction, hence a reduced system size, and below a critical $c_0 = c_{0,\text{crit}}$ the BEC will collapse as displayed in Fig. 2.17. For $\gamma = 0$, the spin-1 and spin-2 systems become essentially identical and also equivalent to a scalar nonspinor BEC of N atoms. The nonlinearities in the mean-field equations in these three cases are also identical. For a nonspinor spin-0 BEC, the critical c_0 for collapse was obtained previously as $c_{0,\text{crit}} \sim -5.85$ [165, 166]. We find that, for spin-0, spin-1, and spin-2 cases if $\gamma = 0$, then $c_{0,\text{crit}} = -5.86$, which is quite close to the previous

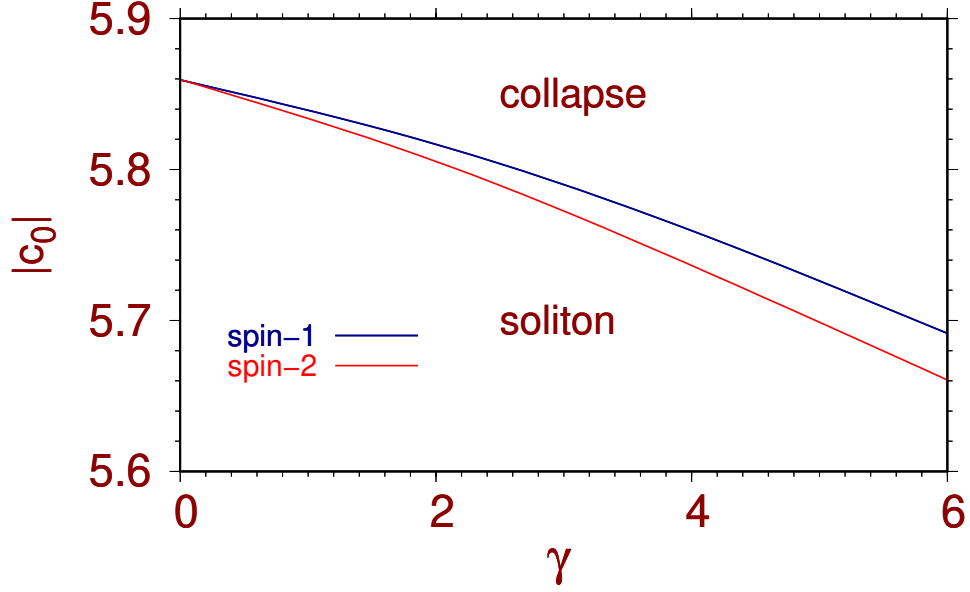


Figure 2.17: The c_0 - γ phase plot illustrating the collapse and soliton formation.

spin-0 result. The $c_{0,\text{crit}}$ for collapse for nonzero γ for spin-1 and spin-2 cases are slightly different as illustrated in Fig. 2.17. On the other hand, an increase in c_0 leads to an increased system size and, for positive (self-repulsive) values of c_0 , the system is no longer self-trapped. For negative (self-attractive) values of c_0 above the critical value ($c_0 > c_{0,\text{crit}}$), the SO-coupled BEC remains self-trapped. We demonstrate in Fig. 2.18 how different types of solitons appear as SOC strength is varied for a fixed c_0 through a phase plot of energy $\delta E \equiv (E + \gamma^2/2)$ against γ , where E denotes the energy of the soliton and $-\gamma^2/2$ corresponds to the energy of single-particle Hamiltonian (2.1) for a spin-1 BEC. We find five different types of q2D solitons for different γ : (a) $(-1, 0, +1)$ and $(0, +1, +2)$ multiring solitons, (b) stripe soliton with a stripe pattern in component densities only, (c) a supersolid-like soliton with component and total densities having the square-lattice pattern, and (d) asymmetric soliton. From Fig. 2.18, we find that for small γ ($\gamma \lesssim 1 \sim 2$) only $(-1, 0, +1)$ - and $(0, +1, +2)$ -type multiring solitons are possible with the $(0, +1, +2)$ soliton being an excited state. For medium γ ($3 \gtrsim \gamma \gtrsim 1.5$), two new types of excited states appear: stripe and asymmetric solitons; of these the stripe soliton has a smaller energy than the asymmetric soliton. For large γ ($\gamma \gtrsim 3$), the square-lattice excited state appears with an energy larger than the asymmetric soliton. For the Rashba SOC, we first investigate the formation of two quasidegenerate multiring vector solitons of $(-1, 0, +1)$ - and $(0, +1, +2)$ -type generated by solving Eqs. (2.25a)-(2.25b) in imaginary time using initial guesses where appropriate vortices

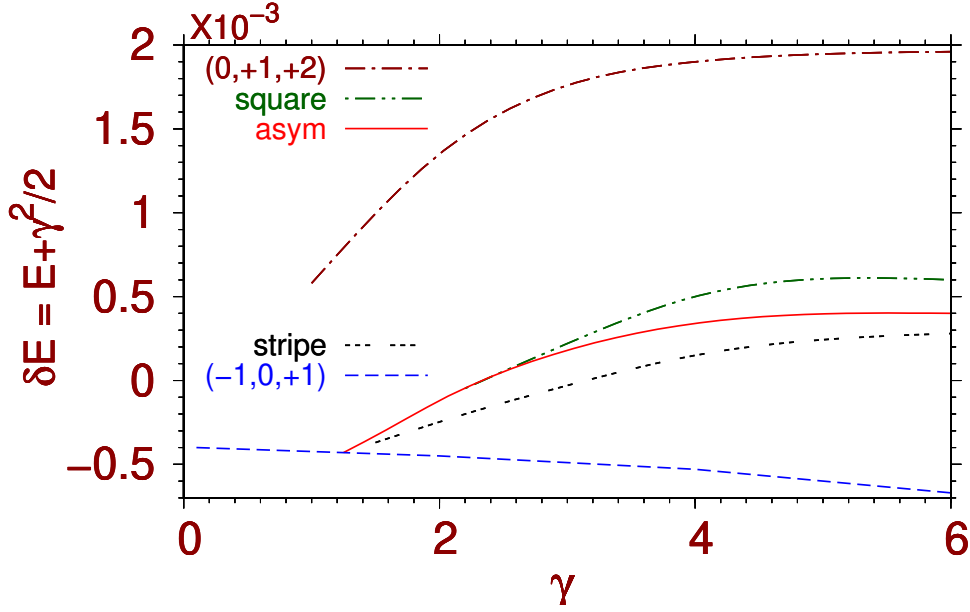


Figure 2.18: The $\delta E \equiv E + \gamma^2/2$ vs γ phase plot for Rashba SO-coupled $(-1, 0, +1)$ -, $(0, +1, +2)$ -type multiring, asymmetric, stripe, and square-lattice solitons. E is the energy of various states calculated using Eq. (2.28) in Sec. 2.4

are imprinted in the components. We show the contour plots of the densities (a) $\rho_{\pm 1}$, (b) ρ_0 , and (c) ρ (total density) in a $(-1, 0, +1)$ -type multiring soliton of the spin-1 BEC with $c_0 = -0.6$ and $\gamma = 4$ in Figs. 2.19(a)-(c). For the same parameters, we show the densities of three components, ρ_j , in a $(0, +1, +2)$ -type multiring soliton in Figs. 2.19(d)-(f). The energies of these $(-1, 0, +1)$ - and $(0, +1, +2)$ -type solitons are $E = -8.001$ and $E = -7.998$, respectively; the latter is an excited state. The phase distributions of ϕ_{+1} and ϕ_{-1} of the $(-1, 0, +1)$ -type multiring soliton shown in Figs. 2.19(g) and 2.19(h) reflect the phase shifts of -2π and 2π , respectively, under a full rotation around the center. Similarly, phase shifts by 2π and 4π , respectively, under a full rotation around the center of ϕ_0 and ϕ_{-1} of the $(0, +1, +2)$ -type multiring soliton can be seen in Figs. 2.19(i) and (j). These phases agree with the vortex/anti-vortex structure of the $(-1, 0, +1)$ and $(0, +1, +2)$ -type solitons.

Besides the two circularly-symmetric solitons, asymmetric, stripe and square-lattice solitons are other stationary states of the BEC with $c_0 = -0.6$ and $\gamma = 4$. The component densities ρ_j of the asymmetric, stripe, and square-lattice solitons are shown, respectively, in Figs. 2.20(a)-(c), 2.20(d)-(f), and 2.20(g)-(i). The energies of these three are -8.000 , -8.000 , and -7.999 ,

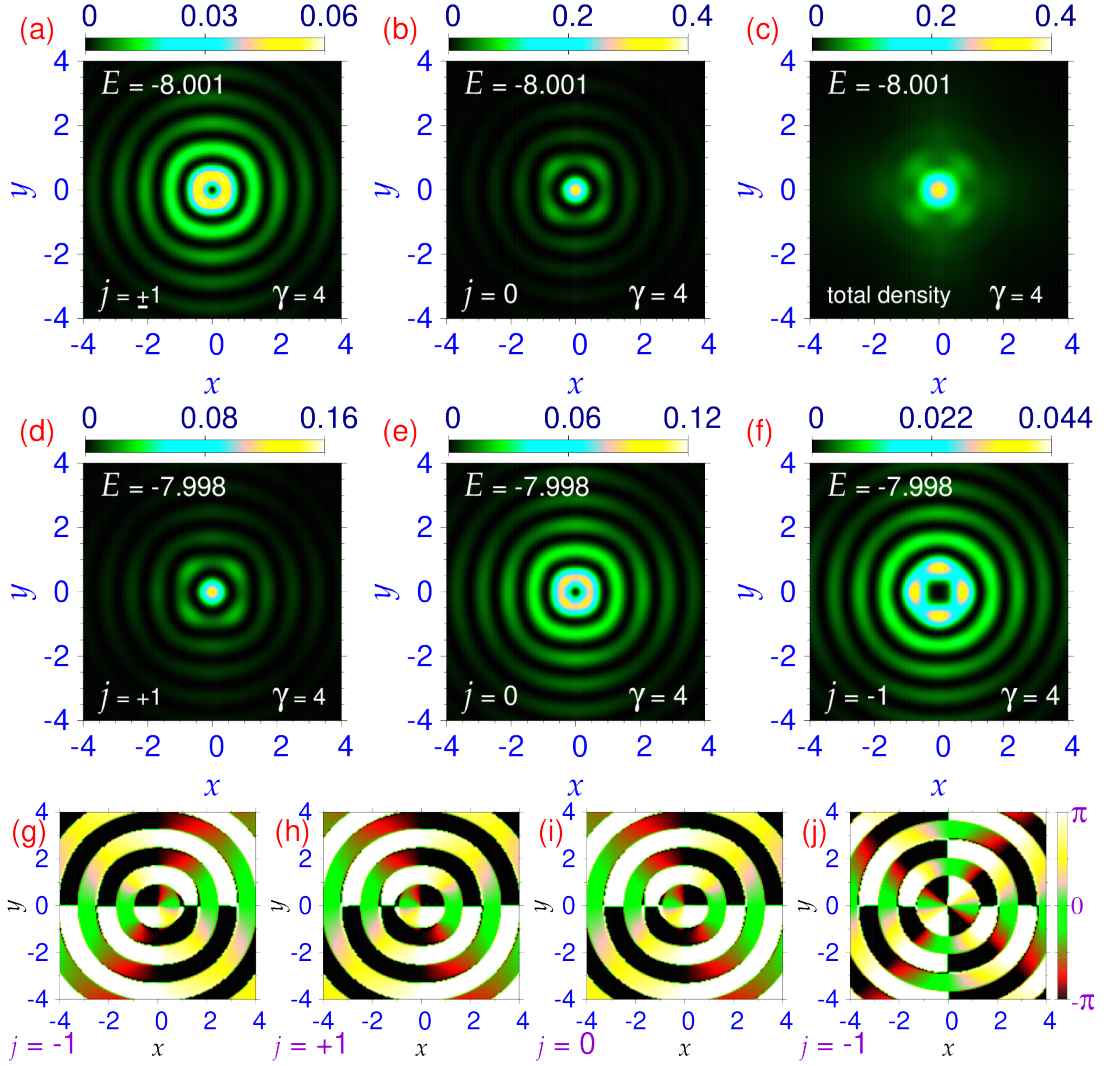


Figure 2.19: Top row: (a) component density of $j = \pm 1$, (b) $j = 0$, and (c) total density ρ of a $(-1, 0, +1)$ -type multiring soliton of the SO-coupled spin-1 BEC with $c_0 = -0.6$ and $\gamma = 4$. Similarly, middle row: (d) component density of $j = +1$, (e) $j = 0$, and (f) $j = -1$ of a $(0, +1, +2)$ -type multiring soliton of the BEC with the same interaction and coupling strengths. Bottom row: phase distributions of wave-function components (g) ϕ_{+1} , (h) ϕ_{-1} of the $(-1, 0, +1)$ -type multiring BEC soliton and those of wave-function components (i) ϕ_0 , (j) ϕ_{-1} of the $(0, +1, +2)$ -type multiring BEC soliton. E is calculated using Eq. (2.28) in Sec. 2.4

respectively. The stripe soliton has a stripe pattern in the density ρ_j of each component, whereas the total density ρ is devoid of this pattern. The square-lattice soliton, on the other hand, has a square-lattice pattern in each component density ρ_j and also in the total density ρ . The energies of the different solitons for $\gamma = 4$ satisfy $E(0, +1, +2) > E(\text{square lattice}) > E(\text{asymmetric}) > E(\text{stripe}) > E(-1, 0, +1)$. The stripe and the square-lattice solitons are efficiently obtained

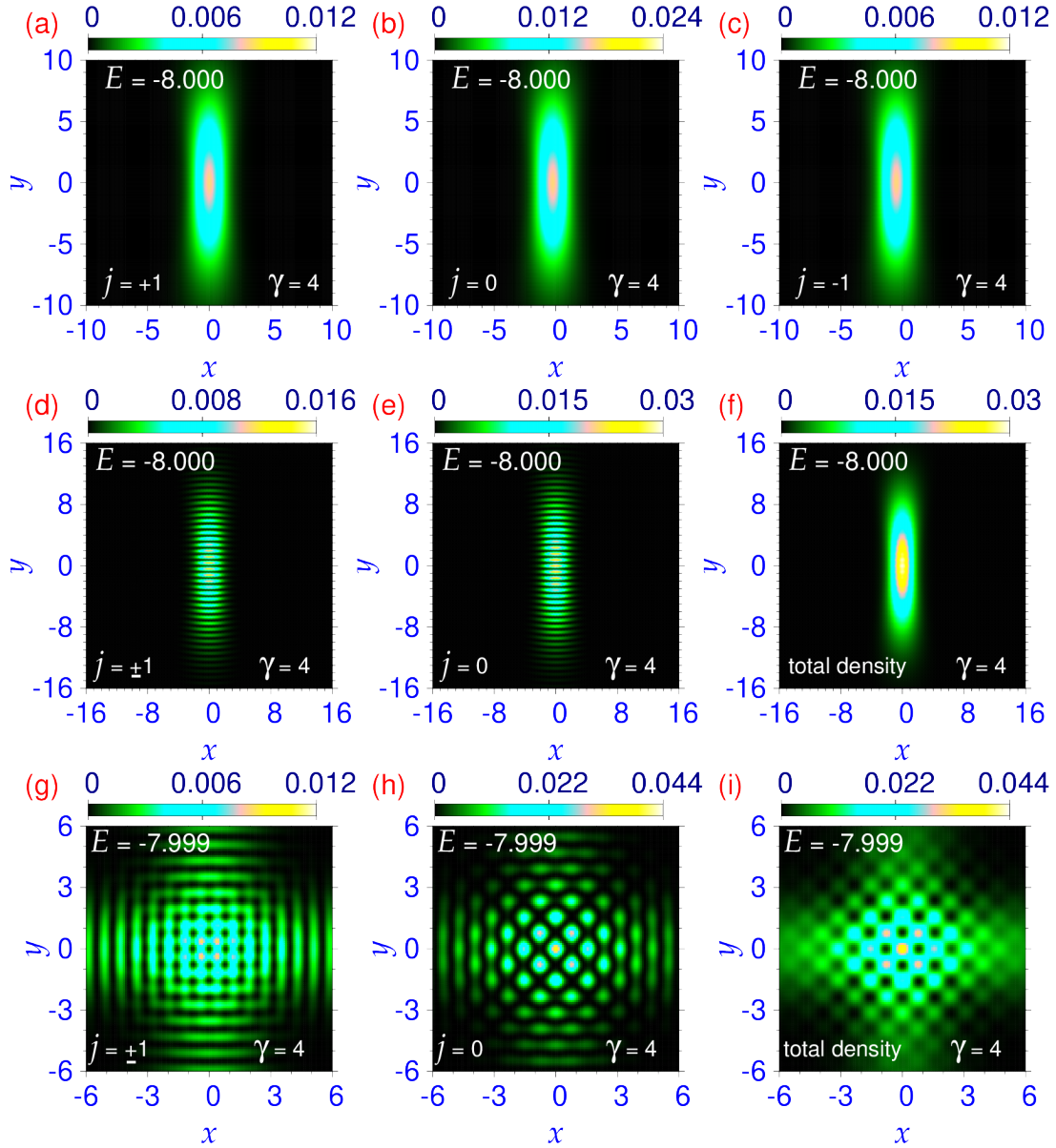


Figure 2.20: Top row: (a) component density of $j = +1$, (b) $j = 0$, and (c) $j = -1$ of an asymmetric soliton of the SO-coupled spin-1 BEC with $c_0 = -0.6$ and $\gamma = 4$. Middle row: (d) component density of $j = \pm 1$, (e) $j = 0$, and (f) total density ρ of a stripe soliton and bottom row: (g) component density of $j = \pm 1$, (h) $j = 0$, and (i) total density ρ of a square-lattice soliton for the same interaction and coupling strengths. E is calculated using Eq. (2.28) in Sec. 2.4

in the numerical calculation if such periodic patterns are imprinted on the initial state [109, 167].

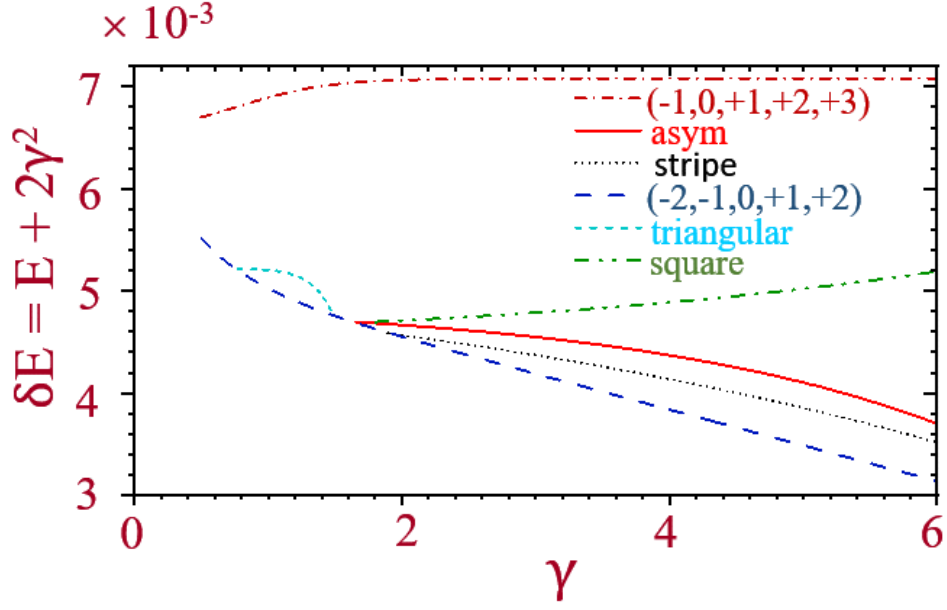


Figure 2.21: The $\delta E \equiv E + 2\gamma^2$ vs γ phase plot for Rashba SO-coupled $(-2, -1, 0, +1, +2)$ - and $(-1, 0, +1, +2, +3)$ -type multiring, asymmetric, triangular-lattice, stripe, and square-lattice solitons. E is calculated using Eq. (2.6) in Sec. 2.1.

2.5.2 Nonmagnetic q2D solitons in an SO-coupled spin-2 BEC

Similar to a nonmagnetic SO-coupled spin-1 BEC, for a nonmagnetic SO-coupled spin-2 BEC, several self-trapped stationary states are possible, including those in which the density ρ of the condensate displays spatially periodic patterns. As in the spin-1 BEC, there are two types of multiring solitons as well as spatially periodic stripe and square-lattice solitons. In addition, we observed a triangular-lattice soliton that was absent in the spin-1 BEC. For $f = 2$, we consider $c_0 = -0.2$. Again, for large $|c_0|$ the system collapses as shown in Fig. 2.17. Here the phase plot of $\delta E = (E + 2\gamma^2)$ versus γ in Fig. 2.21 shows how different types of solitons emerge for Rashba SOC, where E again is the energy of the soliton and $-2\gamma^2$ is that of the single-particle Hamiltonian (2.1) for a spin-2 BEC. We find six different types of q2D solitons for different γ : (a) $(-2, -1, 0, +1, +2)$ - and $(-1, 0, +1, +2, +3)$ -type multiring solitons, (b) stripe soliton with stripe patterns in component densities only, (c) square-lattice soliton having square-lattice patterns in total and all component densities, (d) asymmetric soliton, and (e) triangular-lattice soliton where a triangular-lattice pattern is present in the component and total densities, similar to a supersolid. According to Fig. 2.21, multiring solitons of the types $(-2, -1, 0, +1, +2)$ and $(-1, 0, +1, +2, +3)$ are possible for small γ ($\gamma \lesssim 1$). For intermediate strengths of γ ($\gamma \approx$

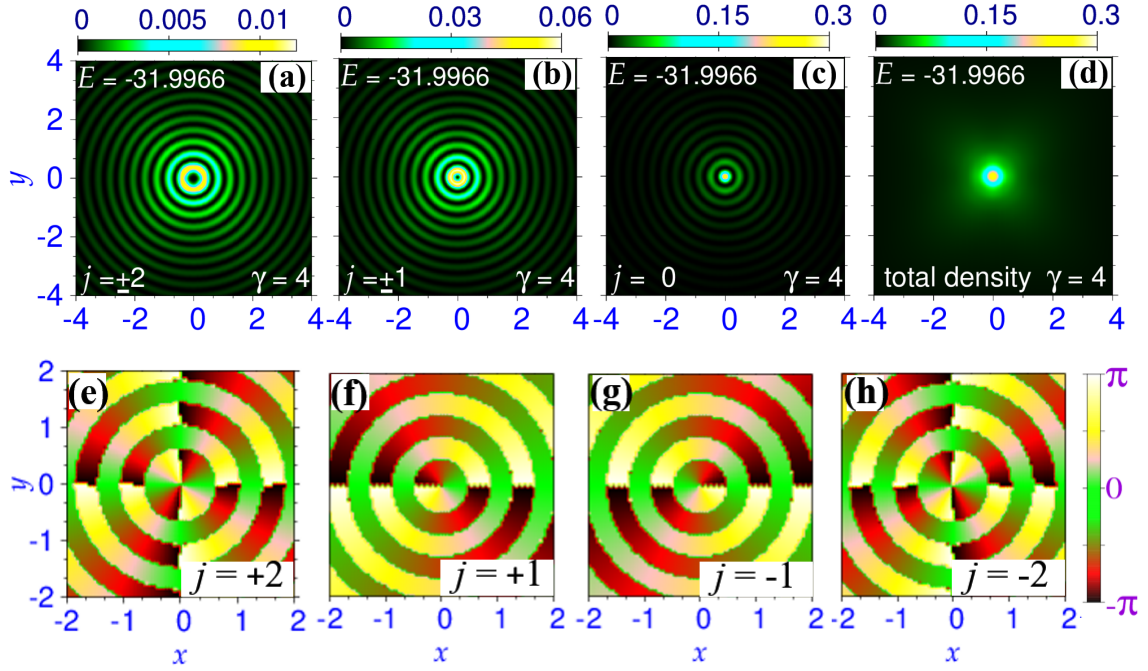


Figure 2.22: Upper row: (a) component density $\rho_{\pm 2}$, (b) $\rho_{\pm 1}$, (c) ρ_0 , and (d) total density ρ of a $(-2, -1, 0, +1, +2)$ -type multiring soliton of the SO-coupled spin-2 BEC with $c_0 = -0.2$ and $\gamma = 4$. Lower row: phase distributions of wave-function components (e) ϕ_{+2} , (f) ϕ_{+1} , (g) ϕ_{-1} , and (h) ϕ_{-2} in the same soliton. E is calculated using Eq. (2.6) in Sec. 2.1

1), triangular-lattice soliton also appears as a quasidegenerate state. For larger γ ($\gamma \gtrsim 2$), asymmetric, stripe and square-lattice solitons appear. These excited states in the spin-2 BEC appear in the same order as the corresponding states in the spin-1 case shown in Fig. 2.18. The only difference in the spin-2 case is the appearance of the triangular-lattice soliton which is absent in the spin-1 case. We illustrate the formation of a $(-2, -1, 0, +1, +2)$ -type multiring soliton for $c_0 = -0.2$ and $\gamma = 4$ having energy -31.9966 in Figs. 2.22(a)- 2.22(d), where we display the contour plots of component densities in panels (a) $\rho_{\pm 2}$, (b) $\rho_{\pm 1}$, (c) ρ_0 , and (d) total density ρ of this soliton. The charge of phase singularities in $\phi_{\pm 2}$ and $\phi_{\pm 1}$ are ascertained from Figs. 2.22(e)- 2.22(h), where we display the contour plots of the phases of wave-function components of the $(-2, -1, 0, +1, +2)$ -type Rashba SO-coupled soliton. The phases correspond to phase changes of $\mp 4\pi$ and $\mp 2\pi$ in $j = \pm 2$ and $j = \pm 1$ components, respectively, under a complete rotation around the center. As discussed earlier, we also have $(-1, 0, +1, +2, +3)$ -type multiring soliton that continues to be the solution of Eqs. (2.26a)-(2.26c) for large SOC strengths. In Fig. 2.23, we show its emergence for $c_0 = -0.2$ and $\gamma = 4$ via contour plots of

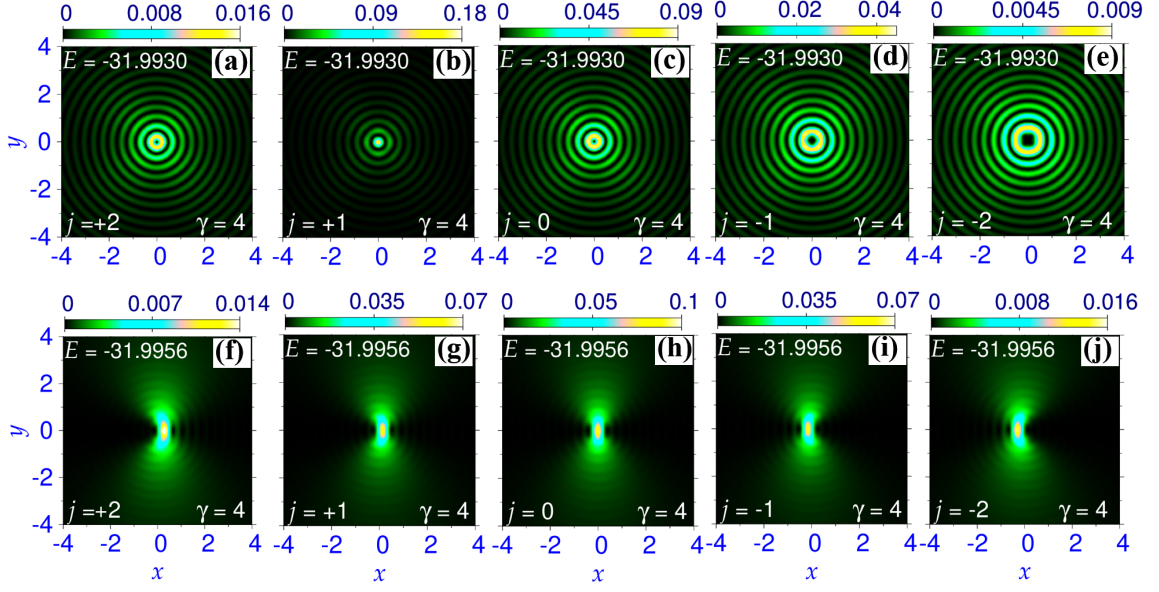


Figure 2.23: Upper row: (a) component density ρ_{+2} , (b) ρ_{+1} , (c) ρ_0 , (d) ρ_{-1} , and (e) ρ_{-2} of a $(-1, 0, +1, +2, +3)$ -type multiring soliton of the SO-coupled spin-1 BEC with $c_0 = -0.2$ and $\gamma = 4$. Bottom row: (f) component density ρ_{+2} , (g) ρ_{+1} , (h) ρ_0 , (i) ρ_{-1} , and (j) ρ_{-2} of an asymmetric soliton for the same interaction and coupling strengths. E is calculated using Eq. (2.6) in Sec. 2.1.

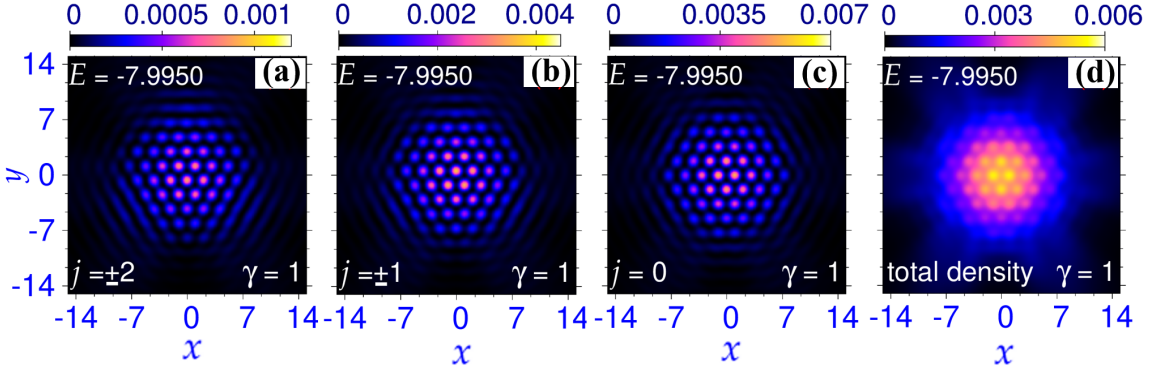


Figure 2.24: (a) Component density $\rho_{\pm 2}$, (b) $\rho_{\pm 1}$, (c) ρ_0 , and (d) total density ρ of a triangular-lattice soliton of the SO-coupled spin-2 BEC with $c_0 = -0.2$ and $\gamma = 1$. E is calculated using Eq. (2.6) in Sec. 2.1

densities (a) ρ_{+2} , (b) ρ_{+1} , (c) ρ_0 , (d) ρ_{-1} , and (e) ρ_{-2} with energy -31.9930 . Next in Fig. 2.23, we show the contour densities (f) ρ_{+2} , (g) ρ_{+1} , (h) ρ_0 , (i) ρ_{-1} , and (j) ρ_{-2} of the asymmetric soliton for $c_0 = -0.2$ and $\gamma = 4$ and with energy -31.9956 . For an intermediate SOC strength of $\gamma = 1$, contour plots of densities (a) $\rho_{\pm 2}$, (b) $\rho_{\pm 1}$, (c) ρ_0 , and (d) total density ρ of the triangular-lattice soliton for $c_0 = -0.2$ and with energy -7.9950 are shown in Figs. 2.24(a)-2.24(d). This soliton has a hexagonal-lattice crystallization in component and total densities. Besides the

asymmetric soliton, two other solitons, which appear explicitly for large SOC strengths, are stripe and square-lattice solitons. In Fig. 2.25, we present the contour plots of (a) $\rho_{\pm 2}$, (b) $\rho_{\pm 1}$, (c) ρ_0 , and (d) total density ρ of the stripe soliton of energy -31.9962 for $c_0 = -0.2$ and $\gamma = 4$. Similar to the stripe soliton in the SO-coupled spin-1 BEC, the component densities have a stripe pattern which is not present in their sum. The scenario is different in the case of a square-lattice soliton. For example, the component and total densities of the square-lattice soliton of energy -31.9950 for $c_0 = -0.2$ and $\gamma = 4$ are shown in Fig. 2.25: (e) $\rho_{\pm 2}$, (f) $\rho_{\pm 1}$, (g) ρ_0 , and (h) total density ρ , where the square-lattice pattern in the total density as well as the component densities is explicit.

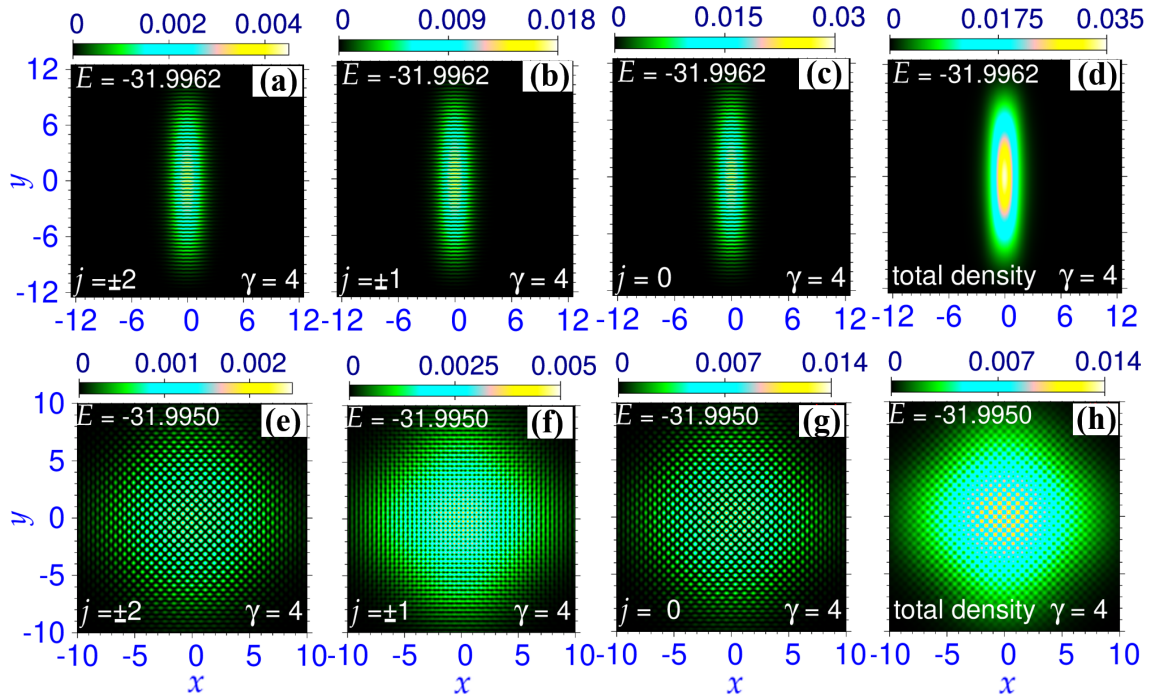


Figure 2.25: Upper row: (a) component density $\rho_{\pm 2}$, (b) $\rho_{\pm 1}$, (c) ρ_0 , and (d) total density ρ of a stripe soliton with $c_0 = -0.2$ and $\gamma = 4$. Lower row: (a) component density $\rho_{\pm 2}$, (b) $\rho_{\pm 1}$, (c) ρ_0 , and (d) total density ρ of a square-lattice soliton with the same c_0 and γ . E is calculated using Eq. (2.6) in Sec. 2.1

2.6 Summary

We have demonstrated the emergence of various self-trapped stable solitons with supersolid-like crystallization in a q2D SO-coupled spin-2 BEC employing analytic consideration and numerical

solution of the underlying mean-field GP equation. The minimization of interaction and SOC energies lead to the permissible winding number combinations for axisymmetric solitons. In the absence of interactions, we consider the eigenfunctions of the single-particle Hamiltonian to construct the order parameters consistent with multiring, stripe, triangular-, and square-lattice density profiles. In the presence of (attractive) interactions, we find that various types of solitons with spatially periodic modulation in density appear, including the ones inferred from a study of the eigenfunctions of the single-particle Hamiltonian, due to an interplay of SOC and interactions.

The ground state for a small SOC strength ($\gamma \approx |c_0| \approx 0.5$) is a radially symmetric multiring soliton for weakly ferromagnetic, cyclic, and polar interactions, whereas for a sufficiently strong-ferromagnetic interaction a circularly asymmetric soliton emerges as the ground state. For intermediate SOC strengths ($\gamma \approx 2|c_0| \approx 1$), in addition to the axisymmetric soliton, there could exist a triangular-lattice soliton with a hexagonal crystallization of matter in the soliton, explicit in both component and total densities. On increasing the SOC further, one could have five quasidegenerate solitons, e.g., a multiring soliton, a square-lattice soliton, a stripe soliton, and a superstripe soliton, in all the magnetic phases, and also a circularly asymmetric soliton in the ferromagnetic phase. The quasidegeneracy between the states is in general lifted with either a decrease in the SOC strength γ or an increase in the attractive spin-independent interaction strength $|c_0|$. We also introduced the Galilean-transformed model to study the moving solitons and the head-on collision dynamics between two such solitons. A head-on collision between the two solitons is inelastic at low velocities, and the two solitons can form a bound entity. At large velocities, the collision is quasi-elastic, and the solitons pass through each other without a substantial change of velocity. We considered another scenario in which we investigated spontaneous spatial order in a Rashba SO-coupled nonmagnetic trapless q2D spin-1 and spin-2 BECs for various SOC strengths γ without spinor interactions by numerically solving the CGPEs. For small SOC, $(-1, 0, +1)$ and $(0, +1, +2)$ -type solitons are found for a spin-1 BEC, whereas $(-2, -1, 0, +1, +2)$ and $(-1, 0, +1, +2, +3)$ -type solitons are found for a spin-2 BEC, which develops multiring structure with an increase in SOC strengths. For intermediate strengths of SOC ($\gamma \approx 1$), in spin-2 BEC, triangular-lattice soliton having hexagonal crystallization in component as well as total density appears as quasidegenerate state. For relatively larger SOC strengths, asymmetric, stripe and square-lattice solitons appear as quasidegenerate solitons for

spin-1 and spin-2 BECs. We also established the dynamical stability of these solitonic states by stable real-time simulation over 400 units of time (result not shown here). In conclusion, it is strongly suggestive that the spatially-periodic supersolid-like states found in SO-coupled pseudo spin-1/2 [121, 168, 169], spin-1 [109, 167], and spin-2 [155] spinor BECs are not a consequence of spinor interactions but are a consequence of multicomponent nature of these states in presence of SOC. The results reported in this chapter are discussed in Refs. [155, 170].

Chapter 3

Spin-orbit-coupling-driven superfluid phases in optical lattices

In this chapter and the following one, we will discuss spinor condensates in optical lattices, in contrast to the previous chapter where we considered spinor condensates without any external trap. As we discussed earlier in the introduction to the optical lattice in Sec. 1.6 and the BHM in Sec. 1.6.1, the lattice potential restricts the movement of the atoms, leading to a reduction in kinetic energy and a shift towards a strongly interacting regime. The BHM is the apt model to describe the physics of these systems [129, 130], and we will be using it to describe the ground-state properties of bosonic atoms in a strongly correlated regime. We have also discussed the various effects arising from the SOC in Sec. 1.3.3. However, most of the studies on spinor condensates with SOC have been focused on the continuum case, and the exploration of these systems in optical lattices is still lagging behind. Recent advances in ultracold quantum gas experiments have allowed for the implementation of SOC and competing interactions in strongly correlated many-body systems [65, 171, 172]. These experimental developments afford the possibility to study novel states of matter, phase transitions, and exotic spin models which are not accessible in conventional condensed matter systems [67, 173]. Despite this, the parameter regimes of the superfluid states in SO-coupled BHM, and the effects of thermal fluctuations on the transition between finite-momentum superfluids have not yet been investigated. At finite temperatures, the melting of the stripe superfluid phase leads to a wide domain of stripe normal-fluid (NF) phase [174]. More recently, it has been shown that the SOC leads to the lowering

of the critical temperature for the superfluid to NF phase transition, and reduces the coherence and spatial orders of magnetic textures [175].

In order to address this, we investigate the ground-state phase diagrams of a Bose-Bose mixture in an optical lattice under the influence of Rashba SOC, both at zero and finite temperature. Our study focuses on the QPTs and the various SOC-driven finite-momentum superfluid states that occur in two different regimes based on interspin interactions.

The chapter is structured as follows. We introduce the Hamiltonian of the SO-coupled pseudo-spinor BECs in optical lattices and give a brief description of the mean-field Gutzwiller approach in Sec. 3.1. We provide a characterization of the superfluid states of the model considered in Sec. 3.2. Moving on to Sec. 3.3, we first examine the zero-temperature phase diagrams of the two-component Bose Hubbard model (TBHM) in the presence of synthetic SOC. Then, we discuss the effects of finite temperature on the SOC-driven superfluid states. Finally, we conclude with a summary of our findings in Sec. 3.5.

3.1 The Model and the method

We consider an SO-coupled pseudospinor system of ultracold bosons loaded into a square optical lattice. The two different atomic hyperfine levels of the same atomic species act as two pseudospin states. The TBHM well describes the system in the presence of Rashba SOC on a 2D optical lattice. The Hamiltonian of the system is [71]

$$\begin{aligned} \hat{H} = & - J \sum_{\langle i,j \rangle} \hat{\Psi}_i^\dagger \hat{\Psi}_j + \sum_{i,\alpha} (\epsilon_{i\alpha} - \mu_\alpha) \hat{n}_i^\alpha + \frac{1}{2} \sum_{i,\alpha} U_{\alpha\alpha} \hat{n}_i^\alpha (\hat{n}_i^\alpha - 1) + U_{\uparrow\downarrow} \sum_i \hat{n}_i^\uparrow \hat{n}_i^\downarrow \\ & + i\gamma \sum_{\langle i,j \rangle} \hat{\Psi}_i^\dagger \hat{\mathbf{z}} \cdot (\vec{\sigma} \times \vec{d}_{ij}) \hat{\Psi}_j + \text{H.c.}, \end{aligned} \quad (3.1)$$

where i is a unique combination of lattice-site indices in two dimensions, i.e., $i \equiv (p, q)$ with p and q site indices in the x and y directions, respectively, and $j \equiv (p', q')$ is a neighboring site of the i^{th} lattice site. Here $\Psi_i = (\hat{b}_i^\uparrow, \hat{b}_i^\downarrow)^T$ is a two-component bosonic annihilation operator at the i^{th} lattice site, $\alpha = \uparrow, \downarrow$ denotes the pseudospin components, J is the spin-independent hopping amplitude of atoms, and for the present case, we consider equal hopping amplitudes for both components and along both directions, $\epsilon_{i\alpha}$ is the energy offset of atoms with α spin due to the

envelope confining potential and is considered to be zero, μ_α is the chemical potential, $\hat{n}_i^\alpha = \hat{b}_i^{\dagger\alpha}\hat{b}_i^\alpha$ is the number operator, and $U_{\alpha\alpha}(U_{\uparrow\downarrow})$ is intraspin (interspin) on-site interaction. The last term represents the SOC generated by Raman lasers which can be tuned in experiments using coherent destructive hopping methods [176] and represents the hopping between neighboring sites with a spin flip. Here γ is the Rashba SOC strength, $\vec{\sigma} = (\sigma_x, \sigma_y, \sigma_z)$ is a vector of Pauli spin matrices, \vec{d}_{ij} is a lattice unit vector between two neighboring sites, and $\hat{\mathbf{z}}$ is a unit vector perpendicular to the lattice plane. Eq. (3.1) then can be written in the expanded form as

$$\begin{aligned} \hat{H} = & - \sum_{p,q,\alpha} \left[\left(J \hat{b}_{p+1,q}^{\dagger\alpha} \hat{b}_{p,q}^\alpha + \text{H.c.} \right) + \left(J \hat{b}_{p,q+1}^{\dagger\alpha} \hat{b}_{p,q}^\alpha + \text{H.c.} \right) - \frac{U_{\alpha\alpha}}{2} \hat{n}_{p,q}^\alpha (\hat{n}_{p,q}^\alpha - 1) + \mu_\alpha \hat{n}_{p,q}^\alpha \right] \\ & + \sum_{p,q} U_{\uparrow\downarrow} \hat{n}_{p,q}^\uparrow \hat{n}_{p,q}^\downarrow + \left[i\gamma \sum_{p,q} \left(-i \hat{b}_{p,q}^{\dagger\uparrow} \hat{b}_{p-1,q}^\downarrow + i \hat{b}_{p,q}^{\dagger\downarrow} \hat{b}_{p-1,q}^\uparrow + i \hat{b}_{p,q}^{\dagger\uparrow} \hat{b}_{p+1,q}^\downarrow \right. \right. \\ & \left. \left. - i \hat{b}_{p,q}^{\dagger\downarrow} \hat{b}_{p+1,q}^\uparrow - \hat{b}_{p,q}^{\dagger\uparrow} \hat{b}_{p,q-1}^\downarrow - \hat{b}_{p,q}^{\dagger\downarrow} \hat{b}_{p,q-1}^\uparrow + \hat{b}_{p,q}^{\dagger\uparrow} \hat{b}_{p,q+1}^\downarrow + \hat{b}_{p,q}^{\dagger\downarrow} \hat{b}_{p,q+1}^\uparrow \right) + \text{H.c.} \right]. \end{aligned} \quad (3.2)$$

To study the ground-state properties of the system in both strong- and weak-coupling limits, we use the single-site Gutzwiller mean-field (SGMF) theory [177–184]. We decompose annihilation ($\hat{b}_{p,q}^\alpha$) and creation ($\hat{b}_{p,q}^{\dagger\alpha}$) operators into the mean-field and fluctuation part as $\hat{b}_{p,q}^\alpha = \phi_{p,q}^\alpha + \delta\hat{b}_{p,q}^\alpha$ and $\hat{b}_{p,q}^{\dagger\alpha} = \phi_{p,q}^{*\alpha} + \delta\hat{b}_{p,q}^{\dagger\alpha}$, where $\phi_{p,q}^\alpha$ ($\phi_{p,q}^{*\alpha}$) is the superfluid order parameter. As an example, the first term $\hat{b}_{p+1,q}^{\dagger\alpha} \hat{b}_{p,q}^\alpha$ after the mean-field approximation results in

$$b_{p+1,q}^{+\alpha} b_{p,q}^\alpha = \phi_{p+1,q}^{*\alpha} \phi_{p,q}^\alpha + \phi_{p+1,q}^{*\alpha} \delta b_{p,q} + \phi_{p,q} \delta b_{p+1,q}^{+\alpha} + \delta b_{p+1,q}^{+\alpha} \delta b_{p,q}^\alpha. \quad (3.3)$$

Neglecting the terms like $\delta b_{p+1,q}^{+\alpha} \delta b_{p,q}^\alpha$ which are second order in the fluctuation operator and substituting $\delta\hat{b}_{p,q}^\alpha = \hat{b}_{p,q}^\alpha - \phi_{p,q}^\alpha$ and $\delta\hat{b}_{p,q}^{\dagger\alpha} = \hat{b}_{p,q}^{\dagger\alpha} - \phi_{p,q}^{*\alpha}$ in Eq. (3.3), we get

$$b_{p+1,q}^{+\alpha} b_{p,q}^\alpha = \phi_{p+1,q}^{*\alpha} b_{p,q}^\alpha + \phi_{p,q}^\alpha \hat{b}_{p+1,q}^{+\alpha} - \phi_{p,q}^\alpha \phi_{p+1,q}^{*\alpha}. \quad (3.4)$$

As a result, the mean-field approximation decouples the Hamiltonian [Eq. (3.2)] as $\hat{H} = \sum_{p,q} \hat{h}_{p,q}$,

3 Spin-orbit-coupling-driven superfluid phases in optical lattices

where

$$\begin{aligned}
\hat{h}_{p,q} = & - \sum_{\alpha} \left[\left(J(\hat{b}_{p,q}^{\dagger\alpha} \phi_{p-1,q}^{\alpha} + \phi_{p+1,q}^{\alpha*} \hat{b}_{p,q}^{\alpha} - \phi_{p,q}^{\alpha*} \phi_{p-1,q}^{\alpha} - \phi_{p+1,q}^{\alpha*} \phi_{p,q}^{\alpha}) + \text{H.c.} \right) \right. \\
& + \left(J(\hat{b}_{p,q}^{\dagger\alpha} \phi_{p,q+1}^{\alpha} + \phi_{p,q-1}^{\alpha*} \hat{b}_{p,q}^{\alpha} - \phi_{p,q}^{\alpha*} \phi_{p,q+1}^{\alpha} - \phi_{p,q-1}^{\alpha*} \phi_{p,q}^{\alpha}) + \text{H.c.} \right) \\
& + \frac{U_{\alpha\alpha}}{2} \hat{n}_{p,q}^{\alpha} (\hat{n}_{p,q}^{\alpha} - 1) - \mu_{p,q}^{\alpha} \hat{n}_{p,q}^{\alpha} \left. \right] + U_{\uparrow\downarrow} \hat{n}_{p,q}^{\uparrow} \hat{n}_{p,q}^{\downarrow} \\
& + i\gamma \left[\hat{b}_{p,q}^{\dagger\uparrow} (i\phi_{p+1,q}^{\downarrow} - i\phi_{p-1,q}^{\downarrow} - \phi_{p,q-1}^{\downarrow} + \phi_{p,q+1}^{\downarrow}) + \hat{b}_{p,q}^{\dagger\downarrow} (i\phi_{p-1,q}^{\uparrow} - i\phi_{p+1,q}^{\uparrow} \right. \\
& - \phi_{p,q-1}^{\uparrow} + \phi_{p,q+1}^{\uparrow}) + \phi_{p,q}^{\uparrow*} (i\phi_{p-1,q}^{\downarrow} - i\phi_{p+1,q}^{\downarrow} + \phi_{p,q-1}^{\downarrow} - \phi_{p,q+1}^{\downarrow}) \\
& \left. + \phi_{p,q}^{\downarrow*} (-i\phi_{p-1,q}^{\uparrow} + i\phi_{p+1,q}^{\uparrow} + \phi_{p,q-1}^{\uparrow} - \phi_{p,q+1}^{\uparrow}) \right] + \text{H.c.}, \tag{3.5}
\end{aligned}$$

is the local Hamiltonian at the $(p, q)^{\text{th}}$ site. To obtain the ground state, we self-consistently diagonalize the Hamiltonian at each lattice site. The many-body Gutzwiller wave function for the ground state at the $(p, q)^{\text{th}}$ site is

$$|\Psi\rangle = \prod_{p,q} |\psi\rangle_{p,q} = \prod_{p,q} \sum_{n_{\uparrow}, n_{\downarrow}} c_{n_{\uparrow}, n_{\downarrow}}^{(p,q)} |n_{\uparrow}, n_{\downarrow}\rangle_{p,q}, \tag{3.6}$$

where $|\psi\rangle_{p,q}$ is the single-site ground state; $|n_{\uparrow}\rangle$ and $|n_{\downarrow}\rangle$ are Fock states with $n_{\alpha} \in [0, N_b - 1]$; N_b is the dimension of the Fock space, and the c-numbers $c_{n_{\uparrow}, n_{\downarrow}}^{(p,q)}$ s are the complex coefficients that satisfy the normalization condition $\sum_{n_{\uparrow}, n_{\downarrow}} |c_{n_{\uparrow}, n_{\downarrow}}^{(p,q)}|^2 = 1$. The superfluid order parameters of the two components are

$$\phi_{p,q}^{\uparrow} = {}_{p,q}\langle\psi|\hat{b}_{p,q}^{\dagger\uparrow}|\psi\rangle_{p,q} = \sum_{n_{\uparrow}, n_{\downarrow}} \sqrt{n_{\uparrow}} c_{n_{\uparrow}-1, n_{\downarrow}}^{(p,q)*} c_{n_{\uparrow}, n_{\downarrow}}^{(p,q)}, \tag{3.7a}$$

$$\phi_{p,q}^{\downarrow} = {}_{p,q}\langle\psi|\hat{b}_{p,q}^{\dagger\downarrow}|\psi\rangle_{p,q} = \sum_{n_{\uparrow}, n_{\downarrow}} \sqrt{n_{\downarrow}} c_{n_{\uparrow}, n_{\downarrow}-1}^{(p,q)*} c_{n_{\uparrow}, n_{\downarrow}}^{(p,q)}. \tag{3.7b}$$

The atomic occupancies of the components at a lattice site (p, q) are the expectation of the number operators and are given by

$$n_{p,q}^{\uparrow} = {}_{p,q}\langle\psi|\hat{n}_{p,q}^{\uparrow}|\psi\rangle_{p,q} = \sum_{n_{\uparrow}, n_{\downarrow}} n_{\uparrow} |c_{n_{\uparrow}, n_{\downarrow}}^{(p,q)}|^2, \tag{3.8a}$$

$$n_{p,q}^{\downarrow} = {}_{p,q}\langle\psi|\hat{n}_{p,q}^{\downarrow}|\psi\rangle_{p,q} = \sum_{n_{\uparrow}, n_{\downarrow}} n_{\downarrow} |c_{n_{\uparrow}, n_{\downarrow}}^{(p,q)}|^2. \tag{3.8b}$$

3.1.1 Weakly interacting limit

We analyze the system in the weakly interacting limit, where $U_{\alpha\alpha} \ll J$. For this regime, the Hamiltonian (3.1) in the momentum space can be written as

$$\hat{H}_{\text{kin}} = \sum_{\mathbf{k}} \begin{pmatrix} \hat{b}_k^{\uparrow\uparrow} & \hat{b}_k^{\uparrow\downarrow} \end{pmatrix} \mathcal{H}_{\mathbf{k}} \begin{pmatrix} \hat{b}_k^{\uparrow} \\ \hat{b}_k^{\downarrow} \end{pmatrix} \quad (3.9)$$

with

$$\mathcal{H}_{\mathbf{k}} = \begin{pmatrix} -2J(\cos k_x + \cos k_y) & 2i\gamma(\sin k_x - i \sin k_y) \\ -2i\gamma(\sin k_x + i \sin k_y) & -2J(\cos k_x + \cos k_y) \end{pmatrix}.$$

The diagonalization of the above Hamiltonian $\mathcal{H}_{\mathbf{k}}$ yields two energy branches

$$E_{\mathbf{k}\pm} = -2J(\cos k_x + \cos k_y) \pm 2\gamma\sqrt{\sin^2 k_x + \sin^2 k_y}, \quad (3.10)$$

where $\mathbf{k} = (k_x, k_y)$ and the first term on the right-hand side is the spin-independent dispersion relation in a 2D square lattice. The energy spectrum $E_{\mathbf{k}\pm}$ remains invariant under the parity transformation ($k_x \rightarrow -k_x, k_y \rightarrow -k_y$) or permutation of k_x and k_y , ($k_x \rightarrow k_y, k_y \rightarrow k_x$). The noninteracting lowest band structure is shown for two different regimes in Fig. 3.1. In the absence of SOC ($\gamma = 0$), the lower branch of the band has one minimum at $\mathbf{k} = (0, 0)$. The SOC term modifies the band structure, where the lower branch has four degenerate minima. The presence of SOC breaks the rotational symmetry in \mathbf{k} space and shifts the minima of the lower branch along the diagonals of the first Brillouin zone.

The four degenerate minima in the lower branch are $\mathbf{q}_1 = (k_0, k_0)$, $\mathbf{q}_2 = (-k_0, k_0)$, $\mathbf{q}_3 = (-k_0, -k_0)$, and $\mathbf{q}_4 = (k_0, -k_0)$, where $k_0 = \arctan(\gamma/\sqrt{2}J)$. Hence, the locations of the minima are determined by the strength of SOC.

3.2 Quantum phases and order parameters

The ground states of ultracold bosons with SOC exhibit insulating and various SF phases. The nature of the SF phase depends on the competition between single-particle hopping and SOC-induced spin-dependent hopping. At lower J , the incompressible insulating phases are identified by the sum and difference of the expectations of the number operators, $\langle \hat{n}_{\pm} \rangle \equiv \langle \hat{n}^{\uparrow} \rangle \pm \langle \hat{n}^{\downarrow} \rangle$. For

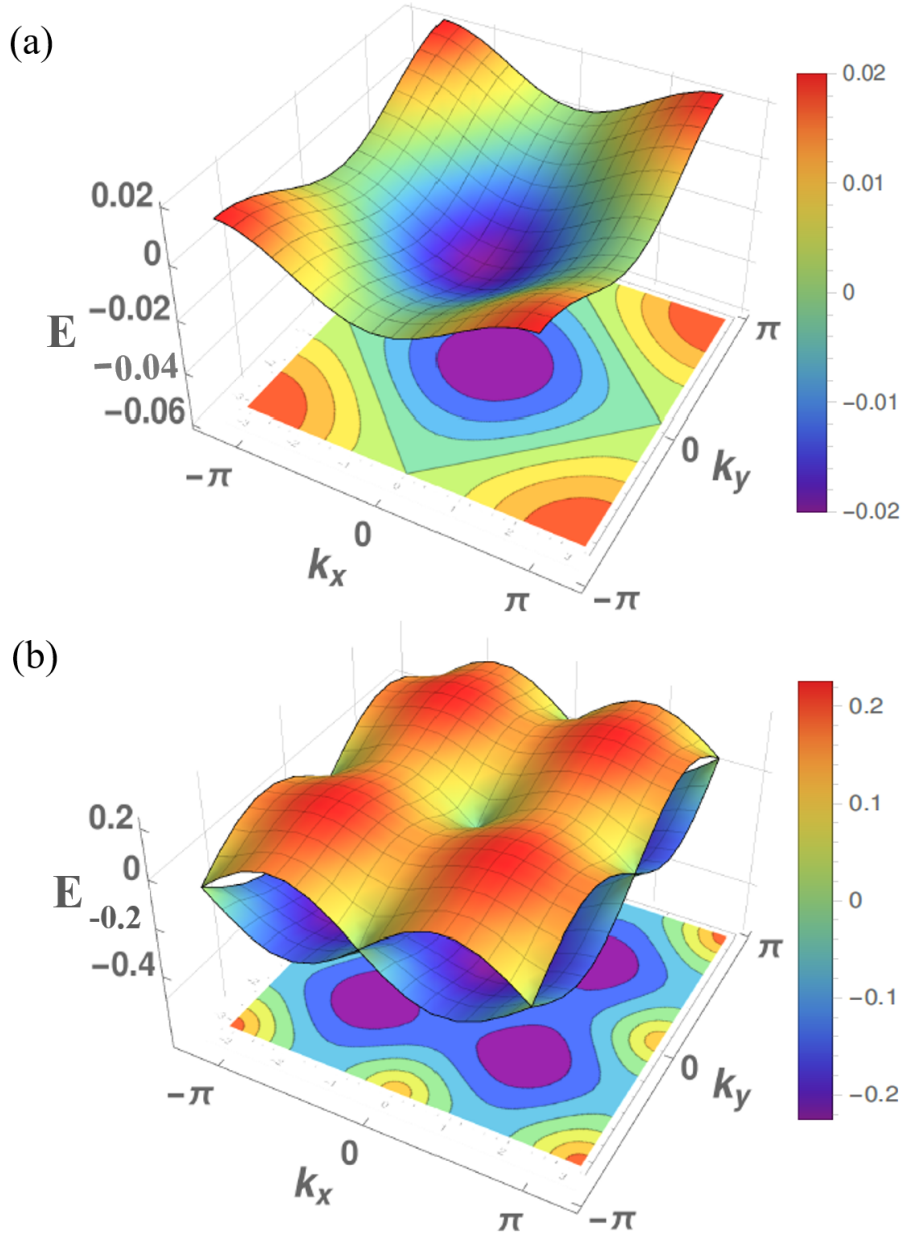


Figure 3.1: Noninteracting band structure of the 2D square optical lattice for two regimes. (a) The case $\gamma/J = 0$ represents the single minimum at $\mathbf{k} = 0$ in the absence of SOC. The other case in (b) is shown for finite SOC of $\gamma/J = 8$, where the competition between γ and J determines the band structure. Here the SOC breaks the rotational symmetry and the minima occur at four finite wave vectors in the lower branch. This is evident from the projection of the lower-energy branch onto the k_x - k_y plane. As γ/J decreases, the minimum of the lower branch tends to approach $\mathbf{k} = 0$.

the MI phase $\langle \hat{n}_{\pm} \rangle$ is an integer, while the SF phases are characterized by real $\langle \hat{n}_{\pm} \rangle$ and a finite value of the compressibility $\kappa = \partial \langle \hat{n} \rangle / \partial \mu$. The SF order parameter $\langle \hat{b}_i^{\alpha} \rangle$ is used to distinguish the MI and SF phases as it is non-zero in the SF and zero in the MI phase. In the absence of SOC, the amplitude and phase of the order parameter $\phi^{\dagger}(\phi^{\downarrow})$ are homogeneous in the miscible domain.

Striking features appear when the spin-dependent hopping due to the SOC is finite. This is a complex hopping; it flips the atomic spin while hopping and causes variations in the phase of SF states. To classify the various SF states which feature distinct phase distributions of the order parameter, we examine the spin-dependent momentum distributions at the wave vector \mathbf{k} ,

$$\langle \rho_{\uparrow,\downarrow}(\mathbf{k}) \rangle = L^{-2} \sum_{i,j} \langle \hat{b}_i^{\uparrow\dagger} \hat{b}_j^{\downarrow} \rangle e^{i\mathbf{k} \cdot (\mathbf{r}_i - \mathbf{r}_j)}, \quad (3.11)$$

where L is the system size and \mathbf{r}_i (\mathbf{r}_j) is the location of i^{th} (j^{th}) lattice site. When the interspin interaction is weaker than the intraspin interaction, the SF state can be of three types. (i) The homogeneous superfluid has a uniform amplitude and phase of the order parameter. For this state, the condensation occurs at zero momentum (ZM) and is also referred to as a ZM-SF state. (ii) The phase-twisted (PT) superfluid state has an amplitude of $\langle \hat{b}_i^{\alpha} \rangle$ that is uniform, but the phase varies diagonally across the lattice. (iii) The stripe (ST) superfluid state has stripe-like variation in the phase of $\langle \hat{b}_i^{\alpha} \rangle$ across the lattice. Thus, we distinguish superfluid states based on their phase variation and momentum distributions. It is worth mentioning that similar SF states have been previously discussed in the continuum where the phases were characterized using the properties of collective excitations [185].

The interplay of spin-dependent hopping (SOC) and single-particle hopping leads to the exotic SF states. We examine the spin-dependent momentum distributions $\langle \rho_{\uparrow,\downarrow}(\mathbf{k}) \rangle$ at $\mathbf{k} = 0$, $\langle \rho_{\uparrow,\downarrow}(\pm k_0, 0) \rangle$, $\langle \rho_{\uparrow,\downarrow}(0, \pm k_0) \rangle$, and $\langle \rho_{\uparrow,\downarrow}(\mathbf{q}_i) \rangle$. Here \mathbf{q}_i and k_0 depend on the ratio of the hopping to the SOC strength, as discussed in Sec. 3.1. For the PT superfluid, the momentum distribution at $\langle \rho_{\uparrow,\downarrow}(\mathbf{q}_i) \rangle$ is finite either at all the \mathbf{q}_i or only at one of the \mathbf{q}_i . This is due to the variation in phase distributions along the diagonal. Hence, this state shows a peak along the diagonal of the Brillouin zone in the \mathbf{k} space. On the other hand, for the ST superfluid states, depending on whether the phase variation is horizontal or vertical, the state exhibits a peak at $\langle \rho_{\uparrow,\downarrow}(\pm k_0, 0) \rangle$ or $\langle \rho_{\uparrow,\downarrow}(0, \pm k_0) \rangle$, respectively. We define $\Phi = \langle \rho_{\uparrow,\downarrow}(k_0, 0) \rangle + \langle \rho_{\uparrow,\downarrow}(-k_0, 0) \rangle + \langle \rho_{\uparrow,\downarrow}(0, k_0) \rangle +$

3 Spin-orbit-coupling-driven superfluid phases in optical lattices

$\langle \rho_{\uparrow,\downarrow}(0, -k_0) \rangle$, which serves as an order parameter to identify the PT-ST phase transition. Here Φ is zero for the PT superfluid and finite for the ST state. As both PT and ST are SOC-driven finite-momentum superfluid states, $\langle \rho_{\uparrow,\downarrow}(0, 0) \rangle = 0$. In the next section, we characterize the various phase transitions and the finite-momentum superfluids based on the aforementioned classification while spanning J/U -axis for each μ . Furthermore, when the interspin interaction is strong $U_{\uparrow\downarrow} > 1$, we also report a ferromagnetic phase where the spins orient along the $\pm z$ axis. This is referred to as the z -polarized ferromagnetic (zFM) superfluid state where $\langle \hat{b}_i^\uparrow \rangle$ ($\langle \hat{b}_i^\downarrow \rangle$) remains finite and homogeneous but $\langle \hat{b}_i^\downarrow \rangle$ ($\langle \hat{b}_i^\uparrow \rangle$) vanishes throughout the lattice. This phase can be easily distinguished from other superfluid states with finite ϕ^\uparrow or ϕ^\downarrow .

3.3 Results and discussion

We study the mean-field ground-state phase diagram of the ultracold bosons and investigate the different SF phases emerging from the competition between the SOC and single-particle hopping. We choose the intraspin interactions to be the same, $U_{\uparrow\uparrow} = U_{\downarrow\downarrow} = U$. We consider U as the scaling parameter for the tunnelling amplitude, chemical potential, interspin interaction, and energy of the system. In particular, we examine the system for weak ($U_{\uparrow\downarrow}/U < 1$) and strong ($U_{\uparrow\downarrow}/U > 1$) interspin interactions. We then employ the finite-temperature Gutzwiller theory to probe the effects of thermal fluctuations on the SF phases of the bosons. To generate the phase diagrams, we consider a system size of 8×8 ; the Fock state dimension at each lattice site is $N_b = 6$. The latter is sufficient to represent the quantum phases of the system up to $\mu = 3U$ [177–180]. It is important to note that the initial states play a key role in determining the ground states. We have performed numerical simulations with different initial states and found that a random SF order parameter as the initial state gives the global minimum. The uniform ϕ is not a good choice for the initial state because for some values of the parameters the converged solution corresponds to a local minimum. This is due to the fact that the uniform ϕ does not contribute to the SOC energy as this depends on the relative phase between the ϕ of both pseudospinor components. To obtain the mean-field phase diagrams, we start with a complex random distribution of Gutzwiller coefficients across the lattice, and then the corresponding SF order parameter is computed. Hence, our initial state has a random SF order parameter with random amplitude and phase. Our algorithm is based on the self-consistent approach. We

diagonalize the single-site Hamiltonians and compute the updated $\phi_{i\alpha}$ at each iteration. This process is repeated until the energy and superfluid order parameter converge up to a tolerance of 10^{-12} . Moreover, we repeat the procedure with 50 random configurations of the initial state to ensure that the ground state has been obtained. We have checked explicitly that the larger number of random configurations does not modify the ground states.

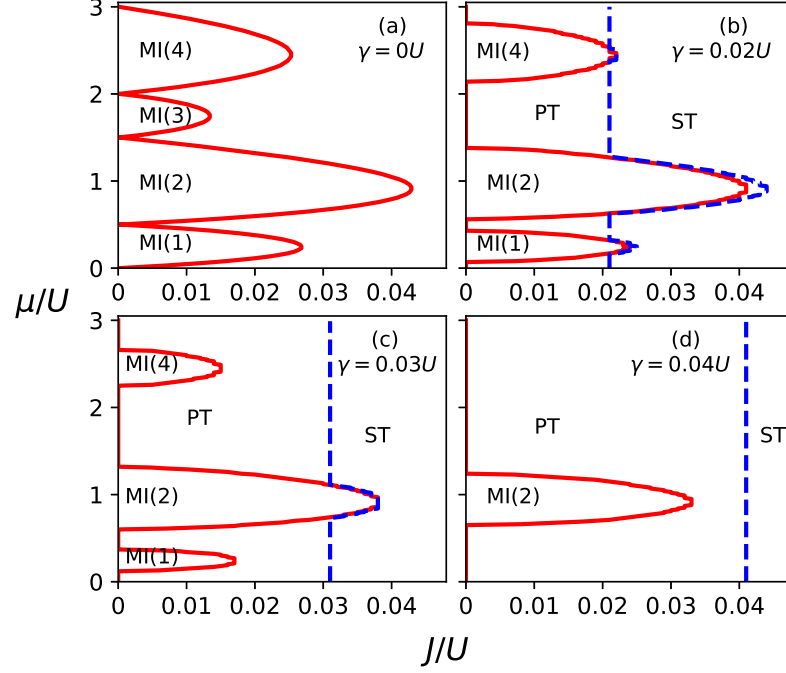


Figure 3.2: Zero-temperature ground-state phase diagram in the presence of Rashba SOC for various SOC strengths: (a) $\gamma = 0U$, (b) $\gamma = 0.02U$, (c) $\gamma = 0.03U$, and (d) $\gamma = 0.04U$. The Mott insulator regime is represented by $MI(n)$, where $n = n^\uparrow + n^\downarrow$ is the total filling or occupancy of the lobe. The interspin interaction $U_{\uparrow\downarrow} = 0.5U$. At $\gamma = 0$, the system exhibits an MI-SF transition, where the SF phase Bose condenses at zero momentum and hence is referred to as the ZM-SF state. The finite γ results in finite-momentum superfluid phases. Here as J is varied, the system undergoes the PT-ST superfluid phase transition, shown by blue dashed lines. The phase diagrams are obtained using random complex initial states with 50 random configurations. The system size $L = 8 \times 8$ and periodic boundary conditions are considered.

3.3.1 $U_{\uparrow\downarrow} = 0.5$

We first examine the quantum phases of the 2D TBHM in the presence of the SOC at zero temperature. The plots in Fig. 3.2 show the ground-state phase diagrams at different values of the SOC strengths γ with $U_{\uparrow\downarrow} = 0.5U$.

3.3.1.1 No SOC ($\gamma = 0$)

In the absence of SOC, the system supports two quantum phases, the incompressible MI phase and the compressible ZM-SF phase. The MI phase occurs in lobes of different integer commensurate densities. It should be noted that the MI lobes with odd-integer occupancies are smaller than those with even occupancies [186]. As $U_{\uparrow\downarrow}$ increases, the size of the odd-integer Mott lobes grows, whereas even-integer lobes remain the same in size but shift to higher μ/U until $U_{\uparrow\downarrow} = U$. In the absence of SOC, the phase diagram shown in Fig. 3.2(a) agrees well with previous studies on the TBHM [186–189].

3.3.1.2 Finite SOC ($\gamma \neq 0$)

The ground-state phase diagrams for finite SOC are shown in Figs. 3.2(b)- 3.2(d). Considering the phase diagram at $\gamma = 0.02U$, a prominent feature is the shrinking of the MI lobes. At higher μ , the MI(3) lobe vanishes and is replaced by the SOC-induced SF phase. Thus, even in the atomic limit $J/U = 0$, for certain ranges of μ , the system is in the SF phase due to the SOC. This is evident from the phase diagram in Fig. 3.2(b), where the SF phase is present at $J/U = 0$ for $\mu/U \leq 0.07$, $0.43 < \mu/U < 0.57$, $1.38 < \mu/U < 2.14$, and $2.8 < \mu/U \leq 3.0$. In the absence of single-particle hopping, i.e., $J = 0$, the superfluidity is due to the transport of atoms in the presence of spin-dependent hopping (SOC). As we increase γ , the MI lobes shrink further, and the SF phase is enhanced. For $\gamma = 0.04U$, only the MI(2) lobe survives, and the system is in the SOC-generated SF phases in the remaining parameter domain. This is due to the larger region covered by the MI(2) lobe even at $\gamma = 0$. Our computations for larger γ show that the MI(2) lobe also vanishes at $\gamma \approx 0.06U$. Hence, the MI lobe with a larger insulating domain and higher J_c will require larger SOC strengths to result in superfluid states occupying the whole domain of the $J/U - \mu/U$ plane. The vanishing of insulating lobes with the formation of SOC-induced SF states is in agreement with the previous studies [71, 190]. Using site-decoupling approximation and second-order perturbation theory, the critical hopping of the MI-SF transition in the presence of SOC is

$$\left(\frac{zJ_c}{U}\right) = \frac{1}{2} \left[\left(\frac{zJ_0}{U}\right) + \sqrt{\left(\frac{zJ_0}{U}\right)^2 - 8\left(\frac{\gamma}{U}\right)^2} \right], \quad (3.12)$$

where J_0 is the critical hopping of the MI-SF transition in the absence of SOC ($\gamma = 0$). The value of J_0 depends on the occupation number of the species [191]. Here $z = 2d$ is the coordination number of the d -dimensional optical lattice. The value of J_c decreases with γ , which confirms our numerical results in the phase diagrams shown in Fig. 3.2. As an illustration, for the MI(2)-SF phase transition, the above expression yields values of J_c as 0.0418 and 0.0402 for $\gamma/U = 0.02$ and 0.03, respectively, which are in close agreement with the numerical values in the phase diagrams in Figs. 3.2(b) and 3.2(c). Using Eq. (3.12), the critical SOC strengths where the MI(2) and MI(4) lobes are destroyed are 0.061 and 0.035, respectively, and these are consistent with our numerical results.

At $\gamma = 0$, the only superfluid phase of the system is the ZM superfluid, whereas, at a nonzero γ value, it is replaced by finite-momentum superfluids. The nature of superfluid phases near the MI-SF transition can be understood by analyzing the mean-field energies [190]. The hopping energy depends on the relative phase between the same spin state, while the SOC energy depends on the relative phase between different components. For the $\gamma = 0$ case, the minimization of hopping energy leads to a zero phase difference between the states, which corresponds to the ZM superfluid [Fig. 3.2(a)]. For finite γ , the energies depend on γ/J , relative phases, and the ratio of the amplitudes of ϕ^\downarrow and ϕ^\uparrow . For fixed γ/J and assuming a uniform amplitude of order parameters, the minimization of energies with respect to relative phases corresponds to finite but uniform relative phases [190], which are identified as the PT superfluid state.

The characteristic properties of the finite-momentum and ZM-superfluid states are shown in Fig. 3.3. The phase variations and the momentum distributions of the finite-momentum superfluids are shown for fixed $\gamma = 0.02U$, $\mu = 1.5U$, and two different J values corresponding to PT and ST superfluids. For the PT superfluid state, the random initial state yields a uniform amplitude and twisted diagonal site variation in the phase, as evident from Fig. 3.3(a). The phase variation is shown for one of the components, although it should be noted that the other component also follows similar distributions. However, the relative phase of the ϕ between the components is finite, i.e., $\theta_i^\uparrow \neq \theta_i^\downarrow$ [190]. In the presence of the interactions, the fourfold symmetry of the lower branch of the lowest-energy band is spontaneously broken. For the PT superfluid phase, the system chooses to be in one of the minima, and therefore we observe a single peak at $\mathbf{k} \neq 0$ in the momentum distribution. In particular, the peak in the \mathbf{k} space appears at the diagonal of the Brillouin zone, as represented in Fig. 3.3(d).

3 Spin-orbit-coupling-driven superfluid phases in optical lattices

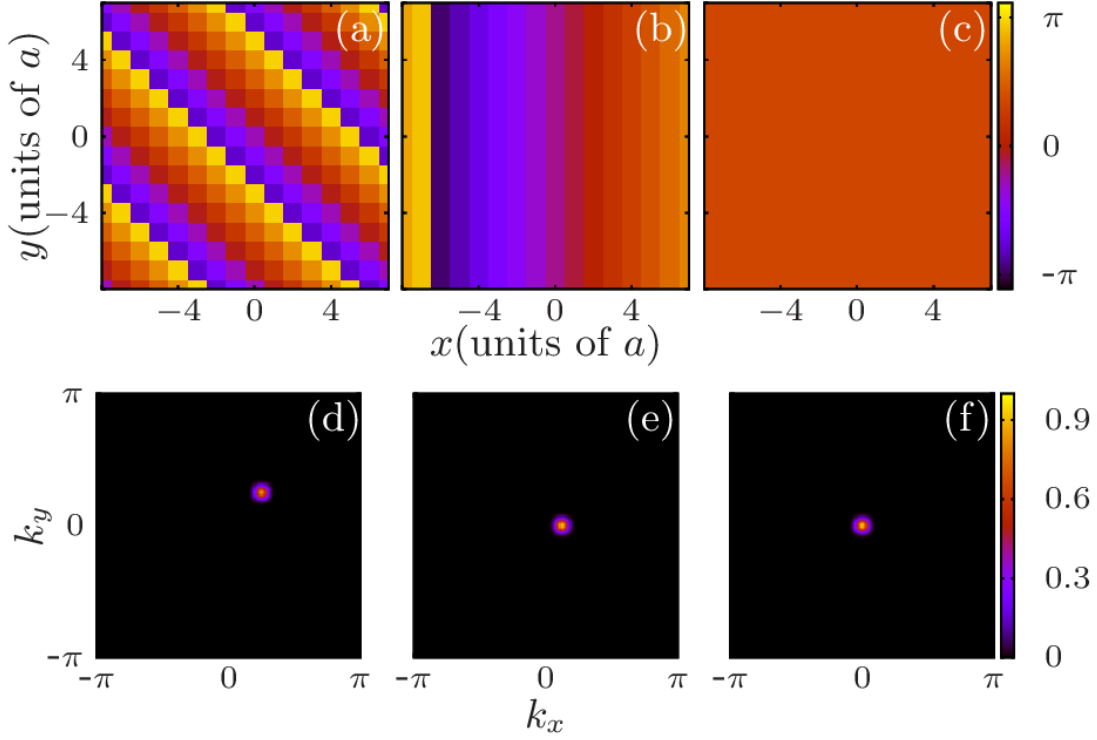


Figure 3.3: The lattice-site distributions of the phase variation and spin-dependent momentum distributions of various superfluid states. The upper panel represents the phase distributions for (a) PT, (b) ST, and (c) ZM superfluid whereas the lower panel (d)-(f) the corresponding momentum distributions. The finite-momentum superfluids are obtained using the Gutzwiller mean-field approach for $\gamma = 0.02U$ and $\mu = 1.5U$. The hopping amplitude in terms of U corresponding to PT and ST are 0.015 and 0.04, respectively. The (c) ZM superfluid is plotted for $\gamma = 0$, $\mu = 1.5$, and $J = 0.04U$. The spatial variation of phase and momentum distributions are shown for one of the components, as the other component also has the similar distributions. The peak in the spin-dependent momentum distributions appears at $\mathbf{k} \neq 0$ for (d) PT and (e) ST states, whereas for (f) ZM superfluid it appears at $\mathbf{k} = 0$. Here, a is the lattice constant.

As J is increased, the PT phase undergoes a transition to the ST phase. In the ST superfluid phase obtained with the SGMF approach, the amplitude of ϕ_i^α remains spatially uniform and phase distributions exhibit striplike variation [Fig. 3.3(b)]. The momentum peak is located at $\mathbf{k} \neq 0$ and in particular it lies on x or y axis, depending on the variation in phase [Fig. 3.3(e)].

To examine the quantum phase transition between the phase-twisted and the ST superfluid states, we analyze the properties of $\langle \rho_{\uparrow\downarrow}(\mathbf{k}) \rangle$. Since both states are finite-momentum superfluids, the location of their momentum peaks in \mathbf{k} space can serve as an order parameter to identify them. As mentioned earlier in Sec. 3.2, we in particular analyze the evolution of the order parameter Φ , which is the sum of $\langle \rho_{\uparrow\downarrow}(\mathbf{k}) \rangle$ at $\mathbf{k} = (\pm k_0, 0)$ and $(0, \pm k_0)$, as a function of J . For

each μ value, we have spanned along the J/U axis, and whenever Φ takes a nonzero value, the critical hopping strength for the PT-ST transition is determined. The error involved in analyzing the phase transition is 10^{-3} , which is the step size (ΔJ) used to span J/U in the numerical computations. Hence, we find that the PT-ST phase transition is sharp. As a representative case, the evolution of Φ at $\mu/U = 1.8$ for three different γ values is shown in Fig. 3.4. At lower hopping strengths, the ground state is either the MI phase or the finite-momentum PT superfluid and hence Φ remains zero. This is due to the fact that the PT state corresponds to the condensation in $\mathbf{k} = \mathbf{q}_i$ along diagonals of the first Brillouin zone. As J/U increases, a striped ordering of the phase develops with finite Φ , which characterizes the PT-ST superfluid phase transition of the spin-orbit coupled bosons. The critical hopping strength of the PT-ST transition increases as the value of the SOC strength increases. As shown in Fig. 3.4, the J_c of the PT-ST transition is 0.02, 0.03, and 0.04 for $\gamma = 0.02, 0.03$, and 0.04, respectively. The behavior of Φ and the corresponding transitions for $U_{\uparrow\downarrow} = 0.5$ (Fig. 3.2) suggest that the PT to ST superfluid phase transition occurs when $\gamma/J \approx 1$. In addition, the PT phase is expected for $\gamma/J \gtrsim 1$, whereas the ST phase appears for $\gamma/J \lesssim 1$. Our computations using random configurations of complex $\phi_{p,q}^\alpha$ suggest an increase in J_c as the system size increases. Since the real cold-atom experiments are with the trapped finite-size systems, the transition between finite-momentum superfluids can be observed near the trap center [71].

The SGMF approach fails to capture the density oscillations that should ideally be there in a stripe phase; the reason is that the SGMF theory does not include the intersite atomic correlations. In order to overcome this limitation of the SGMF theory and obtain the nonuniform magnetic ordering and the resulting inhomogeneous superfluidity, one has to use the diagonalization of the cluster of lattice sites as suggested in Ref. [67]. Considering this, we probe the parameter space of the stripe superfluid state obtained from the SGMF theory with the cluster Gutzwiller approach (CGA). The latter improves the intersite correlations and incorporates the effects of the quantum fluctuations. In this approach, the lattice sites are partitioned into a finite number of clusters, where the model terms within the lattice sites of a cluster are treated exactly. A detailed description of the approach is given in these works [157, 184, 186, 192, 193]. To examine the parameter domain corresponding to the stripe superfluid, we use a 2×2 cluster and $N_b = 3$. The size of the cluster is sufficient to probe the effects of the atomic correlations on the magnetic ordering of the SOC-driven superfluids. Like in the case of the SGMF theory,

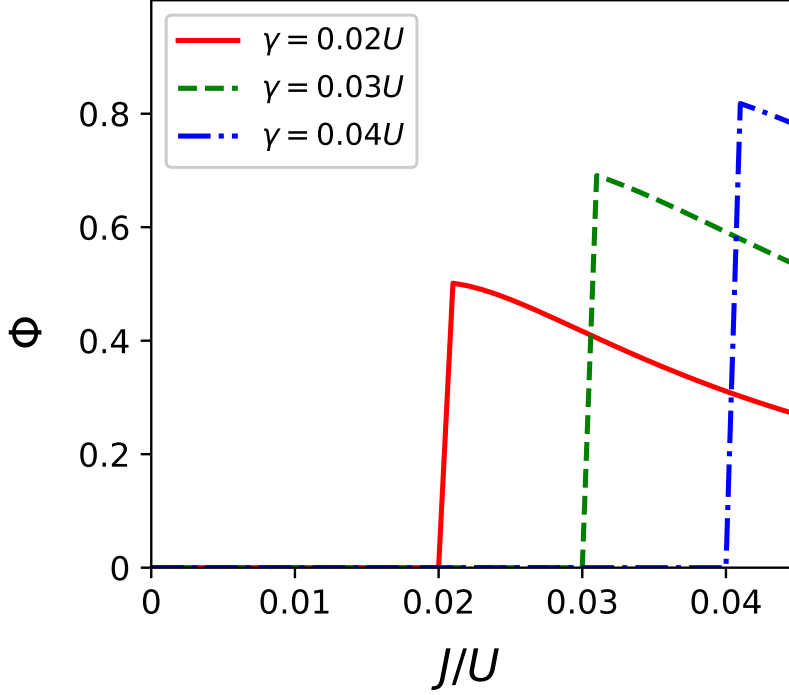


Figure 3.4: Evolution of the order parameter Φ , characterizing the finite-momentum PT and ST superfluid states, as a function of the hopping strength J/U . The chemical potential $\mu/U = 1.8$ and interspin interaction $U_{\uparrow\downarrow} = 0.5U$. The Φ is defined in Sec. 3.2. The variation in Φ from zero to a finite value shows the PT(MI)-ST phase transition.

sometimes the solution obtained from the CGA is a metastable state corresponding to a local minimum. To avoid this we consider several random configurations of the SF order parameters as the initial states with the CGA and choose the global minimum-energy state as the ground-state phase. The lattice-site distributions of the occupancy and the amplitude and phase of the SF order parameter are shown in Fig. 3.5. The profiles are shown for one of the components $|\uparrow\rangle$; however, the other component also follows similar distributions. We observe stripe variation in the number occupancy $\langle \hat{n}_i^\alpha \rangle$ and $|\phi_i^\alpha|$ and hence refer to it as the ST_{den} phase. The amplitudes of the variations remain smaller, which we expect can be enhanced by considering a larger cluster of sites.

We further investigate the parameter domain of the stripe superfluid (using the CGA) and find that the ST_{den} phase persists for larger hopping strengths. It continues to the domain where one would get the ZM superfluid transition using the SGMF theory. As an example, for

the parameters $L = 8 \times 8$, $\gamma = 0.02U$, $\mu = 1.8U$, and $J = 0.1U$, the SGMF theory predicts ZM superfluidity, whereas the CGA gives the ST_{den} phase for these parameters. Hence, the latter extends the parameter space of the ST_{den} phase by taking into account the quantum correlations. This suggests the applicability of the SGMF theory to describe the QPTs usually for $J/U \rightarrow 0$ [67, 71, 190]. Therefore, in this chapter, we investigate the phase transitions in the range from $J = 0$ to $J \approx 0.08U$. The stability of the ST_{den} superfluid in a wider parameter regime is consistent with the observation of this state in the presence of a weak lattice potential in a recent experiment [194]. In this thesis, the CGA is used to ascertain the nature of the ST and ZM phases obtained from the SGMF theory.

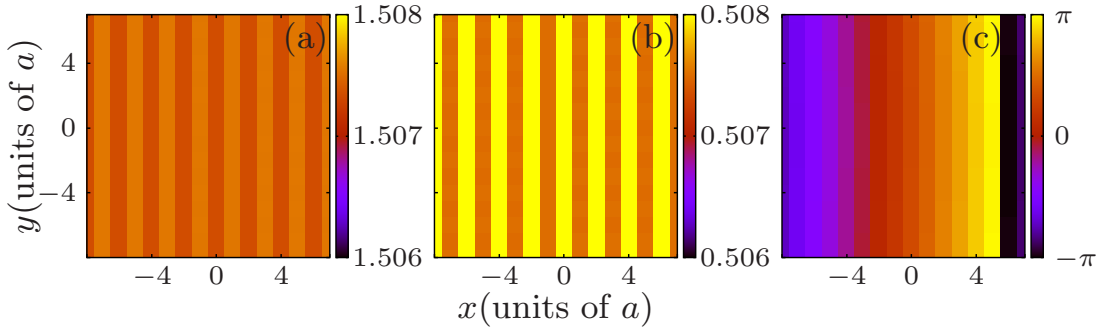


Figure 3.5: Lattice-site distributions in the ST_{den} phase obtained using the cluster Gutzwiller approach. The (a) occupancy, (b) amplitude of the order parameter, and (c) phase of a ST_{den} state are shown. The parameters are $\gamma = 0.02U$, $\mu = 1.8U$, and $J = 0.05U$. These distributions are shown for interspin interaction $U_{\uparrow\downarrow} = 0.5U$.

3.3.2 $U_{\uparrow\downarrow} = 1.5$

Here we discuss the quantum phases generated due to the effects of SOC when the interspin interaction is stronger than the intraspin one ($U_{\uparrow\downarrow}/U > 1$). In this parameter regime, we first review the phase diagram of the two-component interacting bosonic system in the absence of SOC. The phase diagram for $U_{\uparrow\downarrow} = 1.5U$ at $\gamma = 0$ is shown in Fig. 3.6(a). Above the phase separation criterion, at $J = 0$, the width of all MI lobes is $\Delta\mu/U = 1$. Moreover, the critical hopping of the MI(1)-SF transition in Fig. 3.6(a) becomes identical to the MI(2)-SF for $U_{\uparrow\downarrow} < U$ case as shown in Fig. 3.2(a). Details of the quantum phase transitions as a function of $U_{\uparrow\downarrow}$ for the two-component interacting scalar-bosonic system are reported in Sec. 4.1.1. In the phase-separated superfluid, the condensation occurs in one of the components only, and it resembles the zFM phase [67, 175]. We further examine the SOC-driven superfluid phases

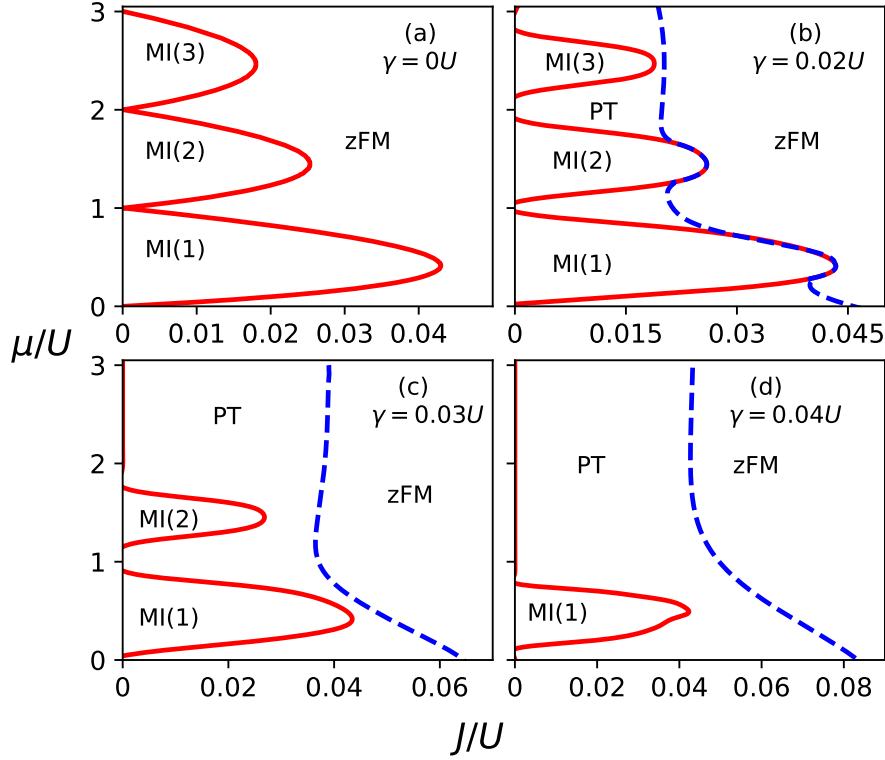


Figure 3.6: Zero-temperature ground-state phase diagram in the presence of Rashba SOC for various SOC strengths: (a) $\gamma = 0U$, (b) $\gamma = 0.02U$, (c) $\gamma = 0.03U$, and (d) $\gamma = 0.04U$. The filling or occupancy of the Mott lobe is represented by n in $\text{MI}(n)$. The interspin interaction $U_{\uparrow\downarrow} = 1.5U$. The superfluidity near the MI lobes is twisted in character, while at higher J the system is in the zFM state.

and their parameter space as γ varied. The phase diagrams for three representative cases are shown in Figs. 3.6(b)-3.6(d). At $\gamma = 0.02U$, for lower hopping strengths, the phase-modulated PT superfluid emerges between the insulating lobes as shown in Fig. 3.6(b). For the phase-separated regime, the uniform occupancy of the PT state is observed for $n_i = n_i^{\uparrow} + n_i^{\downarrow}$ and the phase of each component varies diagonally as shown in Fig. 3.3(a). A further increase in J results in a transition to the zFM superfluid. The effects of SOC at higher strengths $\gamma = 0.03U$ and $0.04U$ are shown in Figs. 3.6(c) and 3.6(d), respectively. At $\gamma = 0.03U$, the $\text{MI}(3)$ completely vanishes, and the parameter regime of the PT superfluid phase is enhanced. This is also evident from the SF region between the $\text{MI}(1)$ and $\text{MI}(2)$ lobes. At $\gamma = 0.04U$, the destruction of Mott lobes is enhanced as indicated by the absence of $\text{MI}(2)$. As SOC strength increases, the melting of insulating lobes occurs first for higher-density lobes and then continues to the lower-density

ones. In addition, the J_c of the MI-SF transition also decreases with γ . We find that at higher $\gamma \approx 0.065U$, the MI(1) phase gets completely destroyed and the system exhibits a superfluid phase transition between the PT and zFM states. In the PT phase, both ϕ_i^\uparrow and ϕ_i^\downarrow are finite while in the zFM superfluid only one of them is finite [as mentioned earlier in Sec (3.2)]. Starting from within the PT phase and spanning the J/U axis for a particular μ , we note the J/U value when either ϕ_i^\uparrow or ϕ_i^\downarrow becomes $\leq 10^{-3}$; this is the J/U value at the PT-zFM phase boundary. After repeating this for all the μ values considered, we do a nonlinear least-squares fitting of all the critical J/U values for the PT-zFM transition with the residual of the order of 10^{-3} to smoothen the phase boundary. The transition between the PT and zFM states is broad compared to other zero-temperature phase transitions discussed in this chapter. It is important to note that for a stronger interspin interaction $U_{\uparrow\downarrow}/U > 1$, we do not observe the ST phase. This is consistent with the quantum phases of the continuum system with SOC where the tuning of Raman coupling for a strong interspin interaction does not lead to the ST phase [185].

3.4 Finite temperature

To study the effects of thermal fluctuations at finite temperature, we use the finite-temperature Gutzwiller theory. At finite temperature, the superfluid states are characterized similarly to the case of zero temperature, although we incorporate the effects of the thermal fluctuations at finite temperature by considering the thermal average of the observable quantities.

To compute the thermal average, we first get the full set of eigenspectra obtained from the diagonalization of the mean-field Hamiltonian. We further use the single-site energy spectrum E_i^l and the eigenstates $|\psi\rangle_i^l$ to evaluate the partition function of the system

$$Z_i = \sum_{l=1}^{N_b} e^{-\beta E_i^l}, \quad (3.13)$$

where l is the eigenstate index, N_b is the Fock space dimension, $\beta = (k_B T)^{-1}$, and T is the temperature of the system. At finite T , the region of the phase diagram with a vanishing SF order parameter and the real number occupancy $\langle \hat{n}_i^\alpha \rangle$ is defined as the normal-fluid (NF) state.

From the definition of the partition function, the thermal average of the SF order parameter is

$$\langle \phi_i^\alpha \rangle = \frac{1}{Z_i} \sum_{l=0}^{N_b} \langle \psi | \hat{b}_i^\alpha e^{-\beta E_i^l} | \psi \rangle_i^l, \quad (3.14)$$

where $\alpha = \uparrow, \downarrow$ is the spin-component index and $\langle \cdots \rangle$ represents the thermal averaging of ϕ . Similarly, the atomic occupancy at finite T is defined as

$$\langle \hat{n}_i^\alpha \rangle = \frac{1}{Z_i} \sum_{l=0}^{N_b} \langle \psi | \hat{n}_i^\alpha e^{-\beta E_i^l} | \psi \rangle_i^l. \quad (3.15)$$

The average occupancy is $\langle n^\alpha \rangle = \sum_i \langle \hat{n}_i^\alpha \rangle / L$. At finite T , the spin-dependent momentum distributions $\langle \rho_{\uparrow, \downarrow}(\mathbf{k}) \rangle$ are computed from the thermally averaged SF order parameters.

The NF state at finite temperature is identified in the incompressible phases based on the compressibility κ . In the present chapter, we consider $|n - n_{\text{th}}| \geq 10^{-3}$ as the criterion to identify MI to NF crossover. Here, n and n_{th} are the lattice occupancies at zero and finite temperature, respectively. Such a criterion has been previously used to distinguish the NF phase of the BHM at finite temperatures [195].

3.4.1 Finite-temperature results for $U_{\uparrow\downarrow} = 0.5$

At finite temperatures, the Mott lobe melts into the NF phase due to thermal fluctuations. The NF phase has no long-range order, but it is compressible ($\kappa \neq 0$). Therefore, this phase can be distinguished from the insulating MI phases by finite κ . We examine the melting of the MI phase as a function of temperature for various SOC strengths. In Fig. 3.7 we plot the width of the first Mott lobe MI(1) at $J = 0.01U$ for different values of γ . For $\gamma = 0$, at lower temperatures, the width of the MI lobe first increases for $k_B T/U < 0.004$.

At $k_B T/U \approx 0.004$ the Mott lobe starts melting, and the width of the lobe decreases with temperature. At $k_B T/U \approx 0.046$, the MI phase is completely replaced by the NF phase. However, for finite γ there is a combined effect of SOC and finite temperature on the width of the Mott lobe. For $\gamma = 0.02U$, at low temperatures, the width first increases and then at $k_B T/U \approx 0.009$ the thermal fluctuations overcome the SOC effects; and this leads to a decrease in the width. The effects of SOC are prominent at larger values of γ , as evident for the $\gamma = 0.03U$ and $0.04U$ cases in Fig. 3.7. At higher temperatures, the melting of the MI phase is independent

of γ , and the decrease in the width of the MI lobe is similar to the $\gamma = 0$ case.

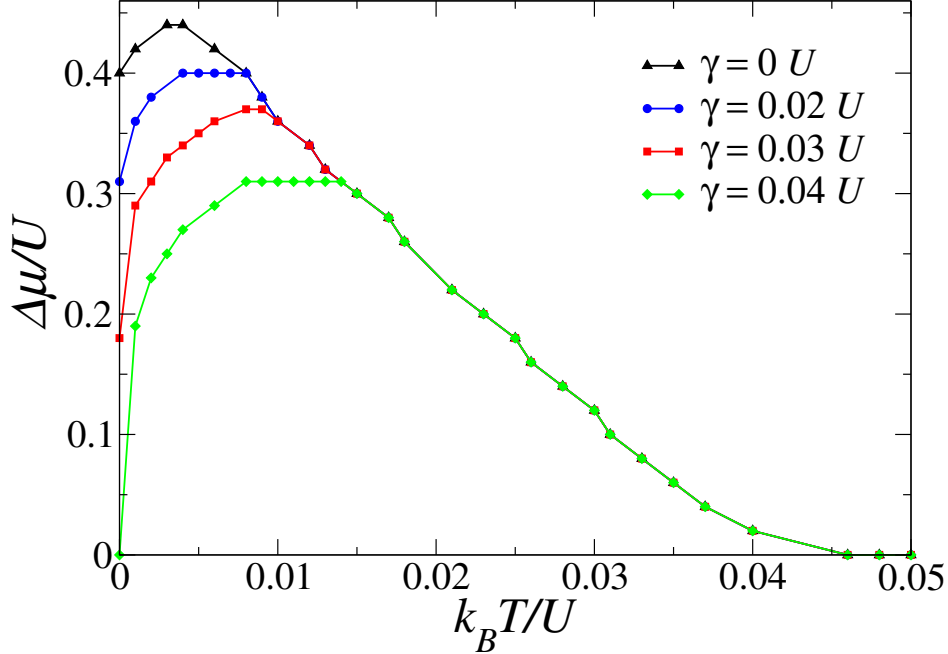


Figure 3.7: Width of the first Mott lobe MI(1) at $J = 0.01U$ as a function of temperature for various SOC strengths. The values of γ in units of U are shown in the legend. Here the interspin interaction $U_{\uparrow\downarrow} = 0.5U$. At lower temperatures, the melting of the MI lobe depends on the value of γ , and at higher $k_B T$ the width remains similar to the $\gamma = 0$ case. For all cases, with and without SOC, the MI(1) phase completely melts and replaced by NF phase at $k_B T/U \approx 0.046$.

We further discuss the finite-temperature phase diagram at $k_B T/U = 0.03$, shown in Fig. 3.8. At $\gamma = 0$, the thermal fluctuations destroy the ODLRO of the SF phase and extend the parameter space of the NF phase. Odd Mott lobes stretch along the J/U axis. For example, at $k_B T = 0$, the critical hopping of the MI(1)-SF transition is 0.0268 in Fig. 3.2(a) and at $k_B T/U = 0.03$, it increases to 0.0422, as evident from Fig. 3.8(a). Similar enhancement is also apparent for MI(3) from a comparison of Figs. 3.8(a) and 3.2(a). In the presence of SOC, there is an interplay of the effects of SOC and finite temperature. For smaller SOC strengths ($\gamma = 0.02$ and 0.03), the remarkable feature of the reemergence of MI lobes at the cost of finite-momentum superfluids at finite temperature is observed. In particular, the SOC-induced PT phase near the atomic limit in Fig. 3.2(b) melts into MI(3) and NF phases as shown in Fig. 3.8(b). The destruction of the PT superfluidity in a wide region of the NF state at finite temperature is consistent with the

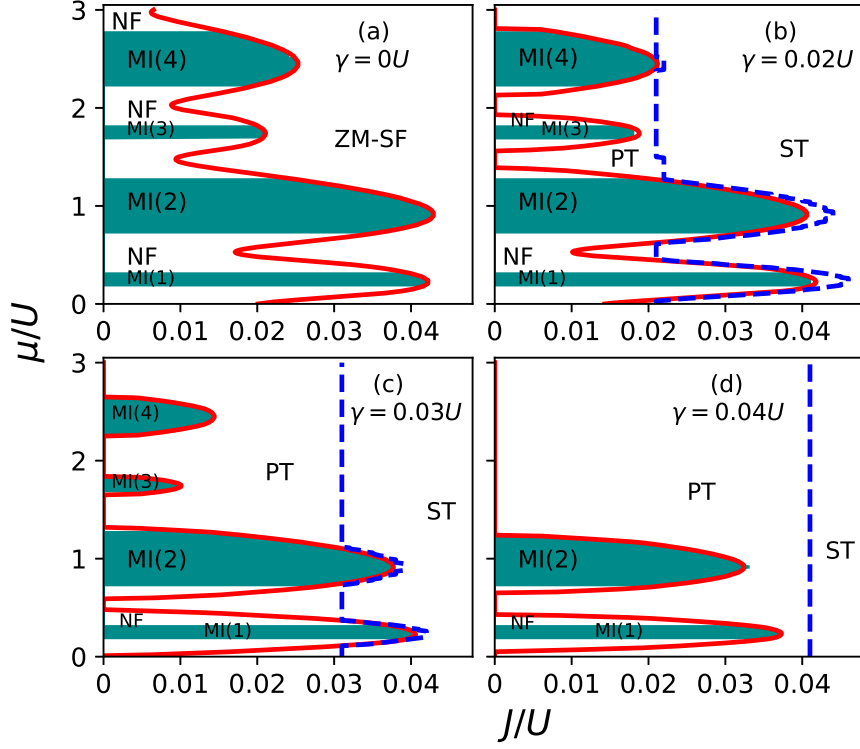


Figure 3.8: Finite-temperature phase diagram of the TBHM for different values of γ at $k_B T/U = 0.03$: (a) $\gamma = 0U$, (b) $\gamma = 0.02U$, (c) $\gamma = 0.03U$, and (d) $\gamma = 0.04U$. The interspin interaction $U_{\uparrow\downarrow} = 0.5U$. The shaded green bands are the insulating MI regions which are distinguished from the NF phase present at finite T . The reemergence of insulating regimes and destruction of PT superfluidity at finite temperatures are observed. The constant width of MI(1) for both zero and finite SOC confirms the behavior reported in Fig. 3.7. The blue dashed line represents the PT-ST superfluid phase transition obtained using the finite-temperature Gutzwiller mean-field approach.

previous Monte Carlo study of strongly correlated bosons with SOC [174]. The reemergence of insulating domains at finite temperature is in agreement with our analysis of the width of the MI lobe with SOC, which is shown in Fig. 3.7. While increasing the SOC strengths from 0.02 [Fig. 3.8(b)] to 0.03 [Fig. 3.8(c)], the PT state is favored by melting the NF and MI phases. At $\gamma = 0.04U$, the phase boundary of the PT to ST superfluid transition, as in the case of zero temperature, remains unchanged and independent of the average particle densities or μ at finite temperatures.

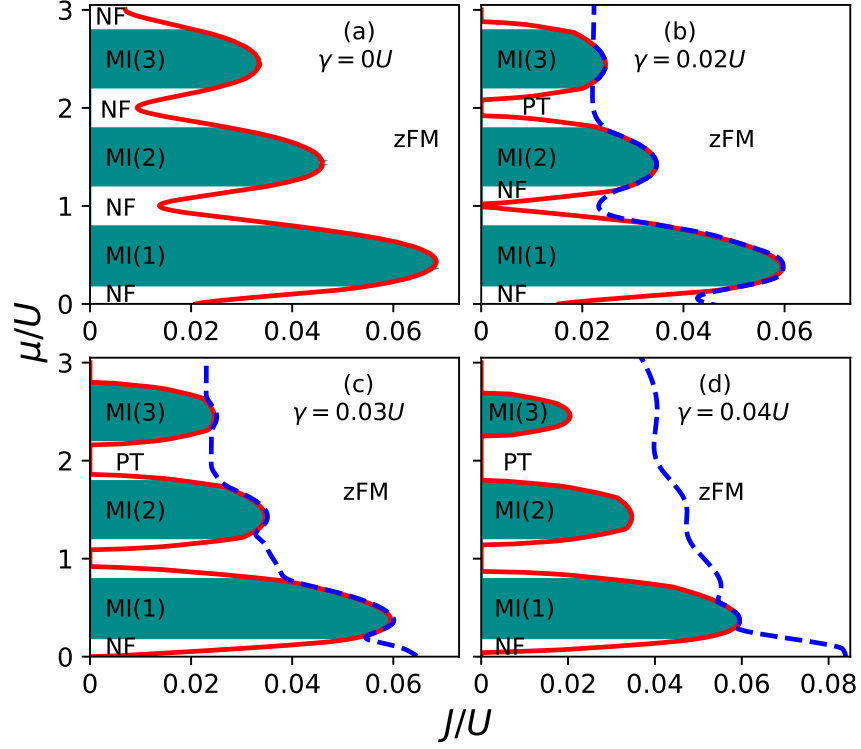


Figure 3.9: Finite-temperature phase diagram of the TBHM for different values of SOC strengths at $U_{\uparrow\downarrow} = 1.5U$: (a) $\gamma = 0U$, (b) $\gamma = 0.02U$, (c) $\gamma = 0.03U$, and (d) $\gamma = 0.04U$. The shaded green bands represent the residual insulating domains in the presence of thermal fluctuations. Outside the bands tiny white regions show the NF phase. The thermal energy corresponding to temperature is $k_B T/U = 0.03$. The finite temperature stabilizes the MI phases against the SOC and suppress the finite-momentum superfluidity. This is evident from (c) and (d), as compared to the corresponding zero temperature cases shown in Figs. 3.6(c)-3.6(d).

3.4.2 Finite-temperature results for $U_{\uparrow\downarrow} = 1.5$

Like in the case of $U_{\uparrow\downarrow} = 0.5U$, we examine the finite-temperature phase diagram in the phase-separated regime with SOC. In particular, we explore the stability of the finite-momentum superfluids with the thermal fluctuations arising from finite T . To gain additional insight, we briefly review the $\gamma = 0$ case. As expected, the insulating lobes melt to the NF phase at $k_B T/U = 0.03$, which is discernible from the phase diagram shown in the Fig. 3.9(a). The phase diagrams of $\gamma \neq 0$ at $k_B T/U = 0.03$ are shown in Figs. 3.9(b)-3.9(d). At $\gamma = 0.02U$, the thermal fluctuations favor the insulating domains, and the emergence of the NF phase between the MI lobes reduces the PT superfluidity, as is evident from a comparison of Fig. 3.9(b) with Fig. 3.6(b). The reemergence of MI lobes at finite T is also seen in this case, as can be confirmed

by comparing Figs. 3.9(c) and 3.9(d) with Figs. 3.6(c) and 3.6(d). At the phase boundaries, the critical hopping of the MI-zFM and PT-zFM transitions is shifted to higher J at finite temperature as compared to the critical J at zero temperature. The effect of the increase in SOC strength leading to the increase in the PT superfluid phase is also evident in the phase diagrams shown in Figs. 3.9(c)-3.9(d) which are similar to $U_{\uparrow\downarrow}/U < 1$ case.

3.5 Conclusions

We have studied the parameter domain of various finite-momentum superfluids of SO-coupled ultracold bosonic atoms in 2D optical lattices. To examine various superfluid states with different atomic densities and phase ordering, we have used spin-dependent momentum distributions, a routinely measured observable in cold-atom experiments. For $U_{\uparrow\downarrow} < U$, with $\gamma/J \gtrsim 1$ the favored superfluid phase is the PT phase, whereas with $\gamma/J \lesssim 1$ the system is in the ST phase. Starting with the PT phase, the increase in J results in the PT to ST superfluid phase transition. We have shown that the inclusion of quantum fluctuations via the CGA results in the ST_{den} phase corresponding to the parameter domain of the ST phase obtained with the SGMF theory. In the limit $U_{\uparrow\downarrow} > U$, the stripe superfluid is absent and the PT to zFM transition is observed as J is varied. We have further shown that the thermal fluctuations destroy the phase-twisted superfluidity and favor the insulating and normal states. The results reported in this chapter are pertinent to the ongoing quantum gas experiments with SOC and offer a parameter space in the $J - \mu$ plane to observe the finite-momentum superfluids. The results reported in this chapter are discussed in Ref. [196].

Chapter 4

Out-of-equilibrium dynamics of Bose-Bose mixtures in optical lattices

In the previous chapter 3, we discussed various phases of the two-component Bose-Hubbard model (TBHM) with and without SOC. The BHM has underpinned our understanding of quantum phase transitions (QPTs) [130, 197]. As discussed in the introduction to the quantum quench dynamics in Sec. 1.6.2, the study of out-of-equilibrium dynamics in interacting quantum systems in search of an adiabatic quantum state for quantum computation is an active research area [136]. The controllability of parameters in cold atom systems, especially over time, naturally sparks interest in the out-of-equilibrium dynamics of the BHM, particularly in the proximity of quantum critical points.

The Kibble-Zurek mechanism (KZM) [137, 138] offers a comprehensive theoretical framework to understand the non-equilibrium dynamics across continuous phase transitions. When an external parameter of the system is quenched with a finite rate across the critical point, non-adiabatic effects set in. This breakdown of the adiabaticity near the critical point is inevitable due to the critical slowing down, which refers to the divergence of the relaxation time of the system near the critical point. The KZM describes spontaneous symmetry breaking and the formation of broken symmetry domains based on the non-adiabatic regime in the dynamics. The theory predicts universal scaling laws with respect to the quench rate [137, 138, 198–200]. The

roots of this theory are in Tom Kibble's [137] studies on predicting the formation of topological defects as a result of local choices of broken-symmetry state during the cooling of the early universe. Zurek tested the ideas of Kibble in non-relativistic condensed matter systems and demonstrated that the competition between the relaxation time and the quenching rate determines the size of the broken-symmetry domains and predicted a universal power-law scaling of these defects in relation to the quench rate, with an exponent directly related to the equilibrium critical exponents [137, 138, 198–200]. Initially proposed to explain the evolution of the early universe [137], the KZM has been experimentally explored in various classical and QPTs. Its application has been demonstrated in numerous systems such as cosmic microwave backgrounds [201], liquid helium [202], superconductors [203], and liquid crystals [204]. More recently, the studies on the KZM have been extended to ultracold quantum gases [141, 142, 146, 205–222]. A recent experiment [146] has explored the dynamics of QPT from the MI to the SF phase and observed a power-law behavior of the coherence length, reminiscent of the KZM. This has led to a surge of interest in exploring QPTs of BECs loaded into an optical lattice to confirm the applicability of the KZM to QPTs. Multicomponent BECs offer a rich variety of QPTs when loaded into an optical lattice which has not been explored in the literature. We theoretically examine the quench dynamics of the MI to SF phase transition in the TBHM without SOC in this chapter.

A two-component Bose mixture in an optical lattice is not just an extension of a one-component Bose gas in a lattice as the phases of the multicomponent and spinor systems in such scenarios are considerably more intricate [223–226]. The MI-SF transition in the one-component BHM is a continuous transition, whereas the TBHM exhibits a tricritical point after which the MI-SF transition changes to a first-order transition [227]. Although the KZM predicts the breakdown of adiabaticity for continuous transitions, both experimental [228, 229] and theoretical studies [219, 221, 230] confirm the critical slowing down for the first-order phase transitions also. Motivated by these studies, we explore both the first-order and second-order MI-SF transitions of the TBHM in this chapter. We study the effects of the inhomogeneity of phases and order of transitions on the impulse regime and scaling exponents.

This chapter is organized as follows. In Sec. 4.1, we introduce the TBHM and describe the mean-field approach to determine the equilibrium phase diagram for three different values of the inter-species interactions corresponding to the miscible-immiscible phase transition. The dynamical Gutzwiller equations and the KZM are presented in Sec. 4.2. Sec. 4.3 discusses the

quantum quench dynamics across the MI(2)-SF and MI(1)-SF transitions of the TBHM. Finally, we summarize our findings in Sec. 4.4.

4.1 Two-component Bose-Hubbard Hamiltonian

We consider a Bose-Bose mixture of two spin states from the same hyperfine-spin manifold in a 2D square optical lattice at zero temperature. The TBHM (3.1) describing the system in the absence of SOC is [231]

$$\begin{aligned} \hat{H} = & - \sum_{p,q,\alpha} \left[\left(J \hat{b}_{p+1,q}^{\dagger\alpha} \hat{b}_{p,q}^{\alpha} + \text{H.c.} \right) + \left(J \hat{b}_{p,q+1}^{\dagger\alpha} \hat{b}_{p,q}^{\alpha} + \text{H.c.} \right) - \frac{U_{\alpha\alpha}}{2} \hat{n}_{p,q}^{\alpha} (\hat{n}_{p,q}^{\alpha} - 1) + \mu_{\alpha} \hat{n}_{p,q}^{\alpha} \right] \\ & + \sum_{p,q} U_{\uparrow\downarrow} \hat{n}_{p,q}^{\uparrow} \hat{n}_{p,q}^{\downarrow}, \end{aligned} \quad (4.1)$$

where the symbols have the same meaning as discussed in Sec. 3.1 of Chapter 3. The superfluid order parameters $\phi_{p,q}^{\alpha}$ and atomic occupancies $n_{p,q}^{\alpha}$ are similarly defined in Eqs. (3.7a)-(3.7b) and Eqs. (3.8a)-(3.8b), respectively.

4.1.1 Equilibrium phase diagrams

In this chapter, we consider identical chemical potentials $\mu_{\alpha} = \mu$ and intraspecies interactions $U_{\alpha\alpha} = U$. We scale all energies with respect to U . Following the phase separation criterion of the two components, determined by the strength of the interspecies interaction, we investigate the two regimes: $U_{\uparrow\downarrow} < 1$ and $U_{\uparrow\downarrow} > 1$. We use the SGMF approach discussed in Sec. 3.1 to obtain phase diagrams of the TBHM. We considered a lattice size of 8×8 and $N_b = 6$ and checked that by increasing the system size or N_b , phase diagrams do not alter. The model exhibits two phases: MI and SF [232–235].

4.1.1.1 Interspecies interaction $U_{\uparrow\downarrow} < 1$

We first consider $U_{\uparrow\downarrow} = 0.5$ and 0.9 in the miscible regime of the TBHM. In the MI phase, $\phi_{p,q}^{\alpha}$ is zero, but it is nonzero in the SF phase. We use this criterion to determine the phase boundary between the MI and SF phases in the J - μ plane. Figs. 4.1(a) and 4.1(b) show the phase diagrams for $U_{\uparrow\downarrow} = 0.5$ and 0.9 .

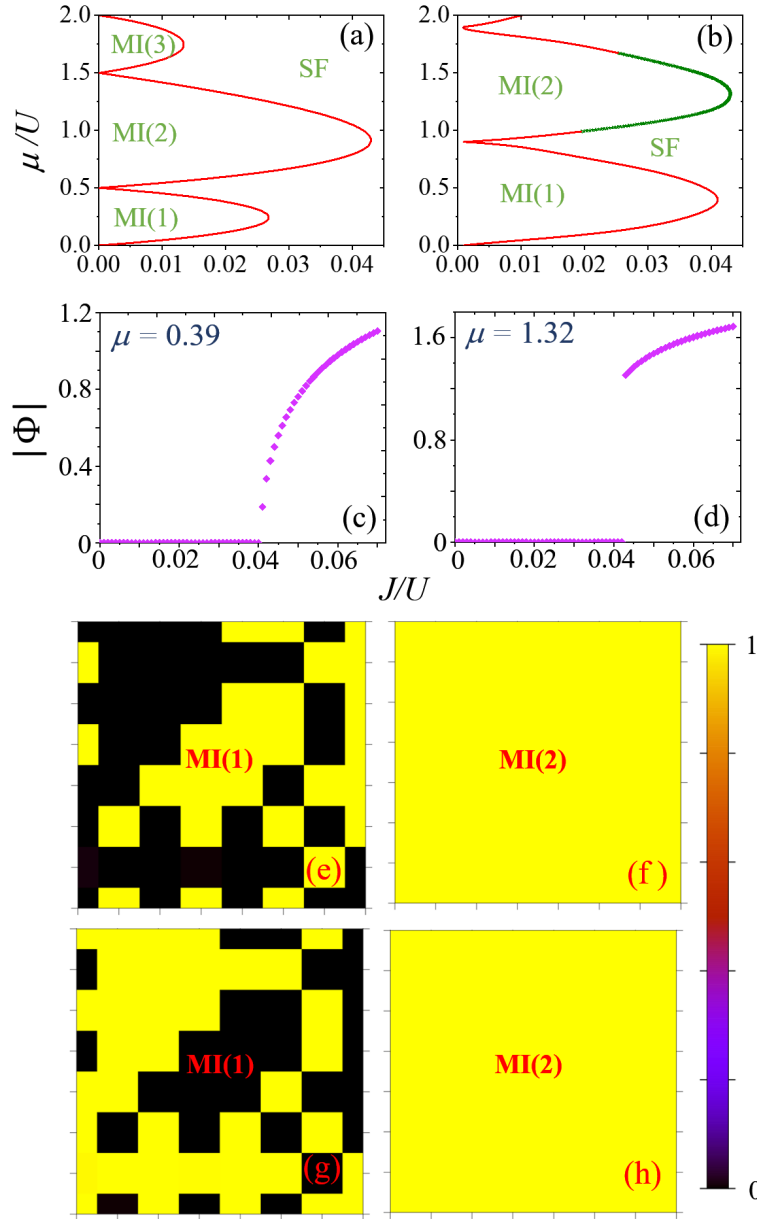


Figure 4.1: Phase diagrams of the TBHM in $J-\mu$ plane for (a) $U_{\uparrow\downarrow} = 0.5$ and (b) $U_{\uparrow\downarrow} = 0.9$. The number in parentheses is the total average atomic occupancy. The phase transitions across all boundaries are of second order except for the green curve in (b) across which the MI(2) to SF transition is of the first order in nature. For $U_{\uparrow\downarrow} = 0.9$, the $|\Phi|$ as a function of J are shown for (c) the MI(1)-SF transition at $\mu = 0.39$ and (d) the MI(2)-SF transition at $\mu = 1.32$. In the panels (e)-(h), sample atomic occupancy distributions ($n_{p,q}^\alpha$) of both components on an 8×8 square lattice are shown. (e) and (g) correspond to $n_{p,q}^\uparrow$ and $n_{p,q}^\downarrow$, respectively, in the MI(1) phase. The same for the MI(2) phase are shown in (f) and (h).

The phase diagram depicts two kinds of MI lobes based on the average total occupancy. These are even-integer and odd-integer MI lobes. In $J = 0$ limit, the size of the MI regions on the μ -axis for odd and even total fillings are $U_{\uparrow\downarrow}$ and 1, respectively. As we increase $U_{\uparrow\downarrow}$, the sizes of odd Mott lobes along J -axis increases while those of even Mott lobes remain the same. For the MI(1) phase, the average occupancies $n^\alpha = \sum_{p,q} n_{p,q}^\alpha / N_{\text{lattice}}$ are $0 < n^\uparrow < 1$ and $n^\downarrow = 1 - n^\uparrow$ and for the even-integer MI(2) phase, $n^\uparrow = n^\downarrow = 1$ [232]. Here N_{lattice} is the number of lattice sites.

At $U_{\uparrow\downarrow} = 0.5$, the MI-SF QPTs for both odd- and even-occupancy Mott lobes are second-order transitions. However, at $U_{\uparrow\downarrow} = 0.9$, the MI-SF transitions are not entirely second order. We find that the change in the order-of-transition, near the tip of the MI(2) lobe, occurs at $U_{\uparrow\downarrow} = 0.65$. For $U_{\uparrow\downarrow} = 0.9$, as shown in Fig. 4.1(b), the tricritical points on μ -axis exist at 0.99 and 1.67 [189, 233, 234]. For the regime between these two μ values, the MI(2)-SF transition is of the first order and marked by green points in Fig. 4.1(b). To confirm the order of these transitions, we have calculated the amplitude of the superfluid order parameter as a function of J for a fixed μ across the critical hopping strength. The continuous variation of $|\Phi| = \sum_{p,q,\alpha} |\phi_{p,q}^\alpha| / N_{\text{lattice}}$ with J represents a second-order phase transition as illustrated in Fig. 4.1(c) for the MI(1)-SF phase transition with $\mu = 0.39$ and $U_{\uparrow\downarrow} = 0.9$. On the other hand, a discontinuity in $|\Phi|$ across MI(2)-SF phase boundary in Fig. 4.1(d) for $\mu = 1.32$ and $U_{\uparrow\downarrow} = 0.9$ is indicative of the first-order phase transition.

The sample atomic occupancy distributions $n_{p,q}^\alpha$ in MI(1) and MI(2) phases confined in $N_{\text{lattice}} = 8 \times 8$ square lattice are shown in Figs. 4.1(e), 4.1(g) and Figs. 4.1(f), 4.1(h), respectively. The atomic occupancy distributions in the SF phase are uniform and identical for both components with real average occupancy.

4.1.1.2 Interspecies interaction $U_{\uparrow\downarrow} > 1$

For $U_{\uparrow\downarrow} > 1$, phase separation of the mixture of bosonic species occurs. We have shown the phase diagram for $U_{\uparrow\downarrow} = 1.5$ in Fig. 4.2(a) which does not change with an increase in $U_{\uparrow\downarrow}$. The continuous nature of the amplitude of the average superfluid order parameter Φ as a function of J for $\mu = 0.415$ and 1.45 in Fig. 4.2(b) and Fig. 4.2(c), respectively, confirms the second-order nature of the MI-SF phase transitions. In this regime, only one of the components, chosen randomly, occupies the lattice site. The occupancy of the other component remains zero at that

site. This applies to both the MI and SF phases. However, for the latter, the occupancy of one component is a real number and for the other is zero.

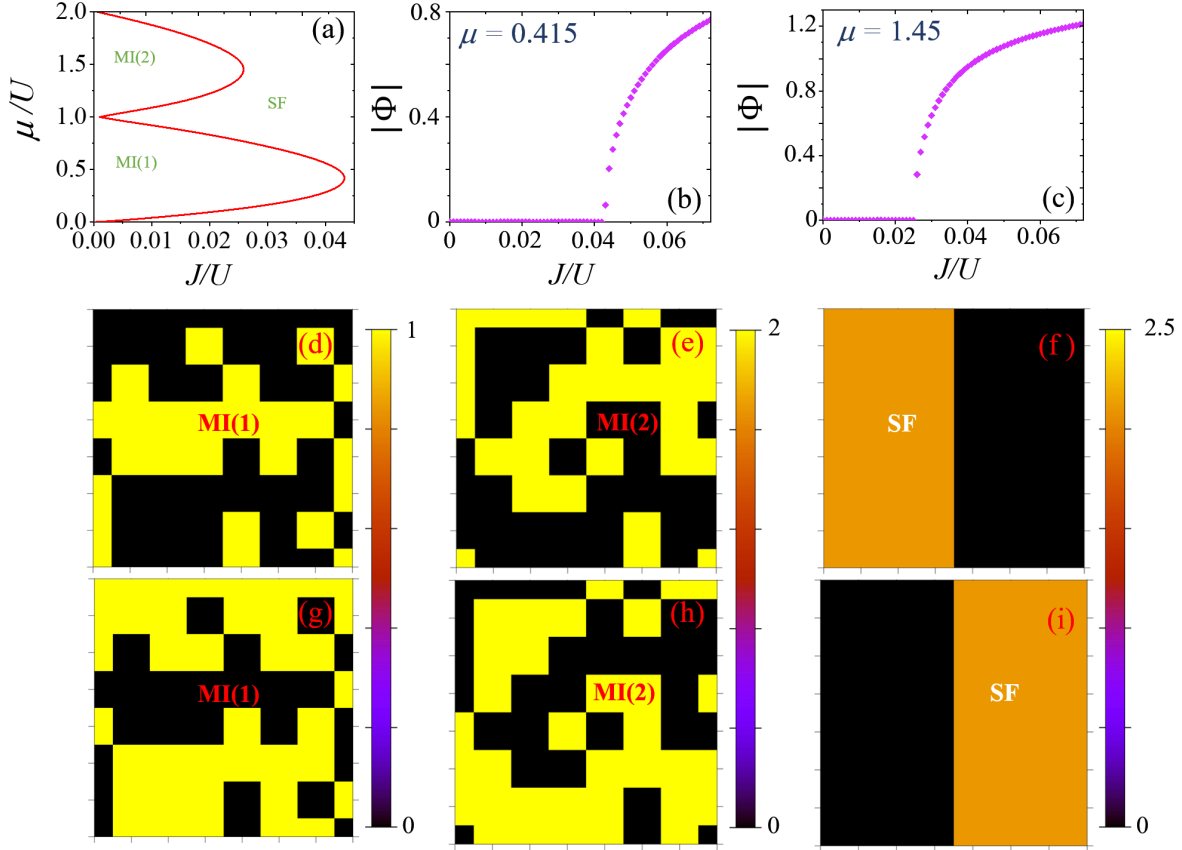


Figure 4.2: (a) The phase diagram of the TBHM in $J - \mu$ plane in the immiscible regime. (b) The variation of $|\Phi|$ as a function of J with $\mu = 0.415$, corresponding to the MI(1)-SF phase transition and (c) with $\mu = 1.45$ corresponding to the MI(2)-SF transition; these are plotted for $U_{\uparrow\downarrow} = 1.5$. The sample $n_{p,q}^{\uparrow}$ distributions in (d) MI(1), (e) MI(2), and (f) SF phases for $U_{\uparrow\downarrow} = 1.5$. Similarly, corresponding $n_{p,q}^{\downarrow}$ distributions are in (g), (h), and (i).

The sample atomic occupancy distributions for MI(1), MI(2), and SF phases are presented in Figs. 4.2(d) and 4.2(g); Figs. 4.2(e) and 4.2(h); and Figs. 4.2(f) and 4.2(i), respectively.

4.2 Quench dynamics

4.2.1 Time-dependent Gutzwiller approach

To study the out-of-equilibrium dynamics, we quench the hopping parameter in time, $J \rightarrow J(t)$, whereas all other model parameters remain steady in time. This results in the time dependence

in the TBHM. As J is ramped up in the quench, the system is expected to undergo the MI-SF phase transition. The time evolution of the single-site Gutzwiller wave function is governed by the time-dependent Gutzwiller equation given as

$$i\hbar\partial_t|\psi(t)\rangle_{p,q} = \hat{h}_{p,q}|\psi(t)\rangle_{p,q}. \quad (4.2)$$

The single-site Hamiltonian in (4.2) can be written as

$$\hat{h}_{p,q} = \hat{h}_{p,q}^1 + \hat{h}_{p,q}^2 + \hat{h}_{p,q}^3 + \hat{h}_{p,q}^4 + \hat{h}_{p,q}^5, \quad (4.3a)$$

$$= \mathcal{C}_1 \hat{b}_{p,q}^\dagger + \mathcal{C}_2 \hat{b}_{p,q}^\dagger + \mathcal{C}_3 \hat{b}_{p,q}^\dagger + \mathcal{C}_4 \hat{b}_{p,q}^\dagger + \mathcal{C}_5, \quad (4.3b)$$

where

$$\mathcal{C}_1 = -\left(J\phi_{p+1,q}^{\dagger*} + J^*\phi_{p-1,q}^{\dagger*} + J\phi_{p,q-1}^{\dagger*} + J^*\phi_{p,q+1}^{\dagger*}\right), \quad \mathcal{C}_1^* = \mathcal{C}_3, \quad (4.4a)$$

$$\mathcal{C}_2 = -\left(J\phi_{p+1,q}^{\downarrow*} + J^*\phi_{p-1,q}^{\downarrow*} + J\phi_{p,q-1}^{\downarrow*} + J^*\phi_{p,q+1}^{\downarrow*}\right), \quad \mathcal{C}_2^* = \mathcal{C}_4, \quad (4.4b)$$

$$\begin{aligned} \mathcal{C}_5 = & -\phi_{p,q}^{\dagger*}\mathcal{C}_1^* - \phi_{p,q}^{\downarrow*}\mathcal{C}_2^* - \phi_{p,q}^\dagger\mathcal{C}_1 - \phi_{p,q}^\downarrow\mathcal{C}_2 + \frac{U_{\downarrow\downarrow}}{2}\hat{n}_{p,q}\left(n_{p,q}^\downarrow - 1\right) \\ & + \frac{U_{\uparrow\uparrow}}{2}\hat{n}_{p,q}^\dagger\left(\hat{n}_{p,q}^\dagger - 1\right) - \mu_{p,q}^\dagger n_{p,q}^\dagger - \mu_{p,q}^2 n_{p,q}^\downarrow + U_{\uparrow\downarrow}\hat{n}_{p,q}^\dagger\hat{n}_{p,q}^\downarrow. \end{aligned} \quad (4.4c)$$

The time-dependent Gutzwiller equation can be cast into a set of coupled first-order differential equations for $c_{n_\uparrow, n_\downarrow}^{(p,q)}(t)$ using the single-site Lagrangian

$$L_{p,q} = i_{p,q}\langle\psi(t)|\partial_t|\psi(t)\rangle_{p,q} - {}_{p,q}\langle\psi(t)|\hat{h}_{p,q}|\psi(t)\rangle_{p,q}. \quad (4.5)$$

The first and second terms on the right-hand side of Eq. (4.5), respectively, are

$$i_{p,q}\langle\psi(t)|\partial_t|\psi(t)\rangle_{p,q} = i c_{m_\uparrow m_\downarrow}^{*(p,q)} \partial_t c_{n_\uparrow n_\downarrow}^{(p,q)} \langle m_\uparrow, m_\downarrow | n_\uparrow, n_\downarrow \rangle = i c_{n_\uparrow n_\downarrow}^{*(p,q)} \partial_t c_{n_\uparrow n_\downarrow}^{(p,q)} \quad (4.6a)$$

$$\begin{aligned} {}_{p,q}\langle\psi(t)|\hat{h}_{p,q}|\psi(t)\rangle_{p,q} = & c_{m_\uparrow, m_\downarrow}^{*(p,q)} c_{n_\uparrow, n_\downarrow}^{(p,q)} [\mathcal{C}_1 \sqrt{n_\uparrow} \delta_{m_\uparrow, n_\uparrow-1} \delta_{m_\downarrow, n_\downarrow} + \mathcal{C}_2 \sqrt{n_\downarrow} \delta_{m_\uparrow, n_\uparrow} \delta_{m_\downarrow, n_\downarrow-1} \\ & + \mathcal{C}_1^* \sqrt{n_\uparrow+1} \delta_{m_\uparrow, n_\uparrow+1} \delta_{m_\downarrow, n_\downarrow} + \mathcal{C}_2^* \sqrt{n_\downarrow+1} \delta_{m_\uparrow, n_\uparrow} \delta_{m_\downarrow, n_\downarrow+1} \\ & + \mathcal{C}_5 \delta_{m_\uparrow, n_\uparrow} \delta_{m_\downarrow, n_\downarrow}], \end{aligned} \quad (4.6b)$$

where explicit time dependence of $c_{n_\uparrow n_\downarrow}^{(p,q)}$ has been suppressed to compactify the notation. Using the Lagrange's equation of motion

$$\partial_t \left[\frac{\partial L}{\partial \left(\partial_t c_{n_\uparrow n_\downarrow}^{(p,q)} \right)} \right] = \left[\frac{\partial L}{\partial c_{n_\uparrow n_\downarrow}^{(p,q)}} \right], \quad (4.7)$$

the following set of first-order coupled differential equations for $c_{n_\uparrow n_\downarrow}^{(p,q)}(t)$ is then obtained:

$$\begin{aligned} i\partial_t c_{n_\uparrow n_\downarrow}^{(p,q)} = & \left[\mathcal{C}_3 \sqrt{n_\uparrow} c_{n_\uparrow-1, n_\downarrow}^{(p,q)} + \mathcal{C}_4 \sqrt{n_\downarrow} c_{n_\uparrow, n_\downarrow-1}^{(p,q)} + \mathcal{C}_1 \sqrt{n_\uparrow + 1} c_{n_\uparrow+1, n_\downarrow}^{*(p,q)} \right. \\ & \left. + \mathcal{C}_2 \sqrt{n_\downarrow + 1} c_{n_\uparrow, n_\downarrow+1}^{*(p,q)} + \mathcal{C}_5 c_{n_\uparrow n_\downarrow}^{*(p,q)} \right], \end{aligned} \quad (4.8)$$

where coupling is through $\mathcal{C}_1, \mathcal{C}_2, \dots, \mathcal{C}_5$. To solve these coupled equations, we use the fourth-order Runge-Kutta method to compute the wave function of the system at a specific time instant t , where the requisite Gutzwiller coefficients at the start of quench are obtained from the static Gutzwiller approach. However, to derive the QPT, quantum fluctuations are needed. To generate the effects of quantum fluctuations, we add an initial random noise to the equilibrium coefficients $c_{n_\uparrow n_\downarrow}^{(p,q)}$ of the state at the start of the quench. We first generate univariate random phases within the range of $[0, 2\pi]$ and add them to the (phases of) non-zero coefficients. Next, we add density fluctuations by applying noise to the amplitudes of the coefficients. This is achieved by generating univariate random numbers within the range of $[0, \delta]$, where δ is set to be 10^{-4} in this chapter. To ensure reliable results, we consider 10 initial states that are randomized using the methods described previously. Each of these initial states is then evolved in time by performing the appropriate parameter quench. We further calculate the physical observables of interest averaged over all these 10 samples. Additionally, for each sample, the observable is averaged across the entire lattice.

4.2.2 Kibble-Zurek mechanism

In this thesis, we consider a linear quench protocol given as

$$J(t) = J_i + \frac{(J_c - J_i)}{\tau_Q}(t + \tau_Q). \quad t \in [-\tau_Q, t], \quad (4.9)$$

which involves a quench time τ_Q to determine the quench rate. The critical value of J , denoted by J_c , is crossed at $t = 0$. It is assumed that the quench is initiated at time $t = -\tau_Q$ such that $J(-\tau_Q) = J_i$. The system's relaxation time determines the fate of the evolving state.

The relaxation time is short when the quenched parameter is far from the critical point. This results in an adiabatic evolution where the evolving state is close to the actual ground state. However, as the critical point is approached, the divergence of relaxation time breaks the adiabaticity, leading to a frozen state. This state does not change for some time near the critical point. The time interval during which the state remains frozen is termed the impulse regime. It starts evolving after a time instant \hat{t} that is delayed time or transition time after which evolution is again adiabatic. Thus, the two adiabatic regimes are separated by a non-adiabatic regime near the critical point. The transition between these regimes is a significant aspect of the KZM. The non-adiabatic evolution of the system during the quench inevitably leads to excitations and defects in the evolved state.

In the Kibble-Zurek hypothesis, for a second-order phase transition, the scaling relation between the quench time τ_Q and the transition time \hat{t} is defined by $\hat{t} \propto \tau_Q^{\nu z/(1+\nu z)}$, where ν is the critical exponent of the equilibrium correlation length and z is the dynamical critical exponent. Additionally, the scaling relation between the density of defects (N_d) and τ_Q in two dimensions is given by $N_d(\hat{t}) \propto \tau_Q^{-2\nu/(1+\nu z)}$. These relations predict the critical behavior of the system near the phase transition and the formation of topological defects during the non-adiabatic evolution of the system. In our case, i.e. during the transition from the MI to SF phase, the global $U(1)$ symmetry spontaneously breaks and gives rise to the vortices. The density of vortices in an optical lattice system can be computed as [216–218, 221]

$$N_v^\alpha = \sum_{p,q} |\Omega_{p,q}^\alpha|, \quad (4.10)$$

with

$$\begin{aligned} \Omega_{p,q}^\alpha = & \frac{1}{4} \left[\sin(\theta_{p+1,q}^\alpha - \theta_{p,q}^\alpha) + \sin(\theta_{p+1,q+1}^\alpha - \theta_{p+1,q}^\alpha) \right. \\ & \left. - \sin(\theta_{p+1,q+1}^\alpha - \theta_{p,q+1}^\alpha) - \sin(\theta_{p,q+1}^\alpha - \theta_{p,q}^\alpha) \right]. \end{aligned} \quad (4.11)$$

Here $\theta_{p,q}^\alpha$ is the phase of the SF order parameter $\phi_{p,q}^\alpha$. Another quantity that serves as an analogue

to the defect density is the excess energy above the ground state. This quantity is termed residual energy [236–238]. This residual energy E_{res} is given by $E_{\text{res}}(\hat{t}) = E_{\text{fin}}(\hat{t}) - E_{\text{gs}}(\hat{t})$, where $E_{\text{fin}}(\hat{t}) = \langle \Psi(\hat{t}) | \hat{H}(\hat{t}) | \Psi(\hat{t}) \rangle$ denotes the energy of the system at time t , while $E_{\text{gs}}(\hat{t}) = \langle \Psi_{\text{gs}} | \hat{H}(\hat{t}) | \Psi_{\text{gs}} \rangle$ is the ground-state energy for Hamiltonian at time \hat{t} . Slower is the evolution, smaller is the residual energy. The scaling relation for the residual energy is $E_{\text{res}}(\hat{t}) \propto -\tau_Q^{2\nu/(1+\nu z)}$ [236–238]. The scaling relations are valid at \hat{t} , but it is very difficult to estimate \hat{t} from the numerical simulations. Prior works are based on determining \hat{t} based on Φ [216–220]. The growth time of the superfluid order parameter depends on the amount of random fluctuations as pointed out in Ref. [239]. We choose the protocol of Ref. [221] to determine \hat{t} . We calculate the overlap $O(t) = |\langle \Psi(0) | \Psi(t) \rangle|$. Since the dynamics are frozen in the impulse regime, $O(t)$ would be equal to unity until the state is in the impulse regime, as soon as it deviates from unity, it indicates that the adiabatic regime has begun and that time instant is \hat{t} . The observables Φ , N_v^α , E_{res} , and $O(t)$ relevant to the quench dynamics are obtained by averaging over 10 initial states perturbed by different random noise distributions.

4.3 Results and discussion

4.3.1 $U_{\uparrow\downarrow} = 0.5$

4.3.1.1 MI(2) to SF phase transition

Considering $\mu = 1$, we start a quench of the hopping parameter from $J_i = 0.02$ that lies deep within the MI lobe. We end the quench at $J_f = 0.064$ within the SF phase. We confirm the slowing down of transition from the growth of the superfluid order parameter that starts after the critical value J_c is passed. We have shown one such dynamics for $\tau_Q = 100$ in Fig. 4.3. $|\Phi|$ is close to zero until J passes the critical J_c at $t = 0$. After $t = \hat{t} = 31$, $|\Phi|$ shows a sudden increase followed by rapid oscillations. Quench is stopped at $t = \tau_Q = 100$. At a longer time, the $|\Phi|$ stabilizes after small oscillatory transients. For illustration, the stable $|\Phi|$ is marked at $t = 160$ in Fig. 4.3. Due to the random noise added to the initial Gutzwiller coefficients, there are many vortices at the beginning of the quench. During the MI to SF phase transition, when the system enters the SF phase, one expects a coherent phase throughout the system. This is due to the breaking of $U(1)$ global gauge symmetry. However, the quench dynamics leads to

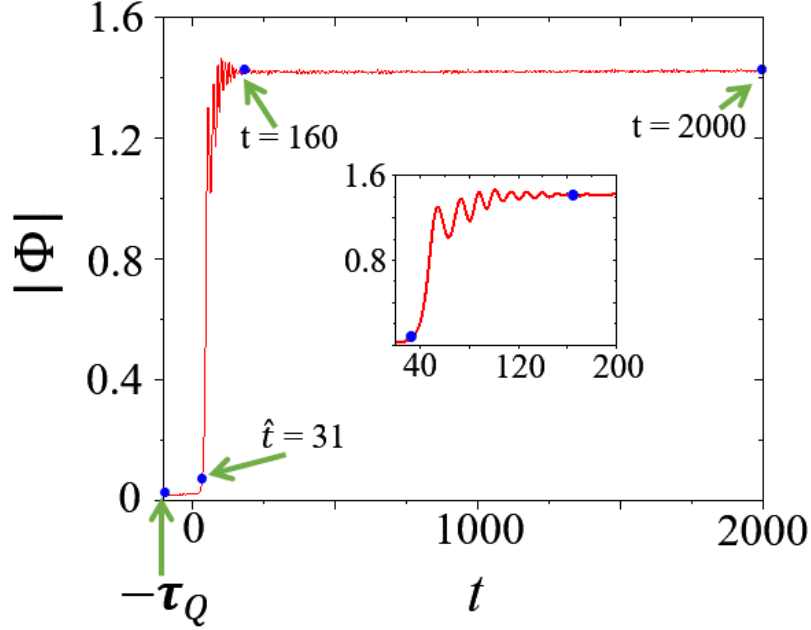


Figure 4.3: The time evolution of $|\Phi|$ for the MI(2)-SF transition with $U_{\uparrow\downarrow} = 0.5$, $\mu = 1$, and $\tau_Q = 100$. Blue points indicate temporal markers referred to in the main text. In the inset, we show the enlarged view of the dynamical evolution at shorter times from $t = 20$ to $t = 200$. $|\Phi|$ is nearly zero for $t < \hat{t} = 31$.

the formation of domains in the system which indicates the existence of local choices of broken symmetry in the SF phase. This results in a domain structure as predicted by the KZM. The phase singularities at the domain boundaries correspond to the vortices, as confirmed by the phase variations. As the system enters into the deep SF phase, the size of domains increases through domain merging. This results in a decrease in the number of topological defects due to pair annihilation, and the system attains phase coherence after long-time evolution.

To illustrate the domain formation and merging in the quench dynamics starting with a single randomized initial state at $t = -\tau_Q = -100$, we have presented the snapshots of $|\phi_{p,q}^\alpha(t)|$ and the respective phases at various times. At the beginning of the quench the $|\phi_{p,q}^\uparrow|$ and $|\phi_{p,q}^\downarrow|$ have random lattice-site distributions with peak values nearly zero as shown in Figs. 4.4(a) and 4.4(e), respectively. The phases of the order parameters for both components are also random, as shown in Figs. 4.4(i) and 4.4(m), respectively. As time evolves, at $t = \hat{t} = 31$, $|\phi_{p,q}^\uparrow|$ and $|\phi_{p,q}^\downarrow|$ acquire relatively large peak values accompanied by domain formation. This is presented in Figs. 4.4(b) and 4.4(f); the corresponding phases are illustrated in Figs. 4.4(j) and 4.4(n). The hopping parameter quenching is stopped at $t = 100$ as stated earlier. At $t = 160$, $|\phi_{p,q}^\uparrow|$ and $|\phi_{p,q}^\downarrow|$

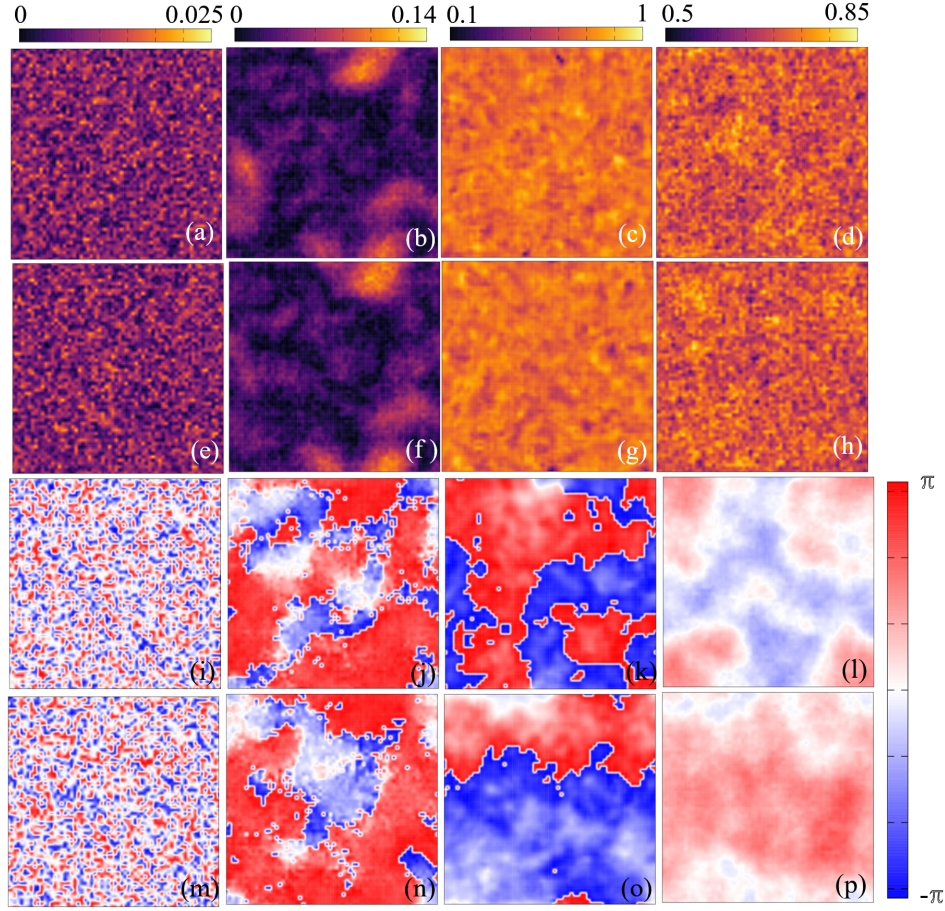


Figure 4.4: $|\phi_{p,q}^{\uparrow}|$ at (a) $t = -100$, (b) $t = 31$, (c) $t = 160$, and (d) $t = 2000$ for the MI(2)-SF phase transitions corresponding to the time evolution in Fig. 4.3. Similarly, $|\phi_{p,q}^{\downarrow}|$ at the same instants are in panels (e)-(h). Phases corresponding to $|\phi_{p,q}^{\uparrow}|$ in panels (a)-(d) are shown in panels (i)-(l), and the same for $|\phi_{p,q}^{\downarrow}|$ in panels (e)-(h) are in panels (m)-(p).

acquire almost uniform distributions as shown in Figs. 4.4(c) and 4.4(g), and their respective phases 4.4(k) and 4.4(o) still have phase singularities. After a very long time of evolution at $t = 2000$, the system relaxes into an almost uniform state where the component densities and phases are quasi-uniform as in Figs. 4.4(d) and 4.4(h); and Figs 4.4(l) and 4.4(p), respectively.

To study the scaling laws, we consider a range of quench times from $\tau_Q = 30$ to $\tau_Q = 400$. We measured \hat{t} corresponding to each τ_Q following the overlap protocol. \hat{t} increases with an increase in τ_Q as is evident in Fig. 4.5(a). On the other hand, the residual energy E_{res} decreases with τ_Q as reported in Fig. 4.5(b) as $J(\hat{t})$ approaches the critical tunneling strength J_c with an increasing τ_Q , [cf. Table-4.1]. Both observables follow power-law scaling with the critical exponents $\nu = 0.45$ and $z = 2.13$. It is pertinent to note that the critical values obtained in our

scaling analysis are in very close agreement with the values predicted by the mean-field theory ($\nu = 0.5$ and $z = 2$).

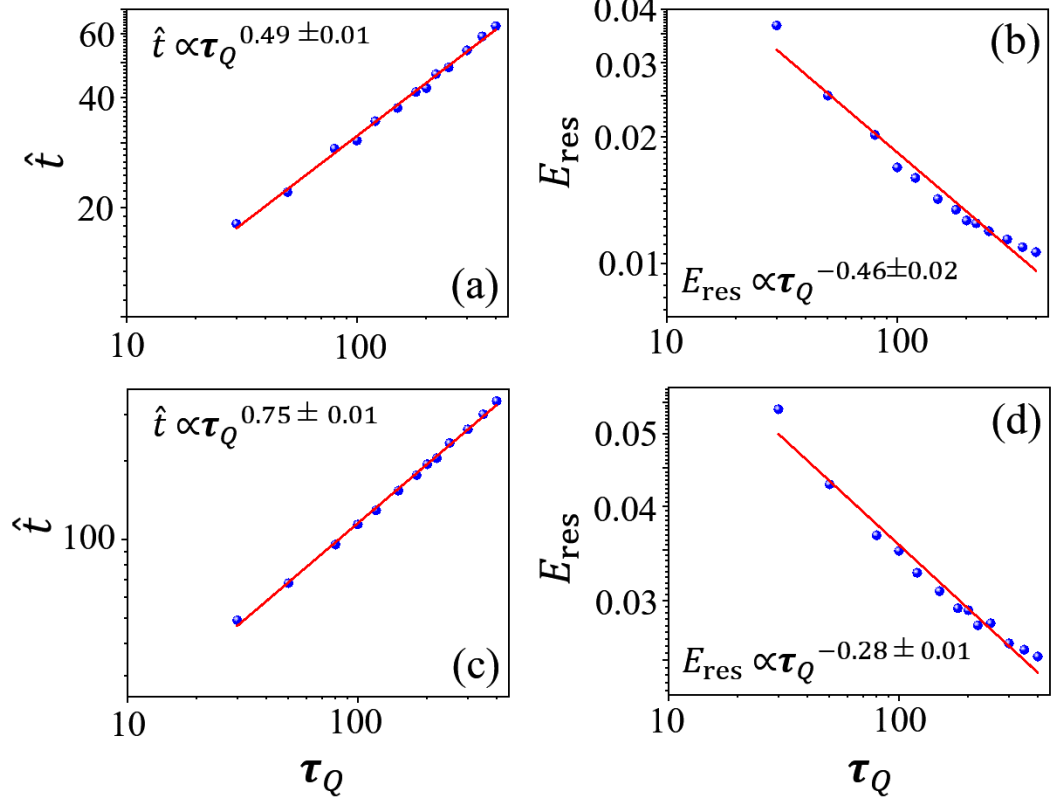


Figure 4.5: For the MI(2)-SF transition with $U_{\uparrow\downarrow} = 0.5$: (a) \hat{t} as a function of τ_Q on a log-log scale with the critical exponent of 0.49 ± 0.01 and (b) E_{res} as a function of τ_Q on the log-log scale with -0.46 ± 0.02 as the critical exponent. (c) and (d) are, similarly, the \hat{t} and E_{res} as functions of τ_Q on the log-log scale for MI(1)-SF transition with $U_{\uparrow\downarrow} = 0.5$.

Table 4.1: The $J(\hat{t})$ for different τ_Q s during quench dynamics from MI(2) to SF phase with $\mu = 1$ and $U_{\uparrow\downarrow} = 0.5$. The critical value of hopping strength J_c is 0.042.

τ_Q	30	50	80	100	150	200	300	400
$J(\hat{t})$	0.055	0.052	0.050	0.049	0.048	0.047	0.046	0.045

4.3.1.2 MI(1) to SF phase transition

The key difference between MI(2) and MI(1) of the TBHM is the density inhomogeneity as shown in the equilibrium lattice-site distributions [see Figs. 4.1(e)-(h)]. This results in a number of differences in the quench dynamics. One is that the impulse regime size increases compared to MI(2)-SF transition for each τ_Q . This is supported by the fact that, for MI(2)-SF transition,

$J(\hat{t})$ always lies between J_c to $2J_c - J_i$, but here it is not the case. Fixing μ at 0.25, we quench J from $J_i = 0.01$ to a sufficiently high hopping strength $J_f = 0.0604$, so that $J(\hat{t})$ lies in between J_i and J_f . The critical value J_c of MI(1)-SF transition is 0.0268. For smaller τ_Q up to about $\tau_Q = 150$, $J(\hat{t})$ is greater than $2J_c - J_i = 0.0436$. Even for the largest value of $\tau_Q = 400$ considered in this chapter, $J(\hat{t})$ is 0.041 as reported in Table 4.2.

Table 4.2: The $J(\hat{t})$ for different τ_Q 's during the quench dynamics from MI(1) to SF phase with $\mu = 0.25$ and $U_{\uparrow\downarrow} = 0.5$. The critical hopping strength is $J_c = 0.0268$.

τ_Q	30	50	80	100	150	200	300	400
$J(\hat{t})$	0.054	0.05	0.047	0.046	0.044	0.043	0.042	0.041

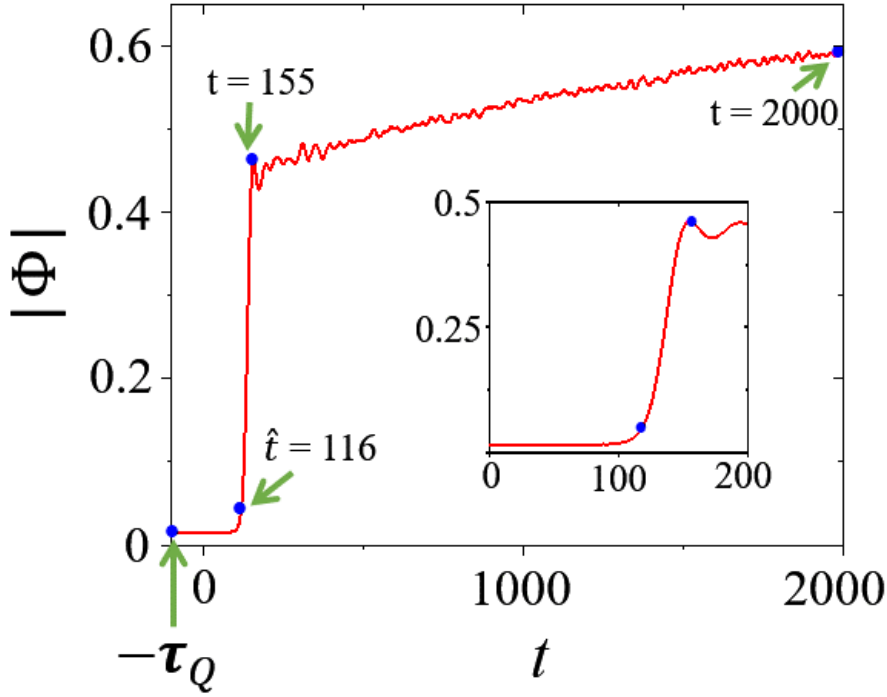


Figure 4.6: $|\Phi|$ as a function of time t for the MI(1)-SF transitions at $U_{\uparrow\downarrow} = 0.5$, $\mu = 0.25$, and $\tau_Q = 100$. Blue points are the temporal markers referred to in the main text. $|\Phi|$ remains nearly zero for $t < \hat{t} = 116$. The hopping quench is performed until $t = 130$. The exponential increase in $|\Phi|$ followed by oscillations are shown in the inset with t varying from $t = 0$ to $t = 200$.

Another difference is that due to the absence of particles of at least one species at each lattice site, vortex density does not give a fair idea about the actual number of vortices. Due to the increase in transition time compared to the MI(2)-SF case, the exponent of transition time with τ_Q is higher, whereas the exponent of residual energy is lower. However, transition time and

residual energy still follow power-law scaling with τ_Q as shown in Figs. 4.5(c) and 4.5(d).

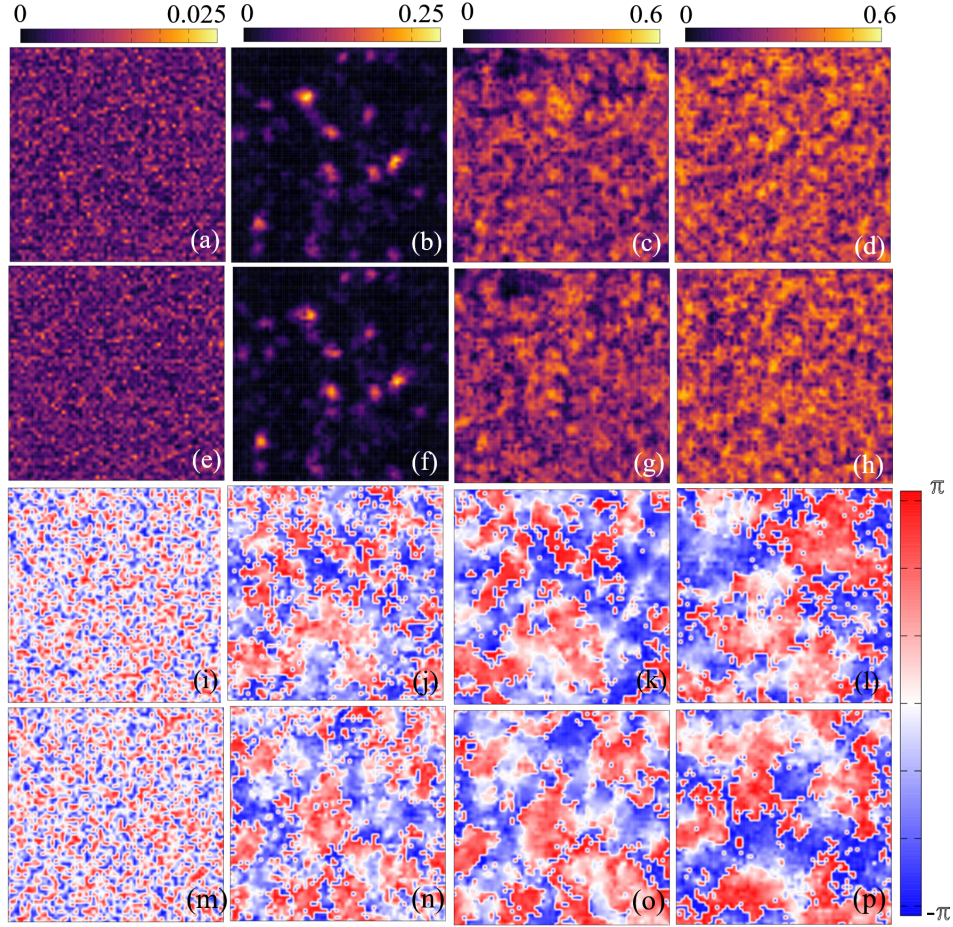


Figure 4.7: $|\phi_{p,q}^\uparrow|$ at (a) $t = -100$, (b) $t = 116$, (c) $t = 155$, and (d) $t = 2000$ for the MI(1)-SF phase transitions corresponding to the time evolution in Fig. 4.6. Similarly, $|\phi_{p,q}^\downarrow|$ at the same instants are in panels (e)-(h). Phases corresponding to $|\phi_{p,q}^\uparrow|$ in panels (a)-(d) are shown in panels (i)-(l), and the same for $|\phi_{p,q}^\downarrow|$ in panels (e)-(h) are in panels (m)-(p).

We have shown the evolution of the superfluid order parameter for $\tau_Q = 100$ in Fig. 4.6. Quench is stopped at $t = 130$ in this case. $|\Phi|$ is close to zero till $t = \hat{t} = 116$, after which it increases rapidly followed by oscillations persisting over long periods during which it increases gradually. This is in stark contrast to the MI(2)-SF transition, where the order parameter stabilizes over a longer time. To see how differently the state relaxes after the quench, we provide snapshots of the amplitude and corresponding phases of $\phi_{p,q}^\alpha$ at various time instants in Fig. 4.7. Randomized $|\phi_{p,q}^\uparrow|$, $|\phi_{p,q}^\downarrow|$ and the corresponding phases at the start of the quench at $t = -100$ are shown in Figs. 4.7(a), 4.7(e), 4.7(i), and 4.7(m), respectively. Next at

$t = \hat{t} = 116$, these quantities are shown in the second column of Fig. 4.7, where a few superfluid domains have started to appear. The number of superfluid domains has increased, and phases of the order parameters also exhibit domain formation in the third column at $t = 155$; this is when oscillations in $|\Phi|$ are triggered. Even after a long period of evolution at $t = 2000$, the $\phi_{p,q}^\alpha$ do not achieve homogeneous distributions, unlike for MI(2)-SF transition.

4.3.2 $U_{\uparrow\downarrow} = 0.9$

We further discuss quench dynamics at higher interspecies interaction strength close to the immiscibility criterion but still in the miscible domain. The phase transition for $\mu = 1.33$ is first order in nature as compared to the MI(2)-SF and MI(1)-SF for $U_{\uparrow\downarrow} = 0.5$. Although some traits of second-order MI(2)-SF transition, discussed in Sec. 4.3.1.1 like slowing down of the transition, oscillations of $|\Phi|$ about a fixed value, order parameter relaxing into an almost complete uniform state after free evolution, and power law scaling of \hat{t} and E_{res} with τ_Q are present, the striking difference appears in the exponents in Fig. 4.8.

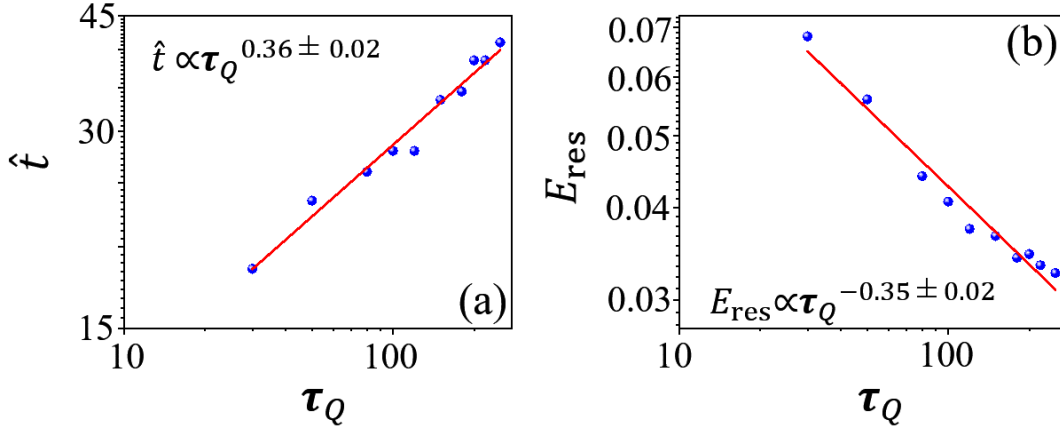


Figure 4.8: For the first-order MI(2)-SF phase transition at $U_{\uparrow\downarrow} = 0.9$ and $\mu = 1.33$: (a) \hat{t} as a function of τ_Q with the critical exponent of 0.36 ± 0.02 and (b) E_{res} as a function of τ_Q on log-log scale with -0.35 ± 0.02 as the critical exponent.

The quench dynamics and the exponents in the scaling laws of the second-order MI(1)-SF transition for $U_{\uparrow\downarrow} = 0.9$ remain almost similar to the MI(1)-SF transition for $U_{\uparrow\downarrow} = 0.5$ as discussed in Sec. 4.3.1.2 and are not shown here for brevity.

4.3.3 $U_{\uparrow\downarrow} = 1.5$

Finally, we discuss quench dynamics for the phase-separated regime, where one of the two components occupies the lattice site. Starting from $\mu = 1.45$ and $J = 0$ which corresponds to

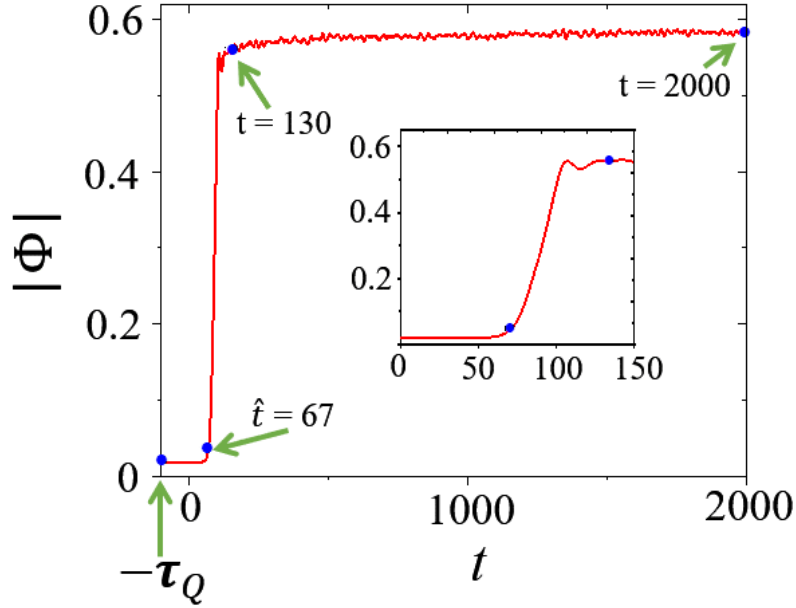


Figure 4.9: The evolution of $|\Phi|$ with t for the MI(2)-SF transitions at $U_{\uparrow\downarrow} = 1.5$, $\mu = 1.45$, and $\tau_Q = 100$. Blue points indicate the temporal markers referred to in the main text. $|\Phi|$ is close to zero until $\hat{t} = 67$. The exponential increase in $|\Phi|$ followed by oscillations are shown in the inset with t varying from $t = 0$ to $t = 150$.

the MI(2) lobe, we perform a quench that terminates at $J = 0.0516$, lying well within the SF phase. The transition is indicated by the growth of the superfluid order parameter and occurs after crossing the critical $J_c = 0.0258$, as demonstrated in Fig. 4.9 for $\tau_Q = 100$. $|\Phi|$ remains close to zero until $t = \hat{t} = 67$, followed by a rapid increase period. The quench is halted at $t = \tau_Q = 100$, but we freely evolve the system up to $t = 2000$ to confirm the ground state of the system. Figs. 4.10(a)-(p) provide snapshots of $|\phi_{p,q}^\alpha|$ and the corresponding phase of $\phi_{p,q}^\alpha$ at different times. At $t = \hat{t} = 67$, domain formation begins as indicated in Figs. 4.10(b) and 4.10(f); the respective phases are shown in Figs. 4.10(j) and 4.10(n). At $t = 130$, both $|\phi_{p,q}^\uparrow|$ and $|\phi_{p,q}^\downarrow|$ have acquired many domains, as indicated in Figs. 4.10(c) and 4.10(g), while the respective phases in Figs. 4.10(k) and 4.10(o) start exhibiting domain merging. The component

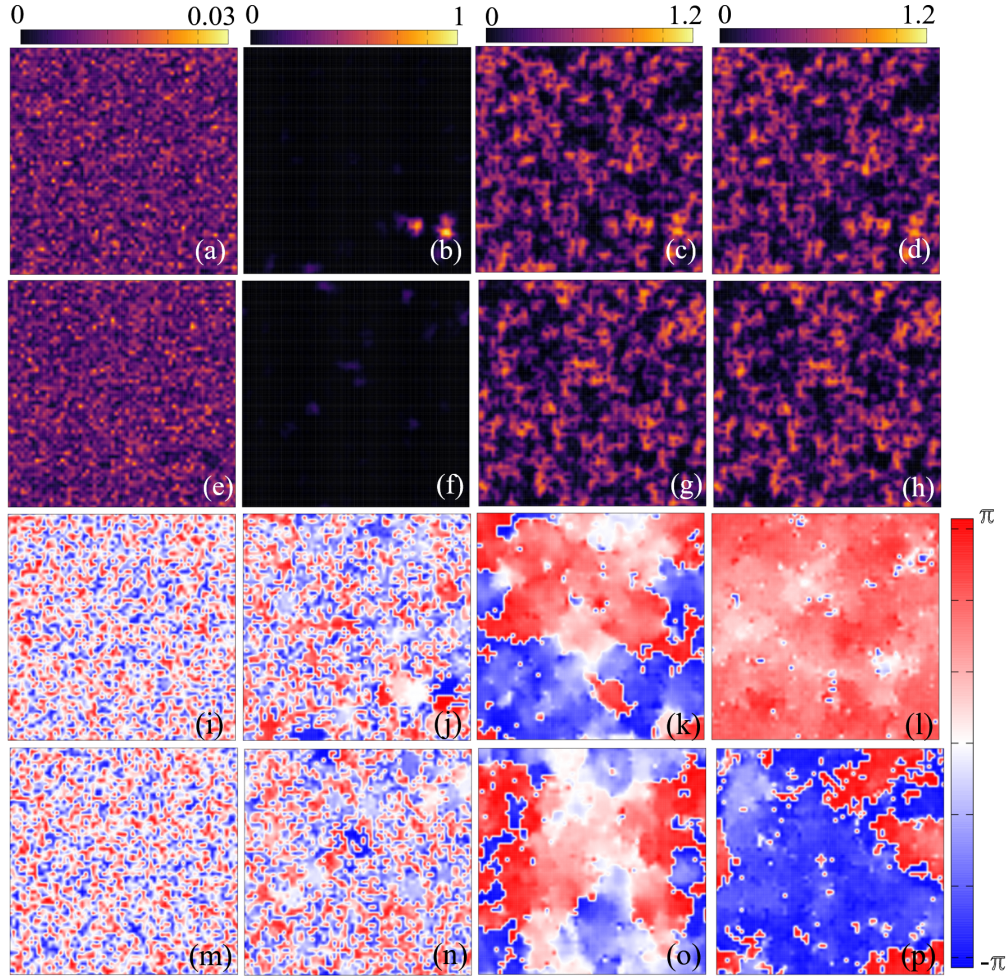


Figure 4.10: $|\phi_{p,q}^{\uparrow}|$ at (a) $t = -100$, (b) $t = 67$, (c) $t = 130$, and (d) $t = 2000$ for MI(2)-SF phase transitions corresponding to the time evolution in Fig. 4.9. Similarly, $|\phi_{p,q}^{\downarrow}|$ at the same instants are in panels (e)-(h). Phases corresponding to $|\phi_{p,q}^{\uparrow}|$ in panels (a)-(d) are shown in panels (i)-(l), and the same for $|\phi_{p,q}^{\downarrow}|$ in panels (e)-(h) are in panels (m)-(p).

order parameters at $t = 2000$ show no discernible difference from those at $t = 130$, as shown in Figs. 4.10(d) and 4.10(h).

Similar to the dynamics at the other two $U_{\uparrow\downarrow}$ values discussed previously, \hat{t} and E_{res} follow power-law scaling as shown in Figs. 4.11(a)-(b) and with the critical exponents similar to those for the MI(1)-SF transition in the miscible domain. This is evident from Figs. 4.5(c)-(d) and Figs. 4.11(a)-(b). Since the system is in the immiscible phase, the nature of MI(1) and MI(2) is similar. This was concluded while studying the static properties of these systems. The quench dynamics of MI(1)-SF for $U_{\uparrow\downarrow} = 1.5$ is similar to that of MI(2)-SF transition and therefore not presented here.

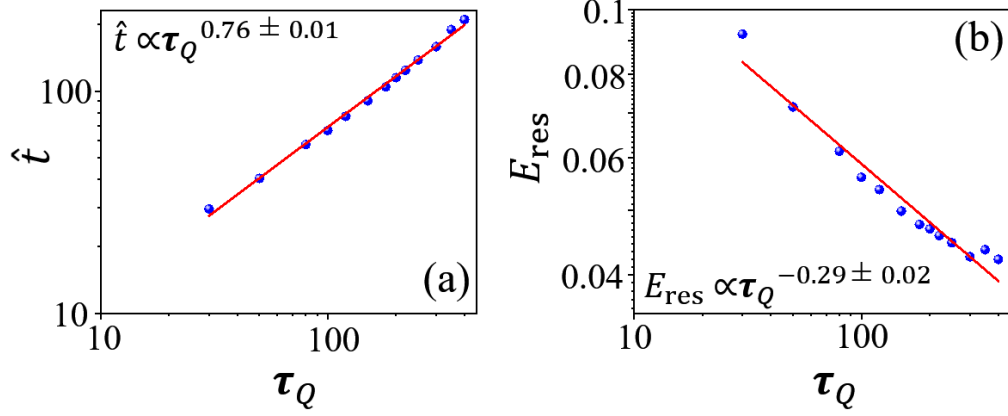


Figure 4.11: For MI(2)-SF phase transition at $U_{\uparrow\downarrow} = 1.5$: (a) \hat{t} as a function of τ_Q with the critical exponent of 0.76 ± 0.01 and (b) E_{res} as a function of τ_Q on log-log scale with -0.29 ± 0.01 as the critical exponents. The critical exponents are similar to those displayed in Figs. 4.5(c)-(d).

4.4 Conclusions

We have studied the out-of-equilibrium dynamics of the TBHM when the tunnelling strength J is quenched across the MI-SF criticality. The equilibrium phase diagram and related phase transitions depend on interspecies interaction strength. We observed that the average filling of the MI lobes and the order of the phase transitions lead to different dynamics from what is observed in a single-component BHM. The MI-SF phase transitions, in the miscible regime, from the Mott lobes with an average occupancy of 1 or 2 are of second order for $U_{\uparrow\downarrow}$ less than a critical strength above which the transitions at and around the tip of the MI(2) lobe are first order. The critical exponents of the second-order phase transition from homogeneous MI to superfluid phase, calculated using scaling analysis, are in good agreement with the mean-field predictions. Due to the inhomogeneity of the atomic occupancy in MI(1), the impulse regime is extended across MI(1)-SF phase transition at $U_{\uparrow\downarrow} = 0.5$. In the immiscible regime, the power-law scaling of the exponents is maintained with exponents similar to those for MI(1)-SF phase transition in the miscible regime. Although the KZM is not suitable for the first-order quantum phase transition, defining scaling relations is possible. However, the nature of the dynamical evolution is very different. We hope the phenomena discussed in this chapter can be realized in cold-atom experiments on strongly correlated bosonic mixtures in optical lattices. Our study serves as a route to understand the dynamics of QPTs in SO-coupled condensates in optical lattices. The exploration in this direction may unveil the role of coupling in quantum mixtures

and the applicability of the KZM to two-component Bose-Hubbard models. The results reported in this chapter are discussed in Ref. [\[240\]](#).

Chapter 5

Summary and future outlook

5.1 Thesis summary

In summary, we have investigated the self-trapped, stable solitons, and their crystalline structure in a quasi-2D spin-2 BEC under the influence of SOC. By employing a combination of analytical insights and numerical solutions of the CGPEs, our research has shed light on the certain aspects of bright solitons. The minimization of interaction and SOC energies demonstrated the permissible winding number combinations for the emergence of axisymmetric solitons. In the absence of interactions, the order parameter constructed from the eigenfunctions of the single-particle Hamiltonian corresponds to various periodic density profiles, including multiring, stripe, triangular-, and square-lattice patterns. In the presence of attractive interactions, the study has revealed the formation of different bright solitons with spatially periodic density modulations. The ground-state phase diagram of the system depends on the strength of SOC. For a weak SOC strength, ground state is a radially symmetric multiring soliton for certain interaction parameters, while sufficiently strong ferromagnetic interactions lead to circularly asymmetric solitons. At intermediate SOC strengths, a triangular-lattice soliton featuring hexagonal crystallization in both component and total densities can also emerge. Further increase in the SOC strength gives rise to multiple quasidegenerate solitons. We have also introduced a Galilean-transformed model to study the moving solitons and their collision dynamics. Depending on the velocities involved, collisions between two solitons can be either inelastic, resulting in the formation of a bound entity, or quasi-elastic, where the solitons pass through each other. We have also considered two

special cases of nonmagnetic spin-1 and spin-2 condensates by considering the spin-dependent interactions as zero. Our studies on the nonmagnetic systems suggest that the spatially periodic supersolid-like states observed in spinor BECs are a consequence of SOC rather than being solely driven by spinor interactions.

Next, we have explored the parameter space for the various finite-momentum superfluids of an SO-coupled two-component spinor BEC confined by a 2D optical lattice. We employed spin-dependent momentum distributions to examine the diverse superfluid phases characterized by different atomic densities and phase ordering. Notably, when $U_{\uparrow\downarrow} < U$ and $\gamma/J \gtrsim 1$, the favored superfluid phase is the PT phase. Conversely, when $\gamma/J \lesssim 1$, the system transitions to the ST superfluid phase. Commencing with the PT phase in a numerical simulation, we have demonstrated that increasing the tunnelling parameter induces a transition from the PT to the ST phase. We have shown that the inclusion of the quantum fluctuations via the CGA can lead to the ST_{den} phase instead of the ST phase obtained with the SGMF theory. In cases where $U_{\uparrow\downarrow} > U$, the ST superfluid phase is absent, and the study reveals a transition from the PT phase to the $z\text{FM}$ phase as J is varied. We also studied the influence of thermal fluctuations on the superfluid behavior. These fluctuations diminish the PT superfluidity, while favoring the insulating and normal states.

Finally, we have explored the dynamics of the TBHM, focusing on the MI-SF transitions. The equilibrium phase diagram and the associated phase transitions in the TBHM are strongly influenced by $U_{\uparrow\downarrow}$. In the miscible regime, where MI lobes have an average occupancy of 1 or 2, the MI-SF phase transitions exhibit second-order behavior when the interspecies interaction strength $U_{\uparrow\downarrow}$ is below a critical threshold. Beyond this threshold, transitions at and around the tip of the MI(2) lobe become first-order. Unlike the dynamics observed in the single-component BHM, the average filling of the MI regions and the order of phase transitions introduce different features in the TBHM dynamics. The calculated critical exponents for the second-order transition from a homogeneous MI to the superfluid phase, based on the scaling analysis, align closely with the mean-field predictions. Due to the non-uniform atomic occupancy in the MI(1) lobe, the impulse regime extends across the MI(1)-SF phase transition when $U_{\uparrow\downarrow} = 0.5$. In the immiscible regime, the power-law scaling of the exponents is similar to those observed for the MI(1)-SF phase transition in the miscible regime. Although the KZM may not be directly applicable to the first-order quantum phase transitions, defining scaling relations remains feasible.

However, the dynamics under first-order transitions differ significantly from the second-order transitions.

5.2 Future directions

The studies on the SO-coupled spinor condensates can be extended in various directions. One immediate extension is to employ the Bogoliubov theory and calculate the collective excitation spectrum by solving the Bogoliubov-de Gennes equations to study the stability of various self-trapped structures discussed in Chapter 2. The low-lying modes will give a good understanding of the stability of these q2D solitons, besides providing valuable information about the supersolid character of these structures. Experiments commonly study the low-energy Goldstone mode as well as its oscillations etc., to classify the system as a supersolid. Attractive BECs can host two types of macroscopic self-bound states of different nature: bright solitons and quantum liquid droplets. Bright solitons and quantum droplets are a priori distinct states which can exist in different parameter space within the same system with the possibility of crossover between them [241]. Since, we have studied bright solitons in this thesis, it would be interesting to examine an SO-coupled system that can host both bright solitons as well as quantum droplets. An SO-coupled pseudospin-1/2 system with beyond mean-field corrections could be a potential candidate for the same [241].

In Chapter 3, we investigated the phase diagrams of a SO-coupled pseudospinor BEC in a 2D optical lattice. It would be interesting to study these phase diagrams using cluster Gutzwiller mean-field methods to account for the fluctuations. These studies can also be extended to other lattice geometries like triangular and hexagonal optical lattices. Another possible direction could be to study an SO-coupled spin-1 system in an optical lattice and study various possible superfluids and the underlying quantum phase transitions. Our studies on the quantum quench dynamics of the MI-SF transition as discussed in Chapter 4 can be extended to study the quench dynamics across the phases that occur in the presence of SOC. Moreover, one can study, in general, the dynamics of first-order quantum phase transitions in view of the Kibble-Zurek-like mechanism. One can also use beyond mean-field methods, such as the projection operator method [242], to study the quench dynamics and related scaling relations. Cluster Gutzwiller mean-field approach can also be used which enhances the inter-site atomic correlations and may

further advance the critical exponents towards the equilibrium values [243].

Appendix A

Coupled Gross-Pitaevskii equations for an SO-coupled spin-1 BEC

The single-particle Hamiltonian of a spin-1 BEC in the presence of anisotropic [52, 244] SOC is given by [80, 150]

$$H_0 = \frac{p_x^2 + p_y^2 + p_z^2}{2m} + \gamma_x p_x f_x + \gamma_y p_y f_y + \gamma_z p_z f_z, \quad (\text{A.1})$$

where $p_x = -i\hbar\partial/\partial x$, $p_y = -i\hbar\partial/\partial y$, and $p_z = -i\hbar\partial/\partial z$ correspond to the momentum operators along x , y , and z directions, respectively, and γ_x , γ_y , and γ_z are the strengths of SOC. Also, m is the mass of each atom and f_x , f_y , and f_z are the irreducible matrix representations of the x , y , and z components of the spin-1 angular momentum operators, respectively, as given in Eqs. (1.17a)-(1.17c) for $f = 1$. In a standard isotropic SOC, $\gamma_x = \gamma_y = \gamma_z = \hbar k_r/m$ is realized by using two counterpropagating Raman lasers of wavelength λ_r aligned at an angle β_r and k_r is given by $k_r = (2\pi \sin \beta_r/2)/\lambda_r$.

For a weakly interacting SO-coupled spin-1 BEC, the properties of the system are well described under mean-field approximation by the following coupled Gross-Pitaevskii equations

(CGPEs) [40, 80, 245, 246]

$$i\hbar \frac{\partial \psi_{\pm 1}}{\partial t} = [\mathcal{H} + c_1(\rho_0 \pm \rho_{-})]\psi_{\pm 1} + c_1\psi_{\mp 1}^*\psi_0^2 - \frac{i\hbar}{\sqrt{2}} \left(\gamma_x \frac{\partial \psi_0}{\partial x} \mp i\gamma_y \frac{\partial \psi_0}{\partial y} \pm \sqrt{2}\gamma_z \frac{\partial \psi_{\pm 1}}{\partial z} \right), \quad (\text{A.2a})$$

$$i\hbar \frac{\partial \psi_0}{\partial t} = (\mathcal{H} + c_1\rho_+)\psi_0 + 2c_1\psi_{+1}\psi_{-1}\psi_0^* - \frac{i\hbar}{\sqrt{2}} \left[\gamma_x \left(\frac{\partial \psi_{+1}}{\partial x} + \frac{\partial \psi_{-1}}{\partial x} \right) + i\gamma_y \left(\frac{\partial \psi_{+1}}{\partial y} - \frac{\partial \psi_{-1}}{\partial y} \right) \right], \quad (\text{A.2b})$$

where

$$\mathcal{H} = \left(-\frac{\hbar^2}{2m} \nabla^2 + V(\mathbf{r}) + c_0\rho \right), \quad \mathbf{r} = (x, y, z), \quad (\text{A.3})$$

and $\Psi = (\psi_{+1}(\mathbf{r}, t), \psi_0(\mathbf{r}, t), \psi_{-1}(\mathbf{r}, t))^T$ with ψ_{+1} , ψ_0 , and ψ_{-1} as the component wave functions, and $V(\mathbf{r}) = m(\omega_x^2 x^2 + \omega_y^2 y^2 + \omega_z^2 z^2)/2$ is a 3D harmonic trap. Also,

$$c_0 = \frac{4\pi\hbar^2(a_0 + 2a_2)}{3m}, \quad c_1 = \frac{4\pi\hbar^2(a_2 - a_0)}{3m}, \quad \nabla^2 = \frac{\partial^2}{\partial x^2} + \frac{\partial^2}{\partial y^2} + \frac{\partial^2}{\partial z^2}, \quad (\text{A.4})$$

where a_0 and a_2 correspond to the s -wave scattering lengths in total spin 0 and 2 channels, respectively; ω_x , ω_y , and ω_z are the confining trap frequencies along x , y , and z directions, respectively; $\rho_{\pm} = \rho_{+1} \pm \rho_{-1}$ where $\rho_j = |\psi_j|^2$ with $j = +1, 0, -1$ are the component densities and $\rho = \sum_{j=-1}^1 |\psi_j|^2$ is the total density.

A.1 Important conserved quantities of a spin-1 BEC

Three important conserved quantities of a spin-1 BEC are the total number of particles N , longitudinal magnetization M (which is conserved on the time scale of spin-1 BEC experiments), and total energy E . These are given as

$$N = \int_{-\infty}^{\infty} d\mathbf{r} \sum_{j=-1}^1 |\psi_j(\mathbf{r})|^2, \quad (\text{A.5a})$$

$$M = \sum_{j=-1}^1 \int j |\psi_j(\mathbf{r}, t)|^2 d\mathbf{r}, \quad (\text{A.5b})$$

$$\begin{aligned}
E = \int d\mathbf{r} & \left[\sum_{j=-1}^1 \psi_j^* \left(-\frac{\hbar^2 \nabla^2}{2m} + V \right) \psi_j + \frac{c_0}{2} \rho^2 + \frac{c_1}{2} (\rho_{+1} + \rho_0 - \rho_{-1}) \rho_{+1} + \frac{c_1}{2} (\rho_0 + \rho_{-1} - \rho_{+1}) \rho_{-1} \right. \\
& + c_1 (\psi_{-1}^* \psi_0^2 \psi_{+1}^* + \psi_{-1} \psi_0^{2*} \psi_{+1}) + \frac{c_1}{2} (\rho_{+1} + \rho_{-1}) \rho_0 - \frac{i\hbar\gamma_x}{\sqrt{2}} \psi_0^* \left(\frac{\partial \psi_{+1}}{\partial x} + \frac{\partial \psi_{-1}}{\partial x} \right) \\
& + \frac{\hbar}{\sqrt{2}} \psi_0^* \left(\gamma_y \frac{\partial \psi_{+1}}{\partial y} - \gamma_x \frac{\partial \psi_{-1}}{\partial x} \right) - \frac{i\hbar\gamma_x}{\sqrt{2}} (\psi_{+1}^* + \psi_{-1}^*) \frac{\partial \psi_0}{\partial x} - \frac{\hbar\gamma_y}{\sqrt{2}} (\psi_{+1}^* - \psi_{-1}^*) \frac{\partial \psi_0}{\partial y} \\
& \left. - i\hbar\gamma_z \left(\psi_{+1}^* \frac{\partial \psi_{+1}}{\partial z} - \psi_{-1}^* \frac{\partial \psi_{-1}}{\partial z} \right) \right]. \tag{A.6}
\end{aligned}$$

A.2 Chemical potential

For stationary states, the wave functions have a trivial time dependence $\psi_j(\mathbf{r}, t) = e^{-i\mu_j t} \psi_j(\mathbf{r})$. By plugging this into Eqs. (A.2a)-(A.2b), the time-independent CGPEs are

$$\begin{aligned}
\mu_{\pm 1} \psi_{\pm 1} &= [\mathcal{H} + c_1(\rho_0 \pm \rho_{\mp})] \psi_{\pm 1} + c_1 \psi_{\mp 1}^* \psi_0^2 \\
&\quad - \frac{i\hbar}{\sqrt{2}} \left(\gamma_x \frac{\partial \psi_0}{\partial x} \mp i\gamma_y \frac{\partial \psi_0}{\partial y} \pm \sqrt{2}\gamma_z \frac{\partial \psi_{\pm 1}}{\partial z} \right), \tag{A.7a}
\end{aligned}$$

$$\begin{aligned}
\mu_0 \psi_0 &= (\mathcal{H} + c_1 \rho_{+}) \psi_0 + 2c_1 \psi_{+1} \psi_{-1} \psi_0^* \\
&\quad - \frac{i\hbar}{\sqrt{2}} \left[\gamma_x \left(\frac{\partial \psi_{+1}}{\partial x} + \frac{\partial \psi_{-1}}{\partial x} \right) + i\gamma_y \left(\frac{\partial \psi_{+1}}{\partial y} - \frac{\partial \psi_{-1}}{\partial y} \right) \right], \tag{A.7b}
\end{aligned}$$

where μ_{+1} , μ_0 , and μ_{-1} are the chemical potentials of the three components. These equations can be used to define the chemical potential functionals analogous to the energy functional.

A.3 Dimensionless formulation of three-dimensional CGPEs

Before solving CGPEs, they are usually written in dimensionless form, wherein one expresses the physical quantities like length, time, energy, etc., in terms of natural scales within the system. This allows one to eliminate cumbersome constants appearing in the CGPEs, which, besides being aesthetically appealing, allows for computationally less intensive floating point operation while numerically solving the equations. Additionally, dimensionless formulation can reveal the inherent equivalence of seemingly disparate systems, e.g. two harmonically trapped scalar BECs with different N, a (s-wave scattering length), and a_{osc} (oscillator length) are equivalent if Na/a_{osc} for them are equal. Eqs. (A.2a)-(A.2b) can be transformed into dimensionless form

by introducing the following dimensionless variables

$$\tilde{t} = \omega_x t/2, \quad \tilde{\mathbf{r}} = \frac{\mathbf{r}}{a_{\text{osc}}}, \quad \phi_j(\tilde{\mathbf{r}}, \tilde{t}) = \frac{a_{\text{osc}}^{3/2}}{\sqrt{N}} \psi_j(\tilde{\mathbf{r}}, \tilde{t}), \quad (\text{A.8})$$

where $a_{\text{osc}} = \sqrt{\hbar/(m\omega_x)}$. This basically fixes the units of length, time, density, and energy as a_{osc} , $(\omega_x/2)^{-1}$, a_{osc}^{-3} , and $\hbar\omega_x$, respectively. After substitution of these new parameters and removing all tildes for notational simplicity, we get the following three-dimensional (3D) dimensionless CGPEs [40, 108]:

$$i\frac{\partial\phi_{\pm 1}}{\partial t} = [\mathcal{H} + 2c_1(\rho_0 \pm \rho_-)]\phi_{\pm 1} + 2c_1\phi_{\mp 1}^*\phi_0^2 - \sqrt{2}i\left(\gamma_x\frac{\partial\phi_0}{\partial x} \mp i\gamma_y\frac{\partial\phi_0}{\partial y} \pm \sqrt{2}\gamma_z\frac{\partial\phi_{\pm 1}}{\partial z}\right), \quad (\text{A.9a})$$

$$i\hbar\frac{\partial\phi_0}{\partial t} = (\mathcal{H} + 2c_1\rho_+)\phi_0 + 4c_1\phi_{+1}\phi_{-1}\phi_0^* - \sqrt{2}i\left[\gamma_x\left(\frac{\partial\phi_{+1}}{\partial x} + \frac{\partial\phi_{-1}}{\partial x}\right) + i\gamma_y\left(\frac{\partial\phi_{+1}}{\partial y} - \frac{\partial\phi_{-1}}{\partial y}\right)\right], \quad (\text{A.9b})$$

where

$$\mathcal{H} = -\nabla^2 + 2V(\mathbf{r}) + 2c_0\rho, \quad V(\mathbf{x}) = (\alpha_x^2 x^2 + \alpha_y^2 y^2 + \alpha_z^2 z^2)/2, \quad (\text{A.10})$$

$\alpha_\eta = \omega_\eta/\omega_x$ with $\eta = x, y, z$ and new c_0 , c_1 , and γ are given by

$$c_0 = \frac{4\pi N(a_0 + 2a_2)}{3a_{\text{osc}}}, \quad c_1 = \frac{4\pi N(a_2 - a_0)}{3a_{\text{osc}}}, \quad \gamma_x = \gamma_y = \gamma_z = k_r a_{\text{osc}}. \quad (\text{A.11})$$

Also, $\rho_j = |\phi_j|^2$ with $j = +1, 0, -1$ are the component densities, $\rho = \sum_{j=-1}^1 |\phi_j|^2$ is the total density, and now it is normalized to unity, i.e. $\int \rho d\mathbf{r} = 1$.

A.4 Dimensionless CGPEs for a q2D spin-1 BEC

If the trapping frequencies along any direction, let us say z , is much larger than the geometric mean of frequencies along the other two directions, i.e. x and y , then $\alpha_x = 1$, $\alpha_y \approx 1$ and $\alpha_z \gg \alpha_x$ [40]. In this case, the dimensionless generalized CGPEs in 3D can be approximated by

two-dimensional (2D) equations by choosing [247]

$$\phi_j(x, y, z, t) = \phi_j(x, y, t)\phi_{\text{ho}}(z), \quad \phi_{\text{ho}}(z) = (\alpha_z/\pi)^{1/4} \exp(-\alpha_z z^2/2). \quad (\text{A.12})$$

Generalized dimensionless 2D CGPEs are given by [40, 107]

$$i\frac{\partial\phi_{\pm 1}}{\partial t} = [\mathcal{H} + 2c_1(\rho_0 \pm \rho_-)]\phi_{\pm 1} + 2c_1\phi_{\mp 1}^*\phi_0^2 - \sqrt{2}i\left(\gamma_x\frac{\partial\phi_0}{\partial x} \mp i\gamma_y\frac{\partial\phi_0}{\partial y}\right), \quad (\text{A.13a})$$

$$i\frac{\partial\phi_0}{\partial t} = (\mathcal{H} + 2c_1\rho_+)\phi_0 + 4c_1\phi_{+1}\phi_{-1}\phi_0^* - \sqrt{2}i\left[\gamma_x\left(\frac{\partial\phi_{+1}}{\partial x} + \frac{\partial\phi_{-1}}{\partial x}\right) + i\gamma_y\left(\frac{\partial\phi_{+1}}{\partial y} - \frac{\partial\phi_{-1}}{\partial y}\right)\right], \quad (\text{A.13b})$$

where

$$\mathcal{H} = -\nabla_{xy}^2 + 2V(\mathbf{r}) + 2c_0\rho, \quad \nabla_{xy}^2 = \frac{\partial^2}{\partial x^2} + \frac{\partial^2}{\partial y^2}, \quad \mathbf{r} = (x, y). \quad (\text{A.14})$$

The trapping potential $V(\mathbf{r})$ and interaction parameters c_0 and c_1 are now defined as

$$V(\mathbf{r}) = \frac{1}{2}(\alpha_x^2 x^2 + \alpha_y^2 y^2), \quad c_0 = \sqrt{\frac{\alpha_z}{2\pi}} \frac{4\pi N(a_0 + 2a_2)}{3a_{\text{osc}}}, \quad c_1 = \sqrt{\frac{\alpha_z}{2\pi}} \frac{4\pi N(a_2 - a_0)}{3a_{\text{osc}}}. \quad (\text{A.15})$$

A.5 Dimensionless CGPEs for a q1D spin-1 BEC

If the trap is much stronger along two directions, say y and z compared to the x direction, then $\alpha_x = 1, \alpha_y \gg \alpha_x, \alpha_z \gg \alpha_x$, and by assuming [247]

$$\phi_j(x, y, z, t) = \phi_j(x, t)\phi_{\text{ho}}(y, z), \quad \phi_{\text{ho}}(y, z) = (\sqrt{\alpha_y\alpha_z}/\pi)^{1/2} \exp[-(\alpha_y y^2 + \alpha_z z^2)/2], \quad (\text{A.16})$$

Eqs. (A.9a)-(A.9b) can be reduced into one-dimensional (1D) equations [5, 40]

$$i\frac{\partial\phi_{\pm 1}}{\partial t} = \mathcal{H}\phi_{\pm 1} + 2c_1(\rho_0 \pm \rho_-)\phi_{\pm 1} + 2c_1\phi_{\mp 1}^*\phi_0^2 - \sqrt{2}i\gamma_x\left(\frac{\partial\phi_0}{\partial x}\right), \quad (\text{A.17a})$$

$$i\frac{\partial\phi_0}{\partial t} = \mathcal{H}\phi_0 + 2c_1\rho_+\phi_0 + 4c_1\phi_1\phi_{-1}\phi_0^* - \sqrt{2}i\gamma_x\left(\frac{\partial\phi_1}{\partial x} + \frac{\partial\phi_{-1}}{\partial x}\right), \quad (\text{A.17b})$$

where

$$\mathcal{H} = -\frac{\partial^2}{\partial x^2} + 2V(x) + 2c_0\rho, \quad V(x) = \frac{1}{2}\gamma_x^2 x^2, \quad (\text{A.18})$$

$$c_0 = \frac{\sqrt{\alpha_y \alpha_z}}{2\pi} \frac{4\pi N(a_0 + 2a_2)}{3a_{\text{osc}}}, \quad c_1 = \frac{\sqrt{\alpha_y \alpha_z}}{2\pi} \frac{4\pi N(a_2 - a_0)}{3a_{\text{osc}}}. \quad (\text{A.19})$$

Appendix B

Fourier pseudospectral method to solve CGPEs

B.1 Solution of q1D CGPEs

Starting with the simplest case of a q1D spin-1 BEC, Eqs. (A.17a)-(A.17b) can be written in a simplified form as

$$i\frac{\partial\Phi}{\partial t} = H\Phi. \quad (\text{B.1})$$

Here $\Phi = (\phi_{+1}, \phi_0, \phi_{-1})^T$ and Hamiltonian H consists of different terms involving kinetic energy operator H_{KE} , trapping potential plus terms resulting from spin-preserving collisions H_{SP} , terms corresponding to spin-exchange collisions H_{SE} , and SOC terms H_{SOC} . Eq. (B.1) can then be written as

$$i\frac{\partial\Phi}{\partial t} = (H_{\text{KE}} + H_{\text{SP}} + H_{\text{SE}} + H_{\text{SOC}})\Phi, \quad (\text{B.2})$$

where H_{KE} , H_{SP} , H_{SE} , and H_{SOC} are 3×3 matrix operators defined as

$$H_{\text{KE}} = \begin{pmatrix} -\partial_{xx} & 0 & 0 \\ 0 & -\partial_{xx} & 0 \\ 0 & 0 & -\partial_{xx} \end{pmatrix}, \quad H_{\text{SOC}} = -\sqrt{2}i\gamma_x \begin{pmatrix} 0 & \partial_x & 0 \\ \partial_x & 0 & \partial_x \\ 0 & \partial_x & 0 \end{pmatrix}, \quad (\text{B.3a})$$

$$H_{\text{SE}} = \begin{pmatrix} 0 & 2c_1\phi_0\phi_{-1}^* & 0 \\ 2c_1\phi_0^*\phi_{-1} & 0 & 2c_1\phi_0^*\phi_1 \\ 0 & 2c_1\phi_0\phi_1^* & 0 \end{pmatrix}, \quad (\text{B.3b})$$

$$H_{\text{SP}} = 2 \begin{pmatrix} V + c_0\rho + c_1(\rho_0 + \rho_-) & 0 & 0 \\ 0 & V + c_0\rho + c_1\rho_+ & 0 \\ 0 & 0 & V + c_0\rho + c_1(\rho_0 - \rho_-) \end{pmatrix}. \quad (\text{B.3c})$$

To solve Eq. (B.2), we use operator splitting which has been extensively used in the numerical solutions of nonlinear Schrödinger equation including the GP [45, 248] and coupled GP equations [40]. Here we use first-order time splitting known as Lie splitting. Solution to Eq. (B.2) after time step δt is given as

$$\Phi(t + \delta t) = \hat{U}\Phi(t), \quad (\text{B.4})$$

which describes the evolution of the wave function by a unitary propagator \hat{U} given as

$$\hat{U} = \exp[-i\delta t(H_{\text{SP}} + H_{\text{SE}} + H_{\text{SOC}} + H_{\text{KE}})]. \quad (\text{B.5})$$

The propagator can be approximated by the split-operator technique as

$$\hat{U} \approx \exp(-i\delta t H_{\text{SP}}) \exp(-i\delta t H_{\text{SE}}) \exp(-i\delta t H_{\text{SOC}}) \exp(-i\delta t H_{\text{KE}}). \quad (\text{B.6})$$

Using (B.6), Eq. (B.4) is equivalent to solving following equations successively

$$i \frac{\partial \Phi}{\partial t} = H_{\text{KE}} \Phi, \quad (\text{B.7a})$$

$$i \frac{\partial \Phi}{\partial t} = H_{\text{SOC}} \Phi, \quad (\text{B.7b})$$

$$i \frac{\partial \Phi}{\partial t} = H_{\text{SE}} \Phi, \quad (\text{B.7c})$$

$$i \frac{\partial \Phi}{\partial t} = H_{\text{SP}} \Phi. \quad (\text{B.7d})$$

Eq. (B.7a) can be written as the following set of decoupled equations

$$i\frac{\partial\phi_j(x,t)}{\partial t} = -\frac{\partial^2\phi_j(x,t)}{\partial x^2}, \quad j = -1, 0, 1. \quad (\text{B.8})$$

Solution of Eq. (B.8) in Fourier space is given as

$$\hat{\phi}_j(k_x, t + \delta t) = \hat{\phi}_j(k_x, t) \exp(-ik_x^2 \delta t), \quad (\text{B.9})$$

where $\hat{\phi}_j$ is the Fourier transform of ϕ_j and k_x is known as Fourier frequency. Now $\hat{\phi}_j(k_x, t + \delta t)$, the transient wave function in Fourier space, is the initial value of the wave function for the Fourier transform of Eq. (B.7b), i.e.,

$$i\frac{\partial\hat{\Phi}(k_x, t)}{\partial t} = \hat{H}_{\text{SOC}}\hat{\Phi}(k_x, t). \quad (\text{B.10})$$

Here \hat{H}_{SOC} is given as

$$\hat{H}_{\text{SOC}} = -\sqrt{2}i\gamma_x \begin{pmatrix} 0 & ik_x & 0 \\ ik_x & 0 & ik_x \\ 0 & ik_x & 0 \end{pmatrix}, \quad (\text{B.11})$$

and $\hat{\Phi}(k_x, t)$ is the Fourier transforms of $\Phi(x, t)$. The solution of Eq. (B.10) is given as [107, 108]

$$\begin{aligned} \hat{\Phi}(k_x, t + \delta t) &= e^{-i\hat{H}_{\text{SOC}}\delta t}\hat{\Phi}(k_x, t) = e^{-i\hat{G}}\hat{\Phi}(k_x, t) \\ &= \left(I + \frac{\cos\beta - 1}{\beta^2}\hat{G}^2 - i\frac{\sin\beta}{\beta}\hat{G} \right) \hat{\Phi}(k_x, t), \end{aligned} \quad (\text{B.12})$$

where $\beta = \sqrt{2}A\delta t$ with $A = \sqrt{2}\gamma_x k_x$ and \hat{G} is defined as

$$\hat{G} = \delta t \begin{pmatrix} 0 & A & 0 \\ A & 0 & A \\ 0 & A & 0 \end{pmatrix}. \quad (\text{B.13})$$

Wave function in Eq. (B.12) is in Fourier space and is inverse Fourier transformed to obtain the transient wave function in coordinate space which serves as the initial solution for Eq. (B.7c).

The solution of Eq. (B.7c) is now given by

$$\begin{aligned}\Phi(x, t + \delta t) &= e^{-iH_{SE}\delta t}\Phi(x, t) = e^{-i\hat{O}}\Phi(x, t) \\ &= \left(I + \frac{\cos \Omega - 1}{\Omega^2} \hat{O}^2 - i \frac{\sin \Omega}{\Omega} \hat{O} \right) \Phi(x, t),\end{aligned}\tag{B.14}$$

where H_{SE} is given in Eq. (B.3b) and \hat{O} is defined as

$$\hat{O} = \delta t \begin{pmatrix} 0 & A & 0 \\ A^* & 0 & B^* \\ 0 & B & 0 \end{pmatrix}\tag{B.15}$$

with $\Omega = \delta t \sqrt{|A|^2 + |B|^2}$, $A = 2c_1\phi_0\phi_{-1}^*$, and $B = 2c_1\phi_0\phi_1^*$.

The transient wave function we get from here is in configuration space and is used as an input wave function for remaining Eq. (B.7d). H_{SP} being diagonal, the solution to Eq. (B.7d) can be calculated analytically as

$$\Phi(x, t + \delta t) = \exp(-i\delta t H_{SP}) \Phi(x, t).\tag{B.16}$$

This final wave function is the solution of Eq. (B.4) after time δt .

B.2 Solution of q2D CGPEs

The method discussed in the previous subsection can be extended to q2D and 3D systems with some modifications which we will elaborate on in the rest of this section. In q2D spin-1 BECs, Eqs. (A.13a)-(A.13b) can again be written in simplified form as Eq. (B.1). Here too H can be considered as consisting of, aptly defined, H_{KE} , H_{SOC} , H_{SE} , and H_{SP} . Now, H_{KE} and H_{SOC} for q2D SO-coupled BECs are given as

$$H_{KE} = \begin{pmatrix} -\nabla_{xy}^2 & 0 & 0 \\ 0 & -\nabla_{xy}^2 & 0 \\ 0 & 0 & -\nabla_{xy}^2 \end{pmatrix},\tag{B.17a}$$

$$H_{\text{SOC}} = -\sqrt{2}i \begin{pmatrix} 0 & \gamma_x \partial_x - i\gamma_y \partial_y & 0 \\ \gamma_x \partial_x + i\gamma_y \partial_y & 0 & \gamma_x \partial_x - i\gamma_y \partial_y \\ 0 & \gamma_x \partial_x + i\gamma_y \partial_y & 0 \end{pmatrix}, \quad (\text{B.17b})$$

whereas H_{SE} and H_{SP} are again defined by Eqs. (B.3b) and (B.3c), respectively, where V , c_0 and c_1 are now given by Eq. (A.15). Again as in q1D systems, the solution of Eqs. (A.13a)-(A.13b) is approximated by solving Eqs. (B.7a)-(B.7d) successively. Solution to Eq. (B.7a) with H_{KE} defined by Eq. (B.17a) in this case is given in Fourier space as

$$\hat{\phi}_j(k_x, k_y, t + \delta t) = \hat{\phi}_j(k_x, k_y, t) \exp[-i(k_x^2 + k_y^2)\delta t]. \quad (\text{B.18})$$

Fourier transform of Eq. (B.7b) corresponding to H_{SOC} given by Eq. (B.17b) is given as

$$\frac{i\partial \hat{\Phi}(k_x, k_y, t)}{\partial t} = \hat{H}_{\text{SOC}} \hat{\Phi}(k_x, k_y, t), \quad (\text{B.19})$$

where \hat{H}_{SOC} in Fourier space is given as

$$\hat{H}_{\text{SOC}} = -\sqrt{2}i \begin{pmatrix} 0 & i\gamma_x k_x + \gamma_y k_y & 0 \\ i\gamma_x k_x - \gamma_y k_y & 0 & i\gamma_x k_x + \gamma_y k_y \\ 0 & i\gamma_x k_x - \gamma_y k_y & 0 \end{pmatrix}. \quad (\text{B.20})$$

Solution to (B.19) is given as [107, 108]

$$\begin{aligned} \hat{\Phi}(k_x, k_y, t + \delta t) &= e^{-i\hat{H}_{\text{SOC}}\delta t} \hat{\Phi}(k_x, k_y, t) = e^{-i\hat{G}} \hat{\Phi}(k_x, k_y, t) \\ &= \left(I + \frac{\cos \beta - 1}{\beta^2} \hat{G}^2 - i \frac{\sin \beta}{\beta} \hat{G} \right) \hat{\Phi}(k_x, k_y, t), \end{aligned} \quad (\text{B.21})$$

where $\beta = \sqrt{2}|A|\delta t$, $A = \sqrt{2}(\gamma_x k_x - i\gamma_y k_y)$, $A^* = \sqrt{2}(\gamma_x k_x + i\gamma_y k_y)$, and \hat{G} is defined as

$$\hat{G} = \delta t \begin{pmatrix} 0 & A & 0 \\ A^* & 0 & A \\ 0 & A^* & 0 \end{pmatrix}. \quad (\text{B.22})$$

Eqs. (B.7c) and (B.7d) are solved similarly as in q1D case.

B.3 Solution of 3D CGPEs

In 3D case too, forms of H_{SE} and H_{SP} are same as defined in (B.3b) and (B.3c) where $V(\mathbf{r})$, c_0 and c_1 are defined in Eqs. (A.10)-(A.11) allowing us to use the methods discussed in the q1D case to solve Eqs. (B.7c)-(B.7d). On the other hand, H_{KE} and H_{SOC} are given as

$$H_{KE} = \begin{pmatrix} -\nabla^2 & 0 & 0 \\ 0 & -\nabla^2 & 0 \\ 0 & 0 & -\nabla^2 \end{pmatrix}, \quad (B.23a)$$

$$H_{SOC} = -\sqrt{2}i \begin{pmatrix} \sqrt{2}\gamma_z\partial_z & \gamma_x\partial_x - i\gamma_y\partial_y & 0 \\ \gamma_x\partial_x + i\gamma_y\partial_y & 0 & \gamma_x\partial_x - i\gamma_y\partial_y \\ 0 & \gamma_x\partial_x + i\gamma_y\partial_y & -\sqrt{2}\gamma_z\partial_z \end{pmatrix}. \quad (B.23b)$$

Since H_{SOC} can be considered to consist of the sum of two commuting Hamiltonians, i.e.,

$$\begin{aligned} H_{SOC} &= -\sqrt{2}i \left[\begin{pmatrix} 0 & \gamma_x\partial_x - i\gamma_y\partial_y & 0 \\ \gamma_x\partial_x + i\gamma_y\partial_y & 0 & \gamma_x\partial_x - i\gamma_y\partial_y \\ 0 & \gamma_x\partial_x + i\gamma_y\partial_y & 0 \end{pmatrix} + \sqrt{2}\gamma_z \begin{pmatrix} \partial_z & 0 & 0 \\ 0 & 0 & 0 \\ 0 & 0 & -\partial_z \end{pmatrix} \right], \\ &= H_{xy} + H_z. \end{aligned} \quad (B.24)$$

With this division of H_{SOC} in 3D case, H_{xy} becomes identical to H_{SOC} defined in Eq. (B.17b) for q2D case. The second Hamiltonian H_z being diagonal can be combined with H_{KE} . In other words, we can redefine H_{SOC} as simply H_{xy} and H_{KE} as follows

$$H_{KE} = \begin{pmatrix} -\nabla^2 - 2i\gamma_z\partial_z & 0 & 0 \\ 0 & -\nabla^2 & 0 \\ 0 & 0 & -\nabla^2 + 2i\gamma_z\partial_z \end{pmatrix}. \quad (B.25)$$

The advantage of this redefining H_{SOC} making it identical to H_{SOC} in q2D case is that solution to Eq. (B.7b) is again given by Eq. (B.21) in the Fourier space, whereas solution to Eq. (B.7a)

with H_{KE} defined in Eq. (B.25) is given by

$$\hat{\phi}_{\pm 1}(k_x, k_y, k_z, t + \delta t) = \hat{\phi}_{\pm 1}(k_x, k_y, k_z, t) \exp[-i(k_x^2 + k_y^2 + k_z^2 \pm 2\gamma_z k_z)\delta t], \quad (\text{B.26a})$$

$$\hat{\phi}_0(k_x, k_y, k_z, t + \delta t) = \hat{\phi}_0(k_x, k_y, k_z, t) \exp[-i(k_x^2 + k_y^2 + k_z^2)\delta t]. \quad (\text{B.26b})$$

B.4 Discretization scheme

Spinor BECs can be either confined by external trapping potential or are self-localized by the interplay of the interactions and SOC. This suggests that we can truncate our system from infinite space to some finite domain. In order to solve any equation computationally, we need to discretize our variables. We start by first truncating the spatial domain of the condensate along $\eta = x, y, z$ direction to L_η . Now, we choose $L_\eta = N_\eta \times \Delta\eta$, where $\Delta\eta$ is the space-step size chosen to discretize the spatial variable $\eta \in [-L_\eta/2, L_\eta/2]$ by setting $\eta_p = -L_\eta/2 + (p-1)\Delta\eta$ with $p = 1, 2, \dots, N_\eta + 1$. The point $\eta_{N_\eta+1}$ is excluded from the set of grid points due to the periodicity of the wave function, $\phi(\eta_{N_\eta+1}, t_q) = \phi(\eta_1, t_q)$. Similarly, time is discretized using Δt as temporal step size. The discretization in the Fourier space which avoids the aliasing condition can be achieved by discretizing k_η in N_η equispaced k_η points $\in \left[\frac{-N_\eta\pi}{L_\eta}, \dots, \frac{(N_\eta-2)\pi}{L_\eta} \right]$ with a spacing of $2\pi/L_\eta$. The resultant discretized wave function $\phi_j(\eta_p, t_q)$ ($\hat{\phi}_j(k_\eta^p, t_q)$) in real (Fourier) space, where p is the spatial (Fourier frequency) index and q is the time index, make these amenable to be discrete Fourier transformed by FFTW software library (where ‘‘In forward Fourier transform, positive frequencies are stored in the first half of the output and the negative frequencies are stored in backwards order in the second half of the output’’) [249], if k_η^p are indexed as

$$k_\eta(i) = (i-1)\frac{2\pi}{L_\eta}, \quad i = 1, \dots, \frac{N_\eta}{2} + 1, \quad (\text{B.27a})$$

$$k_\eta(i + 1 + \frac{N_\eta}{2}) = -k_\eta(1 - i + \frac{N_\eta}{2}), \quad i = 1, \dots, \frac{N_\eta}{2} - 1. \quad (\text{B.27b})$$

To summarize, the discrete analogues of the various continuous variables are as follows:

$$\eta \equiv \eta_p, \quad k_\eta \equiv k_\eta^p, \quad t \equiv t_q, \quad (\text{B.28a})$$

$$\phi_j(\eta, t) \equiv \phi_j(\eta_p, t_q), \quad \hat{\phi}_j(k_\eta, t) \equiv \hat{\phi}_j(k_\eta^p, t_q). \quad (\text{B.28b})$$

The N_η is chosen to be the multiple of 2 to have the best performance from the FFTW subroutines [249].

B.5 Imaginary-time propagation

We use imaginary-time propagation, wherein δt is replaced by $-i\delta t$, to compute the ground state of spin-1 BEC. This method neither preserves the norm \mathcal{N} and the magnetization M . To simultaneously fix the norm and magnetization, the component wave functions are redefined as

$$\phi_j(x^p, t_q) \equiv \sigma_j \phi_j(x^p, t_q), \quad (\text{B.29})$$

after each iteration in imaginary time, where σ_j are three projection parameters defined as [3]

$$\sigma_0 = \frac{\sqrt{1 - M^2}}{[N_0 + \sqrt{4(1 - M^2)N_1N_{-1}} + (MN_0)^2]^{1/2}}, \quad (\text{B.30a})$$

$$\sigma_1 = \sqrt{\frac{1 + M - (\sigma_0)^2 N_0}{2N_1}}, \quad \sigma_{-1} = \sqrt{\frac{1 - M - (\sigma_0)^2 N_0}{2N_{-1}}}. \quad (\text{B.30b})$$

This simultaneous fixing of the norm and magnetization is not implemented in the presence of SOC rather only the total norm is fixed. The reason being the existence of a ground-state solution with arbitrary magnetization is not guaranteed in this case.

Appendix C

FORTTRAN programs for solving the CGPEs for spin-1 BECs

Here we describe the FORTRESS software package consisting of a set of three codes written in FORTRAN 90/95 programming language associated with [37] and available here [6]. These three programs, namely **imretime_spin1_1D.f90**, **imretime_spin1_2D.f90**, and **imretime_spin1_3D.f90**, correspond to solving 1D Eqs. (A.17a)-(A.17b), 2D Eqs. (A.13a)-(A.13b) and 3D Eqs. (A.9a)-(A.9b), respectively, using the time-splitting Fourier pseudospectral method described in Appendix B. Each of these programs can solve the aforementioned equations with user-defined *option* of either imaginary- or real-time propagation.

The basic structure of the three codes is the same; thus allowing us to describe the parameters, variables, modules, functions, and subroutines using 1D code as a prototypical example.

C.1 Modules

First, we provide the description of the four modules: BASIC_DATA, CGPE_DATA, SOC_DATA, FFTW_DATA.

BASIC_DATA

The input parameters like the number of iterations (NITER), number of spatial grid points (NX), spatial, and temporal step sizes (DX and DT) are defined at the top of each program in

this module. Besides these parameters, number of OpenMP/FFTW threads, constants like π (PI), $i = \sqrt{-1}$ (CI), atomic mass unit (AMU), \hbar (HBAR), and spatial domain L_x (LX) are also defined in this module.

CGPE_DATA

The FORTRAN variables corresponding to k_x (KX), x (X), $V(x)$ (V), a_{osc} (AOSC), ω_x (OMEGAM), c_0 (C0), c_1 (C2), M (MAG), $\phi_j(x)$ (PHI), $\hat{\phi}_j(k_x)$ (PHIF) are declared in this module. The scattering lengths a_0 (A0), a_2 (A2); anisotropy parameters α_x (ALPHAX), α_y (ALPHAY), and α_z (ALPHAZ); mass m (M) and total number of atoms N (NATOMS) are defined in this module. In addition to this, there are two user-defined integer options: (a) SWITCH_IM which has to be set equal to 1 for imaginary-time propagation or 0 for real-time propagation and (b) OPTION_FERRO_POLAR which has to be set equal to 1, 2 or 3. OPTION_FERRO_POLAR = 1, 2 correspond to suitable initial guess wave functions for ferromagnetic and antiferromagnetic systems, respectively; whereas OPTION_FERRO_POLAR = 3 implies that the Gaussian initial guess wave functions would be used.

SOC_DATA

The strength of SOC γ_x (GAMMAX) is defined in this module. SWITCH_SOC defined in this module has to be set equal to 1 if $\gamma_x \neq 0$ or equal to 0 if $\gamma_x = 0$. **The parameters and variables not listed in the aforementioned three modules do not need to be modified by the user.**

FFTW_DATA

The variable types of the input and output arrays used in the FFTW subroutine to calculate discrete Fourier transform, requisite plans, and thread initialization variables are declared in this module. The module uses the FFTW3 module from the FFTW software library [249] and is not required to be modified by the user.

C.2 Functions and subroutines

Now, we will describe the functions and subroutines which have been used in the programs.

SIMPSON: This function evaluates the 1D integral of the form $\int f(x)dx$ using Simpson's 1/3 rule adapted for even number of grid points.

DIFF: This function evaluates $\partial f(x)/\partial x$ using nine point Richardson's extrapolation formula.

INITIALIZE: This subroutine initializes the initial guess wave functions PHI, space mesh X, trapping potential V, and Fourier frequencies KX.

NORMT: The subroutine normalizes the total density to 1.

NORMC: The subroutine calculates the norms of the individual components, i.e. $\int |\phi_j(x)|^2 dx$.

RAD: The subroutine calculates the root mean square (rms) sizes of the three components.

ENERGY: The subroutine calculates the component chemical potentials μ_j (MU), E (EN), and M (MAG).

FFT: The subroutine calculates the discrete forward Fourier transform using freely available FFTW software library [249]. The subroutine uses the module FFTW3.

BFT: Similarly, the subroutine calculates the discrete backward Fourier transform using FFTW software library [249].

KE: The subroutine evaluates Eq. (B.9) in Fourier space.

SOC: The subroutine implements Eq. (B.12) with \hat{H}_{SOC} given by Eq. (B.11).

SE: The subroutine implements Eq. (B.14) for H_{SE} consisting of spin-exchange terms.

SP: The subroutine implements Eq. (B.16) for H_{SP} consisting of spin-preserving terms.

C.3 2D and 3D programs

As compared to the 1D program which has NX grid points with spacing of DX , the 2D program requires $NX \times NY$ grid points with uniform spacing of DX and DY along x and y directions, respectively. This translates into spatial domain along the two directions as $LX = DX \times NX$, $LY = DY \times NY$. Similarly, the 3D program requires $NX \times NY \times NZ$ grid points with corresponding space steps of DX , DY , and DZ . The spatial domain along three directions here is $LX = DX \times NX$, $LY = DY \times NY$, $LZ = DZ \times NZ$. The additional space variables Y and/or Z would also require corresponding Fourier frequencies KY and/or KZ in the 2D and 3D codes. The role of various subroutines is the direct extension of the roles played by them in the 1D codes as per the discussion in Secs. B.2 and B.3.

C.4 Running the programs

One has to install the FORTRAN compiler(s) and FFTW software library on the computer. If the user is interested in finding the ground state of the spin-1 BEC, the imaginary-time propagation has to be used. The dynamics on the other hand can be studied by real-time propagation using the initial wave function which needs to be supplied by the user in the file ‘initial.sol.dat’. The compilation commands are listed at the top of each program file and also in the ‘README.txt’ file provided with the codes.

C.5 Description of output files

Data is written in four files during and after the execution of the 1D or 2D programs are complete. In the imaginary-time propagation, total norm, rms sizes of the components, energy, absolute values of component wave functions at origin, and magnetization are written after every NSTP iterations, which is defined in the BASIC_DATA module, in the file “file1_im.dat”. In file “file2_im.dat”, energy, chemical potentials, and rms sizes corresponding to each component are

written after every STP iterations which is equivalent to 0.1 (dimensionless) time period. In the file “tmp_solution_file.dat”, which is updated after each NSTP iterations, component densities ρ_j and corresponding phases are written at every space point. The final ρ_j and corresponding phases are written in “solution_file.im.dat”. In real-time-propagation, the corresponding file names are ‘file1_re.dat’, ‘file2_re.dat’ and so on. There is another file, namely “convergence.dat” which is written only in imaginary-time propagation. In this file $\max |\phi_j(x_p, t_q) - \phi_j(x_p, t_q - \Delta t)| / (2\Delta t)$ where $-L_x/2 \leq x_p < L_x/2, j = -1, 0, +1$ and t_q is the discrete imaginary time is written after each iteration. This quantity serves as a suitable convergence parameter, and the execution of the program is stopped if it falls below a user-defined tolerance (TOL) defined in the CGPE_DATA module. *For all the results presented in Appendix D, a convergence tolerance of 10^{-6} has been met.*

In the 3D codes, besides the aforementioned four files, reduced densities in x - y and x - z planes and the corresponding phases are written in the files “tmp_solution_file_xy.dat” and “tmp_solution_file_xz.dat”, respectively.

C.6 Output samples from the codes

Here we present the details of sample output files ‘file1.im.dat’ and/or ‘file1_re.dat’ obtained from the three codes. The contents of this file written in successive lines are (1) time stamp at the time of start; (2) number of OpenMP and FFTW threads used in the run; (3) values of SWITCH_IM, OPTION_FERROPOLAR, SWITCH_SOC, SOC strengths (GAMMAX, GAMMAY, GAMMAZ), and tolerance (TOL) used; (4) values of anisotropy parameters (ALPHAX, ALPHAY, ALPHAZ) chosen; (5) number of space grid points (NX, NY, NZ); (6) values of NITER and NSTP; (7) value of space step(s) (DX, DY, DZ), (7) time step DT, space domain (LX, LY, LZ), and magnetization (MAG); (8) frequency used in scaling (OMEGAM), corresponding oscillator length (AOSC), and values of interaction parameters (C0, C2). Then total norm, rms sizes of the component wave functions, energy, absolute values of component wave functions at the origin, and magnetization are written for the initial solution, for the transient solution obtained after NSTP time iterations, and for the converged solution (this third entry in the real-time codes will simply correspond to the solution after NITER iterations). The time stamp at the end of the run and execution time are the last two entries in this file. The varied

nature of the contents of this file can be used to ascertain the success of the run of the code by verifying the input parameters selected and various output parameters. The sample output files obtained with the test runs of `imretime_spin1_1D.f90`, `imretime_spin1_2D.f90`, and `imretime_spin1_3D.f90` are presented in the Electronic Appendix associated with [37]. In all the test runs, harmonic trapping potential as per the trapping potential corresponding to anisotropy parameters listed in these files has been used. For these test runs, the codes were compiled with the Intel's FORTRAN compiler and the jobs were run on a server with two Intel® Xeon® Platinum 8180 CPU @ 2.50GHz. The samples of all the data files, both input and output, corresponding to the current set of parameters in the codes are available on Mendeley data [250].

C.7 OpenMP parallelization

We have tested the efficiency of OpenMP parallelization of the three codes for both imaginary- and real-time propagations. The tests were done on a 28-core Intel® Xeon® Platinum 8180 CPU @ 2.50GHz processor. The parallelization tests were performed with $NX = 10^6$ for 1D code, $NX = NY = 3000$ for 2D code, and $NX = NY = 256$, $NZ = 128$ for 3D code. The execution time was measured for 1000 iterations starting from the call to INITIALIZE subroutine and did not include the time spent in reading/writing and opening/closing the data files. The execution times $T(n)$ for the three codes compiled with both GNU Fortran 5.4.0 and Intel Fortran 19.1.0.166 compilers are shown as a function of number of threads n in Fig. C.1. It is evident from Fig. C.1 that the codes compiled with the Intel Fortran compiler are faster than those compiled with the GNU Fortran compiler for both the imaginary- and real-time propagations; nonetheless the difference in the execution times for codes compiled with these two compilers is less for real-time propagation. The execution times in all cases shown in Fig. C.1 first decrease very sharply with the increase in the number of threads and then tend to saturate with an increasing number of threads.

To quantify the performance gain with OpenMP parallelization, we have calculated the speedup and efficiency for all these codes compiled with the aforementioned two compilers. Here speedup is defined as the ratio of execution time with 1 thread to the execution time with

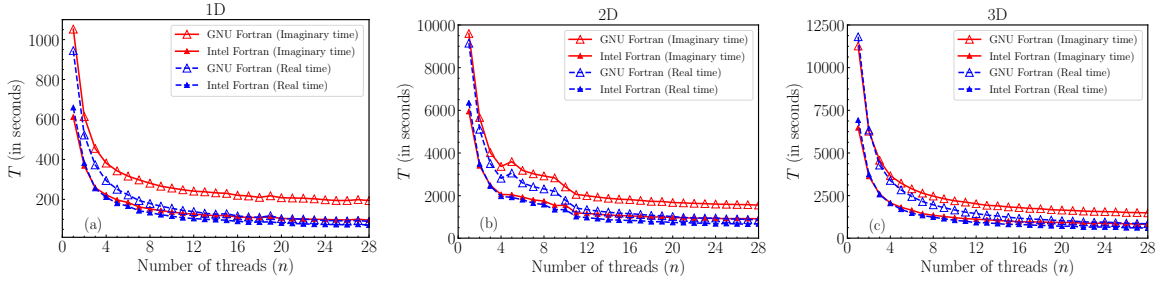


Figure C.1: (Color online) (a) Execution times for 1000 iterations (in seconds) as a function of the number of threads for 1D code compiled with GNU Fortran 5.4.0 and Intel Fortran 19.1.0.166 compilers for imaginary- and real-time propagation. (b) and (c) are the same for 2D and 3D codes.

n threads, i.e. $T(1)/T(n)$, whereas the efficiency is defined as the ratio $T(1)/[nT(n)]$. For all the codes, speedup and efficiency as a function of a number of threads are much better for real-time propagation as compared to imaginary-time propagation. The real-time speedup achieved with 28 threads was more than 9 for both 1D and 2D codes, and more than 11 for 3D code using both the compilers; whereas the corresponding imaginary-time speedup values are more than 5 for 1D, more than 6 for 2D and more than 7 for 3D with both the compilers as is shown in Fig. C.2. The best-performing real-time 3D code has more than 40% efficiency with 28 threads. The better performance of real-time variants is due to the fact that the imaginary-time propagation has to fix the norm and also has to check the convergence criterion during each iteration. Real-time propagation corresponds to the unitary evolution of a converged solution and hence does not need to fix the norm or check the convergence. The results in Figs. C.1 and C.2 were performed for the non-zero value of SOC strength.

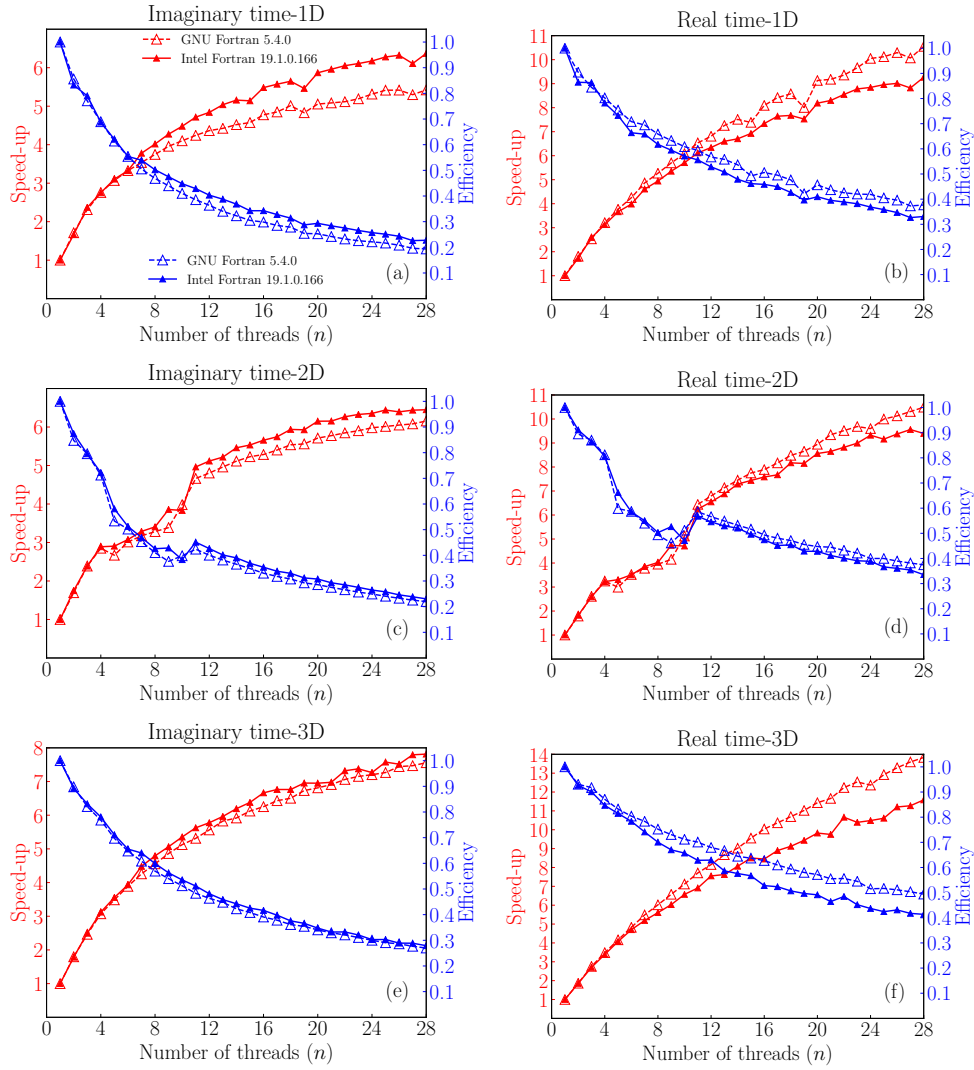


Figure C.2: (Color online) Speedup and efficiency as a function of number of threads n are shown for imaginary- (left column) and real-time propagation (right column). The top, middle, and bottom row figures show the results for 1D, 2D, and 3D codes, respectively.

Appendix D

Sample numerical results

We present the results for energy, chemical potentials, and densities of the ground states in q1D, q2D and 3D spin-1 condensates in continuum using the imaginary-time propagation method with the emphasis on the comparison with the previously published results in the literature [3–5, 107, 108]. We report the results in the presence as well as absence of SOC. To check the accuracy of the numerical method employed by us, we compare our results in the absence of SOC with those in Ref. [3, 4]. In the presence of SOC, we compare our results for q1D, q2D and 3D spin-1 BECs with those in Refs. [108], [107], and [5] respectively. It needs to be emphasized that the method used in Ref. [4] is not applicable to SO-coupled spin-1 BECs.

D.1 Results for q1D spin-1 BECs

D.1.1 Without SOC, $\gamma_x = 0$

We choose our computational domain $L = [-16, 16]$ having spatial step size as $\Delta x = 1/64$ for q1D condensates. We first consider (a) ferromagnetic spin-1 BEC of ^{87}Rb confined in a cigar-shaped trapping potential having interaction parameters in dimensionless units as $c_0 = 0.0885N$ and $c_1 = -0.00041N$ [3] and (b) antiferromagnetic spin-1 condensate of ^{23}Na confined in a cigar-shaped trapping potential having interaction parameters in dimensionless units as $c_0 = 0.0241N$ and $c_1 = 0.00075N$ [3, 4] for our computations in the 1D case. We consider $N = 10^4$ as the total number of atoms in each of these two cases. The comparison of the ground-state energies obtained [3, 4] is excellent as is shown in the table D.1 for $\Delta x \leq 1/64$ and $\Delta t \approx 0.1\Delta x^2$.

Table D.1: Ground-state energies for ^{87}Rb and ^{23}Na q1D BECs obtained using FORTRESS [6] with $\Delta x \leq 0.015625$ and $\Delta t \approx 0.1\Delta x^2$ along with the same from Ref. [3] for the various values of magnetization M .

M	^{87}Rb		^{23}Na	
	E in Ref. [3]	E (present work)	E in Ref. [3,4]	E (present work)
0	36.1365	36.1365	15.2485	15.2485
0.1	36.1365	36.1365	15.2513	15.2513
0.2	36.1365	36.1365	15.2599	15.2599
0.3	36.1365	36.1365	15.2743	15.2743
0.4	36.1365	36.1365	15.2945	15.2945
0.5	36.1365	36.1365	15.3209	15.3209
0.6	36.1365	36.1365	15.3537	15.3537
0.7	36.1365	36.1365	15.3933	15.3933
0.8	36.1365	36.1365	15.4405	15.4405
0.9	36.1365	36.1365	15.4962	15.4962

For q1D ^{87}Rb , we also consider an alternative set of interaction parameters of $c_0 = 0.08716N$, $c_1 = -0.001748N$, and $N = 10000$ for our computations [4]. In this case, again, the ground-state energy obtained is in excellent agreement with the value reported in Ref. [4] as is shown in table D.2 for the same interaction parameters set.

Table D.2: Comparison of the ground-state energy of q1D ^{87}Rb condensate reported in Ref. [4] with the value obtained using FORTRESS [6] with $\Delta x \leq 0.015625$ and $\Delta t \approx 0.1\Delta x^2$.

M	^{87}Rb	
	E in Ref. [4]	E (present work)
0-0.9	35.4007	35.4007[7]

The chemical potential values obtained are in very good agreement with those reported in Ref. [3] as is shown in table D.3.

The ground-state wave functions are also in excellent agreement with Ref. [3]. The absolute values of ground-state wave functions for ^{87}Rb and ^{23}Na with $M = 0$ and 0.5 are shown in Fig. D.1.

D.1.2 With SOC, $\gamma_x \neq 0$

In the presence of SOC with harmonic trapping potential, for ^{87}Rb and ^{23}Na , we again consider (c_0, c_1) equal to $(0.08716N, -0.001748N)$ and $(0.0241N, 0.00075N)$, respectively, where $N =$

Table D.3: Comparison of the chemical potential values for ^{87}Rb and ^{23}Na condensate reported in Ref. [3] with the values obtained using FORTRESS [6] with $\Delta x = 0.0025$, $\Delta t = 0.0000095$. For ^{23}Na , $\mu = (\mu_{+1} + \mu_{-1})/2$, whereas for ^{87}Rb $\mu = \mu_0 = \mu_{\pm 1}$.

	^{87}Rb		^{23}Na	
M	μ in Ref. [3]	μ (present work)	μ in [3]	μ (present work)
0	60.2139	60.2136	25.3857	25.3857
0.1	60.2139	60.2136	25.3847	25.3838
0.2	60.2139	60.2136	25.3815	25.3804
0.3	60.2139	60.2136	25.3762	25.3749
0.4	60.2139	60.2137	25.3682	25.3668
0.5	60.2139	60.2137	25.3572	25.3557
0.6	60.2139	60.2137	25.3423	25.3406
0.7	60.2139	60.2138	25.3220	25.3203
0.8	60.2139	60.2138	25.2939	25.2921
0.9	60.2139	60.2139	25.2527	25.2509

10000. The ground-state energy values in these cases are given in table D.4 for multiple values of γ_x . The component densities for the two systems with $\gamma_x = 0.5$ and 1 are shown in Fig. D.2.

Table D.4: Ground-state energies of ^{87}Rb and ^{23}Na condensates in the presence of harmonic trap and SOC with $\Delta x = 0.015625$, $\Delta t \approx 0.1(\Delta x)^2$. The (c_0, c_1) values are $(0.08716N, -0.001748N)$ and $(0.0241N, 0.00075N)$ with $N = 10000$ for ^{87}Rb and ^{23}Na , respectively.

	^{87}Rb	^{23}Na
γ_x	Energy	Energy
0	35.4007	15.2485
0.1	35.3958	15.2435
0.2	35.3808	15.2285
0.3	35.3558	15.2035
0.4	35.3208	15.1685
0.5	35.2758	15.1235
0.6	35.2208	15.0685
0.7	35.1558	15.0035
0.8	35.0808	14.9285
0.9	34.9958	14.8435
1	34.9008	14.7485

Next, we consider ferromagnetic and antiferromagnetic systems with (c_0, c_1) equal to $(-1.5, -0.3)$ and $(-1.2, 0.3)$, respectively in the absence of any trapping. The ground-state energies of the

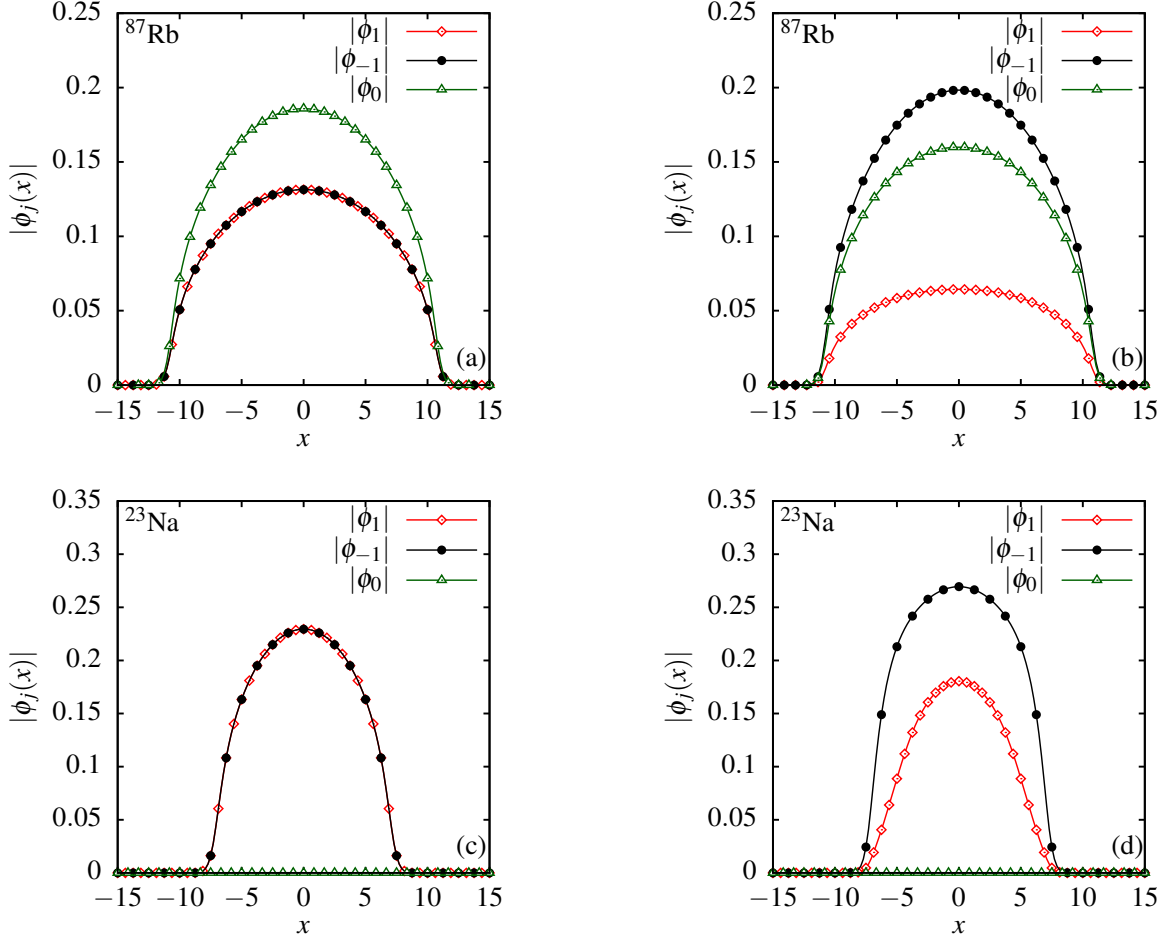


Figure D.1: (Color online) Absolute values of component wave functions $|\phi_j(x)|$ in the ground state of ^{87}Rb for (a) $M = 0$ and (b) $M = 0.5$. (c) and (d) are the same for ^{23}Na with $M = 0$ and $M = 0.5$, respectively. These are in agreement with [3, 4].

self-trapped solutions obtained in these cases are shown in table D.5. The self-trapped nature of the solutions is evident from the ground-state densities shown in Fig. D.3 for $\gamma_x = 1$.

D.2 Real-time check

To check the stationary nature of the solutions one can evolve these solutions using real-time propagation. As an example, we consider the real-time evolution of a self-trapped solution of q1D ^{87}Rb condensate with $c_0 = -1.5, c_1 = -0.3$ and $\gamma_x = 0.5$, which has $E = -0.2600$ as indicated in table D.5. The rms size of the three components of the vector soliton as a function of time is shown in Fig. D.4(a). Similarly, energy E as a function of t is shown in Fig. D.4(b)

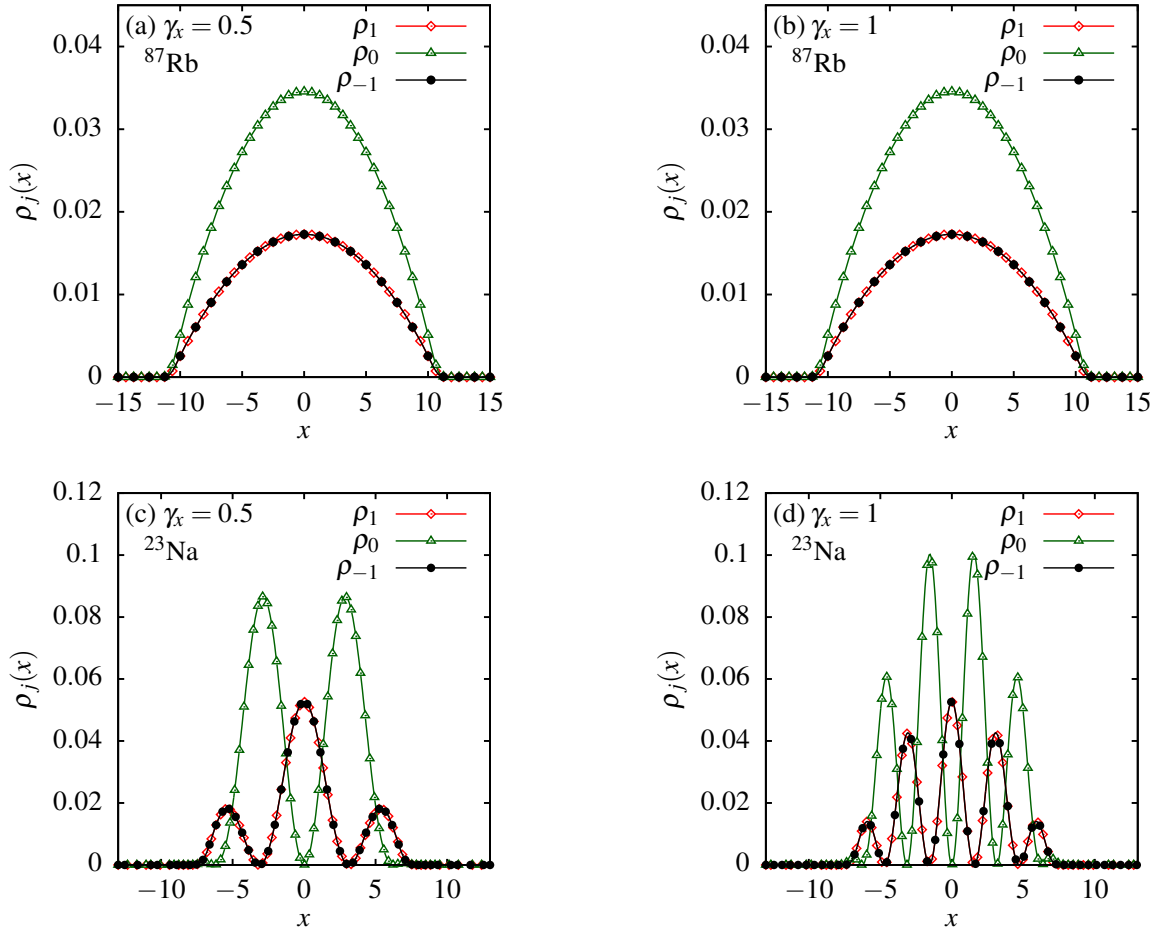


Figure D.2: (Color online) Ground-state density of SO-coupled ^{87}Rb for (a) $\gamma_x = 0.5$, (b) $\gamma_x = 1$. (c) and (d) are the same for ^{23}Na with $\gamma_x = 0.5$ and $\gamma_x = 1.0$, respectively. $M = 0$ in all the cases.

Table D.5: Ground-state energies for self-trapped ferromagnetic and antiferromagnetic condensates in the presence of SOC obtained with $\Delta x = 0.015625$, $\Delta t \approx 0.1(\Delta x)^2$.

	$(c_0, c_1) = (-1.5, -0.3)$	$(c_0, c_1) = (-1.2, 0.3)$
γ_x	Energy	Energy
0	-0.1350	-0.0600
0.1	-0.1400	-0.0650
0.2	-0.1550	-0.0800
0.3	-0.1800	-0.1050
0.4	-0.2150	-0.1400
0.5	-0.2600	-0.1850
0.6	-0.3150	-0.2400
0.7	-0.3800	-0.3050
0.8	-0.4550	-0.3800
0.9	-0.5400	-0.4650
1	-0.6350	-0.5600

which agrees with the reported value of -0.2600 at all times. All the results reported in this Appendix confirm this real-time evolution check.

D.3 Results for q2D and 3D spin-1 BECs

Here we first consider 10^4 atoms of ^{87}Rb with $(a_0, a_2) = (5.387, 5.313)$ nm in a q2D trap with $\alpha_x = \alpha_y = 1$, $\alpha_z = 20$, $\omega_x/(2\pi) = 20$ Hz. Secondly, we consider 10^4 atoms of ^{23}Na with $(a_0, a_2) = (2.646, 2.911)$ nm in a q2D trap with same trapping frequencies as that for ^{87}Rb . This leads to $(c_0, c_1) = (496.4428, -2.2942)$ and $(134.9838, 4.2242)$ for ^{87}Rb and ^{23}Na , respectively. The ground-state energies (in the units $\hbar\omega_x$) for various magnetizations are given in the table [D.6](#).

For q2D case, we also consider $c_0 = -4$, $c_1 = -0.6$ with $\gamma_x = \gamma_y = 0.5$, i.e. isotropic SOC, in the absence of trapping. The ground state in this case is a self-trapped vortex-bright soliton as is shown in Fig. [D.5](#). The ground-state solution corresponds to an asymmetric antivortex and vortex in the $m_f = +1$ and $m_f = -1$ components, respectively as is illustrated in Fig. [D.5\(d\)-\(f\)](#) [[107](#)].

Similarly in the 3D case, we consider $c_0 = -10$, $c_1 = 0.1$ with $\gamma_x = \gamma_y = \gamma_z = 1$ in the absence of trapping. Again, the ground-state solution in this case is a self-trapped vortex-bright soliton. To illustrate this vortex-bright soliton, we plot the 2D contour densities and corresponding phase

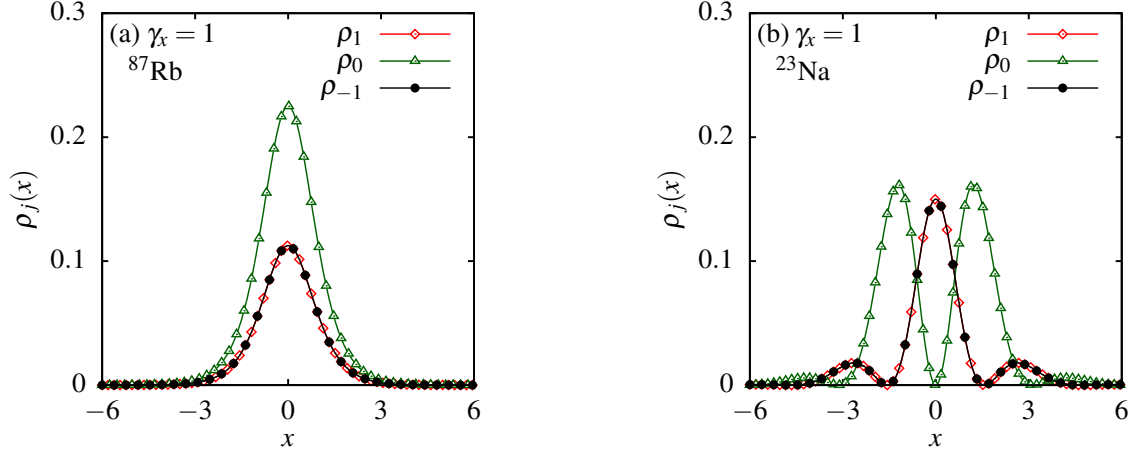


Figure D.3: (Color online) (a) Ground-state density of an SO-coupled spin-1 BEC with $c_0 = -1.5, c_1 = -0.3$ in the absence of trap and $\gamma_x = 1$. (b) The same for $c_0 = -1.2, c_1 = 0.3$. These results are in agreement with Ref. [5] and correspond to $M = 0$.

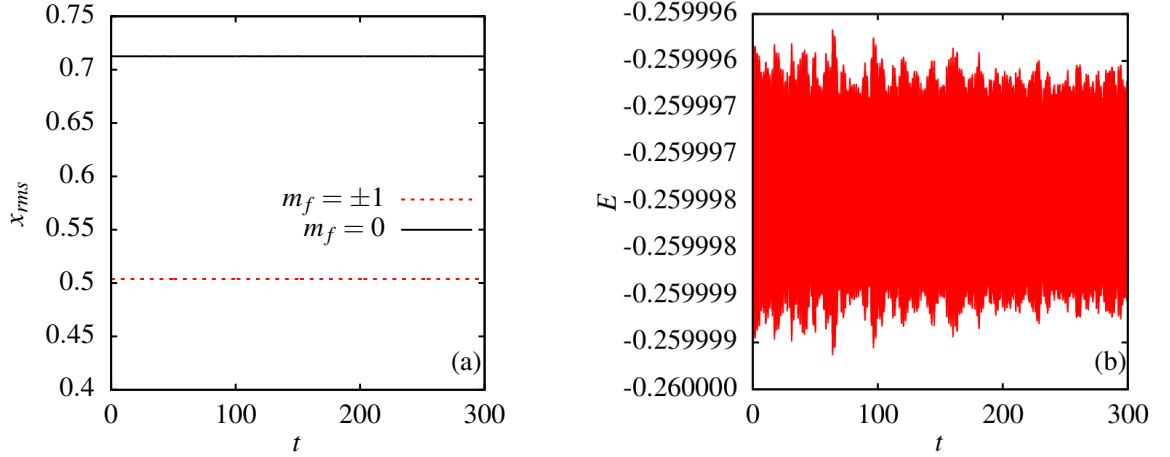


Figure D.4: (Color online) (a) Root-mean-square sizes of the three components of ^{87}Rb with $c_0 = -1.5, c_1 = -0.3$ and $\gamma_x = 0.5$ in the absence of trap as a function of time. (b) The energy of the vector soliton as a function of time.

Table D.6: Ground-state energies for ^{87}Rb and ^{23}Na q2D BECs obtained with $\Delta x = 0.05$, $\Delta y = 0.05$ and $\Delta t = 0.1\Delta x\Delta y/2$ for the various values of magnetization M . 10^4 atoms of each species were considered in trap with $\alpha_x = \alpha_y = 1$, $\alpha_z = 20$, $\omega_x/(2\pi) = 20$ Hz. Together with scattering lengths (a_0, a_2) , these parameters define c_0 and c_1 as per Eq. (A.15).

	^{87}Rb	^{23}Na
M	Energy	Energy
0	8.4629	4.5355
0.1	8.4629	4.5361
0.2	8.4629	4.5380
0.3	8.4629	4.5412
0.4	8.4629	4.5457
0.5	8.4629	4.5515
0.6	8.4629	4.5586
0.7	8.4629	4.5671
0.8	8.4629	4.5771
0.9	8.4629	4.5885

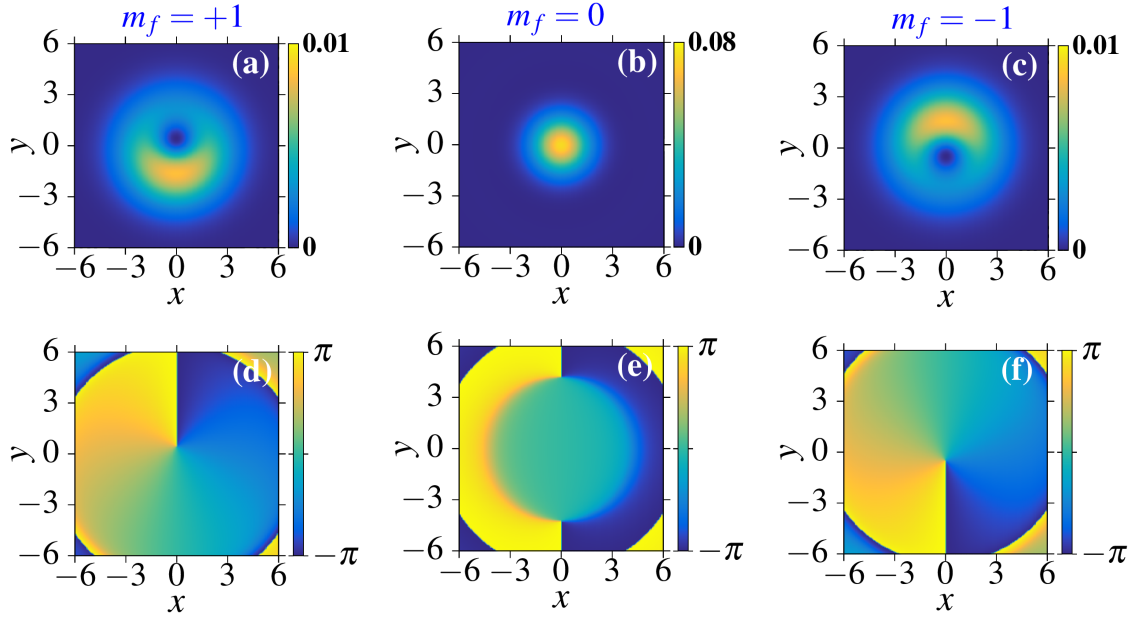


Figure D.5: The 2D contour plot of densities of (a) $m_f = +1$, (b) $m_f = 0$, and (c) $m_f = -1$ components of an asymmetric vortex-bright soliton with $c_0 = -4$, $c_1 = -0.6$, and $\gamma_x = \gamma_y = 0.5$. The corresponding phases are shown in (d) for $m_f = +1$, (e) for $m_f = 0$, and (f) for $m_f = -1$ components.

profiles in the $z = 0$ plane in Fig. D.6. These results are in agreement with [108]. The results reported in this appendix are given in Ref. [37].

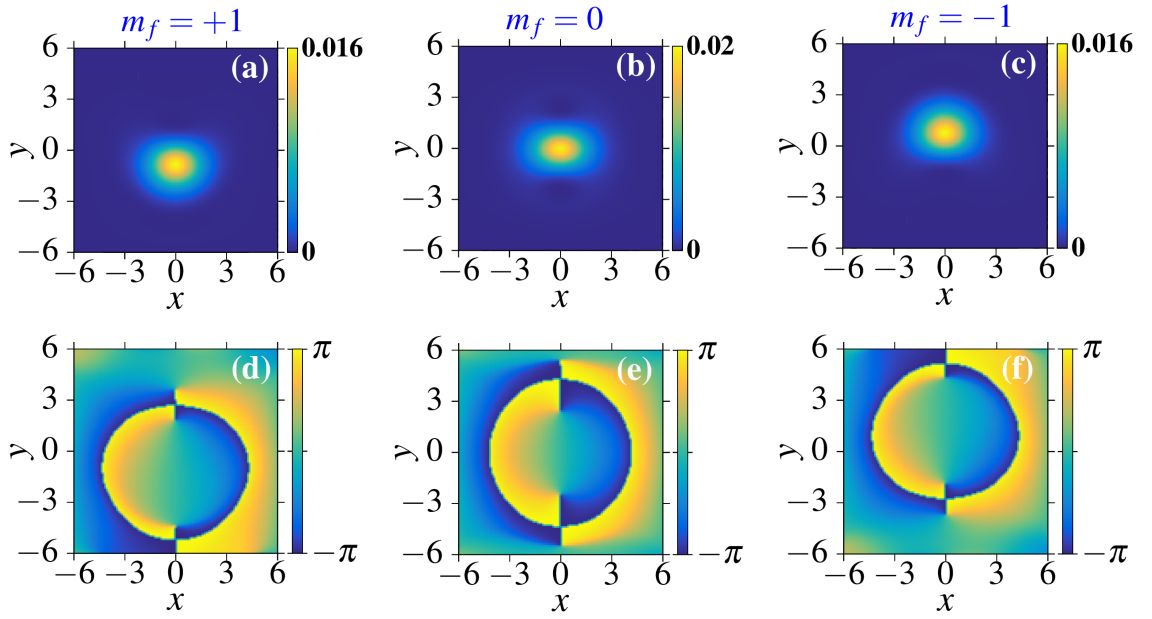


Figure D.6: The 2D contour plots of densities of components in $z = 0$ plane for (a) $m_f = +1$, (b) $m_f = 0$, and (c) $m_f = -1$ of an asymmetric vortex-bright soliton with $c_0 = -10$, $c_1 = -1$, and $\gamma_x = \gamma_y = \gamma_z = 1$. The corresponding phases are shown in (d) for $m_f = +1$, (e) for $m_f = 0$, and (f) for $m_f = -1$ components.

List of Publications

Based on Thesis

1. **Pardeep Kaur**, Kuldeep Suthar, Dilip Angom, and Sandeep Gautam, “Out-of-equilibrium dynamics of Bose-Bose mixtures in optical lattices,” *Phys. Rev. A*, **109** 013308, 2024.
2. **Pardeep Kaur**, Sandeep Gautam, and S.K. Adhikari, “Solitons in two-dimensional non-magnetic spin-orbit coupled spin-1 and spin-2 condensates,” *Phys. Lett. A* **455** 128507, 2022.
3. **Pardeep Kaur**, Sandeep Gautam, and S.K. Adhikari, “Supersolid-like solitons in spin-orbit coupled spin-2 condensate,” *Phys. Rev. A* **105** 023303, 2022.
4. Kuldeep Suthar, **Pardeep Kaur**, Sandeep Gautam, and Dilip Angom “Spin-orbit-coupling-driven superfluid states in optical lattices at zero and finite temperatures,” *Phys. Rev. A* **104** 043320, 2021.
5. **Pardeep Kaur**, Arko Roy, and Sandeep Gautam, “FORTRESS: FORTRAN programs for solving coupled Gross–Pitaevskii equations for a spin–orbit coupled spin-1 Bose-Einstein condensate,” *Comput. Phys. Commun.* **259** 107671, 2020.

Others

1. **Pardeep Kaur**, Sandeep Gautam, and S.K. Adhikari, “Quasi-one- and quasi-two-dimensional Bose-Fermi mixtures from weak coupling to unitarity,” *Eur. Phys. J. Plus.* **138** 754, 2023.
2. Paramjeet Banger, **Pardeep Kaur**, Arko Roy, and Sandeep Gautam, “FORTRESS: FORTRAN programs to solve coupled Gross-Pitaevskii equations for spin-orbit coupled

spin- f Bose-Einstein condensate with spin $f = 1$ or 2 ,” *Comput. Phys. Commun.* **279** 108442, 2022.

3. Paramjeet Banger, **Pardeep Kaur**, and Sandeep Gautam, “Semi-Implicit finite-difference methods to study the spin-orbit and coherently coupled spinor Bose-Einstein condensates,” *Int. J. Mod. Phys. C* **33**(4) 2250046, 2022.

Conference Presentations

1. Poster Presentation

Pardeep Kaur, Sandeep Gautam and S.K. Adhikari “Solitons in two-dimensional non-magnetic spin-orbit coupled spin-1 and spin-2 condensates,” Physics Day 2023, Department of Physics, Indian Institute of Technology Ropar, Punjab, India, 4 March 2023.

2. Poster Presentation

Pardeep Kaur, Sandeep Gautam and S.K. Adhikari “Quasi-one- and quasi-two-dimensional Bose-Fermi mixtures from weak coupling to unitarity,” 23rd National Conference on Atomic and Molecular Physics (NCAMP), Indian Institute of Space Science and Technology, Thiruvananthapuram, 20-23 February 2023.

3. Poster Presentation

Kuldeep Suthar, **Pardeep Kaur**, Sandeep Gautam and Dilip Angom “Spin-orbit-coupling-driven superfluid states in optical lattices at zero and finite temperatures,” Conference on Condensed Matter Physics (CCMP 2023), Physical Research Laboratory, Ahmedabad, 6-8 February 2023.

4. Oral Presentation [*Invited Talk*]

Pardeep Kaur, Sandeep Gautam and S.K. Adhikari “Exotic self-trapped superstructures in spin-orbit coupled spin-2 condensate,” Young Physicists Meet (YPM-2022), Physical Research Laboratory, Ahmedabad, 23-25 February 2022.

5. Poster Presentation

Pardeep Kaur, Sandeep Gautam and S.K. Adhikari “Exotic self-trapped superstruc-

tures in spin-orbit coupled spin-2 condensate,” Conference on Condensed Matter Physics (CCMP 2021), Physical Research Laboratory, Ahmedabad, 16-18 August 2021.

References

- [1] I. B. Spielman. Raman processes and effective gauge potentials. *Phys. Rev. A*, 79:063613, 2009.
- [2] Juraj Radic. *Spin-Orbit-Coupled Quantum Gases*. PhD thesis, University of Maryland, 2015.
- [3] W. Bao and F. Y. Lim. Computing ground states of spin-1 bose–einstein condensates by the normalized gradient flow. *SIAM Journal on Scientific Computing*, 30(4):1925–1948, 2008.
- [4] W. Bao, I.-L. Chern, and Y. Zhang. Efficient numerical methods for computing ground states of spin-1 bose–einstein condensates based on their characterizations. *Journal of Computational Physics*, 253:189–208, 2013.
- [5] S. Gautam and S. K. Adhikari. Mobile vector soliton in a spin–orbit coupled spin-1 condensate. *Laser Physics Letters*, 12(4):045501, 2015.
- [6] <https://data.mendeley.com/datasets/st7md3ss85/1>.
- [7] S. N. Bose. Plancks gesetz und lichtquantenhypothese. *Zeitschrift für Physik*, 26(1):178–181, 1924.
- [8] A. Einstein. Quantum theory of the monatomic ideal gas. *Sitzungsberichte der Preussischen Akademie der Wissenschaften, Physikalisch-mathematische Klasse*, pages 261–267, 1924.

- [9] K. B. Davis, M.-O. Mewes, M. R. Andrews, N. J. van Druten, D. S. Durfee, D. M. Kurn, and W. Ketterle. Bose-einstein condensation in a gas of sodium atoms. *Physical Review Letters*, 75(22):3969, 1995.
- [10] C. C Bradley, C. A. Sackett, J. J. Tollett, and R. G. Hulet. Evidence of bose-einstein condensation in an atomic gas with attractive interactions. *Physical Review Letters*, 75(9):1687, 1995.
- [11] M. H. Anderson, J. R. Ensher, M. R. Matthews, C. E. Wieman, and E. A. Cornell. Observation of bose-einstein condensation in a dilute atomic vapor. *Science*, 269(5221):198–201, 1995.
- [12] C. J. Pethick and H. Smith. *Bose–Einstein condensation in dilute gases*. Cambridge university press, 2008.
- [13] M. Ueda. *Fundamentals and new frontiers of Bose-Einstein condensation*. World Scientific, 2010.
- [14] L. Pitaevskii and S. Stringari. *Bose-Einstein condensation and superfluidity*, volume 164. Oxford University Press, 2016.
- [15] W. D. Phillips. Nobel lecture: Laser cooling and trapping of neutral atoms. *Reviews of Modern Physics*, 70(3):721, 1998.
- [16] F. Dalfovo, S. Giorgini, L. P. Pitaevskii, and S. Stringari. Theory of bose-einstein condensation in trapped gases. *Reviews of Modern Physics*, 71(3):463, 1999.
- [17] K. Huang. *Statistical mechanics*. John Wiley & Sons, 2008.
- [18] N. Bogoliubov. On the theory of superfluidity. *Journal of Physics*, 11(1):23, 1947.
- [19] E. P. Gross. Structure of a quantized vortex in boson systems. *Il Nuovo Cimento (1955-1965)*, 20(3):454–477, 1961.
- [20] L. P. Pitaevskii. Vortex lines in an imperfect bose gas. *Sov. Phys. JETP*, 13(2):451–454, 1961.

- [21] G. P. Agrawal. Nonlinear fiber optics. In *Nonlinear Science at the Dawn of the 21st Century*, pages 195–211. Springer, 2000.
- [22] C. Sulem and P.-L. Sulem. *The nonlinear Schrödinger equation: self-focusing and wave collapse*, volume 139. Springer Science & Business Media, 2007.
- [23] T. Taniuti and H. Washimi. Self-trapping and instability of hydromagnetic waves along the magnetic field in a cold plasma. *Physical Review Letters*, 21(4):209, 1968.
- [24] G. Falkovich. *Fluid mechanics: A short course for physicists*. Cambridge University Press, 2011.
- [25] J. Denschlag, J. E. Simsarian, D. L. Feder, C. W. Clark, L. A. Collins, J. Cubizolles, L. Deng, E. W. Hagley, K. Helmerson, W. P. Reinhardt, et al. Generating solitons by phase engineering of a bose-einstein condensate. *Science*, 287(5450):97–101, 2000.
- [26] S. Burger, K. Bongs, S. Dettmer, W. Ertmer, K. Sengstock, A. Sanpera, G. V. Shlyapnikov, and M. Lewenstein. Dark solitons in bose-einstein condensates. *Physical Review Letters*, 83(25):5198, 1999.
- [27] M. R. Matthews, B. P. Anderson, P. C. Haljan, D. S. Hall, C. E. Wieman, and E. A. Cornell. Vortices in a bose-einstein condensate. *Physical Review Letters*, 83(13):2498, 1999.
- [28] D. M. Stamper-Kurn, M. R. Andrews, A. P. Chikkatur, S. Inouye, H.-J. Miesner, J. Stenger, and W. Ketterle. Optical confinement of a bose-einstein condensate. *Physical Review Letters*, 80(10):2027, 1998.
- [29] Y. Kawaguchi and M. Ueda. Spinor bose-einstein condensates. *Physics Reports*, 520(5):253–381, 2012.
- [30] H. Schmaljohann, M. Erhard, J. Kronjäger, M. Kottke, S. Van Staa, L. Cacciapiuoti, J. J. Arlt, K. Bongs, and K. Sengstock. Dynamics of $f = 2$ spinor bose-einstein condensates. *Physical Review Letters*, 92(4):040402, 2004.
- [31] A. Griesmaier, J. Werner, S. Hensler, J. Stuhler, and T. Pfau. Bose-einstein condensation of chromium. *Physical Review Letters*, 94(16):160401, 2005.

- [32] M.-S. Chang, C. D. Hamley, M. D. Barrett, J. A. Sauer, K. M. Fortier, W. Zhang, L. You, and M. S. Chapman. Observation of spinor dynamics in optically trapped ^{87}Rb bose-einstein condensates. *Phys. Rev. Lett.*, 92:140403, 2004.
- [33] J. M. McGuirk, H. J. Lewandowski, D. M. Harber, T. Nikuni, J. E. Williams, and E. A. Cornell. Spatial resolution of spin waves in an ultracold gas. *Phys. Rev. Lett.*, 89:090402, 2002.
- [34] C. K. Law, H. Pu, and N. P. Bigelow. Quantum spins mixing in spinor bose-einstein condensates. *Phys. Rev. Lett.*, 81:5257–5261, 1998.
- [35] D. M. Stamper-Kurn and M. Ueda. Spinor bose gases: Symmetries, magnetism, and quantum dynamics. *Reviews of Modern Physics*, 85(3):1191, 2013.
- [36] C. Chin, R. Grimm, P. Julienne, and E. Tiesinga. Feshbach resonances in ultracold gases. *Reviews of Modern Physics*, 82(2):1225, 2010.
- [37] P. Kaur, A. Roy, and S. Gautam. Fortress: Fortran programs for solving coupled gross-pitaevskii equations for spin-orbit coupled spin-1 bose-einstein condensate. *Computer Physics Communications*, 259:107671, 2021.
- [38] P. Banger, P. Kaur, A. Roy, and S. Gautam. Fortress: Fortran programs to solve coupled gross-pitaevskii equations for spin-orbit coupled spin- f bose-einstein condensate with spin $f = 1$ or 2 . *Computer Physics Communications*, 279:108442, 2022.
- [39] P. Banger, P. Kaur, and S. Gautam. Semi-implicit finite-difference methods to study the spin-orbit-and coherently-coupled spinor bose-einstein condensates. *International Journal of Modern Physics C*, 33(04):2250046, 2022.
- [40] H. Wang. A time-splitting spectral method for computing dynamics of spinor $f = 1$ bose-einstein condensates. *Computer Mathematics*, 84(6):925–944, 2007.
- [41] P. A. Ruprecht, M. J. Holland, K. Burnett, and M. Edwards. Time-dependent solution of the nonlinear schrödinger equation for bose-condensed trapped neutral atoms. *Physical Review A*, 51(6):4704, 1995.

- [42] M. L. Chiofalo, S. Succi, and M. P. Tosi. Ground state of trapped interacting bose-einstein condensates by an explicit imaginary-time algorithm. *Physical Review E*, 62(5):7438, 2000.
- [43] W. Bao and Q. Du. Computing the ground state solution of bose-einstein condensates by a normalized gradient flow. *SIAM Journal on Scientific Computing*, 25(5):1674–1697, 2004.
- [44] X. Antoine, W. Bao, and C. Besse. Computational methods for the dynamics of the nonlinear schrödinger/gross-pitaevskii equations. *Computer Physics Communications*, 184(12):2621–2633, 2013.
- [45] P. Muruganandam and S. K. Adhikari. Fortran programs for the time-dependent gross-pitaevskii equation in a fully anisotropic trap. *Computer Physics Communications*, 180(10):1888–1912, 2009.
- [46] W. Bao, D. Jaksch, and P. A. Markowich. Numerical solution of the gross-pitaevskii equation for bose-einstein condensation. *Journal of Computational Physics*, 187(1):318–342, 2003.
- [47] S.-M. Chang, W.-W. Lin, and S.-F. Shieh. Gauss-seidel-type methods for energy states of a multi-component bose-einstein condensate. *Journal of Computational Physics*, 202(1):367–390, 2005.
- [48] H. Wang. A projection gradient method for computing ground state of spin-2 bose-einstein condensates. *Journal of Computational Physics*, 274:473–488, 2014.
- [49] W. Bao, S. Jin, and P. A. Markowich. On time-splitting spectral approximations for the schrödinger equation in the semiclassical regime. *Journal of Computational Physics*, 175(2):487–524, 2002.
- [50] Z. F. Ezawa. *Quantum Hall Effects: Recent Theoretical and Experimental Developments*. World Scientific, 3rd edition, 2013.
- [51] M. Z. Hasan and C. L. Kane. Colloquium: Topological insulators. *Reviews of Modern Physics*, 82:3045, 2010.

- [52] Y. A. Bychkov and E. I. Rashba. Oscillatory effects and the magnetic susceptibility of carriers in inversion layers. *Journal of Physics C: Solid state physics*, 17(33):6039, 1984.
- [53] G. Dresselhaus. Spin-orbit coupling effects in zinc blende structures. *Physical Review*, 100(2):580, 1955.
- [54] Y.-J. Lin, R. L. Compton, K. Jimenez-Garcia, W. D. Phillips, J. V. Porto, and I. B. Spielman. A synthetic electric force acting on neutral atoms. *Nature Physics*, 7(7):531–534, 2011.
- [55] Y.-J. Lin, R. L. Compton, K. Jiménez-García, J. V. Porto, and I. B. Spielman. Synthetic magnetic fields for ultracold neutral atoms. *Nature*, 462(7273):628–632, 2009.
- [56] Y.-J. Lin, K. Jiménez-García, and I. B. Spielman. Spin-orbit-coupled bose-einstein condensates. *Nature*, 471:83, 2011.
- [57] S. Zhang, W. S. Cole, A. Paramekanti, and N. Trivedi. Spin-orbit coupling in optical lattices. *Annual Review of Cold Atoms and Molecules*, pages 135–179, 2015.
- [58] H. Zhai. Degenerate quantum gases with spin-orbit coupling: a review. *Reports on Progress in Physics*, 78(2):026001, 2015.
- [59] X.-L. Qi and S.-C. Zhang. Topological insulators and superconductors. *Reviews of Modern Physics*, 83:1057, 2011.
- [60] J. Li, W. Huang, B. Shteynas, S. Burchesky, F. C. Top, E. Su, J. Lee, A. O. Jamison, and W. Ketterle. Spin-orbit coupling and spin textures in optical superlattices. *Physical Review Letters*, 117:185301, 2016.
- [61] J.-R. Li, J. Lee, W. Huang, S. Burchesky, B. Shteynas, F. C. Top, A. O. Jamison, and W. Ketterle. A stripe phase with supersolid properties in spin-orbit-coupled bose-einstein condensates. *Nature*, 543:91, 2017.
- [62] S.-C. Ji, J.-Y. Zhang, L. Zhang, Z.-D. Du, W. Zheng, Y.-J. Deng, H. Zhai, S. Chen, and J.-W. Pan. Experimental determination of the finite-temperature phase diagram of a spin-orbit coupled bose gas. *Nature Physics*, 10:314, 2014.

- [63] D. L. Campbell, G. Juzeliūnas, and I. B. Spielman. Realistic rashba and dresselhaus spin-orbit coupling for neutral atoms. *Physical Review A*, 84(2):025602, 2011.
- [64] V. Galitski, G. Juzeliūnas, and I. B. Spielman. Artificial gauge fields with ultracold atoms. *Physics Today*, 72(1):38–44, 2019.
- [65] W. Sun, B.-Z. Wang, X.-T. Xu, C.-R. Yi, L. Zhang, Z. Wu, Y. Deng, X.-J. Liu, S. Chen, and J.-W. Pan. Highly controllable and robust 2d spin-orbit coupling for quantum gases. *Physical Review Letters*, 121:150401, 2018.
- [66] Z. Cai, X. Zhou, and C. Wu. Magnetic phases of bosons with synthetic spin-orbit coupling in optical lattices. *Physical Review A*, 85:061605, 2012.
- [67] W. S. Cole, S. Zhang, A. Paramekanti, and N. Trivedi. Bose-hubbard models with synthetic spin-orbit coupling: Mott insulators, spin textures, and superfluidity. *Physical Review Letters*, 109:085302, 2012.
- [68] M. Gong, Y. Qian, M. Yan, V. W. Scarola, and C. Zhang. Dzyaloshinskii-moriya interaction and spiral order in spin-orbit coupled optical lattices. *Scientific Reports*, 5:10050, 2015.
- [69] A. T. Bolukbasi and M. Iskin. Superfluid–mott-insulator transition in the spin-orbit-coupled bose-hubbard model. *Physical Review A*, 89:043603, 2014.
- [70] D. Yamamoto, I. B. Spielman, and C. A. R. Sá de Melo. Quantum phases of two-component bosons with spin-orbit coupling in optical lattices. *Physical Review A*, 96:061603, 2017.
- [71] M. Yan, Y. Qian, H.-Y. Hui, M. Gong, C. Zhang, and V. W. Scarola. Spin-orbit-driven transitions between mott insulators and finite-momentum superfluids of bosons in optical lattices. *Physical Review. A*, 96:053619, 2017.
- [72] X.-Q. Xu and J. H. Han. Spin-orbit coupled bose-einstein condensate under rotation. *Physical Review Letters*, 107(20):200401, 2011.
- [73] H. Sakaguchi and B. Li. Vortex lattice solutions to the gross-pitaevskii equation with spin-orbit coupling in optical lattices. *Physical Review A*, 87(1):015602, 2013.

- [74] E. Ruokokoski, J. AM Huhtamäki, and M. Möttönen. Stationary states of trapped spin-orbit-coupled bose-einstein condensates. *Physical Review A*, 86(5):051607, 2012.
- [75] Z. F. Xu, Y. Kawaguchi, L. You, and M. Ueda. Symmetry classification of spin-orbit-coupled spinor bose-einstein condensates. *Physical Review A*, 86(3):033628, 2012.
- [76] A. L. Fetter. Vortex dynamics in spin-orbit-coupled bose-einstein condensates. *Physical Review A*, 89(2):023629, 2014.
- [77] G. J. Conduit. Line of dirac monopoles embedded in a bose-einstein condensate. *Physical Review A*, 86(2):021605, 2012.
- [78] T. Kawakami, T. Mizushima, M. Nitta, and K. Machida. Stable skyrmions in $su(2)$ gauged bose-einstein condensates. *Physical Review Letters*, 109(1):015301, 2012.
- [79] C.-F. Liu and W. M. Liu. Spin-orbit-coupling-induced half-skyrmion excitations in rotating and rapidly quenched spin-1 bose-einstein condensates. *Physical Review A*, 86(3):033602, 2012.
- [80] C. Wang, C. Gao, C.-M. Jian, and H. Zhai. Spin-orbit coupled spinor bose-einstein condensates. *Physical Review Letters*, 105(16):160403, 2010.
- [81] S. Sinha, R. Nath, and L. Santos. Trapped two-dimensional condensates with synthetic spin-orbit coupling. *Physical Review Letters*, 107(27):270401, 2011.
- [82] Y. Li, L. P. Pitaevskii, and S. Stringari. Quantum tricriticality and phase transitions in spin-orbit coupled bose-einstein condensates. *Physical Review Letters*, 108(22):225301, 2012.
- [83] V. Achilleos, D. J. Frantzeskakis, P. G. Kevrekidis, and D. E. Pelinovsky. Matter-wave bright solitons in spin-orbit coupled bose-einstein condensates. *Physical Review Letters*, 110(26):264101, 2013.
- [84] Y. Xu, Y. Zhang, B. Wu, et al. Bright solitons in spin-orbit-coupled bose-einstein condensates. *Physical Review A*, 87(1):013614, 2013.

- [85] L. Salasnich and B. A. Malomed. Localized modes in dense repulsive and attractive bose-einstein condensates with spin-orbit and rabi couplings. *Physical Review A*, 87(6):063625, 2013.
- [86] H. Sakaguchi, B. Li, and B. A. Malomed. Creation of two-dimensional composite solitons in spin-orbit-coupled self-attractive bose-einstein condensates in free space. *Physical Review E*, 89(3):032920, 2014.
- [87] Y.-C. Zhang, Z.-W. Zhou, B. A. Malomed, and H. Pu. Stable solitons in three dimensional free space without the ground state: Self-trapped bose-einstein condensates with spin-orbit coupling. *Physical Review Letters*, 115(25):253902, 2015.
- [88] I. Ferrier-Barbut, H. Kadau, M. Schmitt, M. Wenzel, and T. Pfau. Observation of quantum droplets in a strongly dipolar bose gas. *Physical Review Letters*, 116(21):215301, 2016.
- [89] H. Kadau, M. Schmitt, M. Wenzel, C. Wink, T. Maier, I. Ferrier-Barbut, and T. Pfau. Observing the rosenzweig instability of a quantum ferrofluid. *Nature*, 530(7589):194–197, 2016.
- [90] G. Ferioli, G. Semeghini, L. Masi, G. Giusti, G. Modugno, M. Inguscio, A. Gallemí, A. Recati, and M. Fattori. Collisions of self-bound quantum droplets. *Physical Review Letters*, 122(9):090401, 2019.
- [91] G. Semeghini, G. Ferioli, L. Masi, C. Mazzinghi, L. Wolswijk, F. Minardi, M. Modugno, G. Modugno, M. Inguscio, and M. Fattori. Self-bound quantum droplets of atomic mixtures in free space. *Physical Review Letters*, 120(23):235301, 2018.
- [92] C. R. Cabrera, L. Tanzi, J. Sanz, B. Naylor, P. Thomas, P. Cheiney, and L. Tarruell. Quantum liquid droplets in a mixture of bose-einstein condensates. *Science*, 359(6373):301–304, 2018.
- [93] M. J. Ablowitz and H. Segur. Solitons and the inverse scattering transform, 1981.
- [94] P. G. Drazin and R. S. Johnson. *Solitons: an introduction*, volume 2. Cambridge university press, 1989.
- [95] T. Dauxois and M. Peyrard. *Physics of solitons*. Cambridge University Press, 2006.

- [96] S. A. Morgan, R. J. Ballagh, and K. Burnett. Solitary-wave solutions to nonlinear schrödinger equations. *Physical Review A*, 55(6):4338, 1997.
- [97] B. A. Malomed. Vortex solitons: Old results and new perspectives. *Physica D: Nonlinear Phenomena*, 399:108–137, 2019.
- [98] T. Busch and J. R. Anglin. Dark-bright solitons in inhomogeneous bose-einstein condensates. *Physical Review Letters*, 87(1):010401, 2001.
- [99] C. Becker, S. Stellmer, P. Soltan-Panahi, S. Dörscher, M. Baumert, E.-M. Richter, J. Kronjäger, K. Bongs, and K. Sengstock. Oscillations and interactions of dark and dark-bright solitons in bose-einstein condensates. *Nature Physics*, 4(6):496–501, 2008.
- [100] C. Hamner, J. J. Chang, P. Engels, and M. A. Hoefer. Generation of dark-bright soliton trains in superfluid-superfluid counterflow. *Physical Review Letters*, 106(6):065302, 2011.
- [101] P. Öhberg and L. Santos. Dark solitons in a two-component bose-einstein condensate. *Physical Review Letters*, 86(14):2918, 2001.
- [102] V. M. Perez-Garcia and J. B. Beitia. Symbiotic solitons in heteronuclear multicomponent bose-einstein condensates. *Physical Review A*, 72(3):033620, 2005.
- [103] L. Salasnich and B. A. Malomed. Vector solitons in nearly one-dimensional bose-einstein condensates. *Physical Review A*, 74(5):053610, 2006.
- [104] K. Kasamatsu and M. Tsubota. Multiple domain formation induced by modulation instability in two-component bose-einstein condensates. *Physical Review Letters*, 93(10):100402, 2004.
- [105] J. Sabbatini, W. H. Zurek, and M. J. Davis. Phase separation and pattern formation in a binary bose-einstein condensate. *Physical Review Letters*, 107(23):230402, 2011.
- [106] T. P. Billam, A. L. Marchant, S. L. Cornish, S. A. Gardiner, and N. G. Parker. Bright solitary matter waves: formation, stability and interactions. *Spontaneous Symmetry Breaking, Self-Trapping, and Josephson Oscillations*, pages 403–455, 2013.
- [107] S. Gautam and S.K. Adhikari. Vortex-bright solitons in a spin-orbit-coupled spin-1 condensate. *Physical Review A*, 95(1):013608, 2017.

- [108] S. Gautam and S. K. Adhikari. Three-dimensional vortex-bright solitons in a spin-orbit-coupled spin-1 condensate. *Physical Review A*, 97(1):013629, 2018.
- [109] S.K. Adhikari. Multiring, stripe, and superlattice solitons in a spin-orbit-coupled spin-1 condensate. *Physical Review A*, 103(1):L011301, 2021.
- [110] A. F. Andreev and I. M. Lifshits. Quantum theory of defects in crystals. *Zhur Eksper Teoret Fiziki*, 56(6):2057–2068, 1969.
- [111] A. J. Leggett. Can a solid be” superfluid”? *Physical Review Letters*, 25(22):1543, 1970.
- [112] D. A. Kirzhnits and Y. A. Nepomnyashchii. Coherent crystallization of quantum liquid. *Soviet Physics JETP*, 32(6), 1971.
- [113] M. Boninsegni and N. V. Prokof’ev. Colloquium: Supersolids: What and where are they? *Reviews of Modern Physics*, 84(2):759, 2012.
- [114] V. I. Yukalov. Saga of superfluid solids. *Physics*, 2(1):49–66, 2020.
- [115] D. Y. Kim and M. H. W. Chan. Absence of supersolidity in solid helium in porous vycor glass. *Physical Review Letters*, 109(15):155301, 2012.
- [116] Z.-K. Lu, Y. Li, D. S. Petrov, and G. V. Shlyapnikov. Stable dilute supersolid of two-dimensional dipolar bosons. *Physical Review Letters*, 115(7):075303, 2015.
- [117] M. Schmitt, M. Wenzel, F. Böttcher, I. Ferrier-Barbut, and T. Pfau. Self-bound droplets of a dilute magnetic quantum liquid. *Nature*, 539(7628):259–262, 2016.
- [118] F. Böttcher, J.-N. Schmidt, M. Wenzel, J. Hertkorn, M. Guo, T. Langen, and T. Pfau. Transient supersolid properties in an array of dipolar quantum droplets. *Physical Review X*, 9(1):011051, 2019.
- [119] L. Chomaz, D. Petter, P. Ilzhöfer, G. Natale, A. Trautmann, C. Politi, G. Durastante, R. M. W. Van Bijnen, A. Patscheider, M. Sohmen, et al. Long-lived and transient supersolid behaviors in dipolar quantum gases. *Physical Review X*, 9(2):021012, 2019.
- [120] L. Tanzi, E. Lucioni, F. Famà, J. Catani, A. Fioretti, C. Gabbanini, R. N. Bisset, L. Santos, and G. Modugno. Observation of a dipolar quantum gas with metastable supersolid properties. *Physical Review Letters*, 122(13):130405, 2019.

- [121] J.-R. Li, J. Lee, W. Huang, S. Burchesky, B. Shteynas, F. Ç. Top, A. O. Jamison, and W. Ketterle. A stripe phase with supersolid properties in spin–orbit-coupled bose–einstein condensates. *Nature*, 543(7643):91–94, 2017.
- [122] K. T. Geier, G. I. Martone, P. Hauke, W. Ketterle, and S. Stringari. Dynamics of stripe patterns in supersolid spin-orbit-coupled bose gases. *Physical Review Letters*, 130:156001, 2023.
- [123] Mingyang Guo, Fabian Böttcher, Jens Hertkorn, Jan-Niklas Schmidt, Matthias Wenzel, Hans Peter Büchler, Tim Langen, and Tilman Pfau. The low-energy goldstone mode in a trapped dipolar supersolid. *Nature*, 574(7778):386–389, 2019.
- [124] I. Bloch. Quantum gases in optical lattices. *Physics World*, 17(4):25, 2004.
- [125] M. Lewenstein, A. Sanpera, V. Ahufinger, B. Damski, A. Sen, and U. Sen. Ultracold atomic gases in optical lattices: mimicking condensed matter physics and beyond. *Advances in Physics*, 56(2):243–379, 2007.
- [126] I. Bloch, J. Dalibard, and S. Nascimbene. Quantum simulations with ultracold quantum gases. *Nature Physics*, 8(4):267–276, 2012.
- [127] R. P. Feynman. Simulating physics with computers. In *Feynman and computation*, pages 133–153. CRC Press, 2018.
- [128] Christian Trefzger, C Menotti, B Capogrosso-Sansone, and M Lewenstein. Ultracold dipolar gases in optical lattices. *Journal of Physics B: Atomic, Molecular and Optical Physics*, 44(19):193001, 2011.
- [129] D. Jaksch, C. Bruder, J. I. Cirac, C. W. Gardiner, and P. Zoller. Cold bosonic atoms in optical lattices. *Physical Review Letters*, 81(15):3108, 1998.
- [130] M. P. A. Fisher, P. B. Weichman, G. Grinstein, and D. S. Fisher. Boson localization and the superfluid-insulator transition. *Physical Review B*, 40(1):546, 1989.
- [131] A. Auerbach. *Interacting electrons and quantum magnetism*. Springer Science & Business Media, 1998.

- [132] M. Greiner, O. Mandel, T. Esslinger, T. W. Hänsch, and I. Bloch. Quantum phase transition from a superfluid to a mott insulator in a gas of ultracold atoms. *Nature*, 415(6867):39–44, 2002.
- [133] R. Nandkishore and D. A. Huse. Many-body localization and thermalization in quantum statistical mechanics. *Annual Review of Condensed Matter Physics*, 6(1):15–38, 2015.
- [134] A. Polkovnikov, K. Sengupta, A. Silva, and M. Vengalattore. Colloquium: Nonequilibrium dynamics of closed interacting quantum systems. *Reviews of Modern Physics*, 83(3):863, 2011.
- [135] A. Del Campo and W. H. Zurek. Universality of phase transition dynamics: Topological defects from symmetry breaking. *International Journal of Modern Physics A*, 29(08):1430018, 2014.
- [136] E. Farhi, J. Goldstone, S. Gutmann, J. Lapan, A. Lundgren, and D. Preda. A quantum adiabatic evolution algorithm applied to random instances of an np-complete problem. *Science*, 292(5516):472–475, 2001.
- [137] T. W. B. Kibble. Topology of cosmic domains and strings. *Journal of Physics A: Mathematical and General*, 9(8):1387, 1976.
- [138] W. H. Zurek. Cosmological experiments in superfluid helium? *Nature*, 317(6037):505–508, 1985.
- [139] A. J. Bray. Theory of phase-ordering kinetics. *Advances in Physics*, 51(2):481–587, 2002.
- [140] S. Puri. Kinetics of phase transitions. In *Kinetics of Phase transitions*, pages 13–74. CRC press, 2009.
- [141] T. Donner, S. Ritter, T. Bourdel, A. Ottl, M. Kohl, and T. Esslinger. Critical behavior of a trapped interacting bose gas. *Science*, 315(5818):1556–1558, 2007.
- [142] C. N. Weiler, T. W. Neely, D. R. Scherer, A. S. Bradley, M. J. Davis, and B. P. Anderson. Spontaneous vortices in the formation of bose–einstein condensates. *Nature*, 455(7215):948–951, 2008.

- [143] S. Donadello, S. Serafini, T. Bienaimé, F. Dalfovo, G. Lamporesi, and G. Ferrari. Creation and counting of defects in a temperature-quenched bose-einstein condensate. *Physical Review A*, 94(2):023628, 2016.
- [144] L. Chomaz, L. Corman, T. Bienaimé, R. Desbuquois, C. Weitenberg, S. Nascimbene, J. Beugnon, and J. Dalibard. Emergence of coherence via transverse condensation in a uniform quasi-two-dimensional bose gas. *Nature communications*, 6(1):6162, 2015.
- [145] K. Damle, S. N. Majumdar, and S. Sachdev. Phase ordering kinetics of the bose gas. *Physical Review A*, 54(6):5037, 1996.
- [146] S. Braun, M. Friesdorf, S. S. Hodgman, M. Schreiber, J. P. Ronzheimer, A. Riera, M. Del Rey, I. Bloch, J. Eisert, and U. Schneider. Emergence of coherence and the dynamics of quantum phase transitions. *Proceedings of the National Academy of Sciences*, 112(12):3641–3646, 2015.
- [147] L. Salasnich, W. B. Cardoso, and B. A. Malomed. Localized modes in quasi-two-dimensional bose-einstein condensates with spin-orbit and rabi couplings. *Physical Review A*, 90:033629, 2014.
- [148] H. Sakaguchi and B. A. Malomed. Discrete and continuum composite solitons in bose-einstein condensates with the rashba spin-orbit coupling in one and two dimensions. *Physical Review E*, 90:062922, 2014.
- [149] Z. F. Xu, R. Lü, and L. You. Emergent patterns in a spin-orbit-coupled spin-2 bose-einstein condensate. *Physical Review A*, 83:053602, 2011.
- [150] H. Zhai. Spin-orbit coupled quantum gases. *International Journal of Modern Physics B*, 26(01):1230001, 2012.
- [151] W. Han, X.-F. Zhang, S.-W. Song, H. Saito, W. Zhang, W.-M. Liu, and S.-G. Zhang. Double-quantum spin vortices in su (3) spin-orbit-coupled bose gases. *Physical Review A*, 94(3):033629, 2016.
- [152] A Crubellier, O Dulieu, F Masnou-Seeuws, M Elbs, H Knöckel, and E Tiemann. Simple determination of na2 scattering lengths using observed bound levels at the ground state

asymptote. *The European Physical Journal D-Atomic, Molecular, Optical and Plasma Physics*, 6(2):211–220, 1999.

- [153] S. Gautam and S.K. Adhikari. Vector solitons in a spin-orbit-coupled spin-2 bose-einstein condensate. *Physical Review A*, 91(6):063617, 2015.
- [154] S. K. Adhikari. Supersolid-like states in a two-dimensional trapped spin-orbit-coupled spin-1 condensate. *Journal of Physics: Condensed Matter*, 33(26):265402, 2021.
- [155] P. Kaur, S. Gautam, and S.K. Adhikari. Supersolid-like solitons in a spin-orbit-coupled spin-2 condensate. *Physical Review A*, 105(2):023303, 2022.
- [156] T. Mizushima, K. Machida, and T. Kita. Mermin-ho vortex in ferromagnetic spinor bose-einstein condensates. *Physical Review Letters*, 89(3):030401, 2002.
- [157] S. Pal, R. Bai, S. Bandyopadhyay, K. Suthar, and D. Angom. Enhancement of the bose glass phase in the presence of an artificial gauge field. *Physical Review A*, 99:053610, 2019.
- [158] C. V. Ciobanu, S.-K. Yip, and T.-L. Ho. Phase diagrams of $f = 2$ spinor bose-einstein condensates. *Physical Review A*, 61(3):033607, 2000.
- [159] A. Widera, F. Gerbier, S. Fölling, T. Gericke, O. Mandel, and I. Bloch. Precision measurement of spin-dependent interaction strengths for spin-1 and spin-2 rubidium-87 atoms. *New Journal of Physics*, 8(8):152, 2006.
- [160] S. Inouye, M. R. Andrews, J. Stenger, H.-J. Miesner, D. M. Stamper-Kurn, and W. Ketterle. Observation of feshbach resonances in a bose-einstein condensate. *Nature*, 392(6672):151–154, 1998.
- [161] D. Vudragović, I. Vidanović, A. Balaž, P. Muruganandam, and S. K. Adhikari. C programs for solving the time-dependent gross-pitaevskii equation in a fully anisotropic trap. *Computer Physics Communications*, 183(9):2021–2025, 2012.
- [162] L. E. Young-S, D. Vudragović, P. Muruganandam, S. K. Adhikari, and A. Balaž. Openmp fortran and c programs for solving the time-dependent gross-pitaevskii equation in an anisotropic trap. *Computer Physics Communications*, 204:209–213, 2016.

- [163] L. E. Young-S, P. Muruganandam, S. K. Adhikari, V. Lončar, D. Vudragović, and A. Balaž. Openmp gnu and intel fortran programs for solving the time-dependent gross-pitaevskii equation. *Computer Physics Communications*, 220:503–506, 2017.
- [164] R. Ravisankar, D. Vudragović, P. Muruganandam, A. Balaž, and S. K. Adhikari. Spin-1 spin-orbit-and rabi-coupled bose-einstein condensate solver. *Computer Physics Communications*, 259:107657, 2021.
- [165] H. Sakaguchi and B. A. Malomed. Two-dimensional solitons in the gross-pitaevskii equation with spatially modulated nonlinearity. *Physical Review E*, 73(2):026601, 2006.
- [166] B. Bakkali-Hassani, C. Maury, Y.-Q. Zou, É. Le Cerf, R. Saint-Jalm, P. C. M. Castilho, S. Nascimbene, J. Dalibard, and J. Beugnon. Realization of a townes soliton in a two-component planar bose gas. *Physical Review Letters*, 127(2):023603, 2021.
- [167] S. K. Adhikari. Spontaneous spatial order in two-dimensional ferromagnetic spin-orbit coupled uniform spin-1 condensate solitons. *Physics Letters A*, 388:127042, 2021.
- [168] Y. Li, G. I. Martone, L. P. Pitaevskii, and S. Stringari. Superstripes and the excitation spectrum of a spin-orbit-coupled bose-einstein condensate. *Physical Review Letters*, 110(23):235302, 2013.
- [169] S. K. Adhikari. Spatial order in a two-dimensional spin-orbit-coupled spin-1/2 condensate: superlattice, multi-ring and stripe formation. *Journal of Physics: Condensed Matter*, 33(42):425402, 2021.
- [170] P. Kaur, S. Gautam, and S. K. Adhikari. Supersolid-like solitons in two-dimensional non-magnetic spin-orbit coupled spin-1 and spin-2 condensates. *Physics Letters A*, 455:128507, 2022.
- [171] Z. Wu, L. Zhang, W. Sun, X.-T. Xu, B.-Z. Wang, S.-C. Ji, Y. Deng, S. Chen, X.-J. Liu, and J.-W. Pan. Realization of two-dimensional spin-orbit coupling for bose-einstein condensates. *Science*, 354:83, 2016.
- [172] S. Zhang and G.-B. Jo. Recent advances in spin-orbit coupled quantum gases. *Journal of Physics and Chemistry of Solids*, 128:75, 2019.

- [173] J. Radić, A. Di Ciolo, K. Sun, and V. Galitski. Exotic quantum spin models in spin-orbit-coupled mott insulators. *Physical Review Letters*, 109:085303, 2012.
- [174] C. Hickey and A. Paramekanti. Thermal phase transitions of strongly correlated bosons with spin-orbit coupling. *Physical Review Letters*, 113:265302, 2014.
- [175] A. Dutta, A. Joshi, K. Sengupta, and P. Majumdar. Thermal transitions of the modulated superfluid for spin-orbit coupled correlated bosons in an optical lattice. *Physical Review B*, 99:195126, 2019.
- [176] Y. Zhang, G. Chen, and C. Zhang. Tunable spin-orbit coupling and quantum phase transition in a trapped bose-einstein condensate. *Scientific Reports*, 3:1937, 2013.
- [177] M. C. Gutzwiller. Effect of correlation on the ferromagnetism of transition metals. *Physical Review Letters*, 10:159, 1963.
- [178] D. S. Rokhsar and B. G. Kotliar. Gutzwiller projection for bosons. *Physical Review B*, 44:10328, 1991.
- [179] W. Krauth, M. Caffarel, and J.-P. Bouchaud. Gutzwiller wave function for a model of strongly interacting bosons. *Physical Review B*, 45:3137, 1992.
- [180] K. Sheshadri, H. R. Krishnamurthy, R. Pandit, and T. V. Ramakrishnan. Superfluid and insulating phases in an interacting-boson model: Mean-field theory and the RPA. *EPL*, 22:257, 1993.
- [181] C. Menotti, C. Trefzger, and M. Lewenstein. Metastable states of a gas of dipolar bosons in a 2d optical lattice. *Physical Review Letters*, 98:235301, 2007.
- [182] M. Iskin. Route to supersolidity for the extended bose-hubbard model. *Physical Review A*, 83:051606, 2011.
- [183] S. Bandyopadhyay, R. Bai, S. Pal, K. Suthar, R. Nath, and D. Angom. Quantum phases of canted dipolar bosons in a two-dimensional square optical lattice. *Physical Review A*, 100:053623, 2019.

- [184] K. Suthar, R. Kraus, H. Sable, D. Angom, G. Morigi, and J. Zakrzewski. Staggered superfluid phases of dipolar bosons in two-dimensional square lattices. *Physical Review B*, 102:214503, 2020.
- [185] L. Chen, H. Pu, Z.-Q. Yu, and Y. Zhang. Collective excitation of a trapped bose-einstein condensate with spin-orbit coupling. *Physical Review A*, 95:033616, 2017.
- [186] R. Bai, D. Gaur, H. Sable, S. Bandyopadhyay, K. Suthar, and D. Angom. Segregated quantum phases of dipolar bosonic mixtures in two-dimensional optical lattices. *Physical Review A*, 102:043309, 2020.
- [187] D. Yamamoto, T. Ozaki, C. A. R. Sá de Melo, and I. Danshita. First-order phase transition and anomalous hysteresis of binary bose mixtures in an optical lattice. *Journal of Low Temperature Physics*, 175:258, 2013.
- [188] D. Yamamoto, T. Ozaki, C. A. R. Sá de Melo, and I. Danshita. First-order phase transition and anomalous hysteresis of bose gases in optical lattices. *Physical Review A*, 88:033624, 2013.
- [189] Y. Kato, D. Yamamoto, and I. Danshita. Quantum tricriticality at the superfluid-insulator transition of binary bose mixtures. *Physical Review Letters*, 112:055301, 2014.
- [190] S. Mandal, K. Saha, and K. Sengupta. Superfluid-insulator transition of two-species bosons with spin-orbit coupling. *Physical Review B*, 86:155101, 2012.
- [191] G.-H. Chen and Y.-S. Wu. Quantum phase transition in a multicomponent bose-einstein condensate in optical lattices. *Physical Review A*, 67:013606, 2003.
- [192] R. Bai, S. Bandyopadhyay, S. Pal, K. Suthar, and D. Angom. Bosonic quantum hall states in single-layer two-dimensional optical lattices. *Physical Review A*, 98:023606, 2018.
- [193] K. Suthar, H. Sable, R. Bai, S. Bandyopadhyay, S. Pal, and D. Angom. Supersolid phase of the extended bose-hubbard model with an artificial gauge field. *Physical Review A*, 102:013320, 2020.

- [194] T. M. Bersano, J. Hou, S. Mossman, V. Gokhroo, X.-W. Luo, K. Sun, C. Zhang, and P. Engels. Experimental realization of a long-lived striped bose-einstein condensate induced by momentum-space hopping. *Physical Review A*, 99:051602, 2019.
- [195] P. Buonsante and A. Vezzani. Phase diagram for ultracold bosons in optical lattices and superlattices. *Physical Review A*, 70:033608, 2004.
- [196] K. Suthar, P. Kaur, S. Gautam, and D. Angom. Spin-orbit-coupling-driven superfluid states in optical lattices at zero and finite temperatures. *Physical Review A*, 104(4):043320, 2021.
- [197] S. Sachdev. Quantum phase transitions. *Physics world*, 12(4):33, 1999.
- [198] T. W. B. Kibble. Some implications of a cosmological phase transition. *Physics Reports*, 67(1):183–199, 1980.
- [199] W. H. Zurek. Cosmic strings in laboratory superfluids and the topological remnants of other phase transitions. *Acta physica polonica. B*, 24(7):1301–1311, 1993.
- [200] W. H. Zurek. Cosmological experiments in condensed matter systems. *Physics Reports*, 276(4):177–221, 1996.
- [201] N. Bevis, M. Hindmarsh, M. Kunz, and J. Urrestilla. Fitting cosmic microwave background data with cosmic strings and inflation. *Physical Review Letters*, 100(2):021301, 2008.
- [202] V. M. H. Ruutu, V. B. Eltsov, A. J. Gill, T. W. B. Kibble, M. Krusius, Y. G. Makhlin, B. Placais, G. E. Volovik, and W. Xu. Vortex formation in neutron-irradiated superfluid ^3He as an analogue of cosmological defect formation. *Nature*, 382(6589):334–336, 1996.
- [203] R. Carmi, E. Polturak, and G. Koren. Observation of spontaneous flux generation in a multi-josephson-junction loop. *Physical Review Letters*, 84(21):4966, 2000.
- [204] I. Chuang, R. Durrer, N. Turok, and B. Yurke. Cosmology in the laboratory: Defect dynamics in liquid crystals. *Science*, 251(4999):1336–1342, 1991.
- [205] L. E. Sadler, J. M. Higbie, S. R. Leslie, M. Vengalattore, and D. M. Stamper-Kurn. Spontaneous symmetry breaking in a quenched ferromagnetic spinor bose–einstein condensate. *Nature*, 443(7109):312–315, 2006.

- [206] G. Lamporesi, S. Donadello, S. Serafini, F. Dalfovo, and G. Ferrari. Spontaneous creation of kibble–zurek solitons in a bose–einstein condensate. *Nature Physics*, 9(10):656–660, 2013.
- [207] E. Nicklas, M. Karl, M. Höfer, A. Johnson, W. Muessel, H. Strobel, J. Tomkovič, T. Gasenzer, and M. K. Oberthaler. Observation of scaling in the dynamics of a strongly quenched quantum gas. *Physical Review Letters*, 115(24):245301, 2015.
- [208] N. Navon, A. L. Gaunt, R. P. Smith, and Z. Hadzibabic. Critical dynamics of spontaneous symmetry breaking in a homogeneous bose gas. *Science*, 347(6218):167–170, 2015.
- [209] M. Anquez, B. A. Robbins, H. M. Bharath, M. Boguslawski, T. M. Hoang, and M. S. Chapman. Quantum kibble-zurek mechanism in a spin-1 bose-einstein condensate. *Physical Review Letters*, 116(15):155301, 2016.
- [210] A. Keesling, A. Omran, H. Levine, H. Bernien, H. Pichler, S. Choi, R. Samajdar, S. Schwartz, P. Silvi, S. Sachdev, et al. Quantum kibble–zurek mechanism and critical dynamics on a programmable rydberg simulator. *Nature*, 568(7751):207–211, 2019.
- [211] C.-R. Yi, S. Liu, R.-H. Jiao, J.-Y. Zhang, Y.-S. Zhang, and S. Chen. Exploring inhomogeneous kibble-zurek mechanism in a spin-orbit coupled bose-einstein condensate. *Physical Review Letters*, 125(26):260603, 2020.
- [212] D. Chen, M. White, C. Borries, and B. DeMarco. Quantum quench of an atomic mott insulator. *Physical Review Letters*, 106(23):235304, 2011.
- [213] L. W. Clark, L. Feng, and C. Chin. Universal space-time scaling symmetry in the dynamics of bosons across a quantum phase transition. *Science*, 354(6312):606–610, 2016.
- [214] B. Ko, J. W. Park, and Y.-I. Shin. Kibble–zurek universality in a strongly interacting fermi superfluid. *Nature Physics*, 15(12):1227–1231, 2019.
- [215] X.-P. Liu, X.-C. Yao, Y. Deng, Y.-X. Wang, X.-Q. Wang, X. Li, Q. Chen, Y.-A. Chen, and J.-W. Pan. Dynamic formation of quasicondensate and spontaneous vortices in a strongly interacting fermi gas. *Physical Review Research*, 3(4):043115, 2021.

- [216] K. Shimizu, Y. Kuno, T. Hirano, and I. Ichinose. Dynamics of a quantum phase transition in the bose-hubbard model: Kibble-zurek mechanism and beyond. *Physical Review A*, 97(3):033626, 2018.
- [217] K. Shimizu, T. Hirano, J. Park, Y. Kuno, and I. Ichinose. Out-of-equilibrium dynamics of multiple second-order quantum phase transitions in an extended bose-hubbard model: Superfluid, supersolid, and density wave. *Physical Review A*, 98(6):063603, 2018.
- [218] Y. Zhou, Y. Li, R. Nath, and W. Li. Quench dynamics of rydberg-dressed bosons on two-dimensional square lattices. *Physical Review A*, 101(1):013427, 2020.
- [219] K. Shimizu, T. Hirano, J. Park, Y. Kuno, and I. Ichinose. Dynamics of first-order quantum phase transitions in extended bose-hubbard model: from density wave to superfluid and vice versa. *New Journal of Physics*, 20(8):083006, 2018.
- [220] H. Wang, X. He, S. Li, H. Li, and B. Liu. Non-equilibrium dynamics of ultracold lattice bosons inside a cavity. *arXiv preprint arXiv:2209.12408*, 2022.
- [221] H. Sable, D. Gaur, S. Bandyopadhyay, R. Nath, and D. Angom. Quantum quench dynamics of tilted dipolar bosons in 2d optical lattices. *arXiv preprint arXiv:2106.01725*, 2021.
- [222] J.-M. Cui, Y.-F. Huang, Z. Wang, D.-Y. Cao, J. Wang, W.-M. Lv, L. Luo, A. Del Campo, Y.-J. Han, C.-F. Li, et al. Experimental trapped-ion quantum simulation of the kibble-zurek dynamics in momentum space. *Scientific Reports*, 6(1):33381, 2016.
- [223] E. Demler and F. Zhou. Spinor bosonic atoms in optical lattices: symmetry breaking and fractionalization. *Physical Review Letters*, 88(16):163001, 2002.
- [224] B. Paredes and J. I. Cirac. From cooper pairs to luttinger liquids with bosonic atoms in optical lattices. *Physical Review Letters*, 90(15):150402, 2003.
- [225] A. B. Kuklov and B. V. Svistunov. Counterflow superfluidity of two-species ultracold atoms in a commensurate optical lattice. *Physical Review Letters*, 90(10):100401, 2003.
- [226] S. K. Yip. Dimer state of spin-1 bosons in an optical lattice. *Physical Review Letters*, 90(25):250402, 2003.

- [227] Y. Kato, D. Yamamoto, and I. Danshita. Quantum tricriticality at the superfluid-insulator transition of binary bose mixtures. *Physical Review Letters*, 112(5):055301, 2014.
- [228] L.-Y. Qiu, H.-Y. Liang, Y.-B. Yang, H.-X. Yang, T. Tian, Y. Xu, and L.-M. Duan. Observation of generalized kibble-zurek mechanism across a first-order quantum phase transition in a spinor condensate. *Science Advances*, 6(21):eaba7292, 2020.
- [229] H. Y. Liang, L. Y. Qiu, Y. B. Yang, H. X. Yang, T. Tian, Y. Xu, and L. M. Duan. Observation of heat scaling across a first-order quantum phase transition in a spinor condensate. *New Journal of Physics*, 23(3):033038, 2021.
- [230] I. B. Coulamy, A. Saguia, and M. S. Sarandy. Dynamics of the quantum search and quench-induced first-order phase transitions. *Physical Review E*, 95(2):022127, 2017.
- [231] B. Damski, L. Santos, E. Tiemann, M. Lewenstein, S. Kotochigova, P. Julienne, and P. Zoller. Creation of a dipolar superfluid in optical lattices. *Physical Review Letters*, 90(11):110401, 2003.
- [232] R. Bai, D. Gaur, H. Sable, S. Bandyopadhyay, K. Suthar, and D. Angom. Segregated quantum phases of dipolar bosonic mixtures in two-dimensional optical lattices. *Physical Review A*, 102(4):043309, 2020.
- [233] T. Ozaki, I. Danshita, and T. Nikuni. Bose-bose mixtures in an optical lattice: First-order superfluid-insulator transition and elementary excitations. *arXiv preprint arXiv:1210.1370*, 2012.
- [234] D. Yamamoto, T. Ozaki, C. A. R. S. de Melo, and I. Danshita. First-order phase transition and anomalous hysteresis of bose gases in optical lattices. *Physical Review A*, 88(3):033624, 2013.
- [235] L. D. F. De Parny, F. Hébert, V. G. Rousseau, R. T. Scalettar, and G. G. Batrouni. Ground-state phase diagram of spin- $\frac{1}{2}$ bosons in a two-dimensional optical lattice. *Physical Review B*, 84(6):064529, 2011.
- [236] A. Dhar, D. Rossini, and B. P. Das. Quasiadiabatic dynamics of ultracold bosonic atoms in a one-dimensional optical superlattice. *Physical Review A*, 92(3):033610, 2015.

- [237] T. Caneva, R. Fazio, and G. E. Santoro. Adiabatic quantum dynamics of the lipkin-meshkov-glick model. *Physical Review B*, 78(10):104426, 2008.
- [238] F. Pellegrini, S. Montangero, G. E. Santoro, and R. Fazio. Adiabatic quenches through an extended quantum critical region. *Physical Review B*, 77(14):140404, 2008.
- [239] Y. Machida and K. Kasamatsu. Application of the inhomogeneous kibble-zurek mechanism to quench dynamics in the transition from a mott insulator to a superfluid in a finite system. *Physical Review A*, 103(1):013310, 2021.
- [240] P. Kaur, K. Suthar, D. Angom, and S. Gautam. Out-of-equilibrium dynamics of bose-bose mixtures in optical lattices. *arXiv preprint arXiv:2307.13057*, 2023.
- [241] P Cheiney, CR Cabrera, J Sanz, B Naylor, L Tanzi, and L Tarruell. Bright soliton to quantum droplet transition in a mixture of bose-einstein condensates. *Physical review letters*, 120(13):135301, 2018.
- [242] C Trefzger and K Sengupta. Nonequilibrium dynamics of the bose-hubbard model: a projection-operator approach. *Physical Review Letters*, 106(9):095702, 2011.
- [243] Deepak Gaur, Hrushikesh Sable, and D Angom. Quench dynamics across the mi-sf quantum phase transition with cluster mean field theory. *arXiv preprint arXiv:2309.06272*, 2023.
- [244] D. L. Campbell and I. B. Spielman. Rashba realization: Raman with rf. *New Journal of Physics*, 18(3):033035, 2016.
- [245] T.-L. Ho. Spinor bose condensates in optical traps. *Physical Review Letters*, 81(4):742, 1998.
- [246] T. Ohmi and K. Machida. Bose-einstein condensation with internal degrees of freedom in alkali atom gases. *Journal of the Physical Society of Japan*, 67(6):1822–1825, 1998.
- [247] L. Salasnich, A. Parola, and L. Reatto. Effective wave equations for the dynamics of cigar-shaped and disk-shaped bose condensates. *Physical Review A*, 65(4):043614, 2002.

- [248] R. K. Kumar, V. Lončar, P. Muruganandam, S. K. Adhikari, and A. Balaž. C and fortran openmp programs for rotating bose–einstein condensates. *Computer Physics Communications*, 240:74–82, 2019.
- [249] <http://www.fftw.org/>.
- [250] <https://data.mendeley.com/datasets/tct7vjh994/2>.